Direct Piston Displacement Control of Free-Piston Stirling Engines

Johannes Matthias Strauss

Dissertation presented for the degree
Doctor of Philosophy
in the Faculty of Engineering

Promoter:

Prof M.J. Kamper
Department of Electrical and Electronic Engineering

December 2013

Declaration

By submitting this dissertation electronically, I declare that the entirety of the work contained therein is my own, original work, that I am the sole author thereof (save to the extent explicitly otherwise stated), that reproduction and publication thereof by Stellenbosch University will not infringe any third party rights and that I have not previously in its entirety or in part submitted it for obtaining any qualification.

Date: December 2013 .....

*

Acknowledgements

I would like to hereby thank the following persons:

- Prof Maarten J. Kamper, thank you for your patient guidance.
- My lovely wife, Anneke, who constantly reminded me to persevere. Thank you that we could enjoy every achievement and that you supported me through all uncertainty.
- My children, Roux and Ronel. The mere thought of you was enough for me to never give up.

Soli Deo Gloria.

To Anneke.

Abstract

Control of beta-type free-piston Stirling engines has been the topic of research and development for many years. In this dissertation, an alternative approach to free-piston Stirling engine control, namely direct piston displacement control, is proposed.

Direct piston displacement control entails the instantaneous and direct control of the piston displacement to control the engine according to preferred criteria, e.g. maximum power conversion or efficiency. To control free-piston engines in this manner, it is necessary to independently control both the displacement of the displacer and the power piston in real time. The primary arrangement by which to achieve this is through external control of the instantaneous forces exerted by the linear electrical machines fixed to the pistons. The challenge of displacement control is whether suitable linear machine technology exists or whether technology could be established that would adhere to the requirements of real time direct control.

To answer the question whether direct piston displacement control is at all possible, a process was followed to set specifications that linear machines should adhere to and to set design guidelines for linear machines and free-piston Stirling engines.

The first step was to establish the ability to simulate free-piston Stirling engine dynamics accurately. This was done by adapting a second order formulation and to verify and improve the accuracy thereof by comparing simulated results with experimental results of one of the best documented Stirling engines, namely the GPU-3 engine. It was found that this second order formulation could simulate the GPU-3 engine to a fair degree of accuracy.

Key indicators were defined and later refined with the view of setting specifications. A case study of the influence of a range of variations, including operational, dimensional and other variations, on the dynamics of the GPU-3 was then undertaken. From the findings of this case study, specifications of the key indicators and design guidelines were established.

A design optimisation approach was proposed to evaluate linear machine topologies. This approach makes specific provision for the specifications that linear machines need to adhere to, as well as for representative dynamic responses of the forces exerted on the linear machine by the displacer or the power piston. These representative responses and the associated piston displacement were determined for the displacer, the power piston and the combination of the two from the study conducted to set specifications.

An air-core, longitudinal flux linear machine with surface mounted permanent magnets (LFPM) was then evaluated to determine its suitability for direct piston displacement control. This linear machine topology was optimised for the traditional approach to establish a benchmark with which to compare subsequent optimisations. The LFPM linear machine not only compared well with other topologies for the traditional application in resonant free-piston Stirling engines, but it was found also to be able to perform displacement control for both the displacer and the power piston. For both pistons, displacement should however be limited to sinusoidal displacement, and in the case of the displacer, an important qualification is that the linear machine should be assisted by spring forces to reach practical design optimisations.

Direct piston displacement control is shown to be possible. Future work should concentrate on the practical implementation thereof in free-piston Stirling engines.

Opsomming

Die beheer van beta-tipe vrysuier Stirling enjins is al vir baie jare die onderwerp van navorsing en ontwikkeling. In hierdie proefskrif word 'n alternatiewe benadering tot vrysuier Stirling-enjins voorgestel, naamlik direkte suierverplasingsbeheer.

Direkte suierverplasingsbeheer behels die oombliklike en direkte beheer van die suierverplasing om die enjin volgens voorkeur kriteria, soos maksimum drywingsomsetting of benuttingsgraad, te beheer. Om vrysuier enjins op hierdie wyse te beheer, is dit noodsaaklik om intyds die verplasing van beide die verplaser en die werksuier onafhanklik te beheer. Die primêre wyse om dit te bereik is deur eksterne beheer van die oomblikskragte wat uitgevoer word deur die lineêre masjiene wat vas is aan die suiers. Die uitdaging van verplasingsbeheer is of toepaslike lineêre masjien tegnologie bestaan en of tegnologie gevestig kan word wat sal voldoen aan die vereistes van intydse direkte beheer.

Om die vraag te beantwoord of direkte suierverplasingsbeheer hoegenaamd moontlik is, is 'n proses gevolg om spesifikasies daar te stel waaraan lineêre masjiene moet voldoen en om ontwerpsriglyne vir lineêre masjiene en vrysuier Stirling enjins te stel.

Die eerste stap was om die vermoë daar te stel om vrysuier Stirling enjin dinamika akkuraat te simuleer. Dit is gedoen deur 'n tweede orde formulering aan te pas en om die akkuraatheid daarvan te kontroleer en te verbeter deur gesimuleerde resultate met eksperimentele resultate van een van die bes gedokumenteerde Stirling enjins, naamlik die GPU-3 enjin, te vergelyk. Daar is bevind dat die tweede orde formulering die GPU-3 tot 'n redelike mate akkuraat kon simuleer.

Sleutel aanwysers is gedefinieer en later verfyn met die oog op die daarstelling van spesifikasies. 'n Gevallestudie van die invloed van 'n reeks variasies, insluitende operasionele, dimensionele en ander variasies, op die dinamika van die GPU-3 is onderneem. Gegrond op die bevindinge van hierdie gevallestudie kon spesifikasies en ontwerpsriglyne vasgestel word.

'n Ontwerpsoptimeringsbenadering is voorgestel om lineêre masjiene te evalueer. Hierdie benadering maak spesifiek voorsiening vir die spesifikasies waaraan lineêre masjiene moet voldoen, sowel as verteenwoordigende dinamiese response van die kragte wat op die lineêre masjien van die verplaser en die werksuier uitgeoefen word. Vanaf die bevindinge van die studie wat uitgevoer is om spesifikasies daar te stel, is verteenwoordigende response en ge-

paardgaande suierverplasing bepaal vir die verplaser, die werksuier en die kombinasie van die twee.

'n Lugkern, longitudinale vloed lineêre masjien met oppervlak-gemonteerde permanente magnete (LVPM) is toe geëvalueer om die geskiktheid daarvan te bepaal vir direkte suierverplasingsbeheer. Hierdie lineêre masjien topologie is geoptimeer vir die tradisionele benadering om 'n maatstaf te vestig waarteen daaropvolgende optimerings vergelyk kan word. Die LVPM lineêre masjien vergelyk nie net goed met ander topologieë vir die tradisionele toepassing in resonante vrysuier Stirling enjins nie, maar daar is ook bevind dat dit in staat is om verplasingsbeheer te doen vir beide die verplaser en die werksuier. Vir beide suiers moet die verplasing egter tot sinusvormige verplasing beperk word en in die geval van die verplaser, is 'n belangrike kwalifikasie dat die lineêre masjien ondersteun moet word deur veerkragte om praktiese ontwerpsoptimerings te bereik.

Daar is aangetoon dat direkte suierverplasingsbeheer moontlik is. Toekomstige werk moet konsentreer op die praktiese implementering daarvan in vrysuier Stirling enjins.

Contents

Nomenclature

Roman

A	Bore area or free flow area in the regenerator.
A_{rd}	Displacer rod area.
A_{wg}	Wetted area of the heat exchanger surface.
A_{wgh}	Wetted area of the heater heat exchanger surface.
A_{wgk}	Wetted area of the cooler heat exchanger surface.
c_p	Specific heat capacity at constant pressure.
c_v	Specific heat capacity at constant volume.
C_f	Friction coefficient.
C_{ref}	Reynolds friction coefficient.
f	Cycle frequency.
F	Force of frictional drag force.
F_d	Resultant force acting on the displacer, excluding the pressure difference force.
F_{dlem}	Force exerted by the displacer linear electrical machine.
F_{dsf}	Spring force acting on the displacer.
$F_{d\Delta p}$	Pressure difference force of the displacer.
F_p	Resultant force acting on the power piston, excluding the pressure difference force.
F_{psf}	Spring force acting on the power piston.
F_{plem}	Force exerted by the power piston linear electrical machine.
F_{sf}	Spring force.
$F_{p\Delta p}$	Pressure difference force of the power piston.
$F_{\Delta p}$	Pressure difference force.
i_{lem}	Terminal current of a linear electrical machine.
i_{dlem}	Terminal current of the displacer linear electrical machine.
i_{plem}	Terminal current of the power piston linear electrical machine.
h	Overall heat transfer coefficient.
h_h	Heat transfer coefficient of the heater.
h_k	Heat transfer coefficient of the cooler.
K_{dsf}	Displacer spring constant.
K_{psf}	Power piston spring constant.

l	Length of the regenerator.
L_s	Series inductance.
m_b	Mass of working fluid in the bounce space.
m_c	Mass of working fluid in the compression space.
m_{ck}	Mass of working fluid flowing from the compression space to the cooler heat exchanger.
m_d	Mass of displacer piston.
m_e	Mass of working fluid in the expansion space.
m_{dlem}	Mass of the mover of the displacer linear electrical machine.
m_h	Mass of working fluid in the heater heat exchanger.
m_{he}	Mass of working fluid flowing from the heater heat exchanger to the expansion space.
m_i	Mass of working fluid entering a control volume.
m_{ib}	Mass of working fluid entering the bounce space.
m_k	Mass of working fluid in cooler heat exchanger.
m_{kr}	Mass of working fluid flowing from the cooler heat exchanger to the regenerator.
m_o	Mass of working fluid existing a control volume.
m_{ob}	Mass of working fluid existing the bounce space.
m_p	Mass of power piston.
m_{plem}	Mass of the mover of the power piston linear electrical machine.
m_r	Mass of working fluid in the regenerator.
M	Total mass of working fluid.
m_{rh}	Mass of working fluid flowing from the regenerator to the heater heat exchanger.
N_{Bi}	Beale number for indicated power.
N_{re}	Reynolds number.
NTU	Number of transfer units.
N_{ST}	Stanton number.
p	Instantaneous pressure or instantaneous power.
p_b	Instantaneous pressure of the bounce space.
p_c	Instantaneous pressure of the compression space.
p_e	Instantaneous pressure of the expansion space.
p_{in}	Resultant instantaneous input power.
p_{out}	Resultant instantaneous output power.
p_{ref}	Mean cycle pressure.
P_i	Indicated output power of a Stirling engine.
P_{in}	Resultant average input power.
P_{out}	Resultant average output power.
P_t	Net average output power from free-piston Stirling engine.
Q	Heat transfer.
Q_b	Heat transfer to the bounce space working fluid.
Q_h	Heat transfer to the heater heat exchanger working fluid.
Q_{hi}	Ideal heat transfer to the heater heat exchanger working fluid.

Q_k	Heat transfer to the cooler heat exchanger working fluid.
Q_{ki}	Ideal heat transfer to the cooler heat exchanger working fluid.
Q_r	Heat transfer to the regenerator working fluid.
Q_{rloss}	Regerator enthalpy loss.
$\hat{Q}_{ri}$	Single blow heat transfer to the regenerator working fluid.
R	Gas constant.
R_s	Series resistance.
T_b	Bounce space working fluid temperature.
T_c	Compression space working fluid temperature.
T_{ck}	Compression space or cooler heat exchanger working fluid temperature on condition of direction of flow.
T_e	Expansion space working fluid temperature.
T_h	Heater heat exchanger working fluid temperature.
T_{he}	Heater heat exchanger to expansion space working fluid temperature on condition of direction of flow.
T_{ib}	Working fluid temperature entering the bounce space.
T_k	Cooler heat exchanger working fluid temperature.
T_{kr}	Cooler heat exchanger or regenerator working fluid temperature on condition of direction of flow.
T_{ob}	Working fluid temperature existing the bounce space.
T_r	Regenerator working fluid temperature.
T_{rh}	Regenerator or heater heat exchanger working fluid temperature on condition of direction of flow.
T_{wh}	Heater heat exchanger wall temperature.
T_{wh}	Cooler heat exchanger wall temperature.
u	Fluid velocity.
v_{lem}	Terminal voltage of a linear electrical machine.
v_{dlem}	Terminal voltage of the displacer linear electrical machine.
v_{plem}	Terminal voltage of the power piston linear electrical machine.
v_λ	Voltage obtained from the derivitive of the flux linkage.
V	Volume.
V_b	Bounce space volume.
V_c	Compression space volume.
V_e	Expansion space volume.
V_h	Heater heat exchanger volume.
V_k	Cooler heat exchanger volume.
V_r	Regenerator volume.
V_{sw}	Swept volume.
W	Work done.
W_b	Work done by gas in the bounce space.
W_c	Work done by gas in compression space.
W_e	Work done by gas in expansion space.

x_d	Displacement of the displacer.
x_p	Displacement of the power piston.
X_{stroke}	Stroke length.

Greek letters

γ	Heat capacity ratio.
$\gamma_{Fxf/P}$	Dynamic response of the maximum force, stroke and frequency to net output power ratio.
$\Gamma_{F/F}$	Ratio of maximum forces.
$\Gamma_{F/P}$	Maximum force to power ratio.
$\Gamma_{Fxf/P}$	Maximum force, stroke and frequency to net output power ratio.
$\Gamma_{dF/F}$	Maximum rate of change of force to maximum force ratio.
$\Gamma_{dF/Ff}$	Normalised maximum rate of change of force to maximum force ratio.
ϵ	Regenerator effectiveness.
Δp	Pressure drop or pressure difference.
Δp_{bc}	Bounce space to compression space difference.
Δp_{ce}	Compression space to expansion space difference.
η	Efficiency.
μ	Dynamic viscosity.
ρ	Fluid density.
τ	Shear stress.
χ_{maxF}	Normalised displacement location of maximum force.
χ_{maxdF}	Normalised displacement location of the maximum rate of change of force.

Chapter 1

Introduction

1.1 A short history of Stirling engines

Stirling engines were given their name by the Dutch company N. V. Philips Gloeilampenfabrieken[1] following their initial redevelopment work in the 1940s and 1950s. This type of machine was originally called a hot-air engine by its inventor, Rev. Robert Stirling, who first patented his invention in 1816. In the search for higher power densities and engine efficiency it was found that gases with lighter molecular weight such as helium and hydrogen were superior to air, and the title Stirling engine was therefore considered to be a more appropriate description than "hot-air".

Although Stirling engines have many advantages, not many large engines were running by the beginning of the twentieth century. This is partly attributed to a few technical problems, such as heat withstand capabilities of materials and the engine motion that was not perfectly smooth and uniform. This kept the Stirling engine from becoming a serious rival to steam engines.

As the twentieth century progressed, another serious contender, the internal combustion engine, began to make giant strides to overtake the steam engine as the engine of the future. A serious of smaller Stirling engines were still manufactured early in the twentieth century to pump water and to power small domestic and farm equipment, but by the early 1930s the Stirling engine was nearly completely abandoned.

However, in 1937, the close-cycle air engine was again revisited in a laboratory in the south of the Netherlands. It was found to be the most promising engine to act as a small power unit to power the radio sets manufactured by the Philips Company. Good progress was made up to the beginning of 1940 with the development of several Stirling engines with power capabilities ranging from a few watt up to 500 W. It was realized that the Stirling engine could be utilized to power a much broader spectrum of appliances.

The Stirling engine programme progressed steadily during the Second World War and the development of various types of Stirling engines was seen, including the Type 10 engine ca-

[1] Later known as Philips.

pable of delivering 500 W at 1500 rpm with a maximum efficiency of 16 percent, and the Type 19 engine, a promising double-acting four cylinder engine capable of delivering 6 kW at 3000 rpm at an efficiency of 15 percent, not much different to that of internal combustion engines of the time. During this period, several improvements, such as higher efficiency and better heat transfer and heat withstand capabilities, were realized.

The development at Philips quickly became known in the Netherlands and abroad at the end of the war, resulting in several contracts and joint ventures between Philips, other Dutch firms and government agencies from abroad, such as the US Navy. Work continued on double-acting engines and Stirling refrigerators and it was felt that the Philips engine was on the threshold of commercial exploitation as a serious contender to the internal combustion engine.

In January 1952 the Engine Division was established at Philips to continue work on both Stirling engines and refrigerators. This division was however dissolved only two years later in December 1953. This sudden turn of events was partly due to serious problems encountered with Stirling engines that were felt to be passing difficulties, but that could not be resolved then. These difficulties included, amongst others, the lack of adequate and uniform heat transfer at high temperature to the working gas; lubrication of the pistons; seals and sealing; and regenerator contamination [1].

Just two engineers, namely A.H. Edens and R.J. Meijer continued to work on the Stirling engine. Meijer invented the rhombic drive, with which virtually perfect balancing could be achieved for even single cylinder engines, shortly before the Engine Division was dissolved and it is believed that it is this invention that provided the "silken thread" on which the future of the Philips Stirling hung [1]. Apart from solving the balancing problem, the rhombic drive also provided a solution to quite a few other problems[2]. It is therefore no surprise that Walker named the period following this new invention up to about 1970 as the rhombic phase [2].

General Motors became involved with the development of Stirling engines after a licence agreement in 1958 and up to 1970, much valuable work was carried out in the United States by the General Motors Corporation. However in 1970, General Motors abandoned their Stirling engine project for reasons not directly related to Stirling engines. From the late 1960s, MAN-MWM[3] also negotiated a licence and cooperation agreement with Philips. At more or less the same time United Stirling A.B. was formed and shortly afterwards became a Philips licence holder. Many different engines were developed until the late 1970s with numerous applications in mind. Consortia of industries and universities became involved and it is estimated that well over one hundred groups were working on Stirling engines by 1978 [1, 3].

[2]For a brief listing and further explanation the reader is referred to *The Philips Stirling engine* by C.M. Hargreaves [1].

[3]Mashinenfabrik Augsburg-Nurenberg (MAN) and Motorenwerke Mannheim (MWM) formed the Entwicklungsgruppe Stirlingmotor MAN-MWN.

1.2 Free-piston Stirling engines

A few years after the invention of the rhombic drive, another concept was invented that would also have a substantial influence on Stirling engine development. In the late 1950s[4], William Beale, while a professor of mechanical engineering at the University of Ohio, invented the free-piston Stirling engine (FPSE). While mechanical drive mechanisms are normally employed to rigidly couple the pistons and the output shaft of a Stirling engine, FPSE's operate without the pistons being coupled mechanically. In these engines, the displacement of the reciprocating elements to accomplish the thermodynamic cycle are coupled gas dynamically. Controlled reciprocation results from resonant interaction between various forces, including gas pressure forces, gas spring forces and damping forces [2].

Beale later founded the company Sunpower to develop the free-piston engine commercially after he was unable to secure adequate funds in the university environment. By the beginning of the 1980s, Sunpower was the only company in the world that produced Stirling engines commercially [2]. Serious work on FPSE's only started late in the 1960s and serious investment of resources did not begin before the early 1970s. In the mid 70s both Mechanical Technology Incorporated (MTI) and General Electric (GE), assisted initially by Sunpower, began their work on free-piston engines. Philips also began to look into free-piston engines later in the 70s as cryocoolers and electricity generators. By the late 1970s several groups around the world were working on free-piston Stirling engines [4].

NASA, at the Lewis Research Centre, was involved since the 1960s in Stirling engines for high-power conversion systems in space and is still involved in the development of small isotope heated free-piston engines for deep space missions. From the late 1970s this research centre was also involved in the development of alternative power plants for the US Department of Energy (DOE). Two companies, namely MTI and Stirling Technology Company (STC), were involved in the 1980s and came up with concepts as part of the DOE's Advanced Stirling Conversion System project. Both these concepts utilized free-piston Stirling engines. The expected high efficiency, along with the inherent simpler design, made the free-piston engine the engine of choice for long term solar applications [5, 6].

From the 1990s, numerous efforts were made to utilize Stirling engines, both the kinematic and free-piston types, in energy conversion in solar dish and combined heat and power (CHP) systems. To date, development and commercialization continues with a handful of companies that are currently involved in commercial development and production of Stirling engines. Of these, Sunpower and Infinia Corporation (formerly STC) seem to be the companies seriously involved in free-piston engine development and commercialisation.

Free-piston engines offer several advantages with respect to their kinematic counterparts, but also impose various problems. Due to the advantages that the free-piston topology holds, new application fields were opened for Stirling cycle engines, including utilization as deep space power sources heated by isotope heat sources, and low maintenance remote power systems.

[4] According to some sources William Beale only invented the free-piston Stirling engine in 1964.

A brief listing of some of the advantages that free-piston Stirling engines hold, follows [1, 2]:

1. With no cranks or rotating parts, dry-running pistons became possible resulting in longer operational periods between overhauls.

2. Free-piston engines should be cheaper than their kinematic counterparts due to fewer moving parts.

3. Free-piston engines can be sealed hermetically, reducing loss of gas to virtually zero.

Free-piston Stirling engines are however far less simple than they appear and suffer from, amongst others, the following problems [1, 2]:

1. Amplitudes and phases of the moving parts are determined by the interacting impedances of the entire system, i.e. engine, generator and load, making calculations more complicated.

2. As a result of the resonant behaviour of free-piston engines, power modulation might be necessary when driving variable loads. Control techniques, such as displacer spring or damper changes, serve to dampen piston displacement amplitudes during low or no loading conditions to prevent excessive piston displacement that could result in mechanical failure.

3. Piston centring problems arise from the nonlinear flow of gas between the working and bounce spaces. This flow in close annular gaps is proportional to the difference of the squares of the pressure, resulting in net loss of gas from the working space, because the differential pressure wave is not sinusoidal. This in turn results in the piston creeping toward the working space.

The work presented in this dissertation should be read with these advantages and disadvantages in mind.

1.3 Dissertation overview

Here follows a brief overview of this dissertation:

Chapter 2: An alternative approach to free-piston Stirling engines, that entails direct piston displacement control, is proposed and explained. From this alternative approach, a problem statement and method of approach are presented, highlighting the focus of this dissertation, namely the setting of specifications and guidelines for linear machines to perform direct piston displacement control and the subsequent evaluation of a machine topology to determine its suitability.

Chapter 3: Direct piston displacement control is investigated for the purpose of setting specifications to determine the suitability of linear machine technology. This includes an introduction to the various key indicators, a formulation to determine machine force dynamics and a simulated case study of the well known GPU-3 Stirling engine to set specifications for a broader range of engines.

Chapter 4: A design optimisation approach for linear machines for direct piston displacement control is presented to establish the means to determine the suitability of candidate linear machine topologies. In this design optimisation approach, the application of the specifications derived in Chapter 3 is demonstrated.

Chapter 5: An air-cored, longitudinal flux linear machine with surface mounted permanent magnets is evaluated for both the traditional case and the direct piston displacement case to determine its suitability for direct piston displacement control. From this evaluation, further insight is gained with respect to the possibilities and challenges of direct piston displacement control.

Chapter 6: In this chapter, the work presented and the contributions made in this dissertation are discussed briefly. Recommendations for future work is made as well.

Chapter 2

An alternative approach to the control of free-piston Stirling engines

2.1 Chapter overview

In this chapter an alternative approach to the control of free-piston Stirling engines (FPSE) is proposed with the objective of improving engine performance and to overcome some of the difficulties associated with free-piston engines.

Firstly, a brief discussion is presented in section 2.2 to explain the basic thermodynamic cycle of the Stirling engine and to give an account of the various loss mechanisms and of the influence of mechanical drive mechanism dynamics on the performance of Stirling engines. In kinematic type engines, mechanical drive mechanisms couple pistons rigidly and drive dynamics, and as a consequence engine dynamics are therefore easily predictable compared to free-piston engines. In free-piston engines the dynamics of the engine, that include piston displacement, are highly dependent on a multitude of factors, and various innovations on the manipulation and/or control of free-piston engines to ensure stable operation have already been published and/or patented. In section 2.3, a broad overview of these innovations is presented, with specific reference to piston displacement control.

In section 2.4 the idea to perform direct piston displacement control in free-piston Stirling engines is presented and discussed, including the advantages it holds and the challenges and difficulties associated with it.

Lastly, in section 2.5 and 2.6, a problem statement is presented, followed by a method of approach for the work presented in this dissertation concerning the design optimisation and control of a tubular linear electrical machine with the objective to perform direct piston displacement control in free-piston engines.

2.2 The Stirling cycle

2.2.1 The ideal thermodynamic cycle

The classical ideal thermodynamic cycle of Stirling engines and variations thereof have been comprehensively reported in literature [1–3] and will not be repeated here in detail. In his discussion of the ideal cycle, Walker [2] names the following assumptions as prerequisites to obtain the ideal cycle:

- It is assumed that all of the processes of the ideal cycle are thermodynamically reversible.
- It is assumed that the processes of compression and expansion are isothermal, assuming infinite rates of heat transfer between the cylinder walls and the working gas, or isentropic, that requires zero heat transfer between the cylinder walls and the working gas.
- It is assumed that the entire mass of working gas in the cycle is in the compression space or alternatively in the expansion space at any particular time. The effects of any voids are thereby neglected.
- All of the aerodynamic and mechanical friction effects are ignored.
- Regeneration is assumed to be perfect.

In summary, and with reference to the pressure-volume (pV) diagram shown in figure 2.1, the ideal Stirling cycle is composed of four thermodynamic processes [2]:

- Process a-b: Isothermal compression - heat is transferred from the working gas in the compression space to the external dump at T_{min}.
- Process b-c: Constant volume - working gas is displaced from the compression space to the expansion space. Heat is also transferred to the working gas from the regenerator.
- Process c-d: Isothermal expansion - heat is transferred to the working gas in the expansion space from an external source at T_{max}.
- Process d-a: Constant volume - working gas is displaced from the expansion space to the compression space. Heat is also transferred from the working gas to the regenerator.

The ideal cycle based on the assumptions listed above was however criticized by Organ [7, 8]. One of the difficulties in this regard is pointed out by Organ when he correctly observed that the cycle based on these assumptions embodies gas exchange processes which either cannot be achieved or are not encountered in the practical machine. Organ clearly illustrates that different parts of the total working gas mass are at different temperatures. This is contrary to the assumption that the entire mass of working gas in the cycle is either in the compression space or alternatively in the expansion space at any given time. This is also recognized by Reader [3]. According to Organ, no single temperature characterizes the thermodynamic state

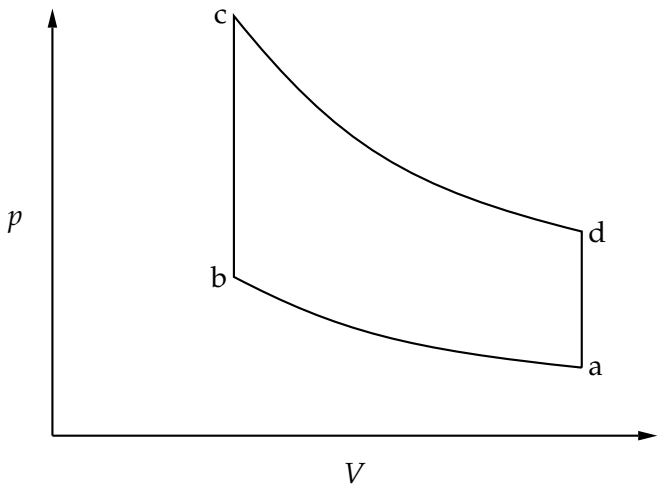

Figure 2.1: Ideal p-V diagram.

of the gas mass and no one value of either specific volume or specific entropy is available at any instant for plotting as is done in figure 2.1. It is therefore wrong to display thermodynamic states that do not represent a limit to any conceivable physical process.

Organ proposes a more realistic approach by following the paths of selected working gas particles present in different locations within the engine. The thermodynamic properties for a spectrum of working gas particles is then plotted on the same graph. While this is the more correct approach from a physical point of view, and while it may provide insight into the operation of the engine not otherwise obtainable, it is rather difficult to explain the influence of various non-ideal phenomena on the overall performance of the engine, in contrast to the more simplistic representation shown in figure 2.1.

It is ironic that for the majority of cyclic heat power plants suitable ideal cycle models do exist, but even though it is one of the few truly cyclic power plants as yet, a completely suitable Stirling ideal cycle has not been found [3]. In the discussion to follow, reference is made to the ideal p-V diagram as presented at the start of this section, but only as a means to illustrate the limiting effect of non-ideal phenomena on the performance of the engine. The approach by Organ would come to the same conclusion, but at the expense of a difficult and cumbersome explanation.

While the various approaches to define the ideal Stirling cycle may differ, there is in agreement on one matter, namely ideal piston displacement. To explain ideal piston displacement as a prerequisite to obtain the ideal cycle, four diagrams are provided in figure 2.2 showing the position of the pistons at critical stages of the cycle for beta-type engines. The four diagrams are denoted by a, b, c, and d to correspond to the positions indicated on the ideal p-V diagram shown in figure 2.1. Piston displacement is further illustrated in figure 2.3 showing the position of the pistons for the entire cycle as a function of time [1, 3]. The critical piston positions shown in the four diagrams of figure 2.2, are again denoted by a, b, c, and d in figure 2.3.

In figure 2.2 the displacer and power pistons are shown along with the hot and cold spaces and the regenerator. The diagrams do not specifically indicate a drive mechanism or connecting rods. No mechanical drive mechanism exist that will cause ideal piston displacement, but

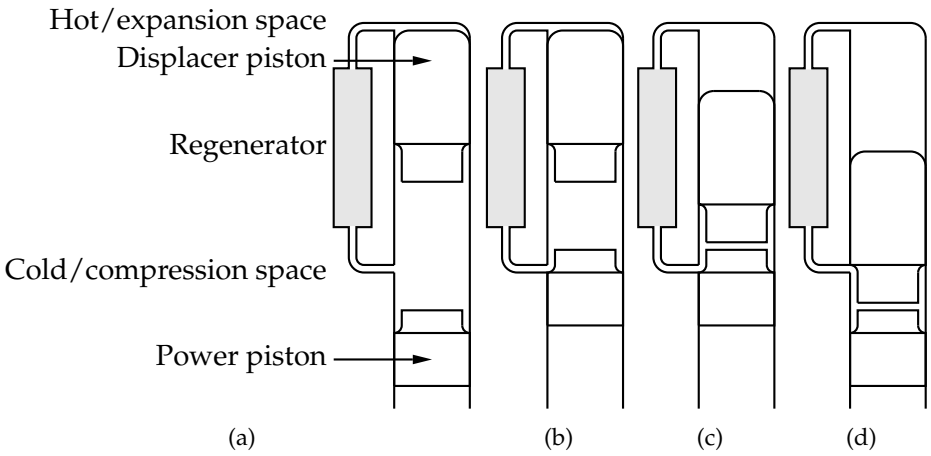

Figure 2.2: Illustration of the different stages for ideal piston displacement in beta type engines.

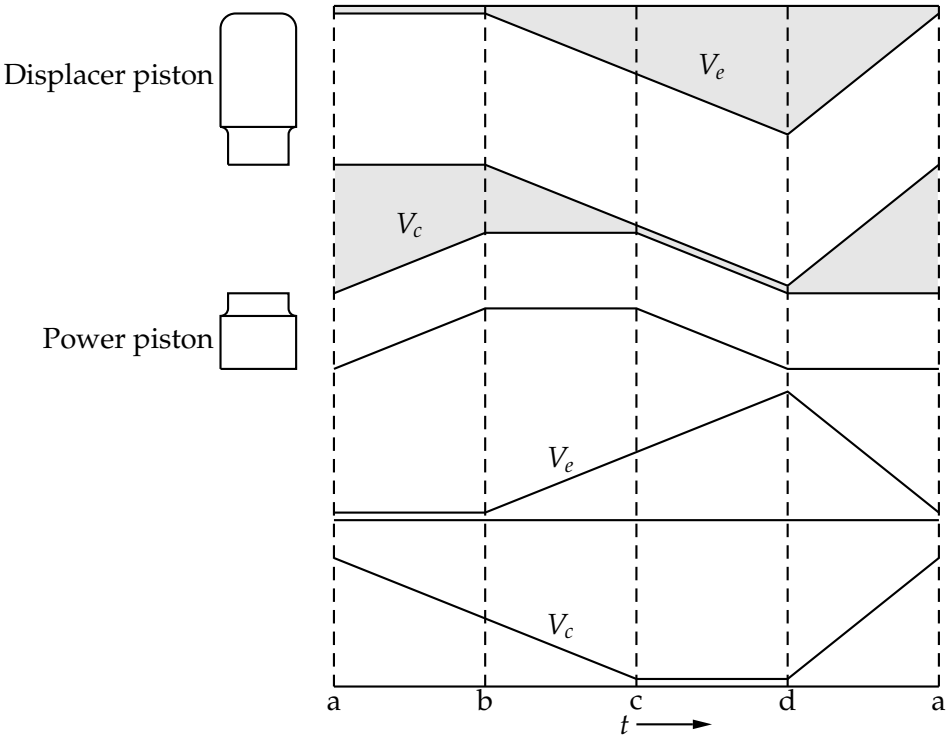

Figure 2.3: Ideal piston displacement of beta type engines.

for the sake of argument, a hypothetical ideal drive mechanism is assumed. The internal gas pressure of the engine is also considered to be higher than the pressure at the back of the power piston for the entire cycle.

In figure 2.3, V_e and V_c refer to the expansion and compression volumes respectively. Note that the volume variation in the two spaces must be out of phase with each other, and the resultant cyclic volume variation must in turn be out of phase with the cyclic pressure, if proper net shaft power is to be obtained.

With the piston position indicated in figure 2.2a, the power piston is in its lowest position, the displacer piston has just moved from its lowest to its highest position displacing all of the gas to the cold space where heat is transferred from the gas to the external dump. The power piston now moves upwards while the displacer remains in its highest position, compressing

the gas while it is at the lower temperature. For this process, energy is transferred from the drive mechanism to the engine. This process is considered to be isothermal, with only the volume and the pressure that changes.

When the power piston reaches the position indicated in figure 2.2b, it has reached its highest position and the displacer now starts to move downwards, effectively displacing the gas to the hot space, allowing heat to be transferred to the gas from an external source. The total volume remains constant during this process, with the temperature and hence the gas pressure that rises.

Once the displacer has reached the position as indicated in figure 2.2c, i.e. just above the power piston, the power piston starts to move downwards with the displacer until the positions is reached as indicated in figure 2.2d, where the power piston is again at its lowest position. During this part of the phase the gas is expanding while it is at its highest temperature, resulting in energy being transferred from the engine to the drive mechanism. This process is also considered to be isothermal.

To complete the cycle the displacer again starts to move upwards to its highest position with no change in total volume and the gas is again displaced to the cold space.

In the Stirling cycle engine acting as a thermal to kinetic energy converter, net work is obtained over one cycle, i.e. more work is delivered by the expanding gas than the work delivered to the gas during compression, because gas expansion occurs during higher pressure than when it is compressed. The total work done can be determined by evaluation of the equation

$$W = \int pdV, \tag{2.1}$$

where p is the instantaneous pressure of the gas and dV is the change in total volume [9].

With reference to the p-V diagram in figure 2.1, the work done by the gas described in (2.1) may also be expressed as the line integral for one cycle as given by

$$W = \oint PdV, \tag{2.2}$$

where the net work delivered over one cycle equals the area enclosed by the p-V diagram.

For Stirling engines, the theoretical maximum thermal efficiency is equal to the Carnot efficiency and depends only on the maximum and minimum temperature of the cycle [2]. In other words, the heat supply and rejection of the ideal thermodynamic cycle at constant temperature as outlined in figure 2.1, satisfies the requirement of the second Law of Thermodynamics for maximum thermal efficiency given by

$$\eta = (T_{max} - T_{min})/T_{max}, \tag{2.3}$$

where T_{max} and T_{min} denote the maximum and the minimum temperature of the working gas respectively.

2.2.2 Deviations from the ideal cycle

A few non-ideal phenomena that cause the actual engine cycle to deviate from the ideal case will now be considered briefly in order to highlight their influence.

Adiabatic compression and expansion

In practical closed cycle Stirling engines, rapid heating and cooling of the gas necessarily means large temperature fluxes[1] through the cylinder walls and since the cylinder has a low surface to volume ratio, it is necessary to pass the working gas through heat exchangers which have large surface areas. A practical engine is therefore not a 3-space engine, but rather a 5-space one, i.e. in addition to the compression space, expansion space and regenerator there is also a hot (heater) and a cold (cooler) heat exchanger. Compression of the gas in the compression space is largely adiabatic and the heat of compression is largely removed afterwards as the gas moves through the cooler. Expansion of the gas also partly takes place in the expansion space after heat is added to the gas as it passes through the heater and consequently the temperature drops as it expands almost adiabatically in the expansion space. This explanation simplifies more complex processes, but clearly demonstrates that these processes are close to being adiabatic and not isothermal [1].

Conduction losses

The cylinder walls of a Stirling engine have to withstand high pressure at very high temperature, resulting in wall thickness of the order of one centimetre in large engines. This results in conduction losses of normally a few percent of total heat input, and consequently a reduction of the gas temperature heated by the heater. For the same reason the gas temperature in the cooler is higher due to finite thermal conductivity [1].

Heat transfer effects of the regenerator

It is known that the regenerator should be able to deal with between four and five times the heat load of the heater and if it is not capable of doing so, then extra loads will be imposed on the heat exchangers to sustain the net output power. The regenerator must be as near perfect as possible, meaning the gas must be delivered from the regenerator to the cold side of the engine at a temperature as close to T_{min} as possible, and to the hot side at a temperature as close to T_{max} as possible. However, due to imperfect heat transfer of the regenerator, the gas enters the compression phase at a temperature higher than T_{min} and the expansion phase at a temperature lower than T_{max}, resulting in the pressure of the gas being too high or too low respectively [3].

Working gas leakage

Leakage of the working gas is inevitable in a practical engine. As a result some form of buffer space with pressure usually higher than the idealized minimum cyclic pressure is normally

[1] Also named heat fluxes. The magnitude of the temperature flux is essentially indicative of the tempo of heat transferred through a material and is obtained from the product of the thermal conductivity of the material and the negative of the derivative of the temperature at a given point in the material.

employed. Gas will therefore leak out of the system at the high cyclic pressure and tend to leak back during the compression phase. Both effects reduce the work output of the cycle [3].

Dead space

Volume that is not swept by the pistons is known as dead space and includes the clearance volume in both the expansion and compression spaces, as well as the total void volume of the heat exchangers and regenerator. Dead space reduces the power output of the Stirling engine, mainly due to its influence on the cyclic pressure. Not all of the gas is in the compression or the expansion space any more, as for the ideal cycle. In the expansion (or 'hot') phase of the cycle some gas will be in the cooler parts of the engine, effectively reducing the overall pressure. The reverse is also true during the compression (or 'cold') phase of operation [3].

Combined effects

Several other effects present in practical engines can be identified, e.g. flow losses or gas dynamic drag losses. All of these effects which cause deviations from the ideal case are interrelated, but not necessarily harmoniously, for example as illustrated by Reader [3], if the heat transfer rate can be enhanced then it may be possible to include less dead space and operate at high speeds, but such operation will increase the drag losses. Thus in engine design all these effects must be carefully balanced to obtain a desirable compromise.

According to Reader [3], deviation from the ideal cycle, whether it is lower expansion space temperature and higher compression space temperature or whatever the case may be, implies a reduced p-V area and with reference to equation (2.2), the net work per cycle is reduced when assuming constant heat energy applied to the engine. As a result, the efficiency of the engine is reduced as well. In practice, because the non-ideal effects are not harmoniously interrelated, the Stirling engine does not necessarily operate at its highest efficiency when delivering maximum power.

2.2.3 The influence of drive mechanisms on engine performance

The influence of drive mechanisms on the thermodynamic cycle was ignored in the previous sections and piece-wise linear ideal piston displacement was assumed. Ideally, the primary role of a drive mechanism must be to reproduce the volumetric changes necessary to produce the ideal cycle as described in section 2.2.1. However, it is highly impractical to match the required displacement with a mechanical drive mechanism. Mechanical designs that are able to produce volumetric changes close to the ideal would render mechanisms with a large number of moving parts likely to have a low mechanical efficiency, effectively negating any potential benefit gained from having near ideal volumetric changes. In addition, a large number of components would lead to greater production, unit and maintenance costs and possibly lower reliability when compared with existing drive mechanisms [3].

Walker names continuous harmonic displacement of the pistons as one of the factors that negatively influence the performance of Stirling engines when compared to the more ideal case [2]. The corners of the ideal p-V diagram as shown in figure 2.1 are rounded off considerably

when taking continuous harmonic displacement into account and the net power delivered for a complete cycle is correspondingly lower, hence the reduction in performance. Hargreaves [1] correctly points out that the efficiency of the engine is however not necessarily affected when compared to the ideal case, since the heat absorbed by the engine is correspondingly less with respect to the lower developed power of the engine.

Adinarayan and Narasimhan [10] examined the merits of different drive mechanisms with respect to specific work output of Stirling engines, i.e. the ratio of delivered power with respect to total swept volume, and also discussed the scope for improving specific work output by alternate drive mechanisms. The study was based on ideal isothermal analysis, assuming constant temperature in the working spaces, perfect regeneration, no losses, ideal working fluid and uniform instantaneous pressure. Dead space was also ignored.

In this study, a purely harmonic arrangement, several near harmonic arrangements including a slider-crank, an offset crank and a Ross yoke drive mechanism, as well as three non-harmonic arrangements, including a rhombic, a modified rhombic and a composite drive mechanism, were considered. The modified rhombic drive entails varying the stroke of the displacer with respect to that of the power piston, and the composite drive entails the hypothetical composition of near harmonic displacer displacement combined with non-harmonic rhombic power piston displacement.

It was found that the specific work potential obtained with most of the arrangements, including with the rhombic drive, but excluding with the modified rhombic and the composite drive, is fairly similar. The compression ratio, i.e. the maximum volume to minimum volume ratio and peak pressure with the rhombic drive is however reported to be much lower than with the harmonic and near harmonic drives. It is not reported, nor is it clear from the specific investigation why this is the case. The lower compression ratio may be a result of increased clearance volume in the compression space and will consequently lead to lower peak pressure as reported in this investigation. However, it is clear from the reported results that if the mass of gas for the rhombic arrangement is increased such that the peak pressure of this arrangement is comparable with the peak pressure of the harmonic and near harmonic arrangements, then the specific work of the rhombic arrangement will increase substantially beyond that of the harmonic and near harmonic arrangements. This would be in correspondence to the perception previously raised in this section that piston displacement closer to the ideal should lead to higher power output. A further finding was that the modified rhombic drive and especially the composite drive yielded results superior to those of the other arrangements.

A further investigation by Narasimhan and Adinarayan [11] on the merits of different drive mechanisms with respect to specific work output of Stirling engines also included the effect of dead space and double-acting arrangements, but attained the ideal isothermal analysis. Similar results were reported as for the previous investigation, with the modified rhombic and especially the composite drive yielding superior specific work output with respect to the beforementioned harmonic and near harmonic arrangements.

While ideal piston displacement will yield superior specific power output in comparison to real drive mechanisms under ideal circumstances, this is not necessarily the case in prac-

tical engines. Some losses, e.g. regenerator enthalpy losses and pumping losses, will greatly increase with more rapid movement of working gas and could prove to degrade the specific power output of an engine with near ideal piston displacement to lower than that of the same engine fitted with a practical drive mechanism. The same argument applies to non-harmonic vs. near harmonic drive mechanisms. The benefit of converting more energy per cycle with a non-harmonic drive when compared to that of a near harmonic drive could be negated by higher losses associated with the gas flow passages that would result in lower, rather than higher specific power output for non-harmonic piston displacement when compared to near harmonic piston displacement. The ideal isothermal analysis employed by Adinarayan and Narasimhan [10, 11] could not provide any clarity on this issue.

The question arises whether ideal piston displacement could also be considered as optimal piston displacement, i.e. where a practical engine would operate at its highest specific power, and if not, then given the available drive mechanisms, which piston displacement would be the closest to being optimal?

In an investigation aimed at addressing this question, Strauss and Dobson [12] compared a similar range of drive mechanisms as investigated by Adinarayan and Narasimhan [10, 11]. Their approach however differed considerably.

In their approach, Strauss and Dobson [12] used a decoupled second order Stirling engine simulation developed by Urieli [13] that takes various non-idealities, e.g. dead space, non-ideal heat transfer in the heat exchangers and adiabatic compression and expansion into consideration during cyclic simulation. Various losses, e.g. regenerator enthalpy losses and pumping losses are calculated afterwards using the cyclic simulation results and are then taken into consideration in calculating the performance parameters, e.g. output power and efficiency.

To evaluate the accuracy of the simulation against experimental data of a high performance Stirling engine, Strauss and Dobson [14] in a recent study compared the results of the second order simulation with measured data of the GPU-3[2] Stirling engine originally built by General Motors Research Laboratories in the 1960's for the US Army [16]. This was done to show that the simulation would be able to accurately simulate the influence of different drive mechanisms on the performance of Stirling engines, and the GPU-3 engine was chosen because it is one of the best documented high performance engines ever built [7, 8, 16], with extensive experimental data available resulting from the tests performed on the engine at the NASA Lewis Research Center at the end of the 1970's and the early 1980's [15, 17].

Strauss and Dobson [14] found that the overall accuracy of the simulations, with the exception of the output power and efficiency, proved to be satisfactory over a wide operational range. They also proposed an alternative method to calculate the performance parameters, and this yielded more accurate results compared to the method originally used by Urieli in estimation of the various other operational variables. Where large inaccuracies occurred for some of the operational variables, i.e. of the order of 10 to 50 percent, the simulated trends in general followed the measurements. It was therefore concluded that the second order simulation is well

[2]GPU refers to Ground Power Unit and was developed for an output capability of 3 kW. In the high power baseline tests performed at the NASA Lewis Research Center in 1981 by Thieme, maximum engine output with helium as working fluid was 4.26 kW at a mean compression-space pressure of 6.9 MPa and a engine speed of 2500 r.p.m. [15].

suited to compare the difference in performance using different drive mechanisms on a specific Stirling engine. A detailed description of the second order formulation as developed by Urieli and adopted by Strauss and Dobson and their investigation into its accuracy are presented in appendix A.

Strauss and Dobson [12] then used this simulation to predict the performance of the GPU-3 when retrofitted with several drive mechanisms. These drives included the following:

- *A purely sinusoidal drive*. Piston displacement of both the power piston and the displacer is purely sinusoidal.
- *Two different rhombic/sinusoidal composite drives*. In their investigation, Adinarayan and Narasimhan [10] included a composite drive that consisted of sinusoidal displacer displacement with the power piston following the displacement of that of the rhombic drive (referred to as a composite drive from here on). Although hypothetical, this drive is considered to be mechanically feasible. In this investigation, an alternative composite with sinusoidal power piston displacement and with the displacer following the displacement of that of the rhombic drive was also included (referred to as a hybrid drive from here on to distinguish it from the composite drive).
- *A rhombic drive and a modified rhombic drive*. For the rhombic drive the two sets of connecting rods for the power piston and the displacer are of same length, but for the modified rhombic the lengths may differ, resulting in different stroke lengths for the power piston and displacer.
- *A pseudo-ideal drive*. For the purposes of comparing the performance of near ideal piston displacement with that of practical drives, two modifications have been applied to ideal piston displacement as described in literature [2], yielding more practical ideal displacement. Firstly, the power piston stroke was allowed to vary up to the maximum of 0.75 of displacer stroke and the piecewise linear displacement (refer to figure 2.3) was filtered to obtain smooth transition from one displacement phase to the next, hence the reference to pseudo-ideal displacement.

Of these mechanisms, only the rhombic and the modified rhombic drives are known practical drives, although the modified rhombic drive is not commonly found in Stirling engines. The purely sinusoidal drive and the two composite drives were included in imitation of Adinarayan and Narasimhan [10]. The hypothetical pseudo-ideal drive - not perceived as a practical configuration at all - was included only for academic purposes. Although other drives could have been included, these drives were considered to be a good representation of non-harmonic and near harmonic drive mechanisms.

In comparing the influence of the drive mechanisms on the performance of the GPU-3 without giving one drive mechanism an unfair advantage with respect to the others, Strauss and Dobson [12] introduced the following constraints to the simulation and optimisation of the different drive mechanisms:

- A certain peak value of the pressure was not to be exceeded. If the average pressure of the engine or the total mass of gas was kept constant when comparing different drive mechanisms, this would yield different peak pressure values due to the difference in compression ratios and drive dynamics. In practice, the pressure withstand capability of the engine and especially engine seals could be exceeded, that would ultimately lead to damage to the engine for drive mechanisms with higher compression ratios. The rationale behind this constraint is thus to ensure that practical engine operation is maintained irrespective of the drive mechanism. In the simulation, the mass of gas was continuously adjusted for each iteration during optimisation to maintain a certain peak pressure to adhere to this constraint. The peak pressure was chosen as the value of the simulated original rhombic drive of the GPU-3 engine at the particular operational conditions.

- Total overall piston displacement, from the top dead position of the displacer to the bottom dead position of the power piston including clearance distances, should not exceed a certain distance. The rationale of this constraint is that, given a few possible modifications to the original engine, e.g. modifications to the pistons to allow further overlapping of the gas passage ways, any crank mechanism can be optimally employed in the original GPU-3 Stirling engine.

- Various other drive specific constraints were also set to maintain practical drive dimensions, but these were carefully chosen to ensure that an unfair disadvantage was not introduced for a specific drive mechanism.

The performance of the drive mechanisms was evaluated according to two criteria, namely for maximum power output and for maximum efficiency. These two performance criteria are mostly not found at the same operating conditions, i.e. maximum power output is not achieved at maximum efficiency. The criteria are shortly explained below:

- The maximum power output criterion entails optimisation for maximum power output at a certain speed, with no restriction on the amount of heat inflow at the hot side of the engine. This is relevant where the heat source is available in abundance, e.g. in some waste heat recovery systems. In this case, it is not necessary to operate the engine at maximum efficiency, but rather to convert as much heat energy as possible.

- The maximum efficiency criterion entails optimisation for maximum power output with the heat inflow at the hot side of the engine limited to a certain rate, hence the reference to maximum efficiency. The speed is allowed to vary however. This is relevant where the engine capability exceeds that of the amount of heat available, i.e. the heat is not available in abundance. In this case, maximum efficiency is necessary to convert as much as possible of the available heat source.

The drive mechanisms were compared for the maximum power output criterion with peak pressure at 9,46 MPa (corresponding to approximately 6,9 MPa average pressure with the original rhombic drive mechanism) for the speed range 500 to 3500 rpm. The heater tube and cooler

tube interior wall temperatures were set to 765,7 °C and 20 °C respectively with the working fluid as helium. For the maximum efficiency criterion, the drive mechanisms were compared for a heat inflow range as opposed to a speed range. This heat inflow range was obtained from the heat inflow rate of the original rhombic drive at each speed value in the before-mentioned speed range.

The drive dimensions for all drive mechanisms were optimised at each speed value or heat inflow rate value of the speed and heat inflow rate ranges to ensure comparison of the drives at an operational point optimised for that operational point. This also provided insight into the changing of the dynamics of each drive mechanism with increase in speed or heat inflow rate.

Tables 2.1 and 2.2 list the simulated results for the maximum power output and maximum efficiency criteria respectively with the operational speed of the original rhombic drive simulated at 3000 rpm.

Output power and efficiency refers to the simulated output power and efficiency of the engine without consideration of mechanical friction and various other losses not included in the simulation. pV power refers to the power derived from the pressure-volume work done as expressed in (2.2) - non-idealities included in the cyclic simulation have been taken into consideration, but not the losses that are calculated afterwards, e.g. regenerator enthalpy losses and pumping losses.

Table 2.1: Simulated results for the optimised drive mechanisms with engine speed and peak pressure at 3000 rpm and 9,46 MPa respectively [12].

Drive mechanism	Output power [kW] (efficiency)	Enthalpy losses [kW]	Pumping losses [kW]	pV power [kW]	Heat input [kW]
Original	9,25 (0,410)	1,52	1,61	12,62	22,57
Rhombic	9,49 (0,401)	1,55	1,95	13,04	23,66
Modified rhombic	9,54 (0,403)	1,63	1,98	13,18	23,69
Composite	9,98 (0,408)	1,78	1,91	13,75	24,44
Hybrid	9,74 (0,404)	2,07	2,00	13,85	24,13
Sinusoidal	8,73 (0,444)	1,57	1,10	11,90	19,65
Pseudo-ideal	9,46 (0,381)	2,18	2,81	14,04	24,84

From the investigation of Strauss and Dobson [12], it is clear that pseudo-ideal piston displacement did not yield the best output results, in fact, regarding maximum efficiency pseudo-ideal piston displacement fared worse than the other drives did. For the maximum power output criterion, the composite drive (with sinusoidal displacer displacement and rhombic-like power piston displacement) and to a lesser extent the hybrid drive (with rhombic-like displacer displacement and sinusoidal power piston displacement) delivered the best output power levels. The sinusoidal drive yielded the best efficiency for both criteria, resulting in the sinusoidal drive being capable of delivering the highest power output levels for the efficiency criterion.

It is interesting to note that the sinusoidal drive could yield higher output power at a

Table 2.2: Simulated results for the drive mechanisms optimised for maximum efficiency with the input heat flow rate at 21.85 kW and peak pressure at 9.41 MPa [12].

Drive mechanism	Output power [kW] (efficiency)	Enthalpy losses [kW]	Pumping losses [kW]	pV power [kW]	Engine speed [r.p.m.]
Original	9,25 (0,410)	1,52	1,61	12,62	3000
Rhombic	9,51 (0.421)	1,54	1,55	12,88	3408
Modified rhombic	9,51 (0,421)	1,72	1,60	13,06	3276
Composite	9,56 (0,423)	1,73	1,50	13,08	3249
Hybrid	9,56 (0,424)	1,72	1,57	13,11	3321
Sinusoidal	9,94 (0,440)	1,83	1,71	13,67	3939
Pseudo-ideal	9,00 (0,399)	2,00	1,93	12,99	3018

slightly lower efficiency when optimised for the efficiency criterion, than for the maximum output power criterion. This is attributed to the interrelated nature of drive mechanism dynamics and the thermodynamic cycle. Contrary to the other drives, the maximum heat input for the sinusoidal drive is less than for the original drive for the maximum power output criterion. It is only when the freedom of varying the speed was allowed that the heat input could reach that of the original drive, but with the advantage of maintaining good conversion efficiency. Strauss and Dobson [12] also observed that as the speed, or alternatively the heat inflow rate, increased, piston displacement of all drives tended to strive towards harmonic displacement.

No conclusions were drawn during the study by Strauss and Dobson [12] as to which particular piston displacement could be considered as optimal, since only known drive mechanisms or displacement closely related to known drives were investigated. Also, not one particular piston displacement will exist, since the exact displacement that the power piston and displacer should follow is specific to the engine, as well as to the operational conditions. It is however possible to conclude that optimal piston displacement will be closer to near harmonic than non-harmonic for engines with similarity to the GPU-3 engine, especially in a maximum efficiency scenario. Practical Stirling engines with ideal displacement or even near ideal displacement suffer from excessively high losses, especially those related to gas flow, and yield inferior results when compared to those with near harmonic displacement.

2.2.4 Conclusions

The practical Stirling cycle deviates from the highly idealised cycle due to non-ideal thermodynamic and gas dynamic behaviour. These factors impact negatively on both engine performance and efficiency and are interrelated, but not necessarily harmoniously.

The effect of different drive mechanisms was shown to also have an impact on engine performance and efficiency. The question was asked as to whether ideal piston displacement could also be considered as optimal and if not, then which piston displacement could be considered closest to optimal. It was concluded that piston displacement closer to near harmonic for engines with similarity to the GPU-3 engine could be considered as optimal and that in general ideal piston displacement could not be considered as optimal. This is in direct contradiction

with some perceptions voiced in literature [1, 2] and findings of previous studies [10, 11].

The discussion above concerning the influence of drive mechanisms centred around mechanical drives. As such, kinematic engines were assumed. The purely sinusoidal drive could however represent free-piston engine displacement, especially in the case of resonant type free-piston engines. Although it is difficult to predict free-piston displacement since no rigid coupling exists between pistons, it is possible to at least investigate certain scenarios by directly assuming piston displacement and to then simulate the influence on the thermodynamic cycle and engine performance. In this way free-piston engine performance may be compared to that of kinematic engines through simulation, and it follows that free-piston engines - having near harmonic to purely harmonic displacement - should compare well with kinematic engines in terms of engine performance and efficiency.

2.3 Control of free-piston Stirling engines

2.3.1 Overview

In kinematic type Stirling engines, pistons are coupled rigidly by mechanical drive mechanisms. Drive dynamics and as a consequence, engine dynamics are therefore more easily predictable. The dynamics of free-piston engines, including piston displacement, are highly dependent on a multitude of factors. Free-piston engines however hold many advantages compared to kinematic engines and it therefore follows that if successful control of free-piston engines is achieved, then free-piston engines should be the preferred technology in many applications.

Free-piston Stirling engines could be designed such that the gas flow in the gas flow passages inherently contribute to the stabilising of the engine. In short, the engine could be stabilised - at least partially - due to the nonlinear damping effect that the gas flow has on the engine dynamics [18]. As the engine becomes unstable, piston stroke increases. The damping effect of the gas flow has been shown to be a function of piston stroke and therefore increases with piston stroke, which again tend to dampen the engine, thus preventing the engine from becoming unstable. Berchowitz [18] and De Monte and Benvenuto [19] conceded however that physical internal or external subsystems is still necessary to ensure particular engine operational stability (e.g. constant voltage output for a wide range of loads) and/or maximum efficiency. In Chapters 3 and 4, this inherent stabilising effect will be further discussed. In the rest of this chapter it will however be ignored. Only engine control by way of physical internal or external subsystems will be considered.

Free-piston engine control is possible through a variety of different strategies, e.g. control of the average pressure, heat input control, different power modulation strategies, etc. All of these strategies have an impact on the thermodynamic cycle of the Stirling engine and could otherwise be seen as methods to influence or manipulate this cycle. For the discussion below however, control or manipulation of the thermodynamic cycle will be limited to strategies related to piston displacement control.

2.3.2 Piston displacement control for free-piston Stirling engines

Due to the resonant behaviour of free-piston Stirling engines driving electrical generators, the applied thermal energy must be converted to electrical energy in a controlled fashion to prevent the engine from over-stroking or alternatively to prevent the engine from stalling. To address the problem of over-stroking and stalling different strategies have been followed to control the dynamics of free-piston engines, including displacer piston control, power piston control or a combination thereof [20].

The appropriate means of controlling the engine dynamics depends on the degree of precision to which the output must be controlled, engine complexity, etc.:

- To control relationships having an influence on engine dynamics, engines are sometimes designed to include controllable sub-systems for this purpose. These sub-systems are considered to yield good overall efficiency and controllability of the engine, eliminating the need for external control arrangements.
- External control systems normally entail electrical systems that control power conversion from the power piston driven linear generator and/or the displacement of the displacer by a linear motor fixed to the displacer. Utilization of these systems is considered to result in simplified engine designs and could also improve engine efficiency over a wide range.

Displacer control entails the control of the dynamics of the displacer piston, which in return is used to control the engine dynamics. The response time of the engine when using this control method is however known to be fairly slow. Displacer piston control is implemented either through driving the displacer with a linear motor, or gas dynamically through adjustment of the displacer gas spring or the displacer damping. Examples of displacer control include the following:

- Walsh [21] describes displacer control as driving the displacer with a linear motor, with the armature secured to and movable with the displacer and the stator incorporated in the engine housing in juxtaposition to the armature. By controlling the linear machine to function as a generator load to extract power from the displacer, the displacer is caused to move with reduced stroke and/or greater phase angle relative to the power piston, and thermodynamic engine operation is dampened to reduce the engine output power. Alternatively, by controlling the linear machine to function as an electric drive motor, input power is supplied to the displacer in addition to the thermodynamic power fed back to the displacer by the periodic pressure wave, whereby the displacer is caused to move with increased stroke and/or a smaller phase angle relative to the power piston to increase power output.
- Vitale [22] describes displacer control for an externally excited free-piston engine that is over-damped at its operating load levels, in other words, it will not freely resonate at any load level. Again a linear drive motor is coupled to and directly drives the displacer. The difference to the previous example lies in the ability through a more advanced control

system to vary steady state power specifically by changing the thermodynamic operation of the free-piston engine during each cycle. This reportedly provides the means to precisely control in a variable and stable manner, the transient engine operations during rapid load changes.

Power piston control can also be described as power conversion control. By matching the power output of the alternator to the converted power of the engine, the engine is controlled to operate in a stable manner, thereby controlling the power piston to not over-stroke or to stall. Examples of power piston control include the following:

- Regan [23] describes various load control techniques investigated at the NASA Glenn Research Center as part of their end-to-end modelling effort of free-piston Stirling engines. This forms part of a programme to develop radioisotope-heated generators for deep space missions. Since radioisotope-heating is not controllable in this application, load control by introduction of parasitic loads is the remaining external control method. As user load is increased, the parasitic load is decreased so that the overall load remains constant. The parasitic loads include dc loads and ac loads that are switched in and out in discrete steps as is required to maintain stability in the engine. These control methods require series tuning capacitors to ensure that the stator current is in phase with piston velocity to achieve stable operation. The tuning capacitor effectively balances out the phase discrepancy between the terminal voltage and the piston velocity caused by the inductance of the stator.

- Controllers that maintain a reference current are also described by Regan [23]. This is where a certain output current is forced to flow in phase with the piston velocity. This current is again utilized to charge rectifying capacitors to energize spacecraft loads or parasitic resistive loads.

- Genstler *et al.* [24] describes an external power control system connected to the output of the linear generator coupled to the power piston for preventing overstroking. This system is very similar to the system descibed by Regan [21]. Part of the power control system comprises a controllable variable load member (typically a resistor bank) that serves as an additional load to a useful load, such as a battery, driven by the linear generator. Power piston dynamics and therefore engine dynamics are controlled such that displacement amplitude remains within a threshold value by adjustment of the additional load member to the linear generator. Adjustment of the load to the linear generator regulates the power output of the linear generator, which in turn controls movement of the power piston.

- Dhar [25] proposes a control system for power modulation for maintaining high engine cycle efficiency over a wide operating range for a system feeding power to a utility grid. An autotransformer is connected in series with tuning capacitance between the linear generator and the grid thus providing a means to modulate the engine power by controlling the voltage applied to the terminals of the linear generator. Alternatively, where the

generator has a field winding and not permanent magnets, suitable control of the field winding excitation may be used in stead of the autotransformer.

- Beale and Redlich [26] describe a linear generator or motor with an integral magnetic spring, where the magnetic spring serves two purposes, namely as a piston centring device and to limit piston stroke during load reduction on the Stirling engine. Stroke limiting is a result of increased spring constant of the magnetic spring past a certain displacement of the piston.

Control of both the power piston and the displacer is normally realised by some form of subsystem that variably couples the displacer to the power piston and therefore influences engine dynamics to enhance stability. Examples of these include the following:

- A variable gas spring with controllable duty cycle between the power piston and the displacer is described by Lane [27] and serves to couple the displacer to the piston to a greater or lesser degree depending on the stiffness of the spring. If the spring is at maximum stiffness, the displacer is essentially locked to the piston, limiting p-V power, and little or no power is generated. With the stiffness set to zero the engine power could rise to maximum to match the demand of the load.

- An example of a variable spring coupling the power piston and displacer as described by Beale [28] is realized electromagnetically and is the equivalent of a conventional linear motor between the displacer and the power piston with the moving magnet attached to the displacer and the flux path and armature winding attached to the power piston. By controlling the armature current appropriately, the forces on the magnets can be of the same phase relation as those of a relative mechanical spring, i.e. in proportion to the relative displacement between displacer and power piston. By controlling the amplitude of the armature current, the magnitude of the forces or in other words the stiffness of the variable spring may be controlled. Beale [29] also describes controllable variable gas springs, or dampers as referred to by Lane [27].

Piston displacement control as highlighted in this section is being proposed or is already being utilized successfully to enhance engine performance and/or to maintain stability. Through variable linkage between the displacer and the power piston, or by increased or decreased power conversion from both pistons, or other methods having an influence on piston displacement, the engine dynamics is influenced in such a way that the engines could operate according to desirable criteria, whether these are optimal performance levels, constant oscillation amplitude, or limited stroke length oscillation, or a combination of these and more.

2.4 Direct piston displacement control for free-piston Stirling engines

2.4.1 Direct piston displacement control defined and explained

A few advantages of free-piston Stirling engines have already been listed in Chapter 1. These include, amongst others, the absence of crank mechanisms or rotating parts, resulting in dry-running pistons and the possibility of very low friction and wear, resulting in very long operational periods without maintenance, that free-piston engines should be cheaper to manufacture than their kinematic counterparts due to fewer moving parts and that free-piston engines can be sealed hermetically, reducing loss of gas virtually to zero.

On the other hand, kinematic engines still hold the advantage that no instability of piston displacement exists due to the pistons being rigidly coupled to a mechanical drive mechanism. Optimal piston displacement can be attained more accurately with kinematic engines, at least for specific operating conditions, especially since piston displacement is well defined in crank driven engines and that it is not necessarily harmonic but near harmonic in nature, as shown in section 2.2.3.

The question arises whether it is possible to combine the different advantages of importance of free-piston engines, namely being hermetically sealed, having very low to negligible friction and maintenance, and low cost of manufacturing and those of kinematic engines, namely having stable and well defined piston displacement?

With reference to the discussion presented in the previous sections, the answer is that with current approaches it is at most partially possible. For example, it was indicated that piston displacement is controlled and restricted in free-piston engines to maintain stable operation, but the resonant behaviour of most free-piston engines dictates harmonic piston displacement and/or makes precise control of piston displacement difficult. Kinematic engines could be sealed hermetically for example by incorporation of the electrical generator as part of the drive mechanism, but the mere presence of a mechanical drive mechanism has the consequence of higher friction levels, the use of lubricants that again requires improved seals, and higher maintenance levels.

To be able to combine the advantages of free-piston engines and kinematic engines an alternative approach to free-piston Stirling engines is proposed:

This entails the instantaneous and direct control of the piston displacement of free-piston Stirling engines in a manner that more closely represents optimal - or any other piston displacement pattern necessary to control the engine according to preferred criteria, e.g. maximum power conversion or efficiency.

To control free-piston engines in this manner it is necessary to independently control both the displacement of the displacer and the power piston in real time. The primary arrangement to achieve this will be through external control of linear machines - fixed to the pistons - in such a manner as to exert instantaneous forces to control piston displacement, much like would have been the case had the pistons been fixed to a mechanical drive mechanism. This

primary control technique could be supplemented with other subsystems to improve stability and controllability.

This proposed alternative differs from current piston displacement control methodologies as discussed in section 2.3.2, in that the displacement of the pistons is not necessarily harmonic. Displacement of both pistons is also simultaneously and independently controlled in real time. In current control methodologies piston displacement is normally expected to be harmonic or near harmonic due to the resonant behaviour of the free-piston engines, and external control is normally limited to one of the pistons, with the displacement of the other piston a function of engine dynamics. External control is also much slower than what is proposed here - typically of the order of one cycle or more, since the control is focussed on the averaged output power or piston peak displacement and not on the instantaneous piston position.

Figure 2.4 shows a graphic representation of an example of a piston displacement control arrangement for a beta type free-piston Stirling engine.

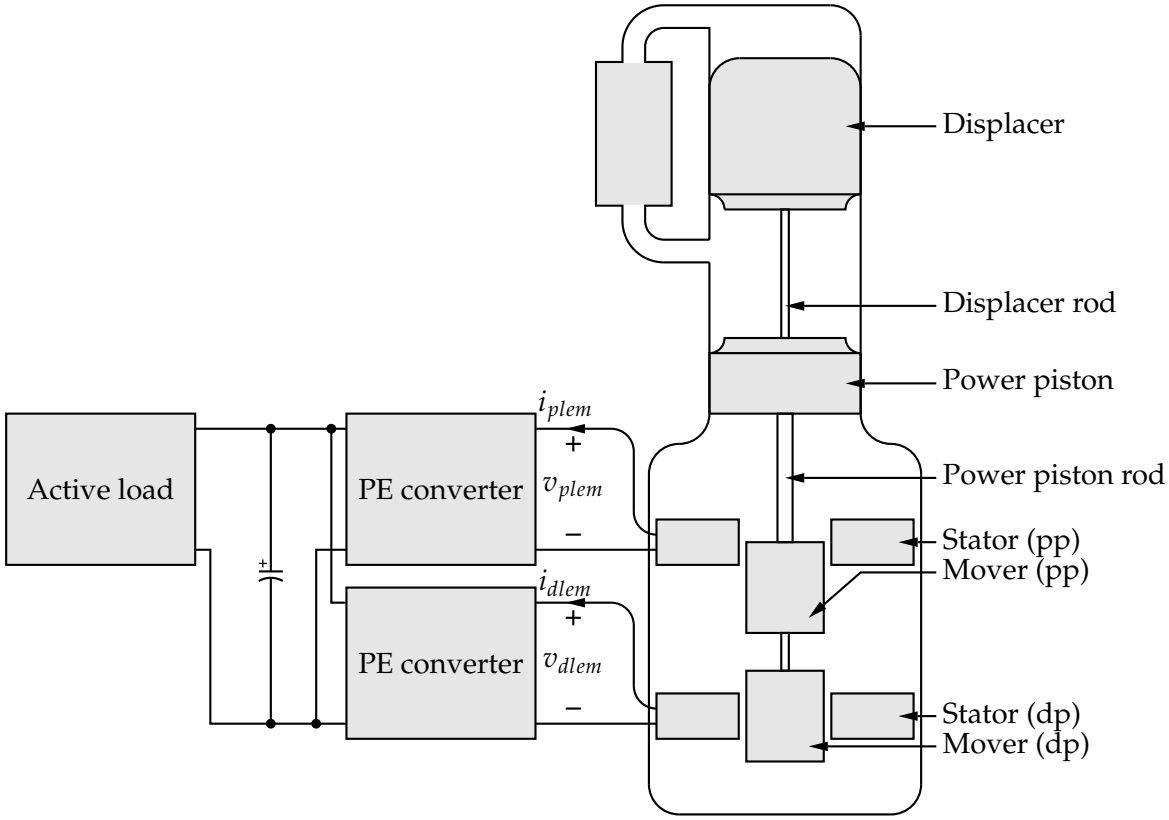

Figure 2.4: An example arrangement for piston displacement control showing all relevant Stirling engine members and power electronic converters.

It is shown in Figure 2.4 that each piston is connected to a linear machine. These machines are each connected again to a power electronic converter with which the current flowing from the linear machine can be controlled in real time. In this specific example, the two converters share a DC bus. An active load, which could be for example a grid-tie inverter or energy storage facility, is also connected to the DC bus.

In this arrangement, with the FPSE utilised as a heat to electrical energy converter, the instantaneous current and therefore the instantaneous force will be controlled to establish a

certain piston displacement. This will yield a certain instantaneous flow of energy that will result in the linear machine of the power piston being operated on average as a generator, i.e. energy flow will be from the electrical machine to the DC bus, and for the linear machine of the displacer being operated on average as a motor/actuator. The instantaneous flow of energy may however reverse for short periods of time during a cycle as is needed to produce a certain displacement.

2.4.2 Possible advantages

A free-piston arrangement where the pistons are controllably manipulated to follow a certain displacement pattern optimal for the current operational conditions, holds the important advantages of normal free-piston engines, but also the additional advantage of kinematic engines, i.e. controlled piston displacement not necessarily being harmonic. Such an arrangement could prove to have higher power-to-weight and power-to-volume ratios than normal free-piston engines and kinematic engines. In addition, such an arrangement could prove to yield high energy conversion efficiency over a wider operational range due to the controllability of the pistons, which might not necessarily be the case with resonant free-piston or kinematic engines.

In comparison with both free-piston with harmonic piston displacement and kinematic engines with non-harmonic piston displacement, the proposed arrangement could be operated to more closely resemble optimal piston displacement than is possible with resonance or mechanical drive mechanisms. Furthermore, the displacement followed could be altered in real time with the proposed arrangement to adjust to changing operational conditions.

Free-piston engines suffer from high vibration levels when compared to kinematic engines, especially those kinematic engines driven by rhombic mechanisms. In order to reduce vibration with beta-type engines, two identical engines are sometimes installed in a back-to-back arrangement [6]. However, with resonant type engines it is still difficult to synchronise piston displacement. With complete control of piston displacement in real time the proposed arrangement holds the advantage that vibration cancellation could be implemented more effectively.

2.4.3 Possible challenges and difficulties

Many of the possible challenges and difficulties associated with the proposed arrangement are related to the linear machines, as this is essentially the only difference when compared to normal free-piston engines.

In the proposed arrangement, the linear machines should be able to exert forces on the pistons of the same order of magnitude as those of drive mechanisms found in kinematic engines, particularly when following non-harmonic displacement patterns. This poses a challenge to the design of a suitable linear machine, as well as to the control of the machine, especially concerning the ability to transfer high quantities of energy in a very short time to and from the machine. In addition, the linear machines should be highly efficient, in order not to cancel through losses all that is gained by real time control of the pistons.

Real time control of this nature further requires for example fast electrical time constants associated with linear generators, as well as low overall inertia of the moving members.

2.5 Problem statement

From the previous section it is clear that **the challenge is whether suitable linear machine technology exists or whether technology could be established that would adhere to the requirements of real time direct piston displacement control.**

In simple terms: **is it at all possible?**

If suitable linear machine technology exists or if technology could be established that would adhere to the requirements of direct piston displacement control, then it could be argued that direct piston displacement control as proposed earlier is indeed possible. The question that was raised in section 2.4.1, namely whether it is possible to combine the different advantages of free-piston engines with those of kinematic engines and that led to the proposed approach of direct piston displacement control, must therefore be preceded by the question whether suitable linear machine technology exists or could be established in order to perform piston displacement control.

This gave rise to the investigation reported in this dissertation, namely:

Direct piston displacement control of free-piston Stirling engines: setting specifications for linear machines and design guidelines for free-piston engines and linear machines, and the evaluation of machine topologies to determine the suitability thereof.

The following two key questions are addressed in this investigation:

- Dynamics of free-piston engines from a piston displacement control perspective were investigated in order to determine specifications that linear machines have to adhere to and design guidelines for free-piston engines and linear machines. A few challenges and difficulties were mentioned in the previous section and these and others must be quantified for this purpose. No previous investigations of this nature could be found in literature.

- Based on the specifications and guidelines as mentioned above, a particular machine topology, namely an air-core, longitudinal flux linear machine with surface mount permanent magnets, was identified and examined according to a proposed design optimisation approach, to establish whether this machine topology is a suitable candidate for direct displacement control.

2.6 Method of approach

To address the question regarding the specifications and guidelines that linear machines will have to adhere to, relevant Stirling engine dynamics from a piston displacement control perspective should be better understood. Not only should the investigation concentrate on re-

quirements for suitable electrical machines, but also on the interrelated nature of engine dimensions and machine requirements to optimise the use of piston displacement control. To achieve this, the following steps were necessary:

- Stirling engine dynamics and how they are influenced by a wide variety of factors were investigated by way of a simulated case study of a well known Stirling engine. These factors include variation in operational conditions, variation in dimensions and variation in displacement patterns. Of special importance is the influence of these factors on the instantaneous pressure - a key variable in engine dynamics relevant to this investigation - that can be expected in high performance Stirling engines and how this, along with other variables such as mover mass, influences the instantaneous forces required from the linear machines. Since Stirling engines are not generally scalable, careful normalisation of findings was done to be more generally applicable.
- From the investigation of the influences on the dynamics of free-piston Stirling engines, machine specifications and design guidelines that linear machines should adhere to for the requirements of piston displacement control were formalised. This also inevitably led to the setting of design guidelines for free-piston engines to limit the extent of the influence of some of the variations.

Comparison of currently available topologies or new topologies for direct piston displacement control is necessary. This is possible by comparing versions of the various topologies, optimised specifically for direct piston displacement control. To achieve this, the following steps were necessary:

- Having specifications and guidelines does not yet provide an optimisation approach to evaluate the suitability of linear electrical machine topologies. An optimisation approach was established to address this issue.
- A tubular air-cored longitudinal flux linear machine topology with surface mount permanent magnets was then evaluated to establish its suitability for direct piston displacement control.

These steps will be addressed in the following chapters.

Chapter 3

Direct piston displacement control

3.1 Introduction

In this chapter, free-piston Stirling engine (FPSE) dynamics are investigated with the view to setting design guidelines and linear machine specifications to successfully perform direct piston displacement control.

To arrive at guidelines and specifications is no trivial exercise. On the one hand, proper data of only a few engines is available, while on the other hand the goal is to set more general guidelines and specifications for linear machines for a broad range of engines. The latter is also important in order to determine which machine topology would best serve the purpose.

To this end, the objective in this chapter is to investigate the specific case where piston displacement control is applied to the GPU-3 Stirling engine, i.e. where this engine is retrofitted and adopted as a free-piston engine with linear machines or where piston displacement control is applied to a free-piston engine with very similar geometric and operational parameters. An effort is then made to show that the findings could be extended to include a much broader range of engines.

3.2 Overview of methodology

A brief overview of the rest of this chapter is listed here to explain the methodology that was followed:

- The dynamic behaviour of kinematic type Stirling engines, i.e. the change in variables such as pressure as a function of crank angle or alternatively as a function of time, may be found by using the second order formulation of Urieli as detailed in appendix A. The second order formulation is also suitable to determine the dynamic behaviour of free-piston engines under displacement control. It may be assumed that piston displacement of free-piston engines is not a function of gas dynamics and of control systems as described in chapter 2 any more, but that the displacement is forced under direct displacement control to follow predetermined and therefore known displacement patterns.

To obtain dynamic information relevant to piston displacement control, further analysis is however necessary. The forces exerted on the pistons are not determined by the second order formulation in appendix A. These forces, amongst others, are needed to determine the forces necessary from the linear machines - a critical indicator to determine the suitability of the machines. To add this to the second order formulation, the following additional analysis as formulated in Section 3.3 is necessary:

  - The dynamic behaviour of variables in the bounce space is not known from the second order formulation. This is to be determined from subsequent simulations.
  - With the pressure in the bounce space known, equations for the force dynamics of both the displacer and power piston are formulated.

- Important force related indicators relevant to the suitability of electrical machine topologies are identified and discussed in Section 3.4. This information is necessary to direct the case study on the GPU-3 engine and the setting of guidelines and specifications thereafter. These indicators are later modified in Section 3.6.
- A comprehensive investigation into the dynamics of the original GPU-3 Stirling engine and its sensitivity to variation of a variety of different variables then follows in Section 3.5 as a simulated case study.
- Finally, a critical evaluation of the results of the simulated case study and the application thereof to the determination of guidelines and specifications for linear machines for a broader range of engines, is presented in Sections 3.7, 3.8 and 3.9.

3.3 Dynamic behaviour of FPSE's

3.3.1 Overview

Dynamic behaviour of FPSE's relevant to direct piston displacement control are considered in the following sections. The nonlinear leakage of working fluid and the way that it is accommodated is discussed in Section 3.3.2. Bounce space dynamics and FPSE force dynamics are then considered in detail in Sections 3.3.3 and 3.3.4 respectively.

Figure 3.1 shows a beta-type free-piston Stirling engine, indicating important members, spaces, as well as engine parameters relevant to this investigation. Figure 3.1 will be discussed during the course of this chapter.

The following general assumptions apply to the analysis in the following sections:

- It is assumed, instead of providing for the more general case, that the body of the engine is rigidly coupled to its surroundings as is the case with most free-piston engines employed as heat to electrical energy converters.
- The position of the power piston as well as the displacer, is taken with respect to the same zero reference, for the discussion below. The usefulness of this choice will be shown later in this chapter.

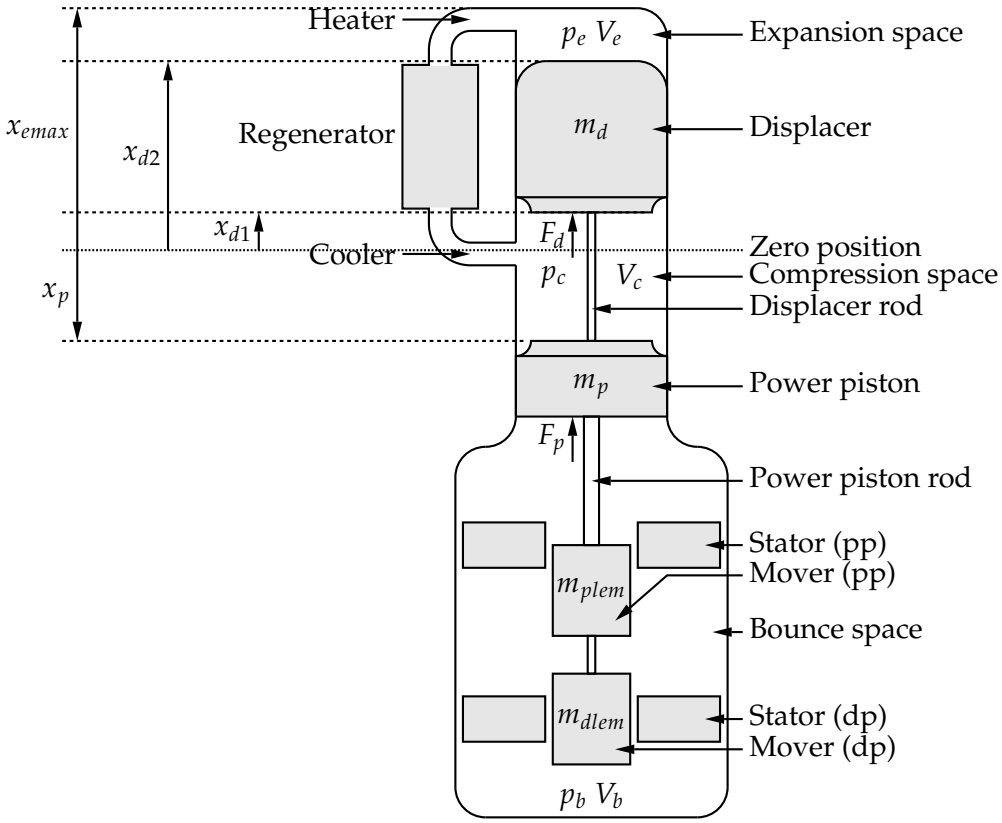

Figure 3.1: Stirling engine members, spaces and parameters relevant to piston displacement control.

- The positive direction of displacement and the forces shown in Figure 3.1 are in the upward direction (x_p therefore has a negative value as shown in the specific representation in Figure 3.1).

3.3.2 Non-linear leakage of working fluid

The average bounce space pressure p_b should ideally be equal to the average of the compression space pressure p_c. In very low maintenance free-piston engines, leakage seals between the power piston and the cylinder wall are utilised in order to attain zero mechanical friction. That means the gas may leak past the power piston to and from the bounce space. The advantage therefore is that if this leakage is kept low enough, the average bounce space pressure will follow the average compression space pressure, without excessive losses due to leakage.

The flow of gas however does not have a linear relation to the pressure difference, but rather a nonlinear dependency, i.e. it is proportional to the differences of the squares of the pressures p_c and p_b [2]. This results in a loss of working fluid from the compression space to the bounce space due to the compression space pressure p_c not normally being purely sinusoidal, which again leads to the power piston creeping towards the compression space.

Mechanisms exist to counter loss of working fluid to the bounce space [2, 4]. With reference to this investigation, provision should be made to counter the resultant force - and as a result piston creepage - due to this loss of working fluid without the need for specific mechanisms, in order to simplify the engine.

3.3.3 Bounce space pressure dynamics

The second order formulation as developed by Urieli [13] and described in appendix A does not make provision for the analysis of the dynamic responses of the pressure and temperature in the bounce space. Ideally, the void volume of the bounce space should be large compared to the swept volume of the power piston, as this would imply relatively small variations in the response of the bounce space pressure. In an effort to keep the overall volume of the engine - or in other words the volume to power ratio - as low as possible, this large difference in the size of the void volume and the swept volume is however not necessarily desired in real engines. Under these circumstances, the response of especially the bounce space pressure is critical to determine the required ability of the electrical machine of the power piston. In this section, a thermodynamic analysis is presented to determine the bounce space dynamic responses.

With proper third order formulations, it would have been possible to fully integrate the thermodynamic analysis of the bounce space, including heat transfer to and from the surroundings, and gas leakage to and from the bounce space, with the rest of the formulation. However, since analysis in this investigation is based on the second order formulation of Urieli [13], the analysis presented below is approached as an add-on performed subsequent to the analysis of the engine.

Figure 3.2 shows the lower section of the beta-type FPSE shown in Figure 3.1 to define a control volume for the bounce space for thermodynamic analysis. Only the relevant thermodynamic variables are shown.

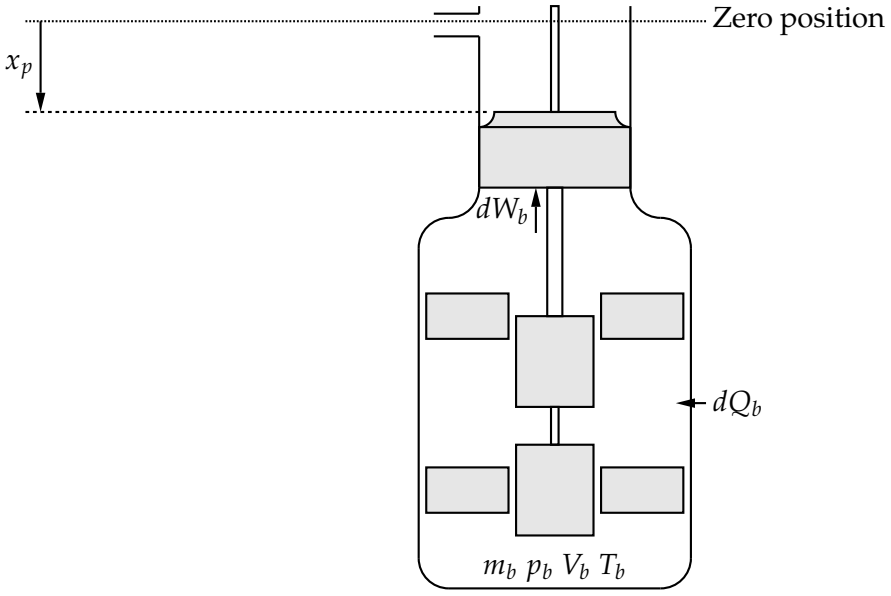

Figure 3.2: Bounce space thermodynamic control volume.

To consider heat flow to and from the surroundings in the analysis below would be difficult, because no real information exists on the actual construction of the bounce volume pressure vessel. A simple workaround to this problem is to assume reversible adiabatic compression and expansion of the gas in the bounce space, i.e. that no net heat flow occurs to or from the bounce space control volume. It is recognised that in reality, the situation might differ slightly, but that this assumption is a fair assumption for the duration of one cycle.

One limiting factor of an analysis of this kind is that gas leakage to and from the bounce space cannot be properly incorporated. It is therefore assumed that the effect of gas leakage to determine bounce space dynamics for one cycle is small enough to be ignored. This is a fair assumption for well designed and manufacturer engines with leakage seals or for engines with seals.

Thermodynamic formulation of the adiabatic case

The thermodynamic analysis of the bounce space starts with the energy equation in (A.1) (in appendix A).[1] With respect to the bounce space variables, the energy equation may then be formulated as

$$dQ_b + \left(c_p T_{ib} m'_{ib} - c_p T_{ob} m'_{ob}\right) = dW_b + c_v d\left(m_b T_b\right), \tag{3.1}$$

where the subscript b refers to the bounce space. With gas leakage ignored (m'_{ib} and m'_{ob} is therefore zero), no enthalpy is carried to or from the bounce space and the mass of gas m_b remains constant. For the adiabatic assumption, Q_b is equal to zero and therefore also dQ_b. The energy equation then simplifies to

$$0 = dW_b + c_v m_b dT_b. \tag{3.2}$$

With the rate of work done by the control volume

$$dW_b = p_b dV_b, \tag{3.3}$$

an expression for the rate of change in the bounce space temperature then follows, namely

$$dT_b = -p_b dV_b / (c_v m_b). \tag{3.4}$$

From the equation of state in (A.2) and the derivative of the equation of state in (A.3) in appendix A, expressions for the bounce space pressure and its derivative are obtained, namely

$$p_b = \left(m_b R T_b\right) / V_b \tag{3.5}$$

and

$$dp_b = \left(dT_b / T_b - dV_b / V_b\right) p_b. \tag{3.6}$$

Substitution of the pressure in (3.4) with the expression in (3.5) yields

$$dT_b = -T_b \frac{R}{c_v} \frac{dV_b}{V_b}. \tag{3.7}$$

[1] For clarity on the meaning of some of the terms and subscripts in this equation and others to follow, the reader is referred to the discussion on these in appendix A.

From (3.6) and (3.7), an expression for the derivative of the pressure is obtained, namely

$$dp_b = -p_b \left(1 + \frac{R}{c_v}\right) \frac{dV_b}{V_b}. \tag{3.8}$$

The derivative of the temperature in (3.7) is not dependent on the pressure and the derivative of the pressure in (3.8) is not dependent on the temperature. With these two equations, the well known adiabatic relationship between the temperature and the volume, and the pressure and the volume can be derived, namely

$$T_b = T_{b0} \left(\frac{V_{b0}}{V_b}\right)^{R/c_v} \tag{3.9}$$

and

$$p_b = p_{b0} \left(\frac{V_{b0}}{V_b}\right)^{\gamma} \tag{3.10}$$

respectively, where T_{b0}, p_{b0} and V_{b0} denote the initial values of the temperature, pressure and volume respectively. The bounce space volume V_b may be written in terms of the bounce space void volume and the swept volume of the power piston, namely

$$V_b = V_{b_{void}} + \left(x_p - \min(x_p)\right)\left(A - A_{rd}\right), \tag{3.11}$$

where the void volume $V_{b_{void}}$ is defined as the total remaining gas volume when the power piston is in its lowest position and A and A_{rd} denote the power piston and displacer rod cross sectional areas respectively. The derivative of the bounce space volume is then given by

$$dV_b = dx_p \left(A - A_{rd}\right). \tag{3.12}$$

The temperature and the pressure of the bounce space may now be calculated from (3.9) and (3.10) and their derivatives from (3.7) and (3.8) respectively. The numerical solution of the temperature, the pressure and their derivatives now follows below.

Numerical solution

With reference to Figure 3.2, only the bounce space volume and its derivative are known variables, provided that the bounce space void volume is known (see (3.11)). There is however other important information available, including the average compression space pressure and temperature, because a solution for the engine - specifically for the compression space - is obtained prior to this analysis.

With the assumptions of an adiabatic control volume with no gas leakage, this information is particularly important. An infinite number of solutions for the variables in Figure 3.2 are possible if no further information exists on for instance the internal energy of the gas in the bounce space control volume. The following assumptions therefore apply:

- The average bounce space pressure is assumed to have a value fixed with respect to that

of the compression space. A short discussion on nonlinear gas leakage was included earlier in this chapter and it was described how a difference between the average of the compression space and bounce space could exist. The average bounce space pressure is therefore assumed to have a fixed ratio of 1 or larger with respect to the average compression space pressure.

- It is assumed that the average gas temperature also has a value fixed with respect to that of the compression space. Several factors will contribute to the bounce space temperature. For the adiabatic assumption, the loss of heat through the walls of the bounce space vessel and the addition of heat due to losses in the electrical machine are ignored, because calculation thereof would require specific information not available for a more general investigation. It is however expected that an equilibrium will be reached where the heat transfer to the surroundings and the heat loss in the generator will be equal, resulting in zero net heat transfer.

  In addition, while the enthalpy carried from the compression space to the bounce space and vice versa due to gas leaking from the one space to the other, is ignored, this mechanism does contribute to bringing the average temperature of the bounce space close to that of the compression space. The average bounce space gas temperature is therefore assumed to have a fixed ratio with respect to the average compression space gas temperature that might vary from smaller than 1 to larger than 1.

With the average bounce space temperature and pressure known, the temperature and pressure profiles may be calculated using (3.9) and (3.10) respectively by assuming an initial value for the temperature and pressure and by scaling the profiles afterwards to have the correct average values. The derivatives of the bounce space temperature and pressure may now be calculated from (3.7) and (3.8) respectively, since the profiles of the temperature and the pressure are known.

3.3.4 Free-piston Stirling engine force dynamics

The equation of motion for the displacer may be written as follows, namely

$$(m_d + m_{dlem})\,\ddot{x}_d = -D_d\dot{x}_d - D_{dp}\dot{x}_p + F_d, \tag{3.13}$$

where x_d denotes either x_{d1} or x_{d2}. The mass m_{dlem} represents the mass of the mover member of the linear machine and the mass m_d represents the mass of rest of the moving member, including the mass of the displacer and any other mechanisms connected thereto. The two damping coefficients D_d and D_{dp} model the viscous forces on the moving gas which accounts for the pressure drop across the heat exchangers and regenerator. F_d represents all other forces acting on the displacer.

Expressions for D_d and D_{dp} can be found from the force on the displacer due to the pressure

drop across the heater, regenerator and cooler, i.e.

$$\sum_{i=h,r,k} (A\Delta p)_i = (A\Delta p)_h + (A\Delta p)_r + (A\Delta p)_k$$
$$= -D_d \dot{x}_d - D_{dp} \dot{x}_p, \tag{3.14}$$

where A denotes the area of the displacer and the subscripts h, r and k denote the heater, renegerator and cooler respectively. The direction of pressure drop in (3.14) is from the compression space to the expansion space.

In his analysis of free-piston engine dynamics, Berchowitz [18] presents expressions for each of the pressure force terms. D_d and D_{dp}[2] are then obtained by grouping terms with displacer speed and power piston speed respectively. Detailed discussion of these expressions is beyond the scope of this dissertation[3].

In resonant free-piston engines, the damping coefficients in (3.14) could play an important role in maintaining stability. It is shown that for turbulent flow heat exchangers, the damping coefficients are dependent on the displacement magnitude of and the phase shift between the displacer and power piston, i.e. $D_d = f\left(X_d, X_p, \phi\right)$ and $D_{dp} = f\left(X_d, X_p, \phi\right)$, where X_d, X_p, and ϕ denote the amplitudes of the displacement of the displacer and power piston and the phase shift of the power piston with respect to the displacer respectively. Damping therefore increases with increasing displacer and piston amplitude, which in turn tends to stabilise oscillations. This does not mean that no additional control devices are required, since in many instances this inherent mechanism is not entirely sufficient to ensure stability.

Where gas flow is entirely laminar in heat exchangers, it is shown that the damping coefficients become constant and are no longer functions of displacer and power piston displacement magnitude. This implies that no inherent stabilising mechanism exists as with turbulent flow heat exchangers.

From a direct piston displacement control point of view, it does not matter whether gas flow is laminar or turbulent, because of the direct and immediate control capability that piston displacement control should offer. Design of heat exchangers from this perspective may therefore concentrate entirely on efficiency, cost, etc. and not on the capability of the heat exchangers to introduce nonlinear damping.

By substituting the damping force terms in (3.13) with the pressure drop force terms in

[2]Berchowitz [18] showed that, given the choice of positive direction for displacement and forces, the displacer/power piston viscous coupling D_{dp} is negative. This is due to the pressure drop force on the displacer being positive for positive piston displacement.

[3]For a detailed derivation of the damping coefficients, the reader is referred to chapter 5 of the PhD dissertation of Berchowitz [18] that deals with the linear dynamics of free-piston Stirling engines. In an earlier and more readily available publication by Redlich and Berchowitz [30], a very similar discussion is presented concerning the linear dynamics of free-piston engines, except that the detailed derivation of the damping coefficients is not presented.

(3.14), a more convenient expression is obtained, namely

$$\begin{aligned}(m_d + m_{dlem})\,\ddot{x}_d &= (A\Delta p)_h + (A\Delta p)_r + (A\Delta p)_k + F_d \\ &= A\left(\Delta p_h + \Delta p_r + \Delta p_k\right) + F_d \\ &= A\Delta p + F_d. \end{aligned} \tag{3.15}$$

It is seldom found that the bores of the displacer and of the power piston differ. There is however a real possibility that the pressure areas for the expansion and compression space may differ due to the presence of a displacer connecting rod, as discussed previously (refer again to Figure 3.1). To make provision for this difference, (3.15) could also be adapted to

$$\begin{aligned}(m_d + m_{dlem})\,\ddot{x}_d &= (A - A_{rd})\,p_c - Ap_e + A_{rd}p_b + F_d \\ &= (p_c - p_e)\,A + (p_b - p_c)\,A_{rd} + F_d, \\ &= A\Delta p_{ce} + A_{rd}\Delta p_{bc} + F_d, \end{aligned} \tag{3.16}$$

where A_{rd} denotes the displacer connecting rod cross-sectional area and Δp_{ce} and Δp_{bc} denote the pressure drop across the displacer and power piston respectively. An expression for the force component due to the pressure difference across the displacer is therefore given by

$$F_{d\Delta p} = A\Delta p_{ce} + A_{rd}\Delta p_{bc} \tag{3.17}$$

and the instantaneous power delivered from the displacer as a result of the pressure difference may now be expressed as

$$\begin{aligned}p_{d\Delta p} &= F_{d\Delta p}\dot{x}_d \\ &= \left(A\Delta p_{ce} + A_{rd}\Delta p_{bc}\right)\dot{x}_d. \end{aligned} \tag{3.18}$$

Substitution of the force component in (3.16) yields

$$\begin{aligned}(m_d + m_{dlem})\,\ddot{x}_d &= F_{d\Delta p} + F_d \\ &= p_{d\Delta p}/\dot{x}_d + F_d. \end{aligned} \tag{3.19}$$

Finally, an expression for the force term F_d is obtained from

$$\begin{aligned}F_d &= (m_d + m_{dlem})\,\ddot{x}_d - F_{d\Delta p} \\ &= (m_d + m_{dlem})\,\ddot{x}_d - p_{d\Delta p}/\dot{x}_d. \end{aligned} \tag{3.20}$$

A similar process may be followed for the power piston. The equation of motion of the power piston may be written in a fairly similar way to that of the displacer, namely

$$\left(m_p + m_{plem}\right)\ddot{x}_p = (A - A_{rd})\,(p_b - p_c) + F_p. \tag{3.21}$$

An expression for the force component due to the pressure difference across the power piston

is therefore given by

$$F_{p\Delta p} = (A - A_{rd})(p_b - p_c) \tag{3.22}$$

and the instantaneous power delivered from the power piston as a result of the pressure difference may now be expressed as

$$\begin{aligned} p_{p\Delta p} &= F_{p\Delta p}\dot{x}_p \\ &= (A - A_{rd})(p_b - p_c)\dot{x}_p. \end{aligned} \tag{3.23}$$

Substitution of the force component in (3.21) yields

$$\begin{aligned} (m_p + m_{plem})\ddot{x}_p &= F_{p\Delta p} + F_p \\ &= p_{p\Delta p}/\dot{x}_d + F_p. \end{aligned} \tag{3.24}$$

Finally, an expression for the force term F_p is obtained from

$$\begin{aligned} F_p &= (m_p + m_{plem})\ddot{x}_p - F_{p\Delta p} \\ &= (m_p + m_{plem})\ddot{x}_p - p_{p\Delta p}/\dot{x}_p. \end{aligned} \tag{3.25}$$

If the instantaneous pressures are known, the resultant forces could be calculated from (3.16) and (3.21) in order to obtain a certain acceleration. If the piston acceleration can be controlled by controlling the instantaneous forces F_d and F_p, then the displacement of the pistons can be controlled to follow a certain displacement pattern. This is essentially what direct piston displacement control entails.

Alternatively, by knowing the acceleration and velocity of a predetermined displacement pattern and the instantaneous pressures resulting from those patterns, the resultant forces necessary to follow those patterns could be calculated according to (3.20) and (3.25). This will provide much needed insight into the force dynamics resulting from direct piston displacement control.

3.4 Force indicators

The force capability of electrical machines is an important property for performing direct piston displacement control. The following force related indicators, two ratios and two normalised displacement locations, are considered as important for the case study in Section 3.5:

- **Maximum force to power ratio:**

  The maximum force to power ratio is obtained by taking the maximum of the absolute of the force profile divided by the average power obtained from or delivered to the electrical machine, i.e.

$$\Gamma_{F/P} = \max\left(|F_{lem}/\overline{p_{lem}}|\right), \tag{3.26}$$

where $\Gamma_{F/P}$ denotes the maximum force to power ratio[4]. F_{lem} and p_{lem} denote the instantaneous force and instantaneous power of the electrical machine, denoted by the subscript lem, respectively.

The forces exerted by electrical machines are directly dependent on the current of the electrical machines. The higher the maximum force, the higher the maximum current will be to obtain that force maximum. But the current also gives rise to conduction losses, directly proportionate the cube of the current. Higher maximum force to power ratios will then inevitably lead to reduced efficiency. Preferred electrical machine topologies will be those that can provide higher forces, while maintaining high efficiency. It is therefore important to know what typical maximum force to power ratios are necessary.

- **Maximum rate of change of force to maximum force ratio:**

  The maximum rate of change of the force to maximum force ratio is obtained by taking the maximum of the absolute of the rate of change of the force divided by the maximum of the absolute of the force itself, i.e.

$$\Gamma_{dF/F} = \max\left(|dF_{lem}|\right) / \max\left(|F_{lem}|\right), \tag{3.27}$$

  where $\Gamma_{dF/F}$ denotes the maximum rate of change of the force to maximum force ratio and dF_{lem} denotes the instantaneous rate of change of the force of the electrical machine.

  This indicator should give a clear indication of the dynamic force response demanded of the electrical machine by providing a value of maximum rate of change normalised with respect to the maximum force itself. The maximum rate of change of the force as well as the internal impedance of a particular electrical machine will have an influence on the drive electronics to control the current. Preferred electrical machine topologies will be those with lower series impedance as this will demand less of the drive electronics at higher rates of change of force and as a consequence on the current.

- **Normalised displacement location of maximum force:**

  The normalised displacement location of the maximum force is obtained by dividing by half a stroke length the displacement location where the maximum of the absolute of the force occurs, i.e.

$$\chi_{maxF} = x_{maxF} / \max(x), \tag{3.28}$$

  where χ_{maxF} [5] and x_{maxF} denote the normalised displacement location and the displacement location at the maximum of the absolute of the force F respectively. It is assumed that the displacement x was offset adjusted such that half a stroke length is equal to the maximum of the displacement. The value of χ_{maxF} will therefore vary between -1 and 1.

[4]The Greek letter Γ was chosen as symbol to designate two of the force indicators, namely the maximum force to power ratio and the maximum rate of change of the force to maximum force ratio respectively, with the subscripts acting to differentiate between the two.

[5]The Greek letter χ was chosen as symbol to designate two of the force indicators, namely the normalised displacement locations at the maximum of the absolute of the force and the maximum of the absolute rate of change of the force respectively, with the subscripts acting to differentiate between the two.

Electrical machines topologies have different abilities to exert forces as a function of displacement. It is therefore necessary to have a clear understanding of where during a displacement cycle maximum force could be expected. This indicator will provide that information. Preferred electrical machine topologies will be those that will be able to easily exert the maximum force at a specific location.

- **Normalised displacement location of maximum rate of change of force:**

  The normalised displacement location of maximum rate of change of force is calculated in a similar way as the previous indicator was calculated, except that instead of indicating the position of the maximum force, the position of maximum rate of change of force is indicated, i.e.

  $$\chi_{maxdF} = x_{maxdF} / \max(x), \tag{3.29}$$

  where x_{maxdF} denotes the displacement location at the maximum of the absolute of the rate of change of the force dF.

  The properties of some electrical machine topologies are more dependent on the displacement position of the machine than others. An example is those properties that are dependent on the slope of the flux linkage, such as the series inductance of the machine. In some topologies, saturation would make these properties highly dependent on position. These properties will also have an influence on the drive electronics. It is therefore necessary to have a clear understanding of where during a displacement cycle maximum rate of change of the force can be expected. This indicator will provide that information. Preferred electrical machine topologies will be those where a maximum rate of change of the force can be easily established at a specific location.

3.5 Simulated case study: GPU-3

3.5.1 Overview

The purpose of this case study was to gain insight into the dynamics - especially force dynamics - of the original GPU-3 engine, as well as to investigate the influence of a wide range of different variations on the dynamics of the engine - especially the force dynamics demanded of both the displacer and the power piston electrical machines.

While the original GPU-3 engine is of the kinematic type fitted with a rhombic drive mechanism, the approach of this investigation was as if that engine was retrofitted and adapted as a free-piston engine with linear machines (or where piston displacement control was applied to a free-piston engine with very similar geometric and operational parameters).

The influence of variation of the following was investigated:

- Mean operating pressure.
- Engine speed.
- Hot side and cold side temperatures.

- Displacement connecting rod diameter.
- Stroke to bore area ratio.
- Piston displacement patterns.
- Masses of the power piston and displacer moving members.
- Spring constants of flexure bearings.
- Bounce space void volume to swept volume ratio.
- Compression space and bounce space mean pressure difference.

In the following section, key results of a simulation of the original GPU-3 engine are presented. The influence of the variations is then discussed in the sections to follow thereafter. Relevant graphical output and other results are given in appendix C and will be referred to frequently.

3.5.2 Original GPU-3 at default operational conditions

A broad range of results of a simulation of the original GPU-3 engine (with default operational conditions listed in Table C.1) is listed in Table 3.1. Relevant quantities are also plotted against crank angle and displacement in Figures C.1 to C.6 (pages 205 to 206).

Quantities related to the forces exerted on the displacer and the power piston due to pressure differences are denoted with subscripts $d\Delta p$ and $p\Delta p$ respectively. Quantities related to the forces exerted by the displacer and the power piston electrical machines are denoted with subscripts *dlem* and *plem* respectively. Quantities related to the mass acceleration forces for the displacer and the power piston are denoted with subscripts *dm* and *pm* respectively. Where maximum values are given, these imply the maximum of the absolute of the profiles.

Table 3.1: Simulation results obtained for GPU-3 with default conditions.

Average gas temperature results			
Expansion space			880,5 K (607,3 °C)
Heater			973,0 K (699,8 °C)
Cooler			323,5 K (50,3 °C)
Compression space			347,1 K (73,9 °C)
Pressure results	Average	Maximum	Swing
Expansion space	4,156 MPa	5,652 MPa	2,904 MPa
Compression space	4,140 MPa	5,701 MPa	3,029 MPa
p_e to p_c pressure drop	15,5 kPa		249,5 kPa
Pressure phase angle results			
Expansion space maximum pressure			85°
Expansion space minimum pressure			303°
Compression space maximum pressure			84°
Compression space minimum pressure			296°
Power results			
Input power			11,462 kW
p-V power before pumping losses			6,542 kW

Power lost by cooler		6,869 kW
Output power		4,463 kW
Output efficiency		38,9%
Net electrical power generated		5,942 kW
Power loss results		
Regenerator net enthalpy loss		597,8 W
Regenerator wall heat loss		1067,0 W
Pumping loss: Total		850,7 W
Pumping loss: Heater		51,7 W
Pumping loss: Regenerator		769,8 W
Pumping loss: Cooler		29,3 W
Force results	Average	Maximum
$F_{d\Delta p}$	-59,29 N	627,74 N
$F_{p\Delta p}$	0,00 kN	5,99 kN

A discrepancy exists between the calculated power values as reflected by the net electrical power generated (5,942 kW) and the calculated output power (4,463 kW).

The calculated output power as listed in Table 3.1 has been shown in appendix A to represent the output power obtained from the engine after consideration of various losses, but without consideration of mechanical losses.

The electrical power generated for each electrical machine is obtained from the average of the instantaneous power profile of the electrical machine for a complete cycle, again calculated from the product of the instantaneous speed and force of the electrical machine as indicated by (3.18) and (3.23) for the displacer and the power piston respectively. The net electrical power generated is then obtained by adding the power of the two electrical machines. This value is therefore closely related to the net p-V power of the Stirling cycle due to the structure of the second order formulation. Approximately the only difference is the total pumping losses not reflected in the net value of the p-V power. Calculation of the p-V power using the recalculated compression space and expansion space pressures, i.e. after consideration of the pressure drop across the heat exchangers and regenerator, yields exactly the same power value as obtained for the net electrical power generated. This, as well as a more detailed listing of calculated power values, is shown in Table 3.2.

The difference between the calculated output power and the net electrical output power is therefore approximately half of the pumping losses, the regenerator enthalpy losses and the wall heat leakages losses, while in reality, these two values should be equal. The problem with this discrepancy of values is that the power converted by the power piston electrical machine and to a lesser extent by the displacer electrical machine, is greatly over-estimated by of the order of 33%. This could jeopardise the effort to determine guidelines and specifications for linear machines.

One possible way to explain this difference is that the pressure swings are over-estimated, but this would only account for a difference of up to 3% (see Table A.3). The only remaining

Table 3.2: More detailed listing of calculated power values.

Description	Power
p-V power before pumping losses	
Expansion space p-V power	11,281 kW
Compression space p-V power	-4,739 kW
Resultant p-V power	6,542 kW
p-V power after pumping losses (postcalculated)	
Expansion space p-V power	10,678 kW
Compression space p-V power	-4,737 kW
Resultant p-V power	5,942 kW
Electrical machine power	
Power to power piston electrical machine	6,648 kW
Power to displacer electrical machine	-0,707 kW
Net electrical power generated	5,942 kW

possibility is that the pressure phase angle is simulated incorrectly. This issue will be addressed in the following section.

3.5.3 Simulated pressure phase angle error

Sullivan [31] raises an issue that he considers to have a substantial influence on the accuracy of simulations that he conducted, especially for the GPU-3. He argues that, while the pressure amplitude was predicted accurately, the power prediction error could be largely attributed to the inaccuracy in predicting the pressure phase angle, i.e. the angle between top dead centre of the displacer (in other words minimum expansion space volume) and the maximum gas pressure. He goes on to show that this error could be attributed to inaccurate modelling of the rate of heat transfer in the heater or alternatively in the rate of mass flow from the expansion and compression spaces due to gas leakage. Sullivan reports that the prediction error was approximately 12 degrees. In another table he indicates that the error was closer to between 5 to 7 degrees.

If it is indeed the case that the pressure phase angle is predicted inaccurately, then the influence thereof needs investigation. To address this issue, simulations were performed using the default operational conditions listed in Table C.1 in appendix C. The pressure profiles were then shifted with several degrees during post-processing to observe the influence thereof on the relevant calculated results. This investigation differs from the other variation investigations in this case study, in that a variation in simulation output is introduced and not a variation in physical engine characteristics or operational conditions.

Table 3.3 lists relevant measured data and simulated results of an investigation into the simulated pressure phase angle error. Measured pressure phase angle data as provided by Thieme [17] are listed for minimum and maximum pressure amplitudes for both the expansion and compression spaces. The simulated minima and maxima are listed in three columns indicated as 0°, -6° and -12°, corresponding to the degrees phase shift of the pressure profiles. Twelve degrees (and six as half of that) were chosen in following the findings of Sullivan. The

calculated p-V power has already taken the pressure difference between the expansion and compression space and therefore pumping losses, into consideration. The power delivered to the generators was calculated as explained in the previous section.

Table 3.3: Relevant measured data and simulated results of an investigation of the simulated pressure phase angle error.

Measured data			
Expansion space maximum		70°	
Expansion space minimum		295°	
Compression space maximum		70°	
Compression space minimum		285°	
Simulated data	0°	−6°	−12°
Pressure phase angle			
Expansion space maximum	85°	79°	73°
Expansion space minimum	303°	297°	291°
Compression space maximum	84°	78°	72°
Compression space minimum	296°	290°	284°
p-V power			
Expansion space [kW]	10,68	10,73	10,68
Compression space [kW]	-4,74	-5,83	-6,88
Total [kW]	5,94	4,9	3,81
Generator power			
To power piston generator [kW]	6,65	5,55	4,38
To displacer generator [kW]	-0,71	-0,65	-0,58
Resultant [kW]	5,94	4,9	3,81

The pressure phase angles obtained by shifting the pressure profiles with 12 degrees forward ($-12°$) yielded results that are the closest to the measured pressure phase angles, in fact, it is noticed that $-12°$ phase shift could be considered to be close to optimal (phase shifts of a degree or two forward or backward are seen to make the overall accuracy of the phase angles less accurate).

The resultant output power is seen to decrease substantially as the phase angle is shifted forward, to the point that the output power for the $-12°$ phase shift is fairly close to the measured output power without consideration of mechanical losses (indicated output power) as listed in Table A.3. The implication of this result and the fact that the pressure swings are predicted accurately are that the output power of a real engine is degraded by losses, not by lowering of the pressure amplitudes, but by shifting of the pressure profiles. While unverified, it is therefore expected that a more complex third order simulation that incorporates loss mechanisms as part of the cyclic simulation will yield pressure profiles closer to the actual measured profiles, i.e. with less phase angle error.

The significance of the results lies therein that the output power is lowered, while the force amplitudes remain at higher levels. Accurate prediction of output power levels are therefore not a prerequisite for the accurate prediction of the forces exerted on the pistons due to the

pressure differences. This is better illustrated by plotting the forces as a function of crank angle, or as a function of displacement.

Figures C.7 and C.8 show the expansion and compression space pressure profiles for the various phase shifts, followed by Figures C.9 and C.10 showing the pressure difference forces as a function of crank angle, and Figures C.11 and C.12 showing the pressure difference forces as a function of displacement. (The figures may be found on page 209 to 210. The zero references for the displacer and power piston are shifted to the centre of the respective piston displacements in Figures C.11 and C.12. This will be the case throughout Appendix C where plotting is done against displacement.)

In Figures C.11 and C.12, the reason for the sharp decline in the output power is illustrated clearly. The work done per cycle is equal to the area enclosed by the plot of force against displacement (equivalent to the discussion on p-V work presented in Section 2.2). It is shown that with increasing phase shift the area for work done by the power piston decreases, resulting in a net decrease of work done per cycle.

Not only does the introduction of a phase shift have a direct affect on the output power as shown above, but it will also effect the force indicators introduced in Section 3.4 by yielding more accurate results.

3.5.4 Mean pressure

The influence of the mean pressure was investigated by running simulations with mean pressure at 1,38 MPa, 2,76 MPa, 4,14 MPa, 5,52 MPa and 6,89 MPa respectively.

Figures C.13 to C.18 (page 211 to 212) show the pressures and forces plotted against crank angle and displacement.

The force profiles in Figures C.15 and C.16 reflect the increase in pressure difference between the expansion space and compression space and the compression space and bounce space respectively. Do note that the various bounce space pressures were equal to the average of the compression space pressures during the simulations. Maximum positive and negative forces were fairly equal for the power piston electrical machine, but show a substantial unbalance towards the positive maximum for the displacer electrical machine.

Table 3.4 lists the output power, absolute maximum force, as well as the force indicators for the displacer and power piston electrical machines respectively as derived from the simulations for variation of the mean pressure.

It is well known from the Beale equation that an increase of the mean pressure has a proportionate influence on the net power delivered by the engine and as a consequence, the power to weight and power to volume ratio of the engine. This is also approximately the case in reality. The increase of the power delivered to the displacer electrical machine however follows a different relation with increase in average pressure as shown in Table 3.4.

Variation of the mean pressure does however not substantially influence the maximum force to power ratio ($\Gamma_{F/P}$) and even less the maximum rate of change of force to maximum force ratio ($\Gamma_{dF/F}$) for the mean pressure range investigated. This simply means that the power

Table 3.4: Output power, absolute maximum force and force indicators as derived from the simulations for variation of the mean pressure.

Pressure	Power	Max. force	$\Gamma_{F/P}$	$\Gamma_{dF/F}$	χ_{maxF}	χ_{maxdF}
Displacer and electrical machine						
1,38 MPa	-429,2 W	456,4 N	1,063 N/W	296,5 s^{-1}	-0,633	0,347
2,75 MPa	-507,1 W	547,2 N	1,079 N/W	294,7 s^{-1}	-0,638	0,273
4,14 MPa	-576,0 W	627,7 N	1,090 N/W	295,0 s^{-1}	-0,640	0,241
5,52 MPa	-639,8 W	702,2 N	1,098 N/W	295,9 s^{-1}	-0,641	0,223
6,89 MPa	-699,5 W	771,9 N	1,103 N/W	296,9 s^{-1}	-0,643	0,206
Power piston and electrical machine						
1,38 MPa	1,550 kW	2,024 kN	1,306 N/W	334,8 s^{-1}	0,972	0,488
2,75 MPa	2,992 kW	4,015 kN	1,342 N/W	334,5 s^{-1}	0,974	0,480
4,14 MPa	4,381 kW	5,991 kN	1,368 N/W	334,3 s^{-1}	0,976	0,475
5,52 MPa	5,731 kW	7,956 kN	1,388 N/W	334,1 s^{-1}	0,977	0,471
6,89 MPa	7,039 kW	9,897 kN	1,406 N/W	333,9 s^{-1}	0,978	0,467

capability of the electrical machines will have to scale to some relation to the mean pressure, and that their ability to handle the increasing forces should scale accordingly.

Lastly, the last two indicators show that the displacement location of the maximum force and maximum rate of change of force does not vary substantially. This, in conjunction with the very small change in $\Gamma_{dF/F}$, supports the conclusion that, apart from scaling with the maximum force, the pressure dynamics are not influenced substantially.

3.5.5 Engine speed

The influence of engine speed variation was investigated by running simulations with engine speeds of 1000 rpm, 1500 rpm, 2000 rpm, 2500 rpm and 3000 rpm respectively.

Figures C.19 to C.24 (page 213 to 214) show the pressures and forces plotted against crank angle or displacement.

With the mean pressure fixed at 4,14 MPa, the compression space pressure profiles remained almost unchanged and therefore also the maximum force of the power piston electrical machine. The expansion space to compression space pressure difference, and as a result the maximum force of the displacer electrical machine increased with increase in speed.

Table 3.5 lists the output power, absolute maximum force, as well as the force indicators for the displacer and power piston electrical machines respectively, as derived from the simulations for variation of the engine speed.

The power delivered to both the electrical machines increases with speed, but at higher than the rate of increase of the speed for the displacer electrical machine and lower than the rate of increase of the speed for the power piston electrical machine. The rate of increase of the maximum force of the displacer electrical machine is also higher than that of the speed.

The $\Gamma_{F/P}$ indicator is close to reversely proportionate to the speed, i.e. it decreases for both electrical machines with factors of close to 3 from 1000 rpm to 3000 rpm. The $\Gamma_{dF/F}$ indicator

Table 3.5: Output power, absolute maximum force and force indicators as derived from the simulations for variation of the engine speed.

Speed	Power	Max. force	$\Gamma_{F/P}$	$\Gamma_{dF/F}$	χ_{maxF}	χ_{maxdF}
Displacer and electrical machine						
1000 rpm	-71,3 W	190,3 N	2,668 N/W	118,3 s^{-1}	-0,633	0,313
1500 rpm	-177,3 W	318,1 N	1,794 N/W	176,9 s^{-1}	-0,637	0,279
2000 rpm	-342,7 W	464,3 N	1,355 N/W	235,7 s^{-1}	-0,638	0,261
2500 rpm	-576,0 W	627,7 N	1,090 N/W	295,0 s^{-1}	-0,640	0,241
3000 rpm	-885,3 W	807,6 N	0,912 N/W	354,6 s^{-1}	-0,641	0,229
Power piston and electrical machine						
1000 rpm	1,844 kW	6,059 kN	3,286 N/W	133,9 s^{-1}	0,972	0,486
1500 rpm	2,709 kW	6,031 kN	2,226 N/W	200,7 s^{-1}	0,974	0,482
2000 rpm	3,553 kW	6,009 kN	1,691 N/W	267,5 s^{-1}	0,975	0,478
2500 rpm	4,381 kW	5,991 kN	1,368 N/W	334,3 s^{-1}	0,976	0,475
3000 rpm	5,195 kW	5,976 kN	1,150 N/W	401,0 s^{-1}	0,976	0,473

is again close to directly proportionate to the speed. The location indicators show that the displacement location of the maximum force and maximum rate of change of force does not vary substantially as in the case for mean pressure variation. Variation of force dynamics is therefore largely determined by the speed.

3.5.6 Hot and cold side temperature

The influence of hot and cold side temperature variation was investigated by running simulations with combinations of hot and cold side temperatures with the hot side temperature at 715,6 °C, 765,7 °C and 815,6 °C and the cold side temperature at 20,0 °C, 40,0 °C and 60,0 °C.

Figures C.25 to C.30 (page 215 to 216) show the pressures and forces plotted against crank angle or displacement. The profiles for pressure and force show very little change due to the variation of temperatures.

Table 3.6 lists the output power, absolute maximum force, as well as the force indicators for the displacer and power piston electrical machines respectively as derived from the simulations for variation of the hot and cold side temperatures.

None of the displacer electrical machine related values or indicators show any substantial variation due to a variation in temperature. The power delivered to and maximum force of the power piston electrical machine is however affected as either of the temperatures vary. This leads to a variation in the $\Gamma_{F/P}$ indicator. No substantial variation can however be seen for the rest of the indicators. Apart from scaling with the maximum force, force dynamics for either electrical machine are therefore not substantially influenced.

3.5.7 Displacer connecting rod diameter

While both the displacer and the power piston are connected to electrical machines to perform displacement control, only the electrical machine connected to the power piston is shown in

Table 3.6: Output power, absolute maximum force and force indicators as derived from the simulations for variation of the hot and cold side temperatures.

Temperatures	Power	Max. force	$\Gamma_{F/P}$	$\Gamma_{dF/F}$	χ_{maxF}	χ_{maxdF}
Displacer and electrical machine						
715,6 °C; 20,0 °C	-574,1 W	623,9 N	1,087 N/W	296,6 s^{-1}	-0,633	0,241
765,6 °C; 20,0 °C	-576,0 W	627,7 N	1,090 N/W	295,0 s^{-1}	-0,640	0,241
815,6 °C; 20,0 °C	-578,1 W	631,6 N	1,093 N/W	293,5 s^{-1}	-0,646	0,241
765,6 °C; 40,0 °C	-575,7 W	623,6 N	1,083 N/W	296,8 s^{-1}	-0,632	0,251
765,6 °C; 60,0 °C	-575,6 W	619,7 N	1,077 N/W	298,6 s^{-1}	-0,622	0,259
Power piston and electrical machine						
715,6 °C; 20,0 °C	4,033 kW	5,891 kN	1,461 N/W	333,4 s^{-1}	0,980	0,458
765,6 °C; 20,0 °C	4,381 kW	5,991 kN	1,368 N/W	334,3 s^{-1}	0,976	0,475
815,6 °C; 20,0 °C	4,713 kW	6,090 kN	1,292 N/W	334,9 s^{-1}	0,971	0,491
765,6 °C; 40,0 °C	3,946 kW	5,866 kN	1,487 N/W	333,2 s^{-1}	0,981	0,453
765,6 °C; 60,0 °C	3,537 kW	5,755 kN	1,627 N/W	331,9 s^{-1}	0,987	0,432

Figure 3.1. The connecting rod that will connect the displacer to its electrical machine is however shown to extend through the power piston and its connecting rod as well as the mover of the electrical machine of the power piston. This arrangement is found in all kinematic engines and in some free-piston engines [7, 27, 28]. The alternative arrangement, where the displacer connecting rod does not extend beyond the compression space is found in some free-piston engines [5, 24].

Both arrangements have several advantages and disadvantages. As for piston displacement control, a difference in the instantaneous pressure and forces are found due to the difference in effective power piston area and compression space volume. Perhaps the most significant difference between the two arrangements lies in the appropriate topology for the displacer electrical machine. When the connecting rod extends into the bounce space, more freedom is allowed in the choice of machine topology than is the case for the alternative, where the electrical machine will have to be incorporated as part of the displacer and the cylinder wall.

Variation of the rod area to bore area ratio was chosen to more easily apply the results to a broader range of engines. The influence of a variation of the displacer connecting rod diameter was investigated by running simulations with connecting rod area to bore area percentage ratios of 0%, 1%, 2%[6], 5% and 10%.

Figures C.31 to C.36 (page 217 to 218) show the pressures and forces plotted against crank angle or displacement.

The pressure profiles show relatively small variation. It is noted however that the swing of both the expansion space to compression space pressure drop and the compression space pressure decreases as the ratio increases. The force of the power piston electrical machine is lowered even more, with both the pressure across as well as the area of the power piston that decreases.

[6]The actual GPU-3 rod area to bore area percentage ratio is just below 2%.

The most dramatic variation is noted for the displacer electrical machine force. The change in the profiles could be explained from equation (3.18). The $A_{rd}\Delta p_{bc}$ force term is in the direction of the displacer movement for the larger part of the cycle (refer for example also to Figures C.1 and C.3), which means that, on average, positive work is being done *on the displacer* as a result of this force term. Average work is again being done *by the displacer* as a result of the $A\Delta p_{ce}$ force term. As the displacer rod area increases, the $A_{rd}\Delta p_{bc}$ force term becomes increasingly dominant. It should be remembered that the swing of the pressure difference p_{bc} is must larger than that of the p_{ce} pressure difference. A_{rd} could therefore be much smaller than A and still have a substantial influence.

Table 3.7 lists the output power, absolute maximum force, as well as the force indicators for the displacer and power piston electrical machines respectively as derived from the simulations for variation of the displacer rod area to bore area ratio.

Table 3.7: Output power, absolute maximum force and force indicators as derived from the simulations for variation of the displacer rod area to bore area ratio.

Percentage area	Power	Max. force	$\Gamma_{F/P}$	$\Gamma_{dF/F}$	χ_{maxF}	χ_{maxdF}
Displacer and electrical machine						
0,0%	-576,0 W	627,7 N	1,090 N/W	295,0 s^{-1}	-0,640	0,241
1,0%	-461,0 W	579,4 N	1,257 N/W	316,0 s^{-1}	-0,660	0,223
2,0%	-347,6 W	532,1 N	1,531 N/W	340,5 s^{-1}	-0,682	0,204
5,0%	17,0 W	397,1 N	23,29 N/W	444,1 s^{-1}	-0,749	0,147
10,0%	500,1 W	434,3 N	0,868 N/W	409,3 s^{-1}	0,813	0,941
Power piston and electrical machine						
0,0%	4,381 kW	5,991 kN	1,368 N/W	334,3 s^{-1}	0,976	0,475
1,0%	4,267 kW	5,898 kN	1,382 N/W	334,2 s^{-1}	0,976	0,471
2,0%	4,154 kW	5,804 kN	1,397 N/W	334,1 s^{-1}	0,977	0,467
5,0%	3,821 kW	5,529 kN	1,447 N/W	333,7 s^{-1}	0,980	0,454
10,0%	3,786 kW	5,081 kN	1,547 N/W	333,0 s^{-1}	0,984	0,434

The output power as well as the maximum force listed in Table 3.7 for the power piston electrical machine show a gradual decline, resulting in an increasing maximum force to power ratio. No real significant change is seen for the other force indicators. It is therefore concluded that, other than a decrease in the maximum force, the force dynamics of the power piston remain unchanged.

The parameters listed for the displacer electrical machine however show substantial variation, with the power that increases to the extent that it becomes positive for a rod area to bore area percentage of 5% and more, while the maximum force decreases. The maximum force to output power ratio becomes very large due to the low output power at 5%. All of the force indicators are affected by this phenomenon. These are better appreciated by again referring to Figures C.33 and C.35.

It should be noted that while the output power of the power piston electrical machine is lowered, the net output power increases slightly, due to the increase in displacer electrical

machine output power. The diameter of the rod could therefore be of benefit if chosen correctly.

3.5.8 Stroke to bore area ratio

The strokes of free-piston engines are normally short compared to their kinematic counterparts. This is attributed to practical reasons, of which the use of flexure bearings as a means to hold the moving members in place, is considered as one of the most important.

Stroke variation is also important when considering different electrical generator topologies. It is possible that some topologies could become more feasible for longer stroke length and others for shorter stroke length. In addition, a question remains whether piston displacement control could be performed more easily for longer stroke lengths or for shorter stroke lengths. An investigation of a variation of stroke length was therefore considered necessary.

The influence of a variation of the stroke to bore area ratio was investigated by running simulations for normalised stroke to bore area ratios of 0,25, 1,0 and 4,0. Stroke to bore area ratios were chosen in order to vary the stroke length while simultaneously adjusting the bore area in order to maintain the original volumetric change. This in turn is necessary to maintain the original thermodynamic cycle. A normalised stroke to bore area ratio of 0,25 for example entails working with half the stroke length and double the bore area.

Figures C.37 to C.42 (page 219 to 220) show the pressures and forces plotted against crank angle or displacement.

The pressure profiles reflect the unchanged thermodynamic cycle. The forces are therefore only determined by the bore area.

Table 3.8 lists the output power, absolute maximum force, as well as the force indicators for the displacer and power piston electrical machines respectively as derived from the simulations for variation of the stroke to bore area ratio.

Table 3.8: Output power, absolute maximum force and force indicators as derived from the simulations for variation of the stroke to bore area ratio.

Normalised ratio	Power	Max. force	$\Gamma_{F/P}$	$\Gamma_{dF/F}$	χ_{maxF}	χ_{maxdF}
Displacer and electrical machine						
0,25	-576,0 W	1255,5 N	2,180 N/W	295,0 s^{-1}	-0,640	0,241
1,00	-576,0 W	627,7 N	1,090 N/W	295,0 s^{-1}	-0,640	0,241
4,00	-576,0 W	313,9 N	0,545 N/W	295,0 s^{-1}	-0,640	0,241
Power piston and electrical machine						
0,25	4,381 kW	11,982 kN	2,735 N/W	334,3 s^{-1}	0,976	0,475
1,00	4,381 kW	5,991 kN	1,368 N/W	334,3 s^{-1}	0,976	0,475
4,00	4,381 kW	2,996 kN	0,684 N/W	334,3 s^{-1}	0,976	0,475

Variation is shown for only the maximum force and the force to power ratio. These variations are directly proportional to the bore area variation. All other levels and indicators are unchanged.

3.5.9 Piston displacement patterns

The investigation on the influence of different drive mechanisms on the performance of the GPU-3 engine by Strauss and Dobson [12] was already discussed in chapter 2. It was shown that optimised drive mechanisms could enhance the performance of the GPU-3 engine and that different mechanisms performed better under different operational conditions. One of the key advantages of direct piston displacement control is the ability to follow any piston displacement necessary to control the engine for best performance in real time as the operational conditions change.

The influence of different piston displacement patterns was therefore investigated by running simulations for the original rhombic displacement, as well as the composite, sinusoidal and pseudo-ideal displacement patterns obtained from optimisation for maximum power output as reported by Strauss and Dobson. These four particular displacement patterns were chosen since they represent a broad range of displacement dynamics.

Figures C.43 to C.50 (page 221 to 223) show the displacements, pressures and forces plotted against crank angle or displacement.

The influence of the various displacement patterns on the pressures and as a consequence on the electrical machine forces is clearly shown, especially their influence on the areas enclosed by the force against displacement plots in Figures C.49 and C.50.

Table 3.9 lists the output power, absolute maximum force, as well as the force indicators for the displacer and power piston electrical machines respectively as derived from the simulations for different piston displacement patterns.

Table 3.9: Output power, absolute maximum force and force indicators as derived from the simulations for different piston displacement patterns for the maximum output power case.

Displacement	Power	Max. force	$\Gamma_{F/P}$	$\Gamma_{dF/F}$	χ_{maxF}	χ_{maxdF}
Displacer and electrical machine						
Original	-576,0 W	627,7 N	1,090 N/W	295,0 s^{-1}	-0,640	0,241
Composite	-808,2 W	679,3 N	0,841 N/W	400,2 s^{-1}	-0,486	0,336
Sinusoidal	-491,6 W	374,9 N	0,763 N/W	257,0 s^{-1}	-0,803	-0,126
Pseudo-ideal	-1679,8 W	1295,7 N	0,771 N/W	823,6 s^{-1}	-0,901	-0,981
Power piston and electrical machine						
Original	4,381 kW	5,991 kN	1,368 N/W	334,3 s^{-1}	0,976	0,475
Composite	4,758 kW	5,963 kN	1,253 N/W	365,2 s^{-1}	0,974	0,411
Sinusoidal	4,427 kW	5,050 kN	1,115 N/W	258,9 s^{-1}	0,837	0,985
Pseudo-ideal	5,514 kW	6,982 kN	1,266 N/W	391,2 s^{-1}	0,996	0,624

The power delivered to the displacer electrical machine is directly related to the increase in pumping losses due to non-harmonic flow of working fluid. The power delivered to the power piston electrical machines on the other hand reflects the ability to convert more energy during one cycle due to non-harmonic displacement. The most optimal displacement - in this case the composite drive - finds the best balance between increasing fluid flow related losses

and increasing cyclic energy conversion capability. This is in agreement with the findings of Strauss and Dobson.

For both the displacer and power piston electrical machines the highest power delivered, maximum force and maximum rate of change of force to force ratio is demanded by pseudo-ideal displacement. The rest of the indicators show a profound effect on the force dynamics due to the different displacement patterns, as was also reflected in the above-mentioned figures.

The influence of different piston displacement patterns was also investigated by running simulations for the original rhombic displacement, as well as the composite, sinusoidal and pseudo-ideal displacement obtained from optimisation for maximum efficiency as reported by Strauss and Dobson.

Figures C.51 to C.58 (page 224 to 226) show the displacements, pressures and forces plotted against crank angle or displacement.

The same observation could be made as for the maximum output power case shown in Figures C.43 to C.50. In addition, it is observed that piston displacement and as a consequence the pressure profiles and forces, are less non-harmonic than for the maximum output power case.

Table 3.10 lists the output power, absolute maximum force, as well as the force indicators for the displacer and power piston electrical machines respectively, as derived from the simulations for different piston displacement patterns.

Table 3.10: Output power, absolute maximum force and force indicators as derived from the simulations for different piston displacement patterns for the maximum efficiency case.

Displacement	Power	Max. force	$\Gamma_{F/P}$	$\Gamma_{dF/F}$	χ_{maxF}	χ_{maxdF}
Displacer and electrical machine						
Original	-576,0 W	627,7 N	1,090 N/W	295,0 s^{-1}	-0,640	0,241
Composite	-718,2 W	483,4 N	0,673 N/W	228,9 s^{-1}	-0,654	0,426
Sinusoidal	-819,3 W	417,4 N	0,509 N/W	246,3 s^{-1}	-0,714	-0,332
Pseudo-ideal	-1021,0 W	876,6 N	0,859 N/W	301,7 s^{-1}	-0,632	-0,998
Power piston and electrical machine						
Original	4,381 kW	5,991 kN	1,368 N/W	334,3 s^{-1}	0,976	0,475
Composite	5,123 kW	4,761 kN	0,929 N/W	296,9 s^{-1}	0,892	0,714
Sinusoidal	4,759 kW	4,102 kN	0,862 N/W	252,8 s^{-1}	0,889	0,984
Pseudo-ideal	5,097 kW	6,184 kN	1,213 N/W	316,5 s^{-1}	0,952	0,664

The output power of the electrical machines, as well as the maximum force, differs considerably, with the sinusoidal displacement having the lowest maximum force to power ratio and the pseudo-ideal having the highest ratio. The rest of the indicators reflect the variation in dynamics, as shown in Figures C.51 to C.58.

3.5.10 Masses of the power piston and displacer moving members

An important factor not considered yet is the masses of the moving members and the influence thereof on the forces necessary to maintain the required piston displacement.

The influence of a variation of the masses of the moving members (including the electrical generator moving members as well as the pistons and other moving parts) was investigated by running simulations for mass to power ratios of 0,0, 0,5, 1,0, 2,0 and 5,0. Mass to power ratio was chosen to express the mass in relation to the power delivered to the electrical machine.

Figures C.59 to C.64 (page 227 to 220) show the forces plotted against crank angle or displacement.

It is seen that both displacer and power piston electrical machine forces are substantially influenced by increasing mass to power ratios. In the case of the displacer electrical machine, increasing the mass immediately increases the maximum force as well as the profile dynamics. In the case of the power piston electrical machine, increasing the mass initially lowers the maximum force and then increases the maximum force again as the mass acceleration force becomes dominant.

Table 3.11 lists the output power, absolute maximum force, as well as the force indicators for the displacer and power piston electrical machines respectively as derived from the simulations for variation of the masses of the displacer and power piston moving members.

Table 3.11: Output power, absolute maximum force and force indicators as derived from the simulations for variation of the masses of the displacer and the power piston moving members.

Ratio	Power	Max. force	$\Gamma_{F/P}$	$\Gamma_{dF/F}$	χ_{maxF}	χ_{maxdF}
Displacer and electrical machine						
0,0 g/W	-576,0 W	627,7 N	1,090 N/W	295,0 s^{-1}	-0,640	0,241
0,5 g/W	-576,0 W	959,5 N	1,666 N/W	363,1 s^{-1}	-0,794	0,157
1,0 g/W	-576,0 W	1324,8 N	2,300 N/W	388,6 s^{-1}	-0,856	0,124
2,0 g/W	-576,0 W	2084,6 N	3,619 N/W	407,7 s^{-1}	-0,906	0,094
5,0 g/W	-576,0 W	4417,7 N	7,669 N/W	420,6 s^{-1}	-0,943	0,069
Power piston and electrical machine						
0,0 g/W	4,381 kW	5,991 kN	1,368 N/W	334,3 s^{-1}	0,976	0,475
0,5 g/W	4,381 kW	3,686 kN	0,841 N/W	347,1 s^{-1}	0,805	0,769
1,0 g/W	4,381 kW	2,906 kN	0,663 N/W	354,0 s^{-1}	0,216	-0,603
2,0 g/W	4,381 kW	7,461 kN	1,703 N/W	473,3 s^{-1}	0,808	-0,595
5,0 g/W	4,381 kW	24,886 kN	5,680 N/W	449,1 s^{-1}	0,932	-0,590

The maximum force of the power piston electrical machine is shown to remain low up until a mass to power ratio of 1,0 kg/kW. A sharp increase is shown from 1,0 kg/kW to 2,0 kg/kW. The maximum force to power ratio follows this same trend with the power delivered to the electrical machine remaining constant. The rest of the indicators show the substantial influence on the force dynamics as observed in Figures C.59 to C.64.

3.5.11 Spring forces

Flexure bearings are often used in free-piston engines as a means to hold the displacer and the power piston moving members in place in a frictionless manner. This introduces spring forces that act on the moving members and that will have an effect on the ability to perform piston displacement control. Apart from these actual spring forces, similar forces could also exist. An example thereof is the reluctance forces present in permanent magnet iron-cored linear electric machines. The influence of these forces is therefore also considered in this investigation.

The influence of a variation of spring forces was investigated by running simulations for maximum spring force to power ratio of 0,0, 0,1, 0,2 and 0,5. Maximum spring force to power ratio was chosen to simplify a comparison of their influence on the maximum force to power indicator. A range up to 0,5 was chosen since it is considered to provide adequately for a worst case scenario.

Figures C.65 to C.70 (page 229 to 230) show the forces plotted against crank angle or displacement.

A decrease is observed in the maximum force of the displacer electrical machine for the range of maximum spring force to power ratio under consideration, while the force of the power piston electrical machine shows an increase.

Table 3.12 lists the output power, absolute maximum force, as well as the force indicators for the displacer and power piston electrical machines respectively as derived from the simulations for variation of the maximum spring force to power ratio.

Table 3.12: Output power, absolute maximum force and force indicators as derived from the simulations for variation of the maximum spring force to power ratio.

Ratio	Power	Max. force	$\Gamma_{F/P}$	$\Gamma_{dF/F}$	χ_{maxF}	χ_{maxdF}
Displacer and electrical machine						
0,0 N/W	-576,0 W	627,7 N	1,090 N/W	295,0 s^{-1}	-0,640	0,241
0,1 N/W	-576,0 W	592,0 N	1,028 N/W	283,2 s^{-1}	-0,601	0,251
0,2 N/W	-576,0 W	558,7 N	0,970 N/W	268,9 s^{-1}	-0,557	0,636
0,5 N/W	-576,0 W	476,4 N	0,827 N/W	323,7 s^{-1}	-0,388	-0,980
Power piston and electrical machine						
0,5 N/W	4,381 kW	5,991 kN	1,368 N/W	334,3 s^{-1}	0,978	0,475
0,1 N/W	4,381 kW	6,419 kN	1,465 N/W	330,9 s^{-1}	0,978	0,454
0,2 N/W	4,381 kW	6,848 kN	1,563 N/W	328,1 s^{-1}	0,981	0,434
0,5 N/W	4,381 kW	8,141 kN	1,858 N/W	322,4 s^{-1}	0,986	0,382

While the power delivered to the electrical machines remains constant, the maximum force is substantially influenced, as indicated before. A decrease in the maximum force to power ratio is observed for the displacer electrical machine. It is also shown that the rest of the indicators are influenced noticeably by the introduction of spring forces. The maximum force to power ratio of the power piston electrical machine is shown to increase to 1,858 N/W for a maximum spring force to power ratio of 0,5. The rest of the indicators are however not influenced to the same extent.

3.5.12 Bounce space void volume

In this section, a detailed treatment of the influence of the bounce space void volume is presented.

The influence of a variation of bounce space void volume was investigated by running simulations for bounce space void volume to swept volume ratio of 1,0, 2,0, 5,0, 10,0 and infinity. It is considered convenient to express the void volume in terms of a ratio with respect to the swept volume. Knowledge of typical ratios is limited, since bounce space void volumes are not normally disclosed when free-piston engine specifications are published. It is however considered that ratios smaller than of the order of 2,0 will not be easily obtained and that a ratio of 5,0 and higher might be more realistic.

Figures C.71 to C.76 (page 231 to 232) show the forces plotted against crank angle or displacement.

It is shown that a variation in the bounce space pressure does not influence the displacer electrical machine forces, since the displacer connecting rod area is ignored. The pressure swing in the bounce space is out of phase with the pressure in the compression space. This results in the power piston electrical machine force swing increasing as the bounce space void volume to swept volume ratio decreases, to the extent that for a ratio of approximately 2,0 and less, the swing more than doubles.

Table 3.13 lists the output power, absolute maximum force, as well as the force indicators for the displacer and power piston electrical machines respectively as derived from the simulations for variation of the bounce space void volume to swept volume ratio.

Table 3.13: Output power, absolute maximum force and force indicators as derived from the simulation for variation of the bounce space void volume to swept volume ratio.

Ratio	Power	Max. force	$\Gamma_{F/P}$	$\Gamma_{dF/F}$	χ_{maxF}	χ_{maxdF}
Displacer and electrical machine						
1,0	-576,0 W	627,7 N	1,090 N/W	295,0 s^{-1}	-0,640	0,241
2,0	-576,0 W	627,7 N	1,090 N/W	295,0 s^{-1}	-0,640	0,241
5,0	-576,0 W	627,7 N	1,090 N/W	295,0 s^{-1}	-0,640	0,241
10,0	-576,0 W	627,7 N	1,090 N/W	295,0 s^{-1}	-0,640	0,241
∞	-576,0 W	627,7 N	1,090 N/W	295,0 s^{-1}	-0,640	0,241
Power piston and electrical machine						
1,0	4,381 kW	16,343 kN	3,730 N/W	267,2 s^{-1}	-0,997	-0,381
2,0	4,381 kW	11,317 kN	2,583 N/W	293,8 s^{-1}	-0,989	0,093
5,0	4,381 kW	8,421 kN	1,922 N/W	313,4 s^{-1}	0,985	0,337
10,0	4,381 kW	7,301 kN	1,667 N/W	321,6 s^{-1}	0,982	0,407
∞	4,381 kW	5,991 kN	1,368 N/W	334,3 s^{-1}	0,976	0,475

A variation of the bounce space pressure is shown to have no effect on the displacer electrical machine force. Even with consideration of the connecting rod area, a variation is expected to have little influence. The influence on the power piston is similar to the spring forces of flexure bearings, with the maximum force to power ratio for bounce space void volume to swept vol-

ume ratios of approximately 2,0 and less increasing to beyond twice that of the default infinite ratio. A moderate change is seen for the other force indicators.

3.5.13 Bounce space/compression space average pressure difference

In Section 3.3.2, the nonlinear leakage of gas and its influence on free-piston engines were explained. The resultant loss of gas from the compression space to the bounce space will lead to the bounce space pressure having an average pressure higher than that of the compression space. In the light of simplifying the engine, the ability to counter this force resulting from an average pressure difference - and as a result piston creepage - in the electrical machine itself, should be examined.

The influence of a variation of a difference between the average bounce space pressure and the average compression space pressure was investigated by running simulations for bounce space/compression space average pressure differences of 0,0%, 1,0%, 2,0%, 5,0% and 10,0%.

Figures C.77 to C.82 (page 233 to 234) show the forces plotted against crank angle or displacement.

With the default bounce space volume taken as infinite, the bounce space pressure is seen to remain constant, but to increase in value. The effect thereof is seen to merely offset the power piston linear machine force, without changing the dynamics otherwise. No change is noticed for the displacer electrical machine force.

Table 3.14 lists the output power, absolute maximum force, as well as the force indicators for the displacer and power piston electrical machines respectively as derived from the simulations for variation of the bounce space average pressure to compression space average pressure difference.

Table 3.14: Output power, absolute maximum force and force indicators as derived from the simulation for variation of the bounce space average pressure to compression space average pressure difference.

Percentage difference	Power	Max. force	$\Gamma_{F/P}$	$\Gamma_{dF/F}$	χ_{maxF}	χ_{maxdF}
Displacer and electrical machine						
0,0%	-576,0 W	627,7 N	1,090 N/W	295,0 s^{-1}	-0,640	0,241
1,0%	-576,0 W	627,7 N	1,090 N/W	295,0 s^{-1}	-0,640	0,241
2,0%	-576,0 W	627,7 N	1,090 N/W	295,0 s^{-1}	-0,640	0,241
5,0%	-576,0 W	627,7 N	1,090 N/W	295,0 s^{-1}	-0,640	0,241
10,0%	-576,0 W	627,7 N	1,090 N/W	295,0 s^{-1}	-0,640	0,241
Power piston and electrical machine						
0,0%	4,381 kW	5,991 kN	1,368 N/W	334,3 s^{-1}	0,976	0,475
1,0%	4,381 kW	5,831 kN	1,331 N/W	343,4 s^{-1}	0,976	0,475
2,0%	4,381 kW	5,952 kN	1,359 N/W	336,5 s^{-1}	-0,924	0,475
5,0%	4,381 kW	6,428 kN	1,467 N/W	311,5 s^{-1}	-0,924	0,475
10,0%	4,381 kW	7,223 kN	1,649 N/W	277,3 s^{-1}	-0,924	0,475

While the power delivered to the power piston electrical machine remains constant, a change is seen in the electrical machine force. It decreases initially and starts to increase from only between 2,0% to 5,0% pressure difference. A quick verification also shows that the net flow of gas from the compression space to the bounce space reversed to become a net flow from the bounce space to the compression space of between 2,0% to 5,0% pressure difference (It is therefore expected that the pressure difference will stabilise between 2% to 5%.). For the case where the bounce space has a finite volume, the increase in power piston electrical machine force is expected to start earlier. The rest of the indicators show little to moderate variation due to the increase in pressure difference.

No variation is seen for the displacer electrical machine parameters and indicators and little variation is expected even where the displacer connecting rod area is not zero.

3.5.14 Summary of findings

In this section, a short summary of findings is presented.

Table 3.15 lists the influence of the variations that were investigated by assigning different categories of influence, ranging from negligible to extreme, for the output power, maximum force and force indicators of each variation. The categories for the output power, maximum force and the two force indicators $\Gamma_{F/P}$ and $\Gamma_{dF/F}$ were determined by calculating the percentage change of these parameters across the range of variation that was investigated. The categories were then assigned as follows, namely less than 1.0% change as negligible, less than 5% change as very moderate, less than 20% change as moderate, less than 50% change as substantial and more than 50% change as extreme.

In the case of the two force indicators χ_{maxF} and χ_{maxdF}, the categories were assigned as follows, namely less than 0.01 change as negligible, less than 0.05 change as very moderate, less than 0.2 change as moderate, less than 0.5 change as substantial and more than 0.5 change as extreme. Care should be taken however when interpreting these two indicators. In electrical machines that are symmetrical about their centre position in the direction of displacement (no practical machine is known that is not), having an indicator value of 0,9 or -0,9 makes no real difference. The maximum force can be reached at both locations by the same magnitude of current. Some of the categories below that are indicated as extreme for these two indicators could therefore fall within lower categories if the sign of the value of the indicators is ignored.

The **output power** in the majority of cases is influenced either to the extreme or very little. If the operational condition variations (for mean pressure, engine speed and temperature variations) are ignored, then it is only the variation of the displacement connecting rod diameter and piston displacement that influence the output power.

The **maximum force** is however influenced by all variations, except for the forces of the displacer electrical machine for bounce space void volume and average pressure difference variation and this only because the default displacer rod diameter was zero.

The force indicator $\boldsymbol{\Gamma_{F/P}}$ varies as a result of the variation of the output power and the maximum force. In a few instances the output power and the maximum force vary such that

Table 3.15: Influence of the variations on the output power, absolute maximum force and force indicators (■ - extreme, ● - substantial, ○ - moderate, · - very moderate, — - negligible).

Variation	Power	Max. force	$\Gamma_{F/P}$	$\Gamma_{dF/F}$	χ_{maxF}	χ_{maxdF}
Displacer and electrical machine						
Mean pressure	■	■	·	—	·	○
Engine speed	■	■	■	■	—	○
Hot and cold side temperature	—	·	·	·	·	·
Displacer connecting rod diameter	■	■	■	■	■	■
Stroke to bore area ratio	—	■	■	—	—	—
Piston displacement (max. power)	■	■	●	■	●	■
Piston displacement (max. eff.)	■	■	■	●	○	■
Moving member masses	—	■	■	●	●	○
Spring forces	—	●	●	●	●	■
Bounce space void volume	—	—	—	—	—	—
Average pressure difference	—	—	—	—	—	—
Power piston and electrical machine						
Mean pressure	■	■	○	—	—	·
Engine speed	■	·	■	■	—	·
Hot and cold side temperature	●	○	●	—	·	○
Displacer connecting rod diameter	○	○	○	—	—	○
Stroke to bore area ratio	—	■	■	—	—	—
Piston displacement (max. power)	●	●	●	■	○	■
Piston displacement (max. eff.)	○	■	■	●	·	■
Moving member masses	—	■	■	●	■	■
Spring forces	—	■	●	·	—	○
Bounce space void volume	—	■	■	●	■	■
Average pressure difference	—	●	●	●	■	—

$\Gamma_{F/P}$ show very little change, but in the majority of cases $\Gamma_{F/P}$ is also extremely influenced.

The force indicator $\boldsymbol{\Gamma_{dF/F}}$ is less influenced by the variations than $\Gamma_{F/P}$, indicating a better correlation between the change of the force and its derivative than between the output power and the maximum force. In a few instances however, the extreme variation of this indicator shows a dramatic change in the dynamic response of the force profile.

The force indicator $\boldsymbol{\chi_{maxF}}$ shows various degrees of change for both the displacer and power piston electrical machines. It is also seen from previous sections that the majority of values for the displacer are in the region of just less than -0,6 and for the power piston above 0,9. Only in a minority of cases is the maximum value for the force found at other locations.

The force indicator $\boldsymbol{\chi_{maxdF}}$ shows more change for both machines than for the χ_{maxF} indicator. The values of this indicator are also more often found across the spectrum from -1,0 to 1,0 than for χ_{maxF}.

3.5.15 Effect of combined variations

An important question remains. With the influence of a number of variations now known, what will be the combined effect of the variations?

It is clear from results seen in the previous sections that the influence of some of the variations will either add-up to worsen the effect on some of the parameters or that the influence of the variations will counter that of others. An example is that of the influence of the masses of the moving members and that of spring constants or alternatively the bounce volume to swept volume ratio. Where the influence of the masses increases the maximum force of the displacer electrical machine, the introduction of springs (or spring-like forces) decreases the maximum force. It is therefore possible that with careful design, the influence of one variation could be reduced with another.

The extent of the combined effect of these influences are however unknown. To investigate the combined influence of the variations discussed in the previous sections, a subset of each of the variations was carefully selected. These are listed in Table 3.16. Simulations were then run for all possible combinations of these selected variations. The results were analysed by determining the distribution of the output parameter values, and are discussed below. In the plots to follow, the distributions of the output parameters are given as bar graphs and normalisation was done with respect to the bar with the highest value.

In the selection process, some of the variations that are deemed to be impractical or unlikely were excluded. The mean pressure and engine speed variations were chosen to favour high performance engines, i.e. running the engine at high speed and higher pressure. Lastly, for some of the variations such as for the bounce space void volume to swept volume ratio, a few variations were excluded to limit the total amount of possible combinations[7].

Table 3.16: Subset selection of variations for combined influence simulations.

Variation	Subset
Mean pressure [MPa]	4,14, 6,89
Engine speed [rpm]	2500, 3000
Hot side temperature [°C]	715,6, 765,6, 815,6
Cold side temperature [°C]	40,0, 60,0
Displacer connecting rod area to bore area ratio	0,0, 0,02, 0,05
Stroke to bore area ratio [m^{-1}]	0,25, 1,00, 4,00
Piston displacement	Original, Composite, Sinusoidal, Pseudo-ideal
Moving member mass to power ratio [g/W]	0,0, 1,0, 2,0
Spring forces [N/W]	0,0, 0,2, 0,5
Bounce space void volume to swept volume ratio	1,0, 5,0, infinity
Bounce/compression space average pressure difference [%]	0,0, 2,0, 5,0

[7] A total of 183708 possible combinations still remained.

Output power

Figures 3.3 and 3.4 show the normalised distribution of the output power of the displacer and power piston electrical machines respectively.

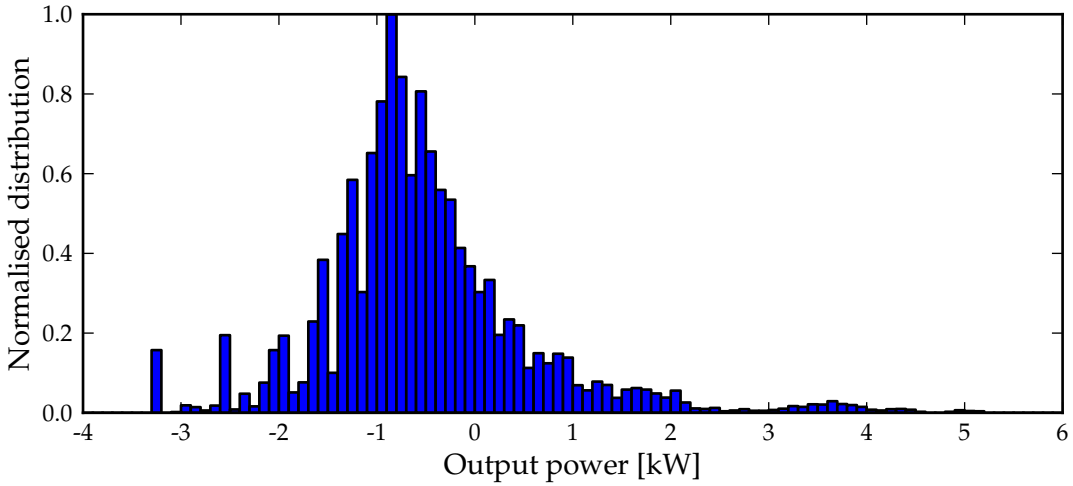

Figure 3.3: Normalised distribution of displacer electrical machine output power for combined variations.

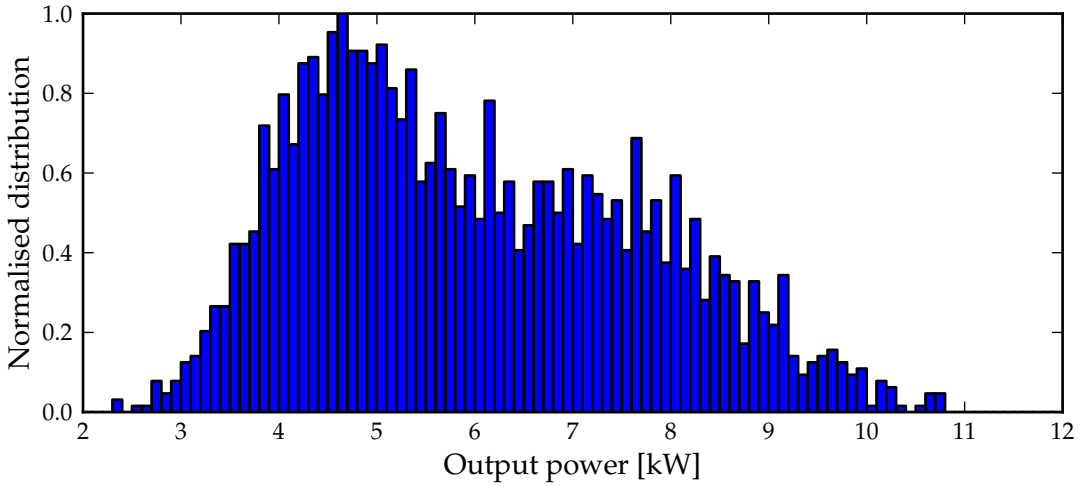

Figure 3.4: Normalised distribution of power piston electrical machine output power for combined variations.

Most of the calculated output power values for the displacer electrical machine are found to be from approximately -3.0 kW to 2,0 kW. Below approximately -1,5 kW, all of the occurrences are attributed to pseudo-ideal piston displacement. The majority of occurrences with values above 0,0 kW are due to a displacer rod area to bore area ratio of 0,05 (almost all of the rest of the values above 0,0 kW are due to a combination of a displacer rod area to bore area ratio of 0,02 and a bounce space void volume to swept volume ratio of 1,0). The values are fairly evenly distributed around the default value of -567,0 W.

From Table 3.15, it is clear that the dominant variations for the output power of the power piston electrical machine are those of the mean pressure and engine speed (refer also to sections 3.5.4 and 3.5.5). Closer examination of the distribution shown in Figure 3.4 reveals that the combination of these two variations determine whether the output power is higher up in the

distribution or lower down (low pressure and low speed will for instance result in the output being lower down in the distribution) with the variations of lesser influence (see Table 3.15) causing smaller variation around these positions.

Maximum force

Figures 3.5 and 3.6 show the normalised distribution of the maximum force of the displacer and power piston electrical machines respectively. For both displacer and power piston electrical machines, occurrences above 10 kN and 100 kN respectively (approximately 9,6% and 0,6% respectively) are not displayed.

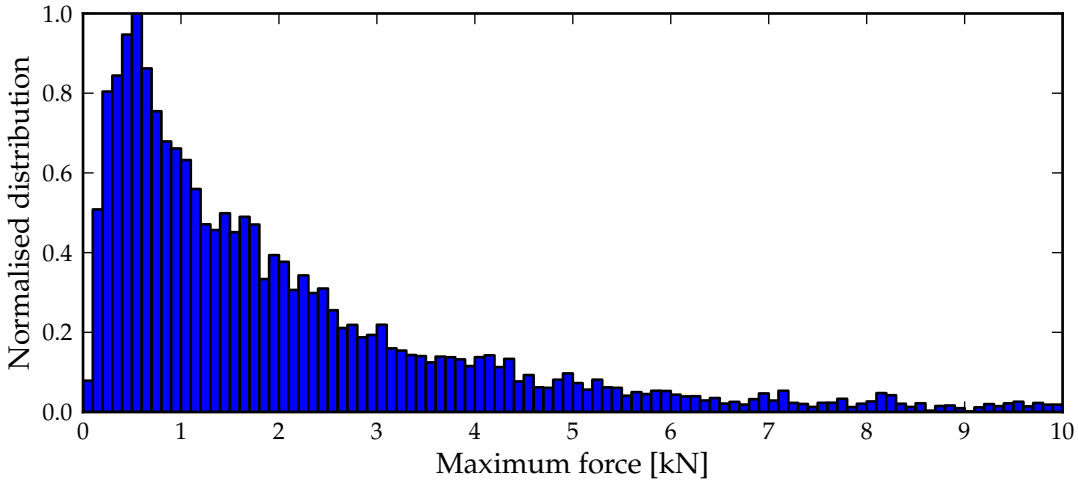

Figure 3.5: Normalised distribution of displacer electrical machine maximum force for combined variations.

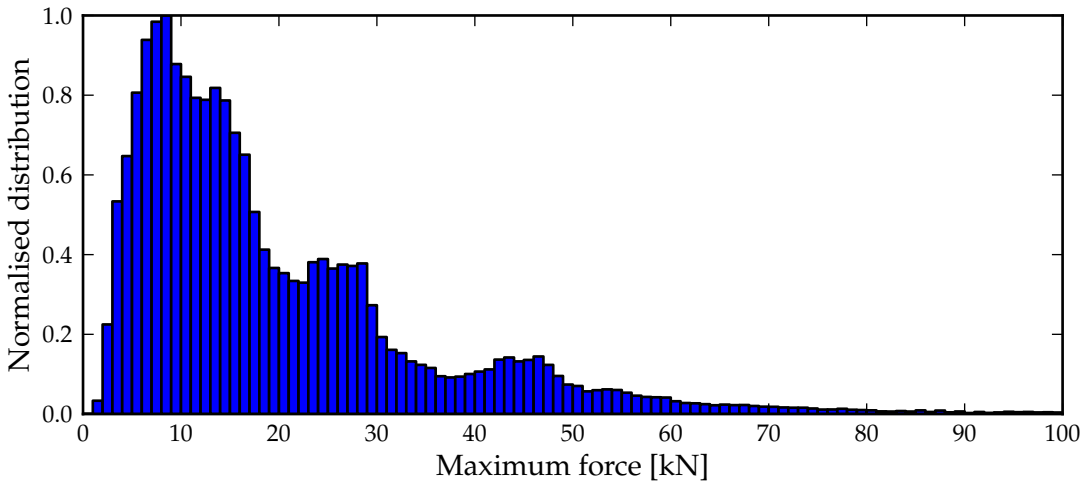

Figure 3.6: Normalised distribution of power piston electrical machine maximum force for combined variations.

The distribution of the maximum force for the displacer electrical machine shows a steep increase to a maximum of between 0,5 to 0,6 kN and then gradually declines. If this is compared to the maximum force obtained for the default simulation, namely 627,7 N, then the majority of values obtained are larger. Close examination reveals that all of the values above approximately 16,3 kN are due to pseudo-ideal piston displacement, while several other variations also

contributed to the higher values, especially all of those listed in Table 3.15 having an extreme influence (e.g. a moving member mass to power ratio of 2,0 g/W).

The maximum force of the power piston electrical machine is distributed over a very large range. Again most of the values are higher than that obtained for the default simulation, namely 5,991 kN, and it is also seen that a very large portion of the values are excessively high. Several of the variations contributed to the higher values, especially including all of those listed in Table 3.15 having an extreme influence.

Maximum force to output power ratio

Figures 3.7 and 3.8 show the normalised distribution of the maximum force to power ratio of the displacer and power piston electrical machines respectively. For both displacer and power piston electrical machines, occurrences above 15 N/W (approximately 7,0% and 0,8% respectively) are not displayed.

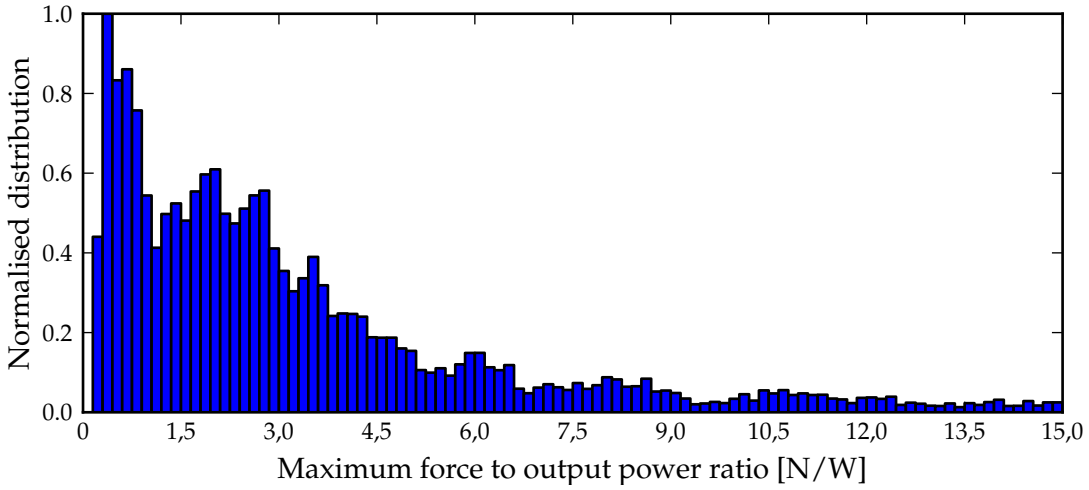

Figure 3.7: Normalised distribution of displacer electrical machine maximum force to output power ratio for combined variations.

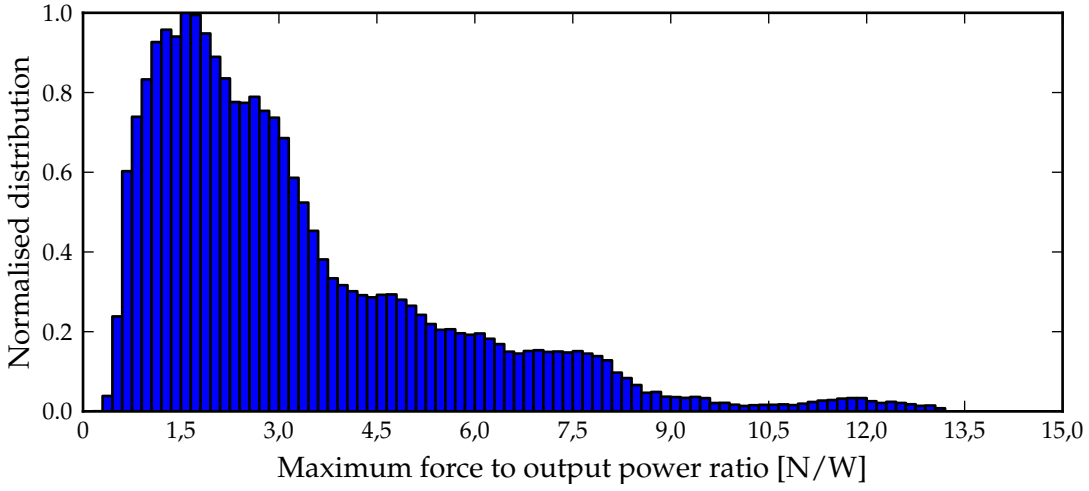

Figure 3.8: Normalised distribution of power piston electrical machine maximum force to output power ratio for combined variations.

The majority of values for the distribution of the displacer electrical machine are found above that of the default simulation, namely 1,090 N/W. Close examination shows that a range of variations contributed to the higher values, with no particular variation that could be identified as being the dominant contributor. Large values however resulted in many cases from average power values being close to zero.

For the distribution of the power piston electrical machine, close examination shows that a range of variations contributed to the higher values, with no particular variation that could be identified as being the dominant contributor. Large values rather resulted from particular combinations of variations. The vast majority of values are found above that of the default simulation, namely 1,368 N/W.

While the maximum force to power ratio distributions of the displacer and power piston may be similar in range, the effect of the connecting rod diameter makes the use of the ratio of the displacer electrical machine useless. It was shown that the average power delivered to the machine could be minimised with certain rod diameters. Having a large maximum force to power ratio therefore results from low average power and not high maximum force in these cases. The maximum force to power ratio is however very meaningful for the power piston electrical machine, since output power varies with operational variations and it is therefore meaningless to merely determine the maximum force.

Maximum rate of change of force to maximum force ratio

Figures 3.9 and 3.10 show the normalised distribution of the maximum rate of change of the force to maximum force ratio of the displacer and power piston electrical machines respectively.

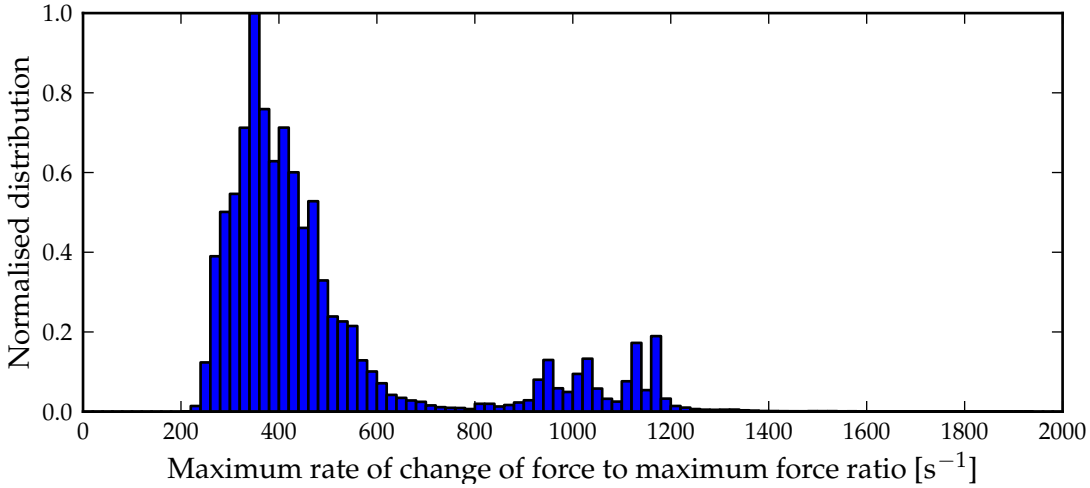

Figure 3.9: Normalised distribution of displacer electrical machine maximum force rate of change to maximum force ratio for combined variations.

The majority of occurrences can be found between approximately 200 s^{-1} to 800 s^{-1} for both electrical machines. The vast majority of values higher than approximately 800 s^{-1} are attributed to pseudo-ideal piston displacement for the displacer electrical machine. The majority of values are higher than that of the default simulation, namely 295,0 s^{-1}.

In the case of the power piston, pseudo-ideal piston displacement is also responsible for the

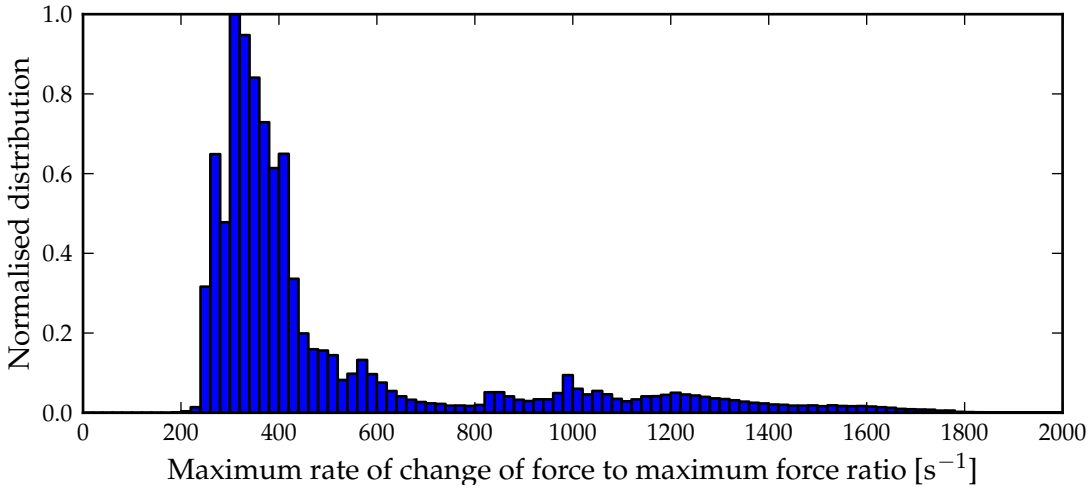

Figure 3.10: Normalised distribution of power piston electrical machine maximum force rate of change to maximum force for combined variations.

higher values (above approximately 1776 s^{-1}), with other variations, e.g. a mass to power ratio of 2,0 g/W and a stroke to bore area ratio of 0,25, contributing as well. Slightly more than half of the values are above that of the default simulation, namely 334,3 s^{-1}.

Normalised location of maximum force and maximum rate of change of force

Figures 3.11 and 3.12 show the normalised location of maximum force and of maximum rate of change of force of the displacer electrical machine respectively, while Figures 3.13 and 3.14 show the normalised location of maximum force and of maximum rate of change of force of the power piston electrical machine respectively.

The distributions of the normalised location of maximum force for the displacer and power piston electrical machines show that in the majority of cases maximum force needs to be exerted at the ends of the stroke, especially for the power piston electrical machine.

From the distributions of the normalised location of the maximum rate of change of force, it is seen that maximum rate of change of force could occur over the entire stroke length, with

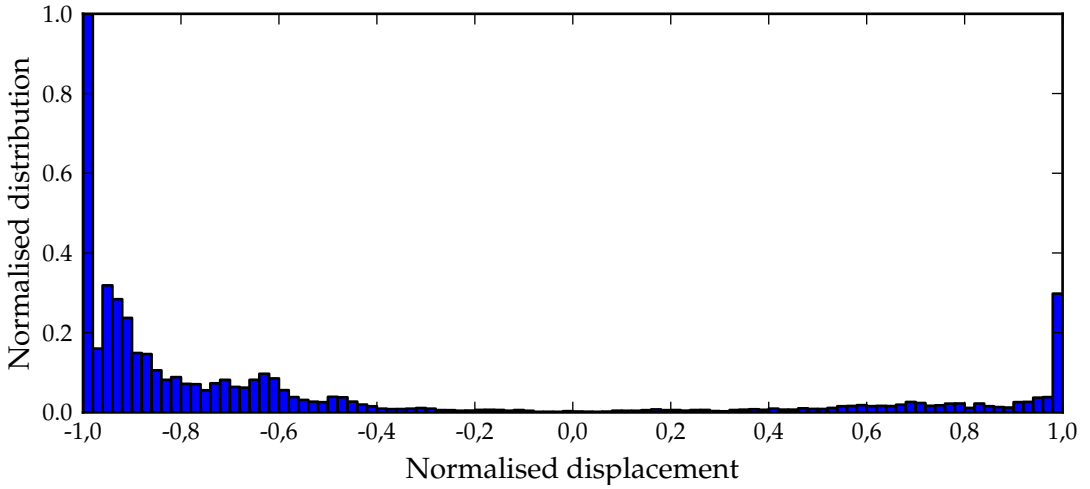

Figure 3.11: Normalised distribution of the normalised location of maximum force for combined variations of the displacer electrical machine.

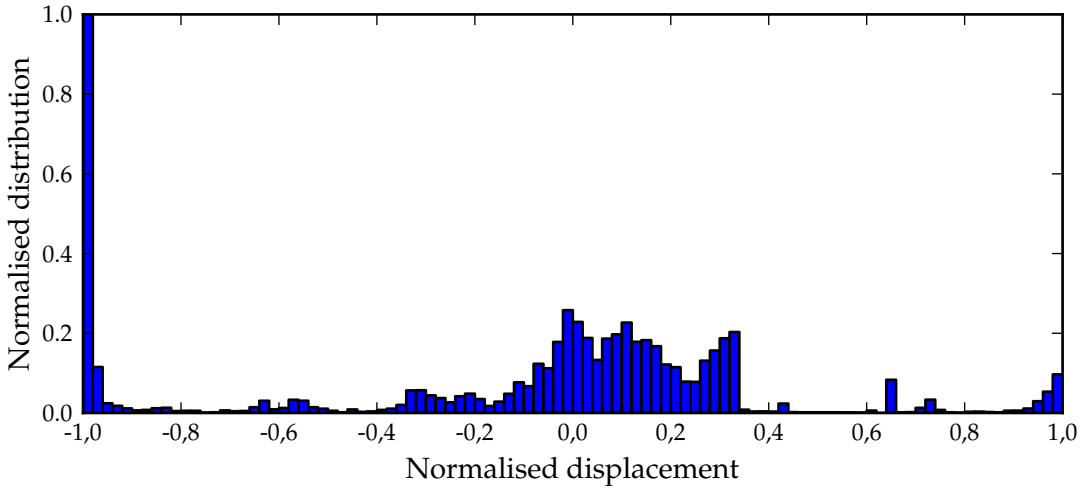

Figure 3.12: Normalised distribution of the normalised location of maximum rate of change of force for combined variations of the displacer electrical machine.

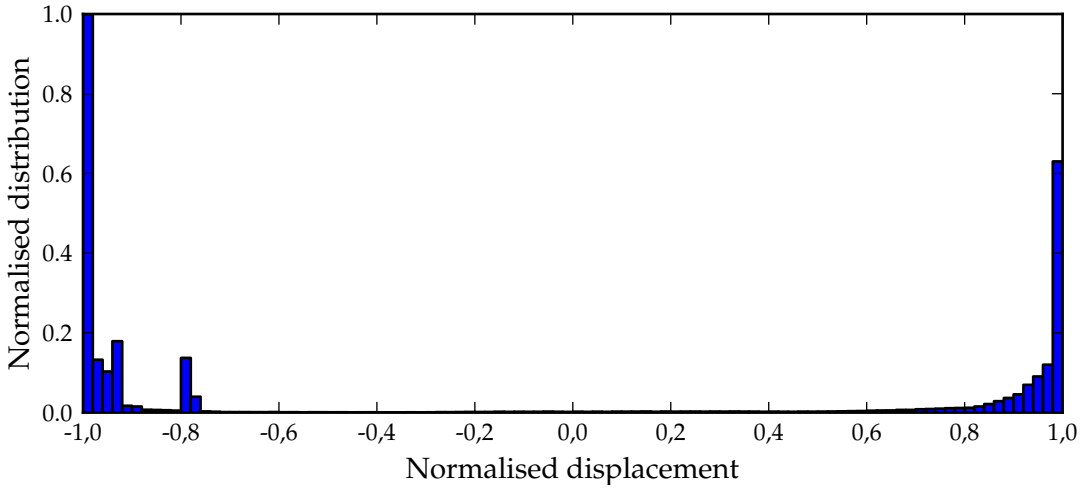

Figure 3.13: Normalised distribution of the normalised location of maximum force for combined variations of the power piston electrical machine.

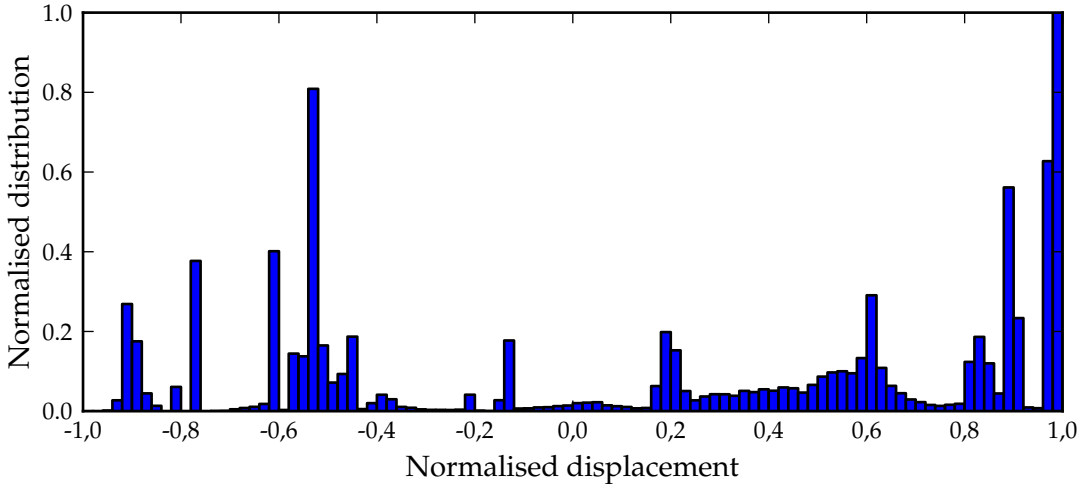

Figure 3.14: Normalised distribution of the normalised location of maximum rate of change of force for combined variations of the power piston electrical machine.

some locations more likely than others.

3.5.16 Concluding remarks

The influence of a variety of variations on the force dynamics of the GPU-3 Stirling engine was investigated. It was shown that the variations had different influences on the output parameters, from little or no influence to the extreme. In fact, with many combinations of variations the force that is necessary to realise the particular piston displacement becomes excessive and are deemed impractical. For the application of direct piston displacement control, linear machine guidelines and specifications as well as engine design, this should be taken into consideration in order to prevent excessive specifications required for the linear machines.

This concludes the case study.

3.6 Modification of the force indicators

With the insight gained in Section 3.5 and before continuing to set design guidelines, a closer look at the definition of some of the force indicators as defined in Section 3.4 is necessary. The purposes include addressing the issue raised earlier concerning the maximum force to power indicator for the displacer and also to generalise the indicators and to align them better with typical engine specifications.

It has already been mentioned during the discussion of the maximum force to output power ratio in the previous section that while the maximum force to power ratio distributions of the displacer and power piston may look similar, the effect of the connecting rod diameter makes the use of this ratio for the displacer electrical machines useless (large ratios result from very small average power and not from high maximum force values). On the other hand, it is still necessary that the maximum force be normalised with respect to some or other quantity in order to provide a specification that is more general in nature. In addition, the individual power output capability of each machine for the displacer and the power piston is not commonly available, but rather the net average output power of the engine (the sum of the output power of the two individual machines of the displacer and the power piston) is available or at least specified. For these reasons, it was decided to rescale the maximum force to output power ratios not with the average output power of each of the individual machines, but with the net average output power of the engine.

Furthermore, it was decided to expand the ratio to include information of variations that have a direct influence on the ratios. This should have the effect of less distributed distributions. Two such variations, namely the stroke length and the cycle frequency, allowed for easy inclusion. This yields a new dimensionless ratio, i.e. (3.26) now becomes

$$\Gamma_{Fxf/P} = X_{stroke} f \max\left(|F_{lem}|\right) / P_t, \tag{3.30}$$

where P_t denotes the net output power, x_{stroke} denotes the stroke length of the respective electrical machines and f denotes the cycle frequency. This new ratio could be referred to as the

maximum force, stroke and frequency to net output power ratio, but will mostly be referred to as the $\Gamma_{Fxf/P}$ ratio in the text to follow.

Figures 3.15 and 3.16 show the resulting distributions of the $\Gamma_{Fxf/P}$ ratio of the displacer and power piston electrical machines respectively for the combined variations as investigated in Section 3.5. For the displacer and power piston electrical machines, occurrences above 2,5 and 25,0 respectively (approximately 15,1% and 5,2% respectively) are not displayed.

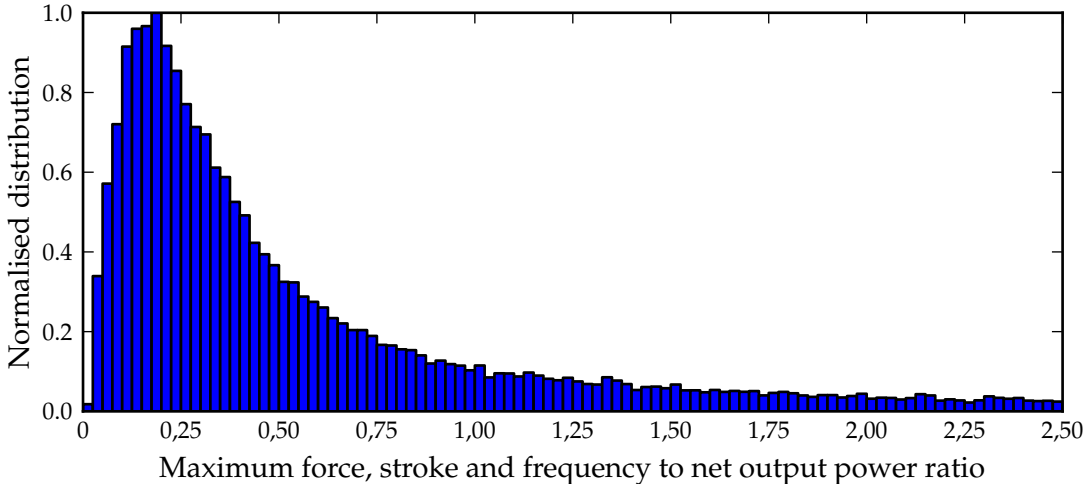

Figure 3.15: Normalised distribution of the displacer electrical machine $\Gamma_{Fxf/P}$ ratio for combined variations.

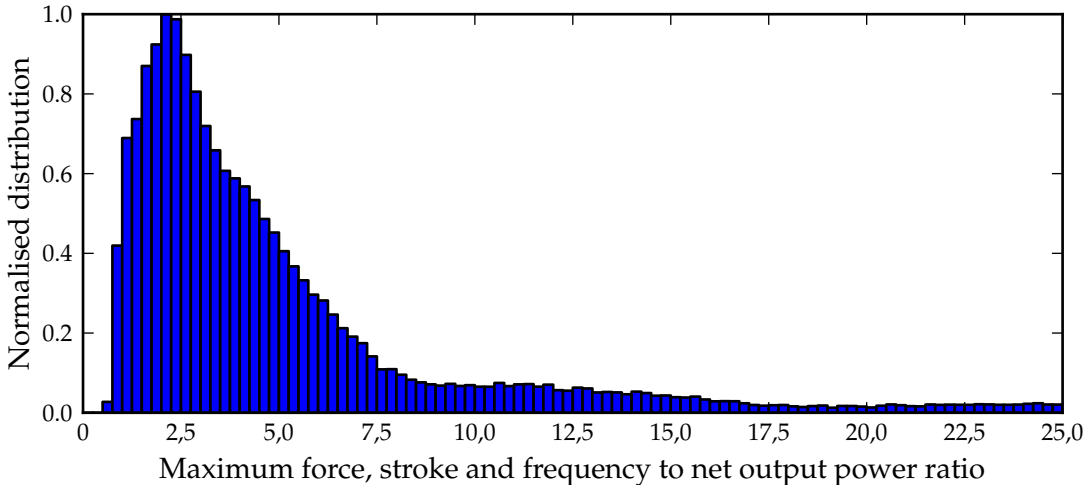

Figure 3.16: Normalised distribution of the power piston electrical machine $\Gamma_{Fxf/P}$ ratio for combined variations.

The distributions of the $\Gamma_{Fxf/P}$ ratio are fairly similar for the displacer and the power piston, with the exception that the x-axis of the displacer distribution is an order of magnitude lower in scale. Inclusion of the stroke length and the cycle frequency furthermore yielded distributions that are less distributed when compared to the original distributions shown in Figures 3.7 and 3.8.

The maximum rate of change of force to maximum force ratio has been expanded by including the cycle frequency - the only variation that has a direct influence on the ratio and that

allows for easy inclusion - in order to obtain a dimensionless ratio, i.e. (3.27) becomes

$$\Gamma_{dF/Ff} = \max\left(\left|dF_g\right|\right) / \max\left(\left|F_g\right|\right) / f. \tag{3.31}$$

This new ratio could be referred to as the normalised maximum rate of change of force to maximum force ratio, but will mostly be referred to as the $\Gamma_{dF/Ff}$ ratio in the text to follow. Figures 3.17 and 3.18 show the resulting distributions of the $\Gamma_{dF/Ff}$ ratio of the displacer and power piston electrical machines respectively for the combined variations as investigated in Section 3.5. For the displacer and power piston electrical machines, occurrences above 30,0 (approximately 0,2% and 3,6% respectively) are not displayed.

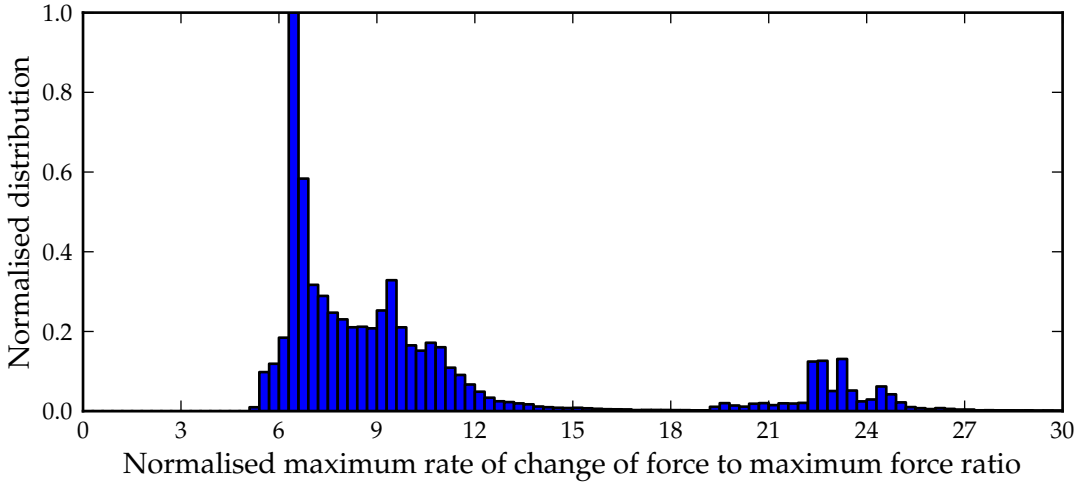

Figure 3.17: Normalised distribution of the displacer electrical machine $\Gamma_{dF/Ff}$ ratio for combined variations.

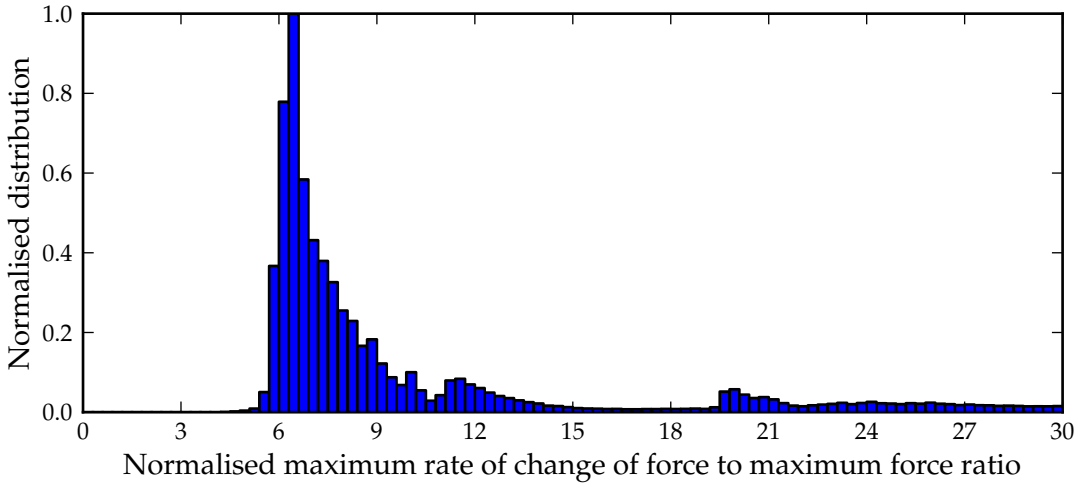

Figure 3.18: Normalised distribution of the power piston electrical machine $\Gamma_{dF/Ff}$ ratio for combined variations.

The distributions of the $\Gamma_{Fxf/P}$ ratio are similar for the displacer and the power piston, with the maximum occurrences between 6,1 and 6,2 for both distributions. Inclusion of the cycle frequency furthermore yielded distributions that are less distributed when compared to those shown in Figures 3.9 and 3.10.

3.7 Design guidelines

3.7.1 Overview

Given the findings and discussions in the previous sections, an effort will now be made to set design guidelines. Guidelines in this context means design guidelines for both the Stirling engine as well as the electrical machines for the variations that were investigated. Specifications derived from the output parameters of Section 3.5 then follow in the next section as a result.

3.7.2 Re-evaluation of variation ranges

With the $\Gamma_{Fxf/P}$ and $\Gamma_{dF/Ff}$ ratios now defined, a process of re-evaluation was undertaken to determine whether the ranges for some of the variations should be altered to be in line with these ratios and/or to be more realistic. As an example, the spring forces have been defined in terms of the default individual output power values of each of the electrical machines till now, but with the $\Gamma_{Fxf/P}$ ratio now defined in terms of the net average output power of the engine, it only makes sense also to define the spring forces with respect to the net average output power. The variations that were considered include the following:

- Piston displacement
- Bounce/compression space average pressure difference
- Displacer connecting rod area to bore area ratio
- Bounce space void volume to swept volume ratio
- Spring forces
- Moving member mass to net power ratios

The rest of the variation ranges that were not altered include those that are related to operational conditions, e.g. mean pressure and engine speed, and the stroke to bore area ratio that was included in the $\Gamma_{Fxf/P}$ ratio.

The final ranges were determined through a process of simulation and decision-making. The extent of this process is such that it is too impractical and cumbersome to report here in full detail. Instead, a short discussion of the process and the final choice of each of the variation ranges will be presented below, with a selection of some of the distributions that will be presented in the subsections to follow.

Initially, only variation of the pressure, engine speed, the hot and cold side temperatures and piston displacement as listed in Table 3.16 were considered, with all of the other variations remaining at default value. A decision was then taken which of the piston displacements should remain or should be excluded by examining the change in the distributions of the $\Gamma_{Fxf/P}$ and $\Gamma_{dF/Ff}$ ratios when including or excluding the piston displacements one by one.

The influence of all of the rest of the variations were then examined by including individual ranges or combinations of ranges of the different variations and again observing the change in the distributions of the $\Gamma_{Fxf/P}$ and $\Gamma_{dF/Ff}$ ratios.

This helped to identify which of the variations are more dominant than others. Particular attention was then paid to the more dominant variations. This, while also taking practical considerations into account, then formed the basis of deciding to what extent the ranges should be limited/altered.

Table 3.17 lists the final chosen range and an explanation of each of the variations listed above.

Table 3.17: Explanation of the final variation ranges.

Final range	**Explanation**
Piston displacement	
Sinusoidal, Composite	In the case of some of the distributions shown in Section 3.5.15, it was mentioned that the higher values could be attributed to non-sinusoidal pseudo-ideal piston displacement. This was again observed for especially the displacer. And while the sinusoidal and composite displacements have been found to be the closest to being optimal by Strauss and Dobson [12], it was finally decided to exclude pseudo-ideal displacement. The original piston displacement - when added to the influence of the sinusoidal and composite displacements - on the other hand did not have a very distinctive influence on the distributions. It will make little difference whether it is included or excluded and it was decided to exclude the original displacement as well to limit the number of variations.
Bounce/compression space average pressure difference	
0% to 5%	It was already mentioned in Section 3.5.13 that the pressure difference will stabilise between 2% to 5% for the GPU-3 engine. This was the decisive factor in determining the final variation range. The pressure difference has very little influence on the distributions of the displacer. Its influence on the power piston distributions is also very limited, with only a slight increase of less than 4% in the maximum values obtained for the $\Gamma_{Fxf/P}$ and $\Gamma_{dF/Ff}$ ratios after inclusion of the pressure difference variation.
Displacer connecting rod area to bore area ratio	
0 to 0,1	The presence of a displacer connecting rod has the surprising effect of greatly influencing the average power delivered to the displacer piston. It was shown in Table 3.7 and later in Figure 3.3 that this could even lead to net average power delivered by the displacer (and not to the displacer). In answering the question as to the maximum ratio, it was found again that this ratio has little or no influence on the power piston distributions of the $\Gamma_{Fxf/P}$ and $\Gamma_{dF/Ff}$ ratios. In fact, the $\Gamma_{Fxf/P}$ distribution was shifted slightly downwards indicating that the presence of a connecting rod could generally slightly ease the requirements expected from the linear generator.

A downward shift was also observed for the $\Gamma_{Fxf/P}$ distribution of the displacer, with very little difference between a range up to 0,05 and a range up to 0,1. The introduction of a variation in the rod diameter however has a definite influence on the distribution of the $\Gamma_{dF/Ff}$ ratio for the displacer, but again there is not much difference between a range up to 0,05 and a range up to 0,1. However, when the range maximum was chosen to be 0,2, the distribution of the $\Gamma_{Fxf/P}$ ratio showed a noticeable shift to the right. This led to the final decision of a maximum of 0,1 to provide for as wide a range as possible[8], without influencing the distributions negatively.

Bounce space void volume to swept volume ratio

5,0 to infinity

It is difficult to make a judgement regarding what the practical minimum bounce space void volume to swept volume ratio could be. Mere inspection of drawings of real free-piston Stirling engines show rather large bounce volumes of several times the swept volume. On the other hand, it is certainly possible to introduce gas springs that would effectively result in ratios of less than unity. This is however not the purpose of this ratio, but rather its purpose is merely to provide for the forces expected from the compression and expansion of the gas in a finite bounce space volume. The limiting factor here is therefore the influence on the distributions.

Only the distribution of the $\Gamma_{Fxf/P}$ ratio for the power piston is directly affected by a change in the bounce space volume. The influence on the other distributions is either negligible or very limited.

Simulations have shown that for ratios of 5,0 and more, the distribution of the $\Gamma_{Fxf/P}$ ratio is not excessively affected. An increase of approximately 64% (from 3.53 to 5.8) was noted for the maximum power piston $\Gamma_{Fxf/P}$ ratio value obtained from a bounce space void volume to swept volume ratio of 5,0 when compared to the default infinite ratio, but the bulk of occurences are still very much within the range of that obtained with only the default ratio. For ratios lower than 5,0, the effect on the $\Gamma_{Fxf/P}$ ratios becomes increasingly more distinct.

Spring forces

Displacer:
0,0 to 0,02 N/W
Power piston:
0,0 to 0,2 N/W

Spring forces were found to have a distinct influence on especially the $\Gamma_{Fxf/P}$ ratios and can have either a positive or negative influence on the maximum required force. The goal was therefore to limit the range, but to still provide for realistic spring forces arising from flexure bearings and/or spring-like reluctance forces of the electrical machines themselves. Flexure bearings are normally introduced in traditional free-piston engines to not only provide spring forces for the displacer and power piston, but also for the important task to hold the displacer and power piston moving members in place.

[8] A maximum of 0,1 is already substantial. The author has not yet seen any displacer connecting rods that would meet this ratio.

Spring constants of flexures bearings could differ by several orders of magnitude. One example of work done on flexures was reported by Gaunekar *et al.* [32]. Gaunekar *et al.* show the spring constant as a function of displacement of a 1 mm thick stainless steel flexure with a diameter of 250 mm to a maximum displacement of 25 mm (i.e. for stroke lengths up to 50 mm). The measured spring constant never exceeded 0,75 N/mm. If this flexure was combined with the machine by Schutte and subsequent machines under investigation (with shorter stroke lengths), then even if 10 of these flexures were utilised, the maximum force to net power ratio would not exceed 0,06 N/W. As another example, spring constants up to 180 N/mm are found in the linear machines of *Qdrive/Chart Industries*™, manufacturers of cryocoolers.

Little information is available regarding the order of magnitude of reluctance forces in typical linear machines. Schutte [33], in studying a PM transverse flux linear machine, determined a maximum reluctance force of 144 N for a 3 kW prototype with a 45 mm stroke length. This represents a force to net power ratio of approximately 0,05 N/W. In subsequent unpublished work to improve on this initial linear machine, it was found that this ratio increased to values of just more than 0,1 N/W (at stroke lengths of 30 mm).

It is therefore considered to be sufficient to make provision for maximum spring to net power ratios of the order of 0,2 N/W for the power piston. Simulations have shown that a maximum ratio of 0,02 N/W has a corresponding influence on the displacer distributions. This is also in correspondence with the fact that the distribution of the $\Gamma_{Fxf/P}$ ratio of the displacer is an order of magnitude lower in scale when compared to that of the power piston.

An increase in the ranges to 0,05 N/W and 0,5 N/W for the displacer and the power piston respectively was also investigated. It was found that the distributions of the $\Gamma_{Fxf/P}$ ratio worsened with an increase in the range before the moving member mass was taken into consideration, but that they improved slightly thereafter. The final decision was therefore taken to allow for a maximum of 0,02 N/W and 0,2 N/W for the maximum spring (and spring-like) force to net power ratio for the displacer and the power piston respectively. While the combined reluctance and spring force to net power might exceed these limits, this will not necessarily worsen what is expected from the linear machines.

Very little difference in influence was observed for the $\Gamma_{dF/Ff}$ ratios for a variation in the range from 0,02 N/W and 0,2 N/W to 0,05 N/W and 0,5 N/W for the displacer and power piston distributions respectively.

Moving member mass to net power ratios

Displacer: 0,0 to 0,1 g/W
Power piston: 0,0 to 1,0 g/W

The last variation considered here is also one of the most important variations, especially due to its influence on the $\Gamma_{Fxf/P}$ ratio. Little information exists that could give some idea of expected mover masses in free-piston Stirling engines. Again, the work by Schutte [33] give some idea of what may be expected. His 3 kW PM transverse flux linear machine had an active mover mass of 4,12 kg, i.e. he obtained a moving member mass to net power ratio of 1,37 g/W. During subsequent studies (as yet unpublished) this number was improved on in some instances to below 1 g/W. It is however possible that this number may be higher for other topologies. It is however important to remember that the ratio describes the entire moving member mass, including that of the linear machine mover, the piston and any joining pieces. Actual moving member mass will therefore be higher than what is quoted here.

The influence on the distributions was investigated for range maxima of 0,1 g/W and 1,0 g/W for the displacer and power piston respectively. This is thought to be the lowest that the range maxima can be chosen when considering what was written in the previous paragraph. The distributions substantially worsened, i.e. the distributions now became more distributed with a substantial number of occurrences at much higher values than before.

The range maxima were also increased to 0,2 g/W and 2,0 g/W for the displacer and the power piston respectively to see whether it is possible to make provision for a larger range of mover masses. The extent to which the distributions further worsened however led to the decision to keep the range maxima at 0,1 g/W and 1,0 g/W respectively.

3.7.3 Final distributions

Based on this re-evaluation of variation ranges, final distributions were determined. Only the distributions for the displacer and power piston $\Gamma_{Fxf/P}$ and $\Gamma_{dF/Ff}$ ratios are shown, but each time for a different set of variations. These different sets of variations may be listed as follows:

- Only the *operational variations*, i.e. variation in pressure, speed, hot and cold side temperatures, as well as the displacement variations.
- The *extended set of variations*, including the operational variations, as well as variations not directly influenced by the linear machines (variation in the stroke to bore ratio, the displacer connecting rod area to bore area ratio and the bounce/compression space average pressure difference). It was decided to also include the bounce space void volume to swept volume ratio, although this variation is influenced by the linear machine, the topology and final dimensions of the machines will have an influence on the void volume. It is however also influenced by design decisions with regard to the bounce volume

pressure vessel and therefore not only by the linear machine. In the final specifications, special provision will be made for this variation.

- For *all variations*, including those influenced by the linear machines, i.e. spring constants and mover mass.

The normalised distributions of the displacer and the power piston $\Gamma_{Fxf/P}$ ratio are shown in Figures 3.19 to 3.21 and Figures 3.22 to 3.24 respectively, while the normalised distributions of the displacer and the power piston $\Gamma_{dF/Ff}$ ratio are shown in Figures 3.25 to 3.27 and Figures 3.28 to 3.30 respectively. Some of the other distributions are included in Appendix D.

These distributions clearly show and provide insight into the range of expected values given the set of variations. The probability of a parameter having a certain value is also clearly demonstrated. Do take note of the similarity of the distributions of the displacer and the power piston.

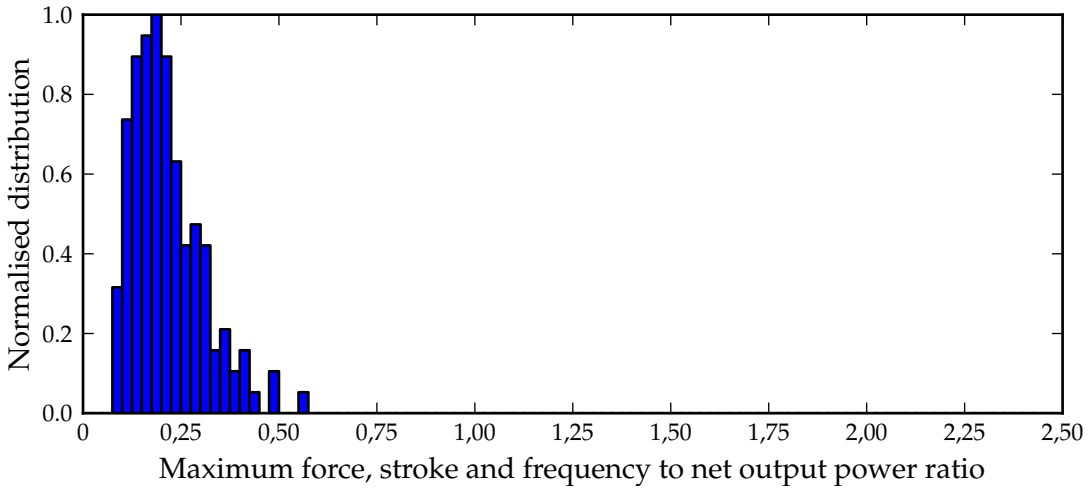

Figure 3.19: Normalised distribution of the displacer $\Gamma_{Fxf/P}$ ratio for only the operational variations.

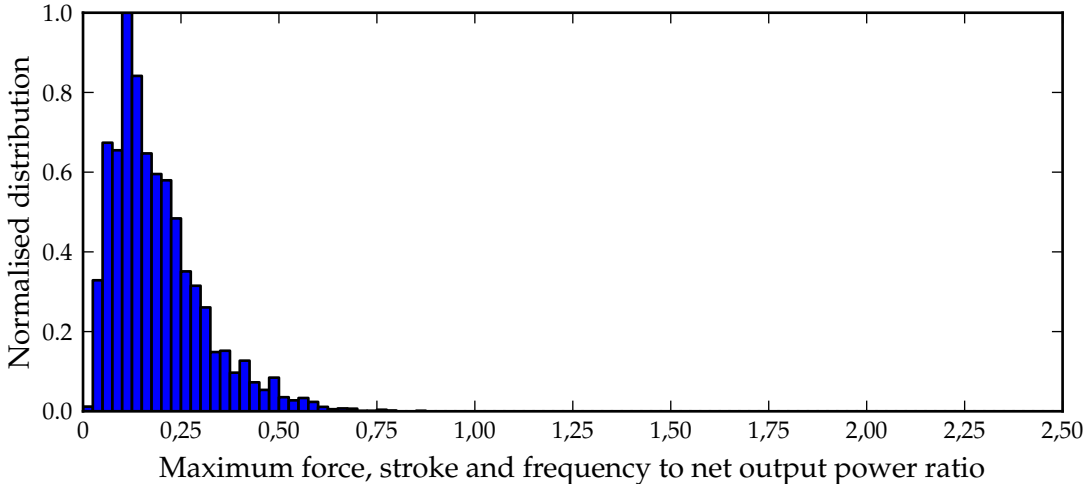

Figure 3.20: Normalised distribution of the displacer $\Gamma_{Fxf/P}$ ratio for the extended set of variations.

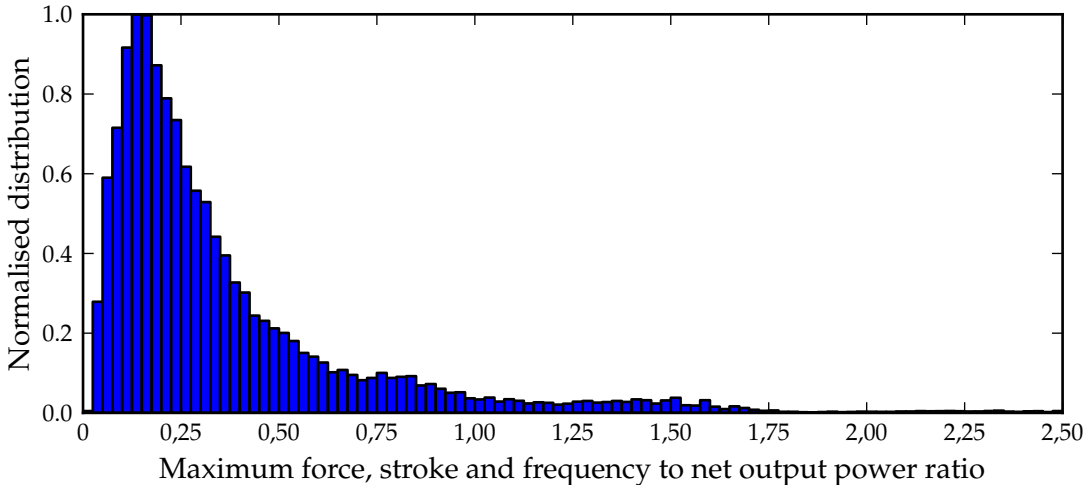

Figure 3.21: Normalised distribution of the displacer $\Gamma_{Fxf/P}$ ratio for all variations.

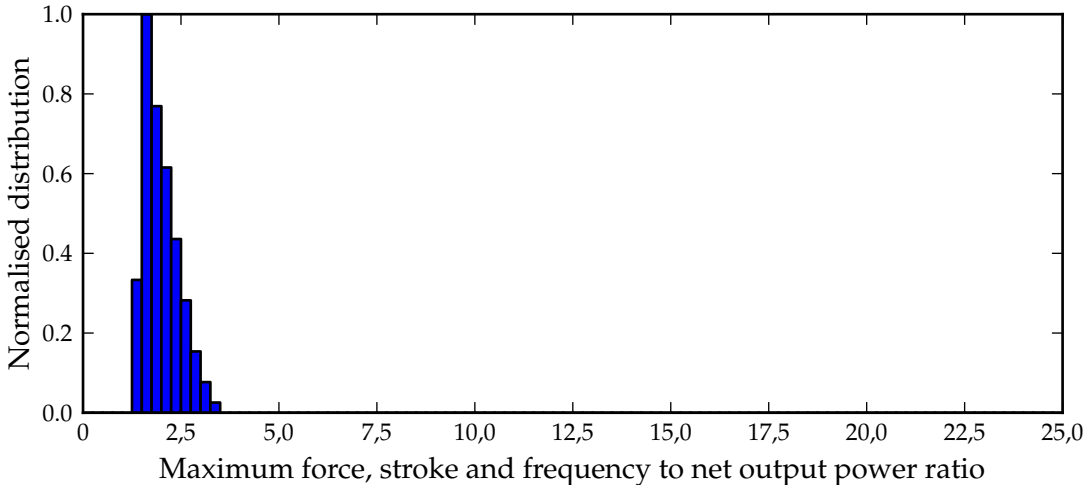

Figure 3.22: Normalised distribution of the power piston $\Gamma_{Fxf/P}$ ratio for only the operational variations.

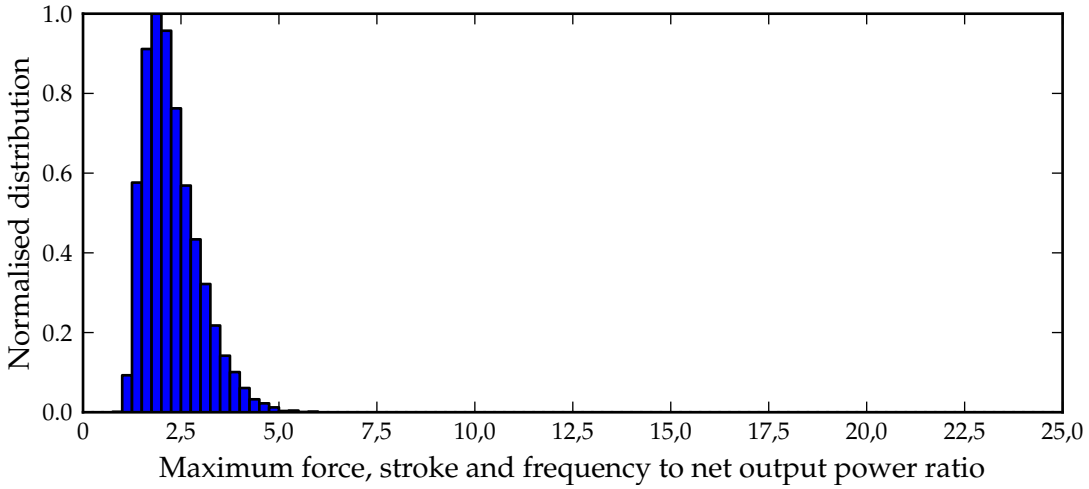

Figure 3.23: Normalised distribution of the power piston $\Gamma_{Fxf/P}$ ratio for the extended set of variations.

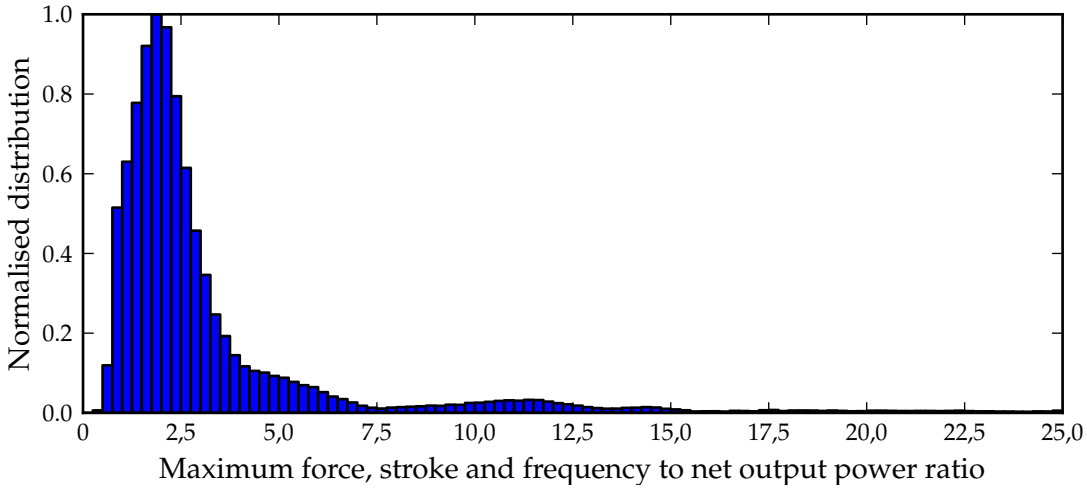

Figure 3.24: Normalised distribution of power piston $\Gamma_{Fxf/P}$ ratio for all variations.

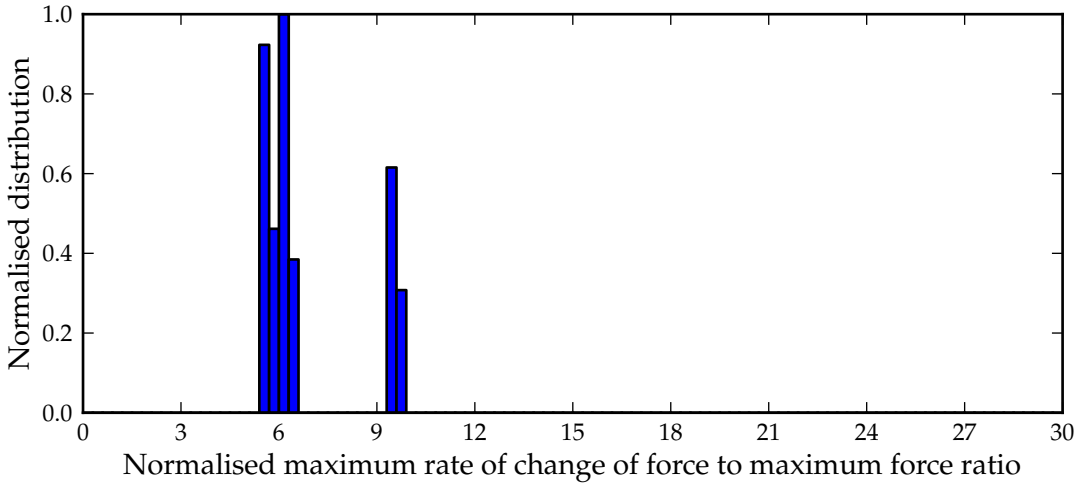

Figure 3.25: Normalised distribution of the displacer $\Gamma_{dF/Ff}$ ratio for only the operational variations.

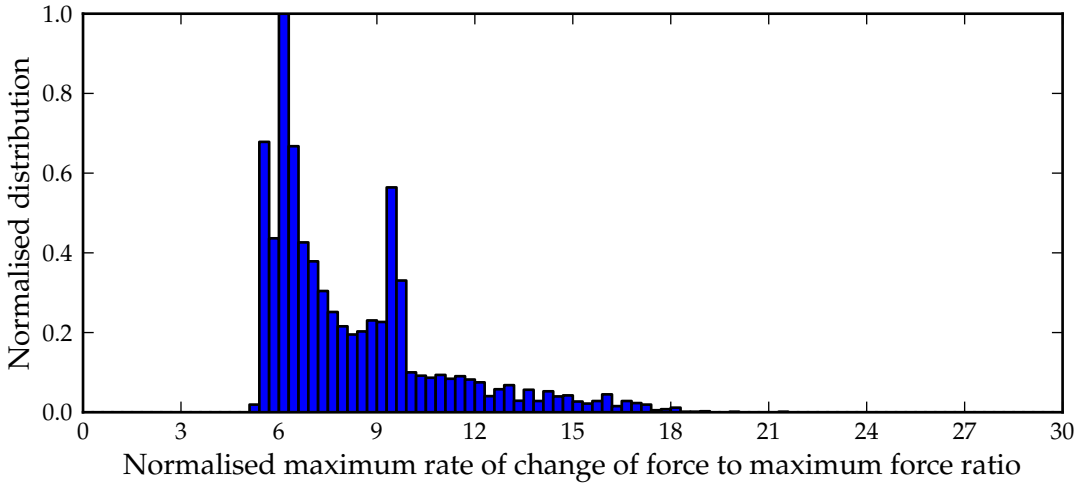

Figure 3.26: Normalised distribution of the displacer $\Gamma_{dF/Ff}$ ratio for the extended set of variations.

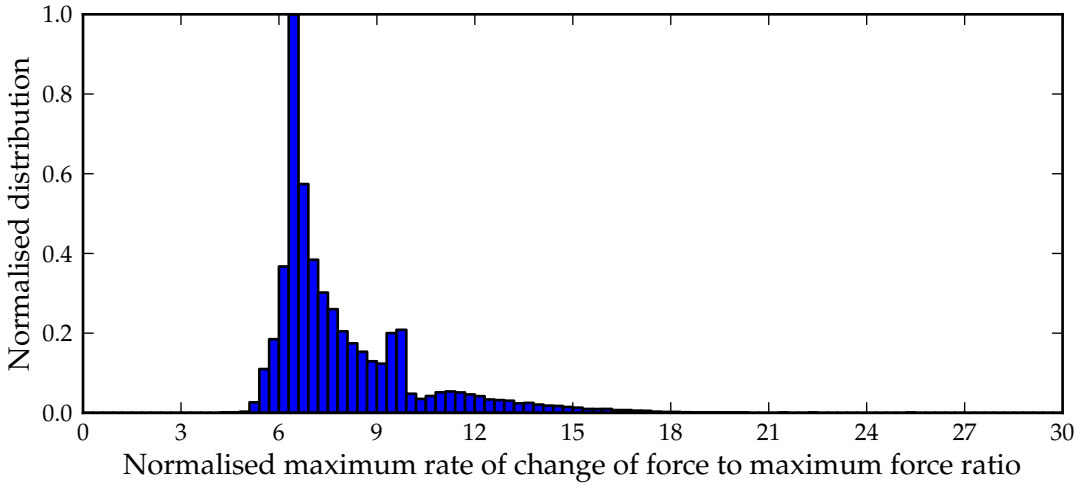

Figure 3.27: Normalised distribution of the displacer $\Gamma_{dF/Ff}$ ratio for all variations.

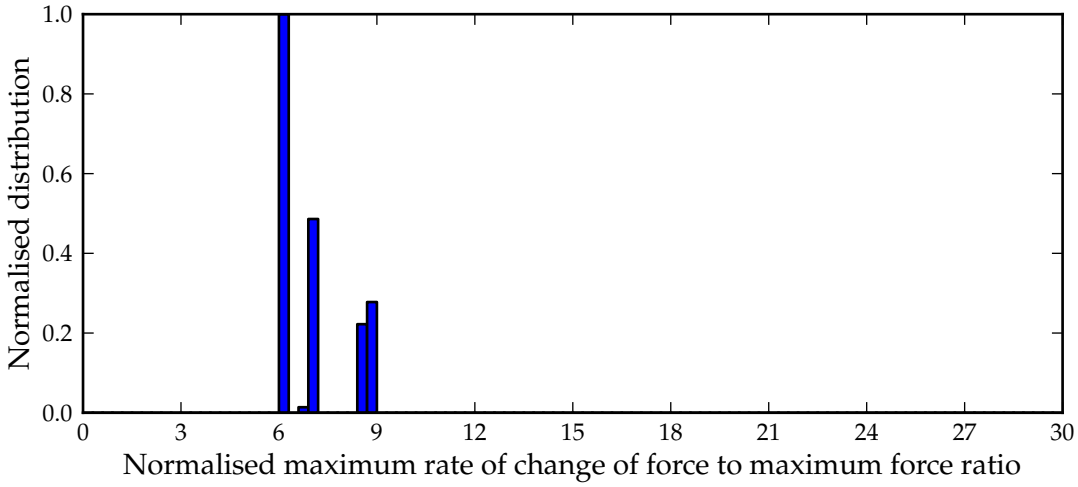

Figure 3.28: Normalised distribution of the power piston $\Gamma_{dF/Ff}$ ratio for only the operational variations.

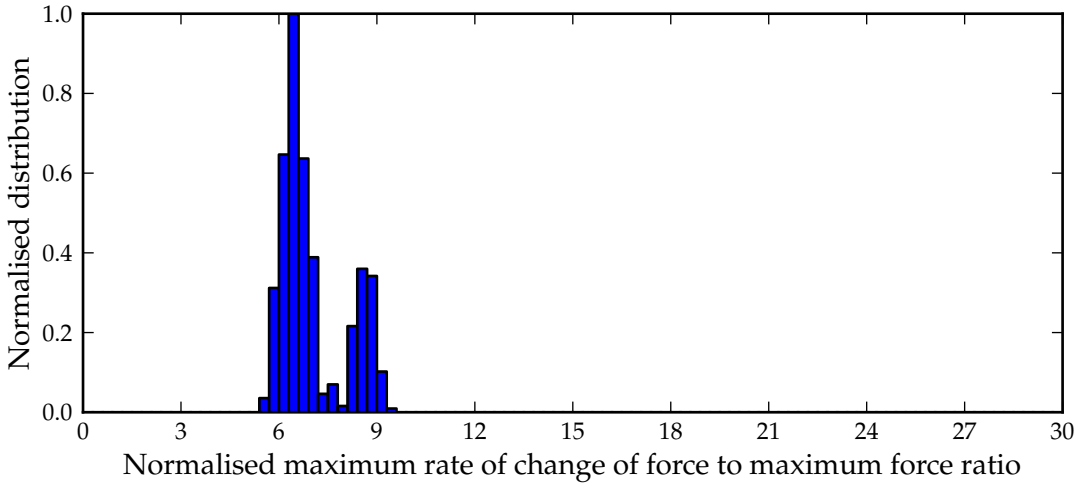

Figure 3.29: Normalised distribution of the power piston $\Gamma_{dF/Ff}$ ratio for the extended set of variations.

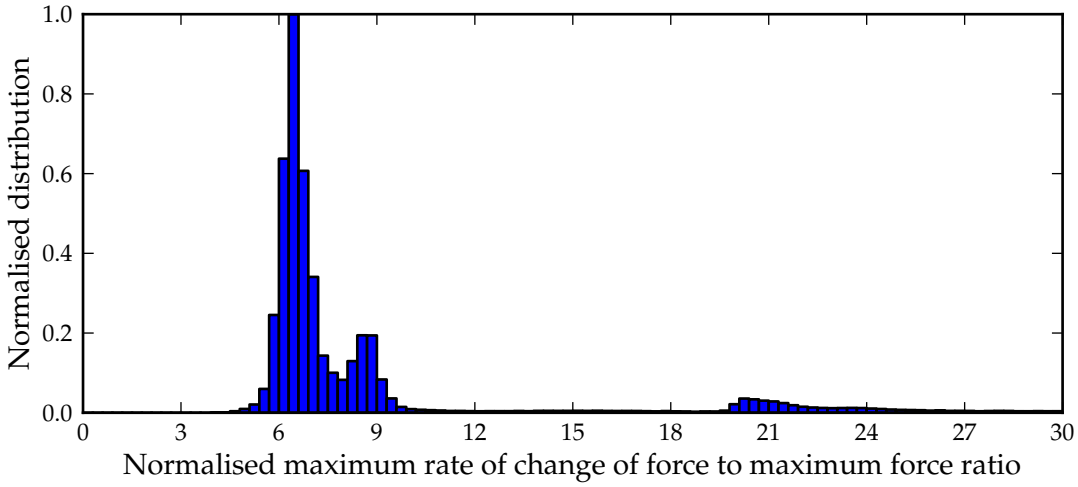

Figure 3.30: Normalised distribution of the power piston $\Gamma_{dF/Ff}$ ratio for all variations.

3.7.4 Design guidelines

The final range maxima/minima of the variations are now determined. These are still only approximate values, since obtaining these - however carefully - involved a qualitative rather than a quantitative process. It is however expected and was indeed seen from the simulations, that as these limits are approached, it will become ever more difficult to adhere to the specifications set for the linear machines and that in the case where all of these are close to the limits, the specifications will be such that it will become extremely difficult to perform piston displacement control. In practise an effort should therefore be made to stay well clear of these limits.

Lastly, these values are nothing less than design guidelines for the engine and linear machines, since they effectively define the maximum or minimum value of a particular engine or linear machine property. Table 3.18 lists these values as design guidelines.

Table 3.18: Design guidelines for engine and linear machines.

Description	Value
Moving member mass to net power ratio: Displacer [g/W]	$< 0{,}1$
Moving member mass to net power ratio: Power piston [g/W]	$< 1{,}0$
Spring forces: Displacer [N/W]	$< 0{,}02$
Spring forces: Power piston [N/W]	$< 0{,}2$
Bounce space void volume to swept volume ratio	$> 5{,}0$
Displacer connecting rod area to bore area ratio	$< 0{,}1$
Piston displacement	Near harmonic

3.8 Linear electrical machine specifications

3.8.1 Specifications from the distributions

Specifications can now be compiled from the final distributions shown in the previous section, provided that the design guidelines above are adhered to. If the design guidelines are violated,

then the distributions are no longer valid and hence any specifications derived from them.

The final distributions shown in the previous section for the $\Gamma_{Fxf/P}$ and $\Gamma_{dF/Ff}$ ratios serves as the basis to finally determine specifications for linear machines. It was realised that it will be extremely difficult to adhere to the requirements of all possible variations. Specifications were therefore determined for the case where the requirements are met for at least 50%, 60%, 75%, 90% and finally 100% of all possible combinations of variations.

The specifications for displacer and power piston linear machines are listed in Table 3.19.

Table 3.19: Specifications for linear machines for all variations.

Description	Min.	50%	60%	75%	90%	100%
Overall						
Efficiency			> 0,9			
Displacer						
$\Gamma_{Fxf/P}$	0,018	0,248	0,305	0,442	0,822	2,848
$\Gamma_{dF/Ff}$	4,215	7,103	7,599	8,832	10,996	25,282
χ_{maxF}	0,0	0,8	0,869	0,952	0,993	1,0
χ_{maxdF}			Over entire stroke length			
Power piston						
$\Gamma_{Fxf/P}$	0,354	2,195	2,483	3,214	6,465	27,444
$\Gamma_{dF/Ff}$	4,127	6,725	6,972	8,399	19,833	35,882
χ_{maxF}	0,0	0,954	0,99	0,996	0,997	1,0
χ_{maxdF}			Over entire stroke length			

Apart from the force indicators, one more parameter was specified, namely the overall efficiency of the electrical machines. One of the perceived advantages of piston displacement control is improved performance of engines. This can however only be achieved when the efficiency of the electrical machines is comparable or better than that of normal resonant type free-piston engines or that of the combination of crank mechanisms and electrical generators in kinematic engines. Thieme [15] determined that the mechanical losses in the GPU-3 lowered the output power by close to 30% in the one test case and close to 15% in the other (see Tables A.3 and A.4 for a more detailed explanation). In these two cases, the mechanical losses amounted to 1050 W and 750 W respectively and this did not include generator losses in the case where electricity is generated. Electrical machine efficiencies of better than 0,9 are therefore specified to not only improve engine operation through optimal piston displacement, but also by lowering losses.

For the normalised location of maximum force, the absolute of the location was considered, with the direction of increase taken from the piston centre position to the outer limits of piston stroke. This decision was based on the observation that the force per unit current for linear machines tends to decrease in that direction normally. At the outer limits of piston displacement, linear machines therefore exert less force per unit current, resulting in the need to compensate by increasing the current. While the occurrences are spread over the entire length, most are close to the outer limits of displacement and it therefore follows as a general rule that linear

machines will exert maximum force at the outer limits of displacement, irrespective of combination of variations. This poses a challenge not required of linear machines in traditional resonant type free-piston Stirling engines.

Table 3.20 also lists the same parameters as in Table 3.19, but for the extended set of variations only. This was included to observe the change in the values of the specifications if the variations directly influenced by the electrical machines are left out. The values listed in Table 3.20 are of importance, since these values are not directly influenced by the electrical machines.

In Table 3.21, a further set of parameters are provided, this time for the extended range of variations, but without the bounce space void volume to swept volume ratio variation. Only the data that differs from the data in Table 3.20 is shown.

Table 3.20: Specifications for linear machines for the extended range of variations only.

Description	Min.	50%	60%	75%	90%	100%
Overall						
Efficiency			> 0,9			
Displacer						
$\Gamma_{Fxf/P}$	0,019	0,160	0,193	0,247	0,348	0,871
$\Gamma_{dF/Ff}$	5,139	7,348	8,273	9,527	11,946	21,349
χ_{maxF}	0,001	0,653	0,693	0,745	0,871	1,0
χ_{maxdF}			Over entire stroke length			
Power piston						
$\Gamma_{Fxf/P}$	0,969	2,132	2,307	2,650	3,227	5,803
$\Gamma_{dF/Ff}$	5,568	6,622	6,777	7,982	8,721	9,420
χ_{maxF}	0,766	0,966	0,972	0,981	0,991	1,0
χ_{maxdF}			Over entire stroke length			

Table 3.21: Specifications for linear machines for the extended range of variations, but excluding the variation of the bounce space void volume to swept volume ratio.

Description	Min.	50%	60%	75%	90%	100%
Displacer						
$\Gamma_{Fxf/P}$	0,029	0,162	0,192	0,24	0,316	0,622
$\Gamma_{dF/Ff}$	5,381	7,22	8,155	9,527	11,990	18,968
χ_{maxF}	0,001	0,67	0,71	0,749	0,829	1,0
Power piston						
$\Gamma_{Fxf/P}$	0,969	1,77	1,914	2,163	2,522	3,526
$\Gamma_{dF/Ff}$	5,568	6,77	7,058	7,978	8,717	9,156
χ_{maxF}	0,766	0,937	0,951	0,969	0,98	1,0

The decrease in the maximum values for the $\Gamma_{Fxf/P}$ and $\Gamma_{dF/Ff}$ ratios in the two tables above when compared to the data provided in Table 3.19, can be seen clearly.

The application of the information in Tables 3.19, 3.20 and 3.21 will be further discussed later in this chapter and in chapter 4. But before focussing on the application of the information, the cross correlation between the various parameters needs to be examined.

3.8.2 Cross influence/correlation of specification percentages

It has not been clear nor can it be seen to this point what the cross influence is between the different specification parameters. For example, does the 50% value of $\Gamma_{dF/Ff}$ apply automatically when choosing the 50% value for $\Gamma_{Fxf/P}$? The answer to this question will have a profound effect on the way that the specifications are used.

To investigate this correlation the distributions of $\Gamma_{Fxf/P}$ and $\Gamma_{dF/Ff}$ for both the displacer and power piston were redetermined, but this time only for occurrences where the values of the other parameter are equal to or less than the specification percentage level under investigation (e.g. the distribution of $\Gamma_{dF/Ff}$, but only for those occurrences where the value of $\Gamma_{Fxf/P}$ is less than or equal to its 50% specification level).

If there is a good correlation between the different specification parameters, then the distribution of one parameter with the values of another limited to a certain percentage level should be influenced in such a way that the distribution should also not exceed it's own corresponding value of that percentage level, e.g. with $\Gamma_{dF/Ff}$ limited to 50%, the distribution of $\Gamma_{Fxf/P}$ should also not exceed the 50% specification level - or at least only a very small amount of values should exceed this level. If little or no change is seen for the distributions when compared to the distributions shown previously in this section, then this is an indication of poor correlation, i.e. then one cannot assume that the same percentage level automatically applies to one specification parameter if it is chosen for another.

Figures 3.31 and 3.32 show the distributions of $\Gamma_{Fxf/P}$ with $\Gamma_{dF/Ff}$ limited to the 50% specification level for the displacer and the power piston respectively[9] for all variations.

Little change is seen when comparing these distributions with the ones in Figures 3.21 and 3.24. This suggests that a poor correlation exists between the $\Gamma_{Fxf/P}$ and $\Gamma_{dF/Ff}$ parameters for both the displacer and power piston. Choosing a 50% limit on the one does not automatically imply a 50% limit on the other.

Figures 3.33 and 3.34 show the distributions of $\Gamma_{Fxf/P}$ with $\Gamma_{dF/Ff}$ limited to the 50% specification level for the displacer and the power piston respectively for the extended set of variations.

Some change is seen when comparing the distribution in Figure 3.33 with that in Figure 3.20 for the displacer. This suggests a weak correlation. Little change is again seen when comparing the distribution in Figure 3.34 with that in Figure 3.23 for the power piston.

It is also necessary to investigate the cross influence of $\Gamma_{Fxf/P}$ and $\Gamma_{dF/Ff}$ of the displacer with respect to the power piston and vice versa. Figures 3.35 and 3.36 show the distribution of $\Gamma_{Fxf/P}$ of the power piston with $\Gamma_{Fxf/P}$ of the displacer limited to the 50% specification level and the distribution of $\Gamma_{dF/Ff}$ of the power piston with $\Gamma_{dF/Ff}$ of the displacer limited to the 50% specification level respectively for all variations.

The distributions shown in Figures 3.35 and 3.36 show considerable change when comparing these distributions with the ones in Figures 3.24 and 3.30 respectively. This suggests that a

[9] Only a few example distributions will be shown for illustration.

better correlation exists between the specification parameters $\Gamma_{Fxf/P}$ and $\Gamma_{dF/Ff}$ of the displacer and the power piston. However, choosing a 50% limit on the one does not imply a 50% limit on the other, but rather one closer to a 75% limit in both cases.

Figures 3.37 and 3.38 show the distribution of $\Gamma_{Fxf/P}$ of the power piston with $\Gamma_{Fxf/P}$ of the displacer limited to the 50% specification level and the distribution of $\Gamma_{dF/Ff}$ of the power piston with $\Gamma_{dF/Ff}$ of the displacer limited to the 50% specification level respectively for the extended set of variations.

The distribution of the $\Gamma_{Fxf/P}$ ratio of the power piston in Figure 3.37 shows an observable decline in higher values when compared to the distribution in Figure 3.23, but not to the extent where the maximum values are also limited to approximately the 50% specification level. The distribution of the $\Gamma_{dF/Ff}$ ratio of the power piston in Figure 3.38 shows and even more pronounced decline when compared to the distribution in Figure 3.29.

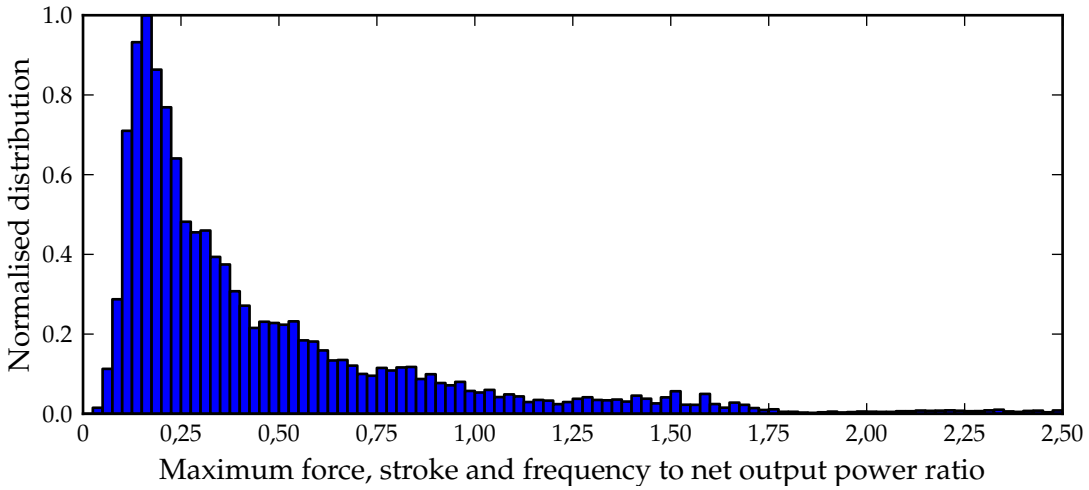

Figure 3.31: Normalised distribution of the $\Gamma_{Fxf/P}$ ratio for the displacer with the $\Gamma_{dF/Ff}$ ratio limited to the 50% specification level for all variations.

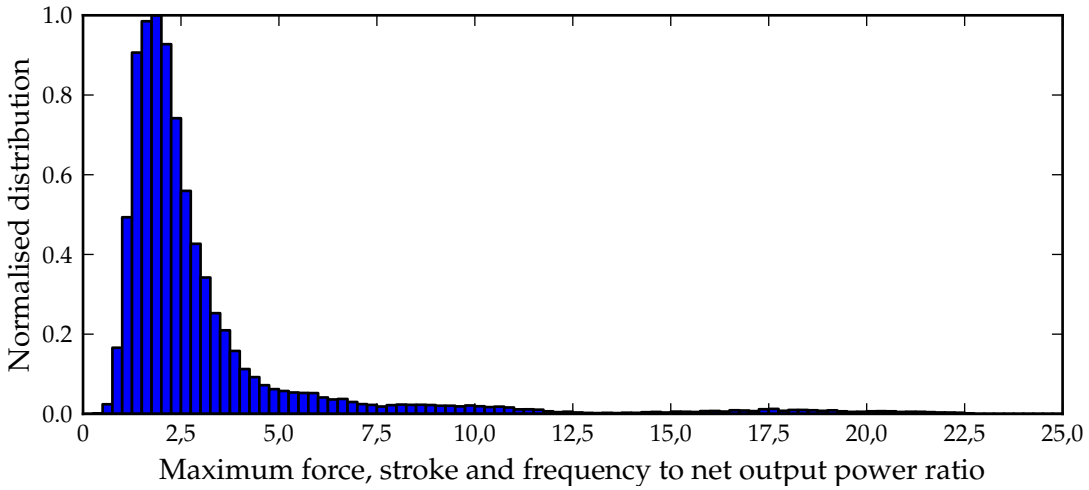

Figure 3.32: Normalised distribution of the $\Gamma_{Fxf/P}$ ratio for the power piston with the $\Gamma_{dF/Ff}$ ratio limited to the 50% specification level for all variations.

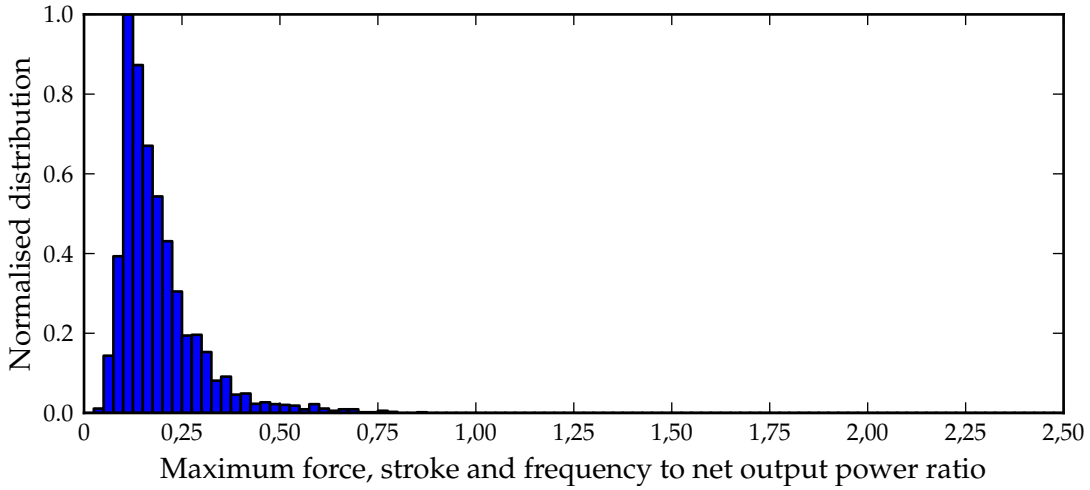

Figure 3.33: Normalised distribution of the $\Gamma_{Fxf/P}$ ratio for the displacer with the $\Gamma_{dF/Ff}$ ratio limited to the 50% specification level for the extended set of variations.

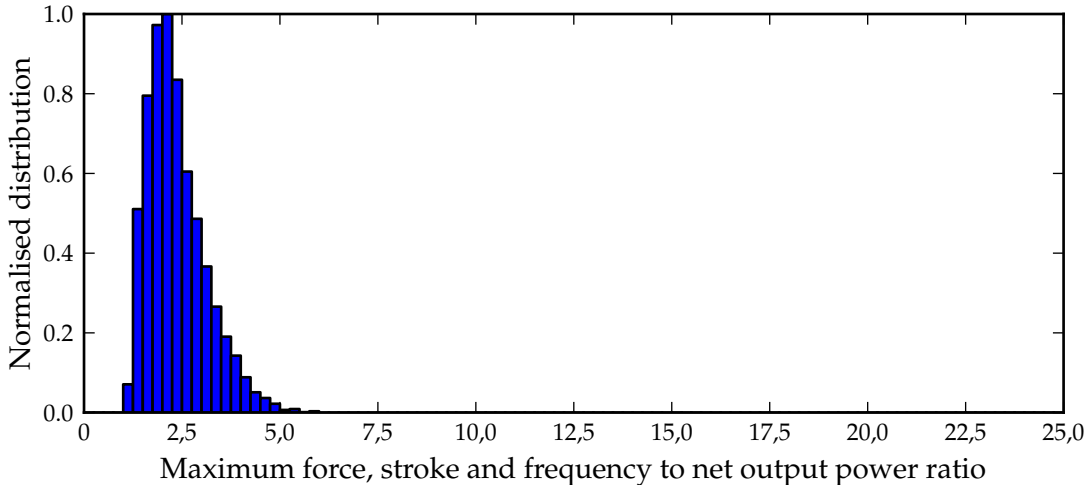

Figure 3.34: Normalised distribution of the $\Gamma_{Fxf/P}$ ratio for the power piston with the $\Gamma_{dF/Ff}$ ratio limited to the 50% specification level for the extended set of variations.

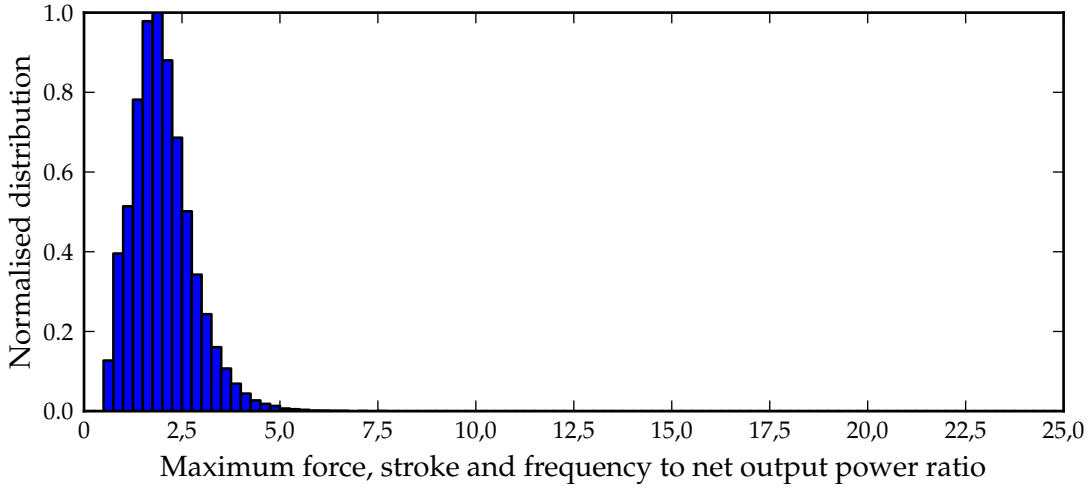

Figure 3.35: Normalised distribution of the $\Gamma_{Fxf/P}$ ratio for the power piston with the $\Gamma_{Fxf/P}$ ratio of the displacer limited to the 50% specification level for all variations.

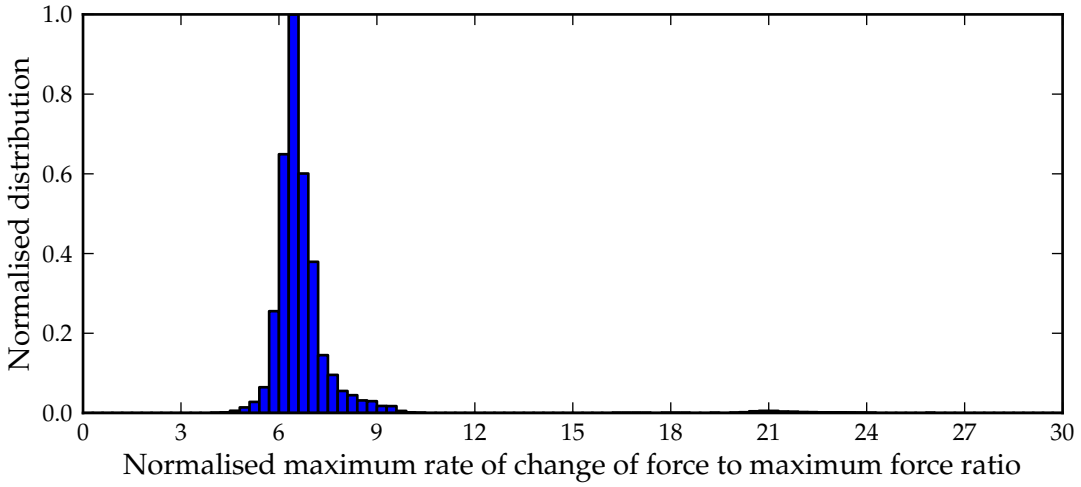

Figure 3.36: Normalised distribution of the $\Gamma_{dF/Ff}$ ratio for the power piston with the $\Gamma_{dF/Ff}$ ratio of the displacer limited to the 50% specification level for all variations.

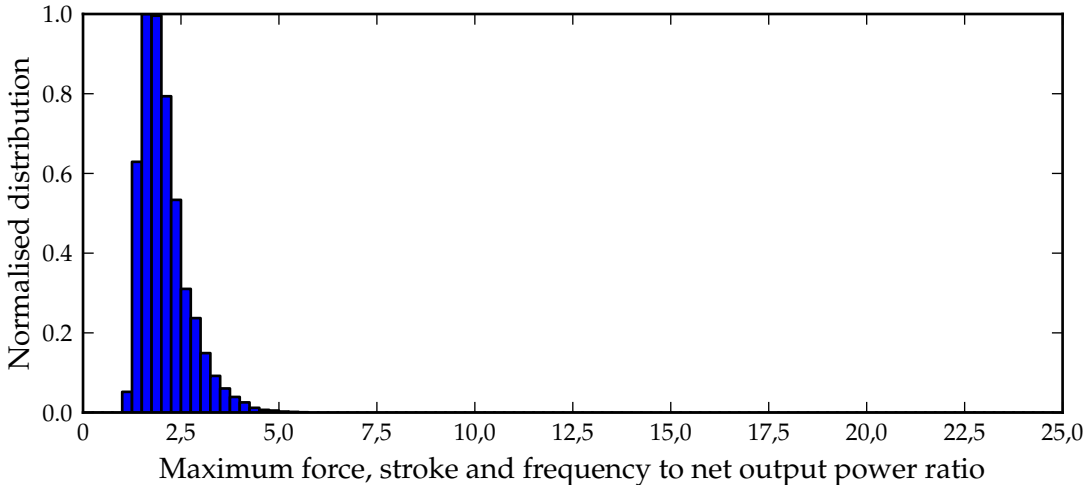

Figure 3.37: Normalised distribution of the $\Gamma_{Fxf/P}$ ratio for the power piston with the $\Gamma_{Fxf/P}$ ratio of the displacer limited to the 50% specification level for the extended set of variations.

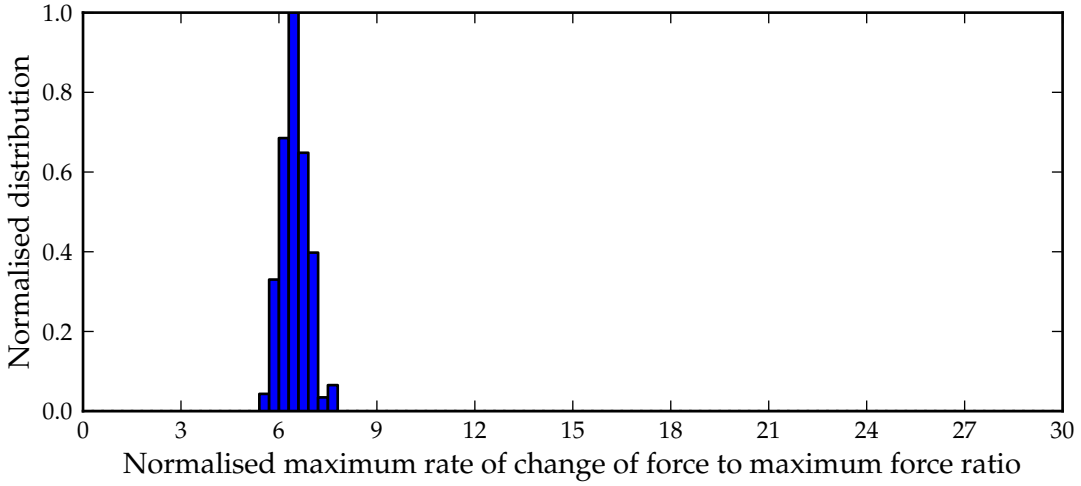

Figure 3.38: Normalised distribution of the $\Gamma_{dF/Ff}$ ratio for the power piston with the $\Gamma_{dF/Ff}$ ratio of the displacer limited to the 50% specification level for the extended set of variations.

While the distributions shown in Figures 3.31 to 3.38 gave a visual impression of the correlation of one parameter to another, it was still deemed necessary give a quantitative view of all possible correlations.

A final investigation was therefore conducted to determine the extent of overlap between two specification parameters by determining the shared occurrences between two specification parameters limited to different percentage levels as a percentage of the total number of occurrences. If for instance the first parameter is limited to 50%, then if good correlation exists with the second parameter, shared occurrences will be close to 50% of the total number of occurrences irrespective of the percentage level at which the second parameter is limited. If poor correlation exists, then the percentage shared occurrences will start at close to 25% and will gradually increase to 50% as the percentage level of the second parameter increases from 50% to 100%. A situation may even exist where an increase in a parameter may correlate well with a decrease in another. If the first parameter is therefore limited to 50%, then the percentage shared occurrences will begin at a very low percentage and will increase again to 50% as the percentage level of the second parameter increases from 50% to 100%.

Tables 3.22 to 3.25 list the percentage shared occurrences of various combinations of the specification parameters $\Gamma_{Fxf/P}$ and $\Gamma_{dF/Ff}$ for both the displacer and power piston for all variations.

It is seen that the comments made for the distributions shown in Figures 3.31 and 3.32 are confirmed by the percentage shared occurrences for the various combinations of specification levels. The results shown in Tables 3.22 to 3.23 confirm that there is no noticeable correlation between the percentage level of $\Gamma_{Fxf/P}$ and $\Gamma_{dF/Ff}$ for either the displacer or the power piston. Choosing a percentage level for the one therefore by no means automatically implies the same percentage level - or any percentage level for that matter - for the other.

The results shown in Tables 3.24 to 3.25 again confirm the conclusions made for the distributions shown in Figures 3.35 and 3.36. It is seen that with one parameter at 50%, almost all occurences are included with the other parameter at 75% and higher. A much better correlation therefore exists than for the previous two tables. What this does not mean is that 50% for the one automatically implies 50% for the other. This is especially the case for lower specification percentage levels.

Tables 3.26 to 3.29 list the percentage shared occurrences of various combinations of the specification parameters $\Gamma_{Fxf/P}$ and $\Gamma_{dF/Ff}$ for both the displacer and power piston for the extended set of variations only.

While slightly better correlations were achieved in some instances, and in other instances worse correlations are shown. Much the same comments can be made for the results in Tables 3.26 to 3.29 as for the corresponding results in Tables 3.22 to 3.25. Further comments on these results will follow later in this chapter.

Table 3.22: Percentage shared occurrences between the specification parameters $\Gamma_{dF/Ff}$ and $\Gamma_{Fxf/P}$ for the displacer limited to various combinations of percentage levels for all variations.

		$\Gamma_{Fxf/P}$				
		50%	60%	75%	90%	100%
	50%	21,0	25,3	32,7	42,2	50,0
	60%	27,1	32,7	41,4	51,8	60,0
$\Gamma_{dF/Ff}$	75%	37,5	43,8	53,3	65,2	75,0
	90%	43,7	51,8	65,3	80,0	90,0
	100%	50,0	60,0	75,0	90,0	100,0

Table 3.23: Percentage shared occurrences between the specification parameters $\Gamma_{dF/Ff}$ and $\Gamma_{Fxf/P}$ for the power piston limited to various combinations of percentage levels for all variations.

		$\Gamma_{Fxf/P}$				
		50%	60%	75%	90%	100%
	50%	25,3	30,6	38,4	46,0	50,0
	60%	31,6	37,6	46,1	54,7	60,0
$\Gamma_{dF/Ff}$	75%	42,4	49,2	59,0	69,5	75,0
	90%	48,2	57,4	71,9	84,4	90,0
	100%	50,0	60,0	75,0	90,0	100,0

Table 3.24: Percentage shared occurrences between the $\Gamma_{Fxf/P}$ specification parameter of the displacer and the power piston limited to various combinations of percentage levels for all variations.

		$\Gamma_{Fxf/P}$ displacer				
		50%	60%	75%	90%	100%
	50%	32,6	38,4	47,2	49,9	50,0
$\Gamma_{Fxf/P}$	60%	38,6	45,4	56,0	59,9	60,0
power	75%	46,5	55,2	68,1	74,8	75,0
piston	90%	50,0	59,9	75,0	87,8	90,0
	100%	50,0	60,0	75,0	90,0	100,0

Table 3.25: Percentage shared occurrences between the $\Gamma_{dF/Ff}$ specification parameters of the displacer and the power piston limited to various combinations of percentage levels for all variations.

		$\Gamma_{dF/Ff}$ displacer				
		50%	60%	75%	90%	100%
	50%	32,9	37,9	45,4	49,0	50,0
$\Gamma_{dF/Ff}$	60%	39,6	45,6	54,5	58,9	60,0
power	75%	48,0	56,4	66,7	72,5	75,0
piston	90%	49,5	58,6	60,7	81,8	90,0
	100%	50,0	60,0	75,0	90,0	100,0

Table 3.26: Percentage shared occurrences between the specification parameters $\Gamma_{dF/Ff}$ and $\Gamma_{Fxf/P}$ for the displacer limited to various combinations of percentage levels for extended set of variations.

		$\Gamma_{Fxf/P}$				
		50%	60%	75%	90%	100%
	50%	25,4	32,6	40,2	46,4	50,0
	60%	32,5	40,2	48,6	55,9	60,0
$\Gamma_{dF/Ff}$	75%	39,0	47,4	58,1	68,1	75,0
	90%	45,4	54,2	66,8	80,0	90,0
	100%	50,0	60,0	75,0	90,0	100,0

Table 3.27: Percentage shared occurrences between the specification parameters $\Gamma_{dF/Ff}$ and $\Gamma_{Fxf/P}$ for the power piston limited to various combinations of percentage levels for extended set of variations.

		$\Gamma_{Fxf/P}$				
		50%	60%	75%	90%	100%
	50%	22,4	27,5	35,5	43,4	50,0
	60%	30,2	36,2	45,1	53,3	60,0
$\Gamma_{dF/Ff}$	75%	44,0	50,8	60,1	68,4	75,0
	90%	46,8	55,4	68,4	81,2	90,0
	100%	50,0	60,0	75,0	90,0	100,0

Table 3.28: Percentage shared occurrences between the $\Gamma_{Fxf/P}$ specification parameter of the displacer and the power piston limited to various combinations of percentage levels for extended set of variations.

		$\Gamma_{Fxf/P}$ displacer				
		50%	60%	75%	90%	100%
	50%	31,6	36,4	41,2	46,1	50,0
$\Gamma_{Fxf/P}$	60%	36,3	42,3	49,3	55,2	60,0
power	75%	42,3	50,2	60,2	68,8	75,0
piston	90%	47,2	56,4	69,6	81,9	90,0
	100%	50,0	60,0	75,0	90,0	100,0

Table 3.29: Percentage shared occurrences between the $\Gamma_{dF/Ff}$ specification parameters of the displacer and the power piston limited to various combinations of percentage levels for extended set of variations.

		$\Gamma_{dF/Ff}$ displacer				
		50%	60%	75%	90%	100%
	50%	33,5	39,2	44,4	48,4	50,0
$\Gamma_{dF/Ff}$	60%	40,6	47,4	53,4	58,3	60,0
power	75%	50,0	59,7	66,9	73,3	75,0
piston	90%	50,0	59,9	71,9	83,2	90,0
	100%	50,0	60,0	75,0	90,0	100,0

3.8.3 Application of specifications

The complexity of the specifications should be obvious. Not only do the specifications lack a one value result - values are dependent on a chosen percentage of included combinations of variations - as shown in Tables 3.19 and 3.20, but it was also shown in the previous section that choosing the value of one of the specifications (e.g. $\Gamma_{Fxf/P}$) based on a chosen percentage does not necessarily imply another specification (e.g. $\Gamma_{dF/Ff}$) for the same percentage. It has also not been indicated yet when the specifications set for all variations (Table 3.19) should be used and when the specifications set for the extended range of variations (Table 3.20) should be used. In the light of these complexities, the final and determining question that arises is: *How should the specifications be applied?* The answer to this question will now be presented here, while further attention will be paid to this question in the next chapter after a design optimisation framework has been proposed.

Ratio of maximum forces

To answer this question, the ratio of the maximum of the absolute of the force after adding the effect of the mover mass and spring constant with respect to the maximum of the absolute of the force before adding the effect of these two variations, will now be examined. This is deemed to be important in answering the question above. This ratio may be expressed as follows, namely

$$\Gamma_{F/F} = \max\left(\left|F_{lem_{with}}\right|\right) / \max\left(\left|F_{lem_{without}}\right|\right), \tag{3.32}$$

where $\Gamma_{F/F}$ denotes the ratio[10] and where the subscripts *with* and *without* denote the forces with and without the mover mass and spring constant variations included respectively. This ratio will vary as the mover mass and/or spring constant varies. Note that this is also equivalent to

$$\Gamma_{F/F} = \Gamma_{Fxf/P_{with}} / \Gamma_{Fxf/P_{without}}, \tag{3.33}$$

since the stroke, frequency and total power is the same for both, where $\Gamma_{Fxf/P_{with}}$ is obtained for a specific combination of moving mass and spring constant.

It was not fully shown in the previous sections what influence the variations of the moving member masses and spring constants have on the maximum of the absolute of the force required of the linear machines. Does the addition of these two variations increase or decrease the maximum force required of the linear machines?

When comparing Figure 3.20 with Figure 3.21 for the displacer and again Figure 3.23 with Figure 3.24 for the power piston, only the distribution of the power piston for all variations show $\Gamma_{Fxf/P}$ ratios lower than for the distribution for the extended range of variations. No similar lowering of the displacer distribution can be seen. Both comparisons however clearly shows a substantial amount of occurrences at higher values for the distributions of all variations.

A certain expectation however exists that for certain mover mass and spring constant com-

[10] The Greek letter Γ was again chosen as symbol.

binations, the ratio should be less than one, i.e. the maximum force required should decrease. It was shown for example in section 3.5.10 that for a variation in the mover mass, the maximum required force initially decreased for an increase in mover mass before starting to increase for the power piston linear machine. It was also shown in section 3.5.11 that for an increase in the spring constant, the maximum required force decreased for the displacer linear machine. To further illustrate this, a few samples from the extended set of variations for three different $\Gamma_{Fxf/P}$ ratios are listed in Table 3.30 and Table 3.31 for the displacer and the power piston respectively, along with the resulting $\Gamma_{Fxf/P}$ ratios when specific mover mass and spring constants are included.

Table 3.30: Sample variations to illustrate the influence of the mover masses and spring constants on the $\Gamma_{Fxf/P}$ indicator for the displacer.

Description	$\Gamma_{Fxf/P}$ without	Spring constant [N/W]	Mover mass [g/W]	$\Gamma_{Fxf/P}$ with	$\Gamma_{F/F}$
Displacer					
Sample 1	0,8713	0,01	0,0	0,9336	1,0715
Net output power: 5472 W	0,8713	0,02	0,0	0,9968	1,1440
Frequency: 65,7 Hz	0,8713	0,0	0,05	0,5723	0,6568
Stroke: 60 mm	0,8713	0,01	0,05	0,5365	0,6157
	0,8713	0,02	0,05	0,5064	0,5812
	0,8713	0,0	0,1	1,3166	1,5111
	0,8713	0,01	0,1	1,2526	1,4376
	0,8713	0,02	0,1	1,1891	1,3647
Sample 2	0,7	0,01	0,0	0,7627	1,0896
Net output power: 4202 W	0,7	0,02	0,0	0,8265	1,1807
Frequency: 54,9 Hz	0,7	0,0	0,05	0,3615	0,5164
Stroke: 60 mm	0,7	0,01	0,05	0,3383	0,4833
	0,7	0,02	0,05	0,3453	0,4933
	0,7	0,0	0,1	0,8085	1,1550
	0,7	0,01	0,1	0,7492	1,0703
	0,7	0,02	0,1	0,6921	0,9887
Sample 3	0,5286	0,01	0,0	0,4922	0,9311
Net output power: 2566 W	0,5286	0,02	0,0	0,5065	0,9582
Frequency: 41,7 Hz	0,5286	0,0	0,05	0,7519	1,4224
Stroke: 60 mm	0,5286	0,01	0,05	0,7072	1,3379
	0,5286	0,02	0,05	0,6642	1,2565
	0,5286	0,0	0,1	1,0245	1,9381
	0,5286	0,01	0,1	0,9696	1,8343
	0,5286	0,02	0,1	0,9166	1,7340

Table 3.31: Sample variations to illustrate the influence of the mover masses and spring constants on the $\Gamma_{Fxf/P}$ indicator for the power piston.

Description	$\Gamma_{Fxf/P}$ without	Spring constant [N/W]	Mover mass [g/W]	$\Gamma_{Fxf/P}$ with	$\Gamma_{F/F}$
Power piston					
Sample 1	5,803	0,1	0,0	5,859	1,010
Net output power: 2566 W	5,803	0,2	0,0	5,915	1,019
Frequency: 41,7 Hz	5,803	0,0	0,5	5,058	0,872
Stroke: 60 mm	5,803	0,1	0,5	5,113	0,881
	5,803	0,2	0,5	5,169	0,891
	5,803	0,0	1,0	4,314	0,743
	5,803	0,1	1,0	4,370	0,753
	5,803	0,2	1,0	4,425	0,763
Sample 2	4,636	0,1	0,0	4,690	1,012
Net output power: 5952 W	4,636	0,2	0,0	4,743	1,023
Frequency: 65,7 Hz	4,636	0,0	0,5	3,918	0,845
Stroke: 15 mm	4,636	0,1	0,5	3,971	0,857
	4,636	0,2	0,5	4,025	0,868
	4,633	0,0	1,0	3,203	0,691
	4,636	0,1	1,0	3,256	0,702
	4,636	0,2	1,0	3,309	0,714
Sample 3	3,526	0,1	0,0	3,580	1,015
Net output power: 4887 W	3,526	0,2	0,0	3,634	1,031
Frequency: 65,7 Hz	3,526	0,0	0,5	2,809	0,797
Stroke: 15 mm	3,526	0,1	0,5	2,862	0,812
	3,526	0,2	0,5	2,914	0,826
	3,523	0,0	1,0	2,156	0,611
	3,526	0,1	1,0	2,200	0,624
	3,526	0,2	1,0	2,245	0,637

While the $\Gamma_{Fxf/P}$ ratio of the second and third samples in Table 3.30 are 0,8 and 0,6 times that of the first sample respectively, all of them are still within the top 90% of all occurrences (refer again Table 3.20). The results shown for the first two samples in Table 3.30 come as a surprise, since it was not expected that the $\Gamma_{Fxf/P}$ ratio would first decrease for an increase in mover mass (refer again Table 3.11). Also, it is shown that an increase in spring constant does not necessarily imply a decrease in the $\Gamma_{Fxf/P}$ ratio (refer again Table 3.12). It is however clear that for specific combinations of mover mass and spring constants the $\Gamma_{Fxf/P}$ ratio may increase or decrease substantially, with both the mover mass and spring constant that could have a substantial influence (especially the mover mass). With the correct mass and spring constant, the maximum force required from the linear machine may therefore decrease substantially.

The $\Gamma_{Fxf/P}$ ratio of the second and third samples in Tables 3.31 were again chosen to be approximately 0,8 and 0,6 times that of the first sample respectively. Again all three of the samples are within the top 90% of all occurences. This time however, the increase/decrease of the $\Gamma_{Fxf/P}$ ratio is consistent with what is expected, i.e. the ratio decreases with an increase in mover mass and increases with an increase in spring constant. Only the mover mass has a substantial influence however, with the spring constant shown to only moderately influence the ratio.

In order to provide a more complete picture, the distributions for the $\Gamma_{F/F}$ ratio were determined for the displacer and the power piston respectively. These distributions are shown in Figures 3.39 and 3.40 respectively.

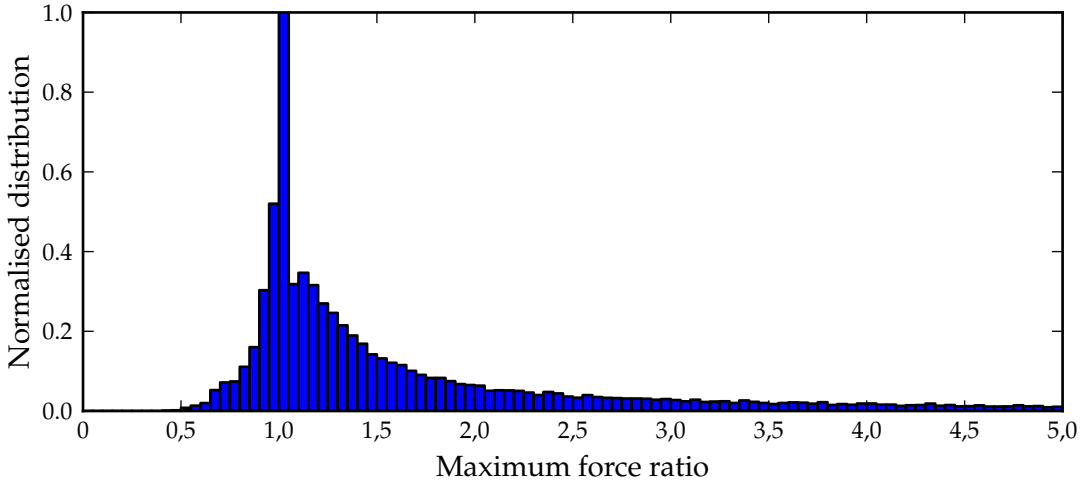

Figure 3.39: Normalised distribution of the $\Gamma_{F/F}$ ratio for the displacer.

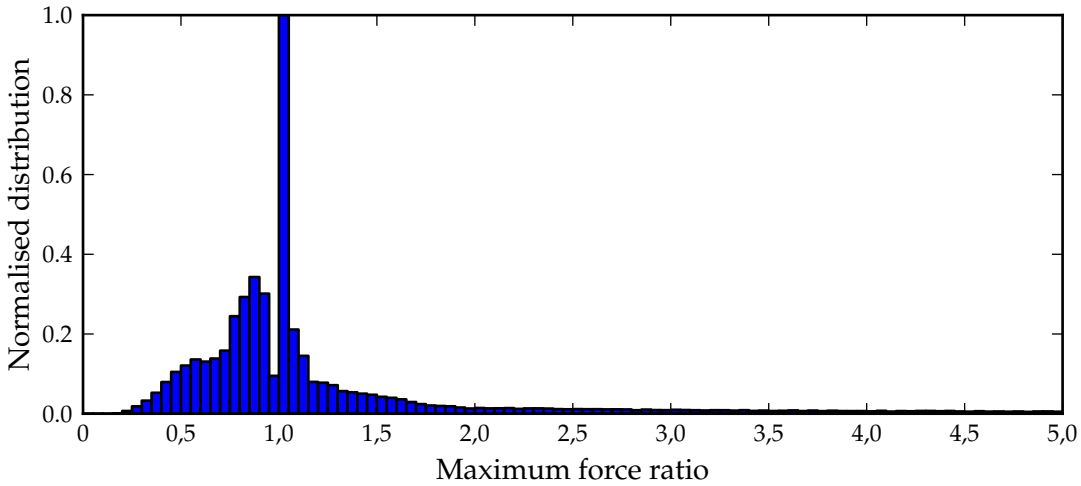

Figure 3.40: Normalised distribution of the $\Gamma_{F/F}$ ratio for the power piston.

The distributions show clearly that the mover mass and spring constant may lead to either higher or to lower maximum forces required of the linear machines when compared to the extended range only. It is seen for the power piston that for just over half of all combinations of variations, the $\Gamma_{F/F}$ ratio was lower than one, i.e. the $\Gamma_{Fxf/P}$ ratio was lowered. Regarding the displacer, in the majority of cases the $\Gamma_{F/F}$ ratio was higher than one, i.e. the $\Gamma_{Fxf/P}$ ratio increased.

This last bit of information will now serve to finally distinguish between the usefulness and/or application of the specification values of all of the variations vs. those for the extended range only.

All variations vs. the extended range only

Up to this point, no clear indication has been given as to the usefulness and/or application of the specification values provided in Tables 3.19 and 3.20 (or alternatively Table 3.21). An effort will now be made to address this issue.

If, for instance, two electrical machine topologies are considered for direct piston displacement control, and one of these yield a mover mass much lower than the other, then, that alone will cause the $\Gamma_{Fxf/P}$ ratios of the two topologies to differ. What applies to one topology from Table 3.19 does not necessarily apply to the other. The influence of variations directly or indirectly influenced by the linear machines is also not easily predictable. This was evident from the results in this chapter as demonstrated in Table 3.30 and Figures 3.39 and 3.40 for instance. The information in Table 3.19 however reveals what can be expected of the extent of the indicators with the influence of the electrical machines included, provided that the design guidelines are adhered to, but without giving a clear indication as to what applies to a specific linear machine.

The information in Table 3.20 on the other hand applies to all electrical machines irrespective of specific topology. But without including the influence of the electrical machines, the indicator values do not necessarily reveal the extent of the final values of the indicators, since a specific electrical machine may cause an increase or a decrease in the indicator values (as is seen from Tables 3.30 and 3.31 and again Figures 3.39 and 3.40).

The most important application of the specifications is considered to be in design optimisation. As will be shown in Chapter 4, the mover mass of the linear machine(s) will generally be determined during iterative optimisation of machine dimensions and other parameters. It is therefore not an input to the optimisation routine, but is a result thereof. The spring constants could be specified as an input to the routine or they could be included as part of the optimisation vector to determine the ideal constant for the specific machine topology and operational conditions. The effect of these two variations should therefore not be included in the specifications when applying the specifications in design optimisation, since the specific combination of mover mass and spring constant will be determined during the optimisation routine.

The specifications listed in Table 3.20 (or alternatively Table 3.21) are therefore particularly useful, with the specifications listed in Table 3.19 having no real usefulness in design optimisation. The data in Table 3.19 rather serves to give insight into the extent of the values of the indicators as mentioned above, providing that the design guidelines are met. In fact, the design guidelines were derived from carefully observing the influence on the various distributions that again led to the data in Table 3.19.

The difference in values in Tables 3.20 and 3.21 gives a clear indication as to the influence of the bounce space void volume. This volume could have been determined during design optimisation, but to determine its influence would require data of the instantaneous pressures

which is not available during design optimisation. The influence of the bounce volume could however be included or excluded by choosing between the values listed in Table 3.20 or Table 3.21.

Importance of the different specifications and specification levels

None of the different specification parameters have been regarded as more important than the others till now, although the emphasis has been on especially the $\Gamma_{Fxf/P}$ ratio and to a lesser extent the $\Gamma_{dF/Ff}$ ratio in investigations in this chapter. The importance of the various indicators will now be considered.

Apart from the force arising from current flowing through the coils, the net exerted force of linear machines is also determined by force components that are highly dependent on the linear machine topology, e.g. position dependent reluctance forces and forces arising from ohmic losses in permanent magnets. While these forces may not be ignored, the force arising from the current is expected to be dominant. Where this is not the case, it is seriously doubted whether such linear machines will be suitable for piston displacement control.

Now, the ratio of exerted force to current is not a constant over the entire stroke length, but is a function of the mover position. For many linear machine topologies, the force exerted per unit current normally lowers towards the outer displacement limits. More current is therefore required at these locations to sustain a certain force.

The χ_{maxF} displacement indicator specifications have been shown in the various tables with increasing percentage towards the outer limits of displacement. For many linear machine topologies, this therefore gives an indication of where maximum force can be expected relative to where decreasing force per unit current is obtained . For the power piston, the majority of χ_{maxF} values are close to the limit of displacement (refer again Tables 3.19, 3.20 and 3.21). For the displacer the values have a wider distribution.

All considering, the usefulness of the χ_{maxF} displacement indicator is limited firstly to the consideration of different force/displacement profiles when compiling these for design optimisation and will be explained in more detail in the next chapter. Secondly, with the χ_{maxF} displacement indicator showing a concentration of maximum force occurrences at the limits of displacement for especially the power piston, research and development could be directed to machine topologies that will yield higher force per unit current at the outer displacement limits. This could result in improved overall operation of free-piston Stirling engines.

The χ_{maxdF} displacement indicator has been dealt with in the listing of the specifications in the various tables by specifying that it may be found over the entire stroke length. There is therefore no directive that could have an influence on the choice of machine topology or the establishment of a design optimisation framework. This indicator therefore has little further usefulness.

Both the $\Gamma_{Fxf/P}$ and $\Gamma_{dF/Ff}$ ratios provide information on the magnitude and/or dynamics of the force profiles. When comparing the values of these two ratios listed in Tables 3.19, 3.20 and 3.21, a slower increase in the values of the $\Gamma_{dF/Ff}$ ratio is seen than for the $\Gamma_{Fxf/P}$ ratio. This

suggests less variation in the force dynamics than in the maximum of the force. Particulars about the dynamics cannot however be fully conveyed by these two ratios alone. This issue will be addressed in the next chapter as well.

The $\Gamma_{Fxf/P}$ ratio is considered important, since this provides information regarding the maximum required force, given the specified operational conditions, e.g. frequency, stroke length and net output power. This will be a key parameter in the optimisation of linear machines.

In considering the $\Gamma_{dF/Ff}$ ratio, a fairly similar argument could be followed as for the χ_{maxF} displacement indicator above. One of the key aspects where this ratio may be useful is to what extent the force exerted by the linear machine must be capable of changing, which indirectly should indicate to what extent the current of the linear machine should be capable of changing. However, with the force per unit current not constant, as argued above, the maximum rate of change of current is topology specific. It follows that the level of importance of the $\Gamma_{dF/Ff}$ ratio should therefore also be topology specific.

With very little experience in the usefulness and application of the $\Gamma_{dF/Ff}$ ratio, it is deemed that in topologies with very low series equivalent inductance, e.g. air-cored topologies, this ratio should be considered less important, based on the knowledge that current can be forced to change very quickly in these topologies. Where these topologies furthermore have fairly flat force per unit current as a function of displacement, this ratio is deemed not to be important at all. For topologies with very large series equivalent inductance, this ratio should be considered to be more important. However, its level of importance when compared to the $\Gamma_{Fxf/P}$ ratio is not known at this stage. If provision is made as described in the next chapter to automatically evaluate or optimise linear machines for $\Gamma_{dF/Ff}$ ratios of a comparable percentage level when compared to the $\Gamma_{Fxf/P}$ ratio, then the uncertainty of its importance should not be a concern.

It is therefore concluded that as long as careful consideration is given to the design optimisation framework in the next chapter, the primary specification parameter is the $\Gamma_{Fxf/P}$ ratio only.

In applying the specifications in design optimisation, the goal should be to include most or all of the occurrences as listed in Table 3.20 or alternatively in Table 3.21. A quick investigation of the data listed in these tables shows that the values of the $\Gamma_{Fxf/P}$ ratios for the 100% column differ considerably from those listed in the 90% column. Compare for instance the difference between the 75% values and the 90% values with the difference between the 90% values and the 100% values.

In choosing a value for the $\Gamma_{Fxf/P}$ ratios, it is proposed to choose the 100% values to include all possible variations. However, if these are found to be difficult to reach, choosing the 90% values should be considered. This will yield considerably lowered maximum required forces, while still including 90% of all possible variations.

3.9 A case for broader application

It should be fairly straightforward to now determine the specifications for linear machines for an exact free-piston equivalent (as explained earlier) of the GPU-3 Stirling engine. The question

however arises as to the applicability of the guidelines and specifications listed in the previous section to a broader range of free-piston engines.

One of two approaches may be followed to gain knowledge of the dynamics of Stirling engines and by extension of the specifications required for linear machines:

- The underlying thermodynamic equations of a Stirling engine may be solved simultaneously for the entire engine according to a second order approach such as the one described in appendix A or according to an even more detailed third order approach such as the one described by Urieli [34]. Case studies similar to the one described in the previous section or even more focussed studies may be undertaken to determine exact requirements of linear machines for the specific engine. Such simulations and studies would however require prior detailed knowledge of engine geometry and operational conditions.
- Instead of solving the underlying thermodynamic equations, Stirling engines may be designed or analysed by the similarity approach. This entails designing an engine from dimensionless scaling parameters obtained from an existing Stirling engine with known performance or by comparing the dimensionless parameters of one engine with that of another. A detailed discussion of this approach is presented by Organ [7, 8] and could provide a basis for comparison of different Stirling engines and by implication the requirements of linear machines, provided that the approach is extended to linear machines.

The first approach would be particularly useful to fine tune the requirements of an electrical machine for a specific Stirling engine, or to propose possible adjustments to a Stirling engine to better accommodate direct piston displacement control. It is however uncertain to what extent the findings of such an approach are useful for determining more general or generic guidelines and specifications for linear machines for a broad range of engines.

The second approach, if extended to linear machines, could offer the capability to apply the findings of a case study according to the first approach, e.g. the GPU-3 case study, to a broad range of engines. It is however considered to be beyond the scope of this dissertation to present a thorough treatment of the subject. Instead, a very basic attempt will be made to motivate that guidelines and specifications set according to the findings of the case study on the GPU-3 should also be directly applicable to a broader range of engines.

Guidelines

The limits to variations, i.e. the design guidelines set in Table 3.18, scale with engine specifications or dimensional variation, e.g. the maximum spring forces scale with net output power. The guidelines may therefore be applied to a broad range of engines.

Maximum force

If two machines share geometric similarity, e.g. compression space to expansion space swept volume ratio, as well as dynamic similarity, e.g. specific heat ratio and characteristic mach

number, then indicated values of ζ (normalised indicated cycle power), N_B (Beale number - equivalent of ζ based on brake output power), and η_{th} (indicated thermal efficiency) are identical. Organ [8] then goes on to show how a smaller engine with brake output power at 546 W at peak output efficiency and 885 rpm can be derived from the GPU-3 Stirling engine[11], based on this scaling by dynamic similarity. It is expected that the derived engine will operate at the same thermal efficiency as the prototype GPU-3 engine of 29,8%.

Stirling engines may also have comparable specific power (ζ, N_B) and efficiency without sharing geometric similarity. More general conditions must therefore exist to achieve a certain level of performance than compliance with rigid dynamic similarity as described above[12]. This is emphasised by the fact that the Beale number of good performing Stirling engines operating close to the rated conditions for which they have been developed averages around 0,15 [8].

An approximate power output of Stirling engines can be determined by the Beale equation, i.e.

$$P_i = N_{Bi} p_{ref} f V_{sw}, \tag{3.34}$$

where P_i denotes the indicated output power, p_{ref} the mean cycle pressure, f the cycle frequency and V_{sw} the swept volume of the power piston in beta-type Stirling engines. Beale observed that the Beale number N_B for many high performance Stirling engines averages around 0,15 (with p_{ref} in MPa and V_{sw} in cm^3). The temperatures at which most of these engines operate are approximately 650 °C for the heater temperature and 65 °C for the cooler temperature [2][13]. In equation (3.34), indicated power and the equivalent Beale number for indicated power N_{Bi} are used, since brake power has already taken mechanical losses into account.

The expression for the $\Gamma_{Fxf/P}$ ratio in (3.30) may be rearranged to obtain an expression for the net output power, i.e.

$$P_t = X_{stroke} f \max\left(|F_{lem}|\right) / \Gamma_{Fxf/P}. \tag{3.35}$$

The net output power as obtained from the second order formulation is nothing other than the net indicated power, since no mechanical losses or electrical machine losses have been taken into account. The expressions in (3.34) and (3.35) may then be equated, i.e.

$$X_{stroke} f \max\left(|F_{lem}|\right) / \Gamma_{Fxf/P} = N_{Bi} p_{ref} f V_{sw}. \tag{3.36}$$

An expression for the maximum force may then be obtained by rearrangement of this equation

[11] The operational conditions for the prototype GPU-3 engine were 6,15 kW at 2000 rpm. Furthermore, while the GPU-3 in this case was operating at 6,8 MPa with hydrogen as working fluid, the derived engine operates at 6,45 MPa with air as working fluid.

[12] Organ [8] presents a thorough treatment of the term 'energetic similarity'. This term is chosen to describe the conditions under which geometric similarity may be relaxed while maintaining specific performance.

[13] As an alternative, the West number and adopted Beale equation could be used, since the West number is independent of the hot side and cold side temperatures. This does however not change the outcome of the argument.

to yield

$$\max\left(|F_{lem}|\right) = \Gamma_{Fxf/P} N_{Bi} p_{ref} V_{sw} / x_{stroke}. \tag{3.37}$$

In (3.37), the maximum force is dependent on $\Gamma_{Fxf/P}$, the well known Beale number applicable to a broad range of good performing engines and three general parameters for Stirling engines. Based on this equation, it does seem that at least the $\Gamma_{Fxf/P}$ ratio is applicable to a broader range of engines, at least in as far as they share the same Beale number of around 0,15 with the GPU-3 engine.

Force dynamics

To what extent can we expect the pressure waveform dynamics to vary, i.e. could we expect the normalised rate of change of force to force ratio to be approximately the same for most engines?

To answer this question, an in depth study of different engines is necessary. It is however regarded as sufficient to declare at this stage that the pressure waveforms observed in literature (e.g. [2, 15, 35]) follow the same dynamics as those shown in appendix C leading to the conclusion that the pressure waveform dynamics and therefore the force dynamics will be much different than for the GPU-3 engine.

It is therefore concluded that the guidelines and specifications should be applicable to a broad range of engines.

3.10 Summary

In this chapter the objective is to provide guidelines and specifications for linear machines to perform direct piston displacement control successfully. To arrive at guidelines and specifications, the second order formulation developed by Urieli was expanded to obtain dynamic information related to the forces necessary for piston displacement control. Following this expansion, important force related indicators were identified.

A thorough case study of the GPU-3 Stirling engine then followed based on and directed by the force indicators. The case study entailed obtaining, amongst others, the force indicators for the GPU-3 engine under a variety of different variations to obtain insight into the influence of individual variations on the force dynamics of the engine. The influence of all possible combinations of the variations was also investigated to gain further insight. This case study then led to the setting of guidelines and specifications for piston displacement control of an exact free-piston equivalent of the GPU-3 engine.

The guidelines and specifications were directly derived from a revised set of variations, where the limits to the maximum/minimum value of the variations were chosen such that no one variation has a dominant effect on the distributions of the output parameters, including the force indicators. With a more sophisticated definition of some of the force indicators, specifications were finally compiled from the distributions of the various force indicators such that the minimum value of the force indicators, below which at least 50%, 60%, and so on of all

possible combinations of variations are included, is known. These then act as a clear indication of the levels that should be reached in order to be capable of piston displacement control for the relevant percentage of combinations of variations.

Finally, a very basic argument was presented that made a case for the broader applicability of the guidelines and specifications.

It became clear that it will be difficult to extremely difficult under certain circumstances to perform piston displacement control. To improve this situation, a combination of improved engine design to lower the requirements and improved linear machine design are necessary. In the next chapter, the focus will be on the latter, and in the process, attention will paid to to the application of the specifications.

Chapter 4

Linear electrical machine topologies: A design optimisation approach

4.1 Introduction

A vast number of different linear machine topologies have been employed or have been proposed before for high speed, oscillating, short stroke applications. These electrical machines find application in reciprocating compressors and water pumps, crankless internal combustion engines and free-piston Stirling engines, and some of these will be discussed in the next chapter.

It should now be possible to evaluate the usefulness of these electrical machines to perform direct piston displacement control as proposed and treated in the previous chapters. But, while chapter 3 ended with specifications and design guidelines, the application thereof to evaluate and even optimise linear machines is not clear. In this chapter, a design optimisation framework for linear machines for the application of direct piston displacement control is presented based on the specifications and design guidelines established in the previous chapter.

An overview of some of the approaches to linear machine optimisation in free-piston Stirling engine applications as described in literature, is provided in section 4.2. This is done by a brief overview of the influence of linear machines on free-piston Stirling engine dynamics and the subsequent optimisation of these linear machines. This is necessary to illustrate the difference between the framework described in this chapter and previous work.

The displacement control approach to linear machine optimisation is then established in section 4.3. Based on this approach to optimisation, an application and adaptation of the specifications is presented in section 4.4. The chapter ends with conclusions in section 4.5.

4.2 Current approaches

4.2.1 Dynamics of free-piston Stirling engines with linear machines

The influence of linear machines plays an important role in the operation and stability of resonant free-piston Stirling engines. In the majority of cases, only linear alternators[1] connected to the power piston are considered in treatments on the dynamics of free-piston Stirling engines.

Redlich and Berchowitz [30] in a treatment on the dynamics of free-piston Stirling engines, describes a linear approach to modelling FPSE/linear alternator combinations and determined amongst others that the frequency of operation is generally dependent upon the load, but that the engine can be configured to operate essentially at constant frequency for a wide variation in the load[2]. They did not deal with the nonlinear thermodynamic and fluid dynamic effects, nor with nonlinear behaviour of the linear alternators. In their treatment of the subject, Redlich and Berchowitz modelled the linear alternator as a pure damping force, i.e.

$$F_{plem} = -D_p \dot{x_p}, \tag{4.1}$$

where F_{plem} denotes the force on the power piston due to the linear alternator and D_p denotes the damping coefficient. This is also the case for several treatments on the dynamics of free-piston Stirling engines [e.g. 20, 36, 37].

This highly idealised model of the linear alternator can only be valid under the following conditions:

- The flux of the machine has a perfectly linear relationship with respect to the displacement, i.e. the slope of the flux against displacement is constant over the entire stroke length. Any nonlinear relationship will introduce a nonlinear relationship between the force of the linear alternator and the speed thereof.
- The current of the linear alternator is in phase with the emf of the generator.
- No reluctance forces are present.
- The forces due to core losses and/or ohmic losses in permanent magnets also act as perfect damping forces, i.e. they are directly proportional to the speed of the linear alternator.

While it is possible, it is highly unlikely for the overall majority of linear alternators employed in free-piston Stirling engines to adhere to these conditions. The most likely candidates are air-cored topologies.

Benvenuto and De Monte [19, 38–41] made a tremendous effort to address the issue of nonlinear phenomena, not only with regard to linear alternators, but also with regard to thermodynamics and gas dynamics. Their approach was to develop a linearisation technique of

[1] In this section, linear machines will be referred to more specifically as linear alternators.
[2] Other findings from the same publication have already been mentioned in chapter 3.

the dynamic balance equations of free-piston Stirling engines, that takes into account the non-linear terms while keeping the linearity of the differential dynamic equations. The equations of motion could therefore be solved analytically, which again allows for algebraic relations linking the various engine parameters to be used. In their treatment of the subject, the force of the linear alternator resisting power piston motion is expressed as

$$F_{plem} = -S_p x_p |x_p|^{n_S-1} - D_p \dot{x_p} |\dot{x_p}|^{n_D-1}, \tag{4.2}$$

where n_S and n_D are real numbers larger than 1,[3] and where S_p denotes the stiffness coefficient required to model linear alternator characteristics associated with displacement, such as reluctance forces, and not speed. The values of the two coefficients S_p and D_p along with n_S and n_D can be determined for every combination of linear alternator and load. This provides for a much more realistic modelling, including a much wider variety of alternator topologies. The force F_{ld} is then represented by an equivalent linearised force

$$F_{plem} = -(b_{p-S} S_p) x_p - (b_{p-D} D_p) \dot{x_p}, \tag{4.3}$$

where the coeffisients b_{p-S} and b_{p-D} take the nonlinear dependence of the force into account as a function of the piston stroke X_{stroke}.

Benvenuto and de Monte could then continue to setup equations describing the force exerted on the power piston by the linear alternator from (4.3) and the governing equations of the linear alternator. This then enabled them to investigate the dynamics of free-piston Stirling engines for a wide variety of variations, including that of the load, which in their case was restricted to a passive R-L load in combination with either a series or shunt tuning capacitor.

The treatments by Benvenuto and De Monte provide good insight into the requirements for stable operation of resonant free-piston Stirling engines in the absence of power control systems, both internal and external (refer to chapter 2 again where an overview of power control systems is provided). One of their main goals was to more accurately determine engine operation in the presence of nonlinear phenomena. This is especially important when trying to predict stable operation, because the stabilising effect of these non-linearities can be accounted for.

With reference to the influence of the linear alternator on the free-piston Stirling engine dynamics as illustrated by Benvenuto and de Monte, the following comments are of importance:

- Benvenuto and De Monte [38] illustrated that not only can the dynamics of FPSE/linear alternator combinations be predicted accurately, but that their approach now also allowed for improved use during the design of FPSE/linear alternators, amongst others, due to the improved ability to predict the piston stroke and therefore the delivered power. The electrical system, including the linear alternator and load, is an integral part of this design

[3] The values of n_S and n_D are clearly indicated several times to be real values larger than 1 by Benvenuto and De Monte [40, 41]. It is the author's opinion that the value equal to 1 should be included, as this would represent the linear case. Nevertheless, equation 4.2 does illustrate the much broader nonlinear modelling approach by Benvenuto and De Monte.

approach, i.e. the output electrical power and chosen operating frequency is directly determined - at least partly - by the electrical system.

- The point was also made that while it is possible to obtain the design value of the load resistance for steady operation of the machine, its value is not critical, because of the presence of stabilizing phenomena inherently part of the engine thermodynamics and gas dynamics [38, 40]. The load was modelled in all treatments by a passive resistor and the influence of different resistor values on the operational stability was examined by analysis and experimentally [19, 39].

- Only linear alternators where the magnetic flux linkage of the windings is a linear function of piston displacement were considered. What the influence of a nonlinear relationship would be, was therefore not illustrated. Furthermore, no stabilising effect was expected from the linear alternator due to its own nonlinearity. The only stabilising effect that could be introduced via the linear alternator would be a power control scheme, but that was what Benvenuto and De Monte wanted to avoid in the first place.

- Benvenuto and De Monte observed that external power control systems lead to reduced engine efficiency over a substantial range of output power. This is certainly true for instance where dummy loads are introduced where the actual load cannot be manipulated (refer again for example to [27]). But Benvenuto and De Monte also made the important observation that a FPSE designed for maximum efficiency will have laminar flow heat exchangers, i.e. no inherently nonlinear stabilising effect in the flow of the working fluid [19]. Although they favour internal power control systems such as the one proposed by Lane and Beale [42], it is certainly possible to say that the efficiency needs not necessarily be lower when using grid-connected power electronic converters as an external power control system.

This very brief discussion does not pretend to be a thorough or completely representative treatment of free-piston Stirling engine dynamics and the influence of linear alternators thereon, but with this background, some attention can now be paid to linear machine optimisation resulting from this approach to FPSE/linear alternator dynamics and operation. This will be done in the following section.

4.2.2 Linear electrical machine optimisation

The mutual influence of free-piston Stirling engines and linear machines has been illustrated in the previous section. The question now arises as to how linear machine optimisation is approached given this mutual influence. In this section, a brief overview is provided of past and current approaches of linear machine optimisation for application in FPSE's.

Boldea and Nasar [43] presented the fundamental equations of a permanent moving magnet, longitudinal flux, single phase and three phase linear alternator for application in Stirling engines. Although they presented basic design guidelines in a companion article [44], they did not provide any guidelines or any framework for optimisation of the linear alternator. Later,

Boldea and Nasar [45] presented a discussion of the design of a transverse flux, moving iron linear alternator with detailed reference to the dynamics of free-piston Stirling engines (where they again referred to the work of Redlich and Berchowitz [30]). Although the design of the machine and even the tuning capacitor value was discussed at length, again no discussion concerning the optimisation was presented.[4]

In another earlier investigation of linear alternators for application in free-piston Stirling engines, Nasar and Chen [47] presented the analysis, design and operation of a tubular PM single phase linear alternator. The study included design guidelines and a design optimisation framework, where the alternator was optimised by a computer-based iterative optimisation algorithm that minimises a penalty function (in their case the sum of the weight to output power ratio and the ratio of iron and copper losses to output power) while adhering to operational and dimensional constraints (e.g. a minimum output power, etc.).

Several articles have been published subsequently concerning the analysis of linear alternators. Some concentrate on a detailed analysis of the linear alternator without giving much background as to the relationship with the free-piston Stirling engine dynamics [e.g. 48], while others concentrate on the interrelated nature of free-piston Stirling engines and linear alternators and the influence of linear alternators on the dynamics [e.g. 37].

More recently, Francois *et al.* [49] reported on a 3D analytical model for a tubular linear induction generator for application in a Stirling cogeneration system. Not only did they present the model, but also an optimisation strategy to minimize generator losses as well as the size of inverter components. In their optimisation approach, Francois *et al.* not only modelled the linear generator, but also included a dynamic model of the Stirling engine. The optimisation algorithm was an NSGA II genetic algorithm that enables the inclusion of multiple parameters with multiple optimisation objectives and constraints.

Another example is that of Schutte and Strauss [46], Schutte *et al.* [50] and Joubert *et al.* [51] who recently reported on the optimisation of permanent magnet, transverse flux, linear alternators for free-piston Stirling engine application. The optimisation entails the minimisation of the mass of the alternator, while keeping the output power and efficiency at predetermined levels. The machine performance is determined through 3D finite element analysis. In all cases, a constrained gradient-based optimisation algorithm was used. If the mass is then minimised, while the power is constrained to a predetermined level, then the power-to-weight ratio is minimised. No attention was paid to engine dynamics and the influence of the linear machine thereon.

For the purposes of this brief overview, the approach to linear machine optimisation for application in free-piston Stirling engines may be categorised in two broad categories:

- A decoupled approach, where the focus is on the linear machine itself without any consideration of the engine dynamics. The link with the rest of the system is through the ratings for which the machine is optimised, e.g. the output power and efficiency, which

[4] It was subsequently shown by Schutte and Strauss [46] that this moving iron topology was not a good candidate for application in Stirling engines, due to its poor mass-to-power ratio.

can be derived from carefully studying the dynamics of the FPSE/linear alternator combination in the way done for example by Benvenuto and De Monte [19, 38–41].

The advantage of such an approach is that all the attention is focussed on the linear machine, allowing more complexity of the machine modelling and optimisation. In cases where the free-piston Stirling engine already exists, this seems to be the better approach.

The disadvantage of such an approach is that the optimisation of the separate components does not necessarily imply an optimised combination. Setting specifications from the system dynamics that the linear machine should adhere to, requires for example an approximation of the mass of the linear machine mover. A decoupled approach could therefore yield results that were not anticipated at first. An iterative process might be required to correct any poor approximations.

- A coupled approach, where the entire system is included in the optimisation effort and where some of the parameters of the Stirling engine could be included as part of the optimisation parameters. This would allow the optimisation of the Stirling engine as well, or at least the incorporation of the effect of the changing influence of the linear machine on the system dynamics.

  The advantage of such an approach, where some Stirling engine parameters are included in the list of optimisation parameters, is that this could lead to a more optimal system when compared to separately optimising components of the system.

  A possible disadvantage is that the modelling of the linear machine may be less complex in order to be less computationally expensive. A too simple approach to the Stirling engine modelling could also lead to incorrect representation of the Stirling engine and could divert the optimisation results away from the real optimal solution.

The brief overview of linear machine optimisation presented here and the even briefer background of Stirling engine dynamics presented in the previous section, should provide sufficient insight into current and past approaches to linear machine optimisation, as well as the ability to distinguish the displacement control approach discussed in the following section with respect to current practises.

4.3 A displacement control approach

4.3.1 Introduction

Generally, the optimisation problem may be mathematically expressed as follows:

Find the minimum of a penalty function as a function of the parameter vector, i.e.

$$\min F = f(\mathbf{X}), \tag{4.4}$$

where

$$\mathbf{X} = x_1, x_2, ..., x_n. \tag{4.5}$$

For constrainted optimisation problems the above is subject to

$$g_j(\mathbf{X}) \leq 0 \qquad j = 1, 2, ..., J \tag{4.6}$$

$$h_k(\mathbf{X}) = 0 \qquad k = 1, 2, ..., K \tag{4.7}$$

$$x_{iL} \leq x_i \leq x_{iU} \qquad i = 1, 2, ..., n, \tag{4.8}$$

where g_j and h_k denote inequality and equality constraint functions respectively and x_{iL} and x_{iU} denote the lower and upper bounds of the ith parameter.

The optimisation problem may be solved by a variety of optimisation algorithms. These could be broadly grouped in two groups of algorithms, namely local and global optimisation algorithms. Since it was not the goal to develop new algorithms, an effort has been made to utilise readily available algorithms.

Venter [52] gave a brief overview of optimisation techniques. In his concluding remarks, he states that global methods should only be considered if local methods are not viable. In the application of these methods to machine optimisation, this is especially true. Simulation of machines by finite element analysis is a real possibility, making the analyses computationally expensive. In addition, gradients are normally available for these problems, at least by way of finite difference calculation, and with proper precaution, numerical noise is not a serious problem. Considering all, it was decided to develop an approach based on gradient based, local search algorithms.

In direct piston displacement control for free-piston Stirling engines it is assumed that the displacement is known or predetermined and not a function of engine/linear machine dynamics. It is after all the goal to control the displacement according to some predetermined displacement pattern. Stirling engine analysis and design could therefore be performed apart from the linear machine analysis and design, and vice versa. At worst, a few iterations may be required to match certain assumptions made considering the two systems. This approach is what was identified as a decoupled approach in the previous section.

A very general flow diagram representation of a gradient based, local search optimisation approach for a decoupled approach to linear machine optimisation could be shown here, but it should also be adequate to give a mere description thereof. In general, it involves the iterative evaluation of the machine through simulations to determine a new search direction and the subsequent determination of a new parameter set if convergence was not reached. This description should be sufficient to provide a starting point for discussion of the optimisation approach proposed here.

A more detailed flow diagram that closely resembles the approaches of Schutte and Strauss [46], Schutte *et al.* [50] and Joubert *et al.* [51] and that adheres to the description above is shown in Figure 4.1. The displacement control approach proposed here was developed from these optimisation approaches.

The following comments are included to provide further clarification of the flow diagram:

- The flow diagram starts with the initialisation of the process, i.e. begin values are chosen

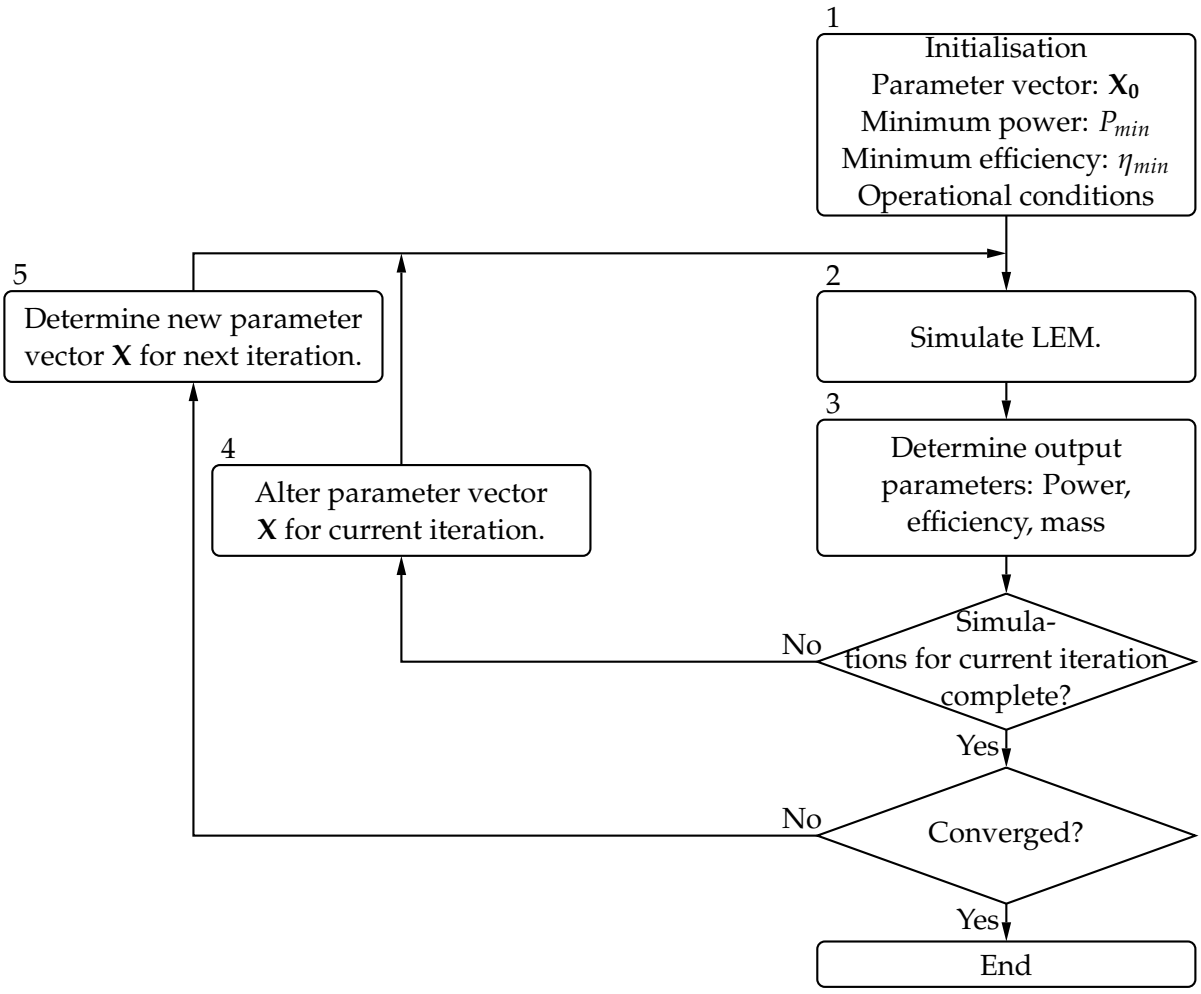

Figure 4.1: A detailed gradient based decoupled optimisation approach.

for the parameter vector, as well as minimum/maximum values for some of the output parameters that will serve as constraints for the optimisation algorithm. Operational conditions are for example operating frequency and stroke length. While only the power (linear machine output power in this case) and the machine efficiency are shown, other constraints may be added, e.g. maximum flux density at different locations.

- The optimisation process then simulates the linear machine several times dependent upon the optimisation algorithm to gather sufficient information for the optimisation algorithm to determine a new search direction/step. To simulate the linear machines, the current was presumed to be sinusoidal and mostly in phase with the EMF of the machine. (Schutte and Strauss [46] included the phase angle of the current with respect to the EMF as part of the optimisation parameter vector and found that the angle was very close to zero.) The magnitude of the current was however included as part of the parameter vector to allow the optimisation algorithm more freedom to optimise the linear machine under investigation.

- Multiple simulation of the electrical machine for each iteration is required, amongst others, to determine gradient information for the goal function as well as the constraint functions by finite difference calculation. Additional simulations of the machine were

performed as needed by the optimisation algorithm.

- Two different optimisation algorithms were used, namely a constrained optimisation by linear approximation (COBYLA) method by Schutte and Strauss [46] and Schutte et al. [50] and a sequential quadratic programming (SQP) method by Joubert *et al.* [51].

- Convergence is obtained when the goal function - the active mass of the linear machine in all cases - is minimised subject to the constraints being met. In keeping the output power at a certain minimum, this means that the power-to-weight ratio was maximised.

In the next section, the development of the piston displacement control approach from the approach shown in Figure 4.1, will be discussed.

4.3.2 Linear electrical machine optimisation

To establish a direct displacement control approach to optimisation, expressions for the linear machine forces need to be established. Under section 3.3.4, expressions describing the displacer and power piston force dynamics of the free-piston Stirling engine were presented. From these, the power exerted on the displacer and the power piston as a result of pressure difference were given as

$$\begin{aligned} F_{d\Delta p} &= A\Delta p_{ce} + A_{rd}\Delta p_{bc} \\ &= A\left(p_c - p_e\right) - A_{rd}\left(p_b - p_c\right) \end{aligned} \tag{4.9}$$

and

$$F_{p\Delta p} = \left(A - A_{rd}\right)\left(p_b - p_c\right) \tag{4.10}$$

respectively. Equations 3.20 and 3.25 then followed as a result, i.e.

$$F_d = \left(m_d + m_{dlem}\right)\ddot{x}_d - F_{d\Delta p} \tag{4.11}$$

and

$$F_p = \left(m_p + m_{plem}\right)\ddot{x}_p - F_{p\Delta p}. \tag{4.12}$$

These two equations describe the remaining forces exerted on the displacer and power piston respectively given the acceleration of the moving members and the forces that result from pressure difference. The cyclic displacements x_d and x_p are known and the cycle frequency is an input variable, thus allowing for the calculation of the accelerations. The forces F_d and F_p will typically originate from the spring forces of linear flexure bearings if present as well as the forces exerted by the linear machines themselves, i.e.

$$F_d = F_{dlem} + F_{dsf} \tag{4.13}$$

and

$$F_p = F_{plem} + F_{psf}, \tag{4.14}$$

where F_{dlem} and F_{plem} denote the forces of the displacer and power piston linear machines respectively and F_{dsf} and F_{psf} denote the spring forces of the flexure bearings. The spring forces may be calculated by

$$F_{dsf} = K_{dsf} x_d \tag{4.15}$$

and

$$F_{psf} = K_{psf} x_p, \tag{4.16}$$

where K_{dsf} and K_{psf} denote the displacer and the power piston spring coefficients respectively. The coefficients may not be constant, but rather functions of displacement as well, and that will again yield non-linear spring forces as a function of displacement. Other forces such as friction forces may also be accounted for, but for the typical envisaged engine configuration, only the flexure spring forces should have any substantial influence. The forces exerted by the linear machines are then simply given by

$$F_{dlem} = (m_d + m_{dlem})\, \ddot{x}_d - F_{d\Delta p} - F_{dsf} \tag{4.17}$$

and

$$F_{plem} = \left(m_p + m_{plem}\right) \ddot{x}_p - F_{p\Delta p} - F_{psf}. \tag{4.18}$$

In the preceding equations, the displacements and therefore the pressures and forces are of course functions of time.

Now, the forces exerted by the linear machines, i.e. F_{dlem} and F_{plem}, are the combination of several different forces. These include reluctance forces, forces arising from iron core losses and ohmic losses in permanent magnets, as well as the forces due to current flowing in the windings. These are nonlinear and specific to the particular machine topology. To obtain a full understanding of the forces for a particular machine topology will require an in depth study of the topology. In general, these forces could however be expressed as

$$F_{dlem} = f\left(x_d, i_{dlem}\right) \tag{4.19}$$

and

$$F_{plem} = f\left(x_p, i_{plem}\right), \tag{4.20}$$

where the specific dependence on the machine topology and current could be simulated from analytical models or finite element analysis as part of an optimisation framework. With in depth knowledge of a particular machine topology, the current could be predicted from the

force as a function of position. However, in the development of the optimisation framework here, it is assumed that this possibility does not exist due to inadequate analytical accuracy or a lack of knowledge of the topology. In this way, provision is made for all possible machine topologies. The optimisation framework can however be adapted easily should such capability exist.

To accomplish this goal, the forces exerted by the linear generators will have to be calculated from equations 4.17 and 4.18. The main difference of the optimisation framework illustrated in Figure 4.1 and the framework proposed here is therefore that in the former the currents serve as input to the simulations, while in the latter the machine forces serve as input to the simulations. But from a simulation point of view, the forces will be determined in terms of equations 4.19 and 4.20, i.e. the forces will be obtained by simulation of a particular machine topology with particular dimensions where the displacement and current serve as inputs to the simulation. The process flow of the optimisation framework will therefore have to make provision for additional steps where the machine current is determined from the the machine force, either directly or by iterative simulation depending on the simulation approach.

For more clarity, the process flow of the proposed optimisation routine for the piston displacement control approach is shown in Figure 4.2.

The process flow of the optimisation framework will now be described in further detail:

- The optimisation routine is initialised again by chosen beginning values for the parameter vector as well as for the constraints, e.g. the minimum power and the minimum efficiency. Operational conditions are again chosen here.

  Apart from the operational conditions, information regarding the displacement and the force required are also initialised here. In section 4.4 this information is described in detail.

  The parameter vector consists of all the dimensions of the particular machine topology. In the case where spring forces are present due to the use of for instance flexure bearings, the coefficients can also be included to determine the optimal spring force for the application. (It was shown in section 3.5.11 that increasing the spring forces leads to smaller maximum forces required of the displacer linear machine.)

- After initialisation, the optimisation routine now enters into an iterative process of evaluation of the machine to determine consecutive search directions to obtain the optimisation objective, while trying not to violate the constraints. The first step is to determine the spring force F_{sf} (i.e. either F_{dsf} or F_{psf}). If the spring force coefficients are not part of the parameter vector, then this step is performed only once at the beginning.

- The mass m_{lem} (i.e. m_{dlem} or m_{plem}) of the moving member of the linear machine is then determined from the dimensions. The weight of the entire moving member, including that of the linear machine, has an influence on this force as part of the mass-acceleration force term as indicated in equations 4.17 and 4.18.

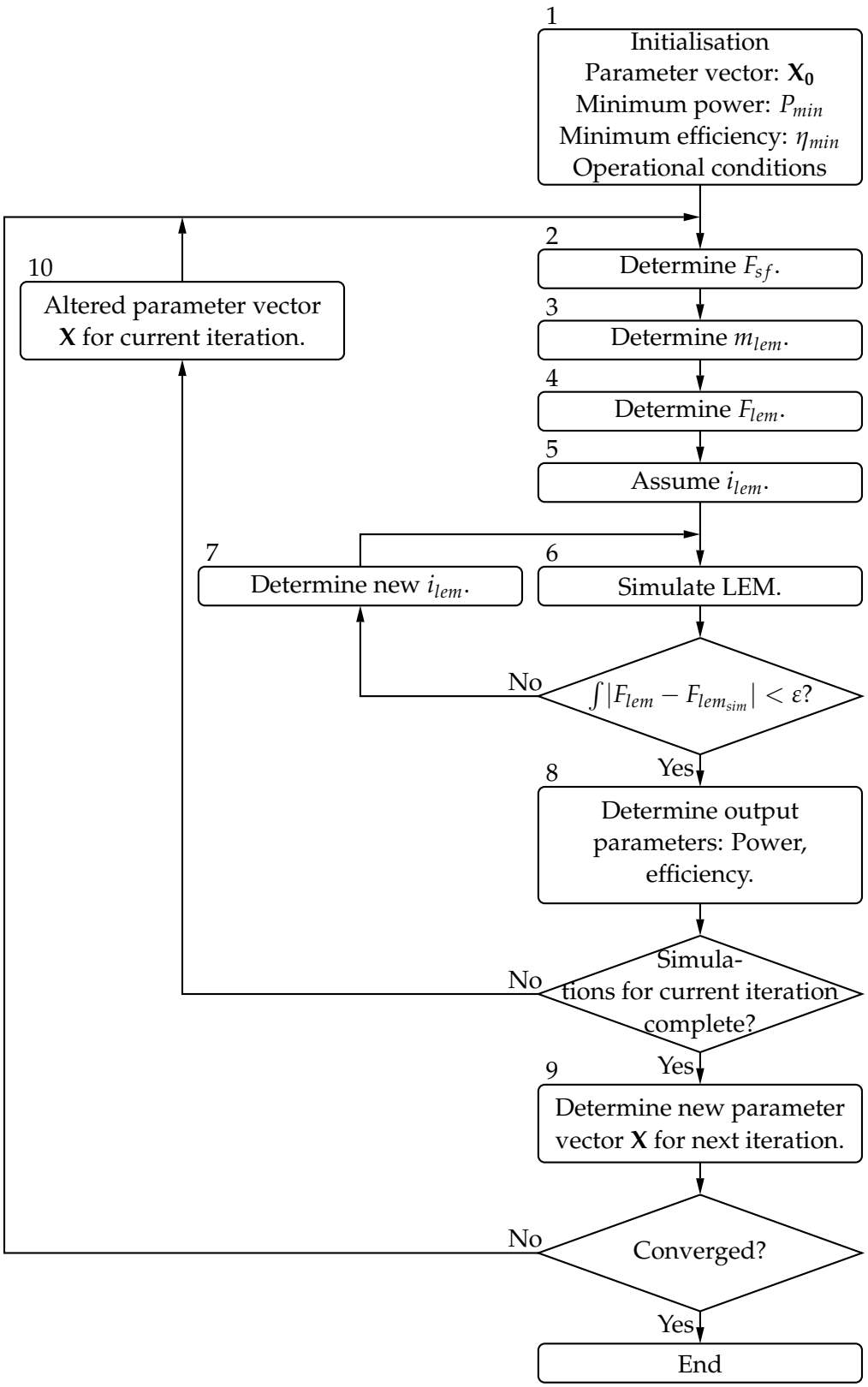

Figure 4.2: Optimisation routine for the piston displacement control approaches.

- The force required of the linear machine F_{lem} (i.e. either F_{dlem} or F_{plem}) in order to follow a certain displacement pattern is then determined from equations 4.17 and 4.18.

- With the required machine force now known, the machine current i_{lem} (again either i_{dlem}

or i_{plem}) is determined. In Figure 4.2, the current is shown to be iteratively determined by first assuming a current and to then adapting the current in order to obtain the required force. This approach to determine the current is specifically focussed on machine simulation by finite element analysis. It is certainly possible that for machines where accurate analytical models exist, the current can be determined through a single process. In such a case, the iterative process will be omitted.

- With the current now known, the performance parameters of the machine, such as the input and output power and efficiency, can be calculated.
- Several simulations may be performed during each iteration to determine for instance the gradients necessary to determine the search direction according to the specific optimisation algorithm.
- A new parameter vector is then determined, again according to the specific optimisation algorithm.
- If convergence has not been reached, the process is then started again where the spring force is determined.

The process depicted in Figure 4.2 focuses on the optimisation of only one machine at a time, i.e. for either the displacer or the power piston. Setting the required efficiency during initialisation therefore implies that this efficiency only applies to one machine. It is not the required efficiency for the entire system as specified in Table 3.20.

The goal to obtain the required efficiency for the entire system, may be reached in two ways:

- The required overall efficiency can be reached through separate optimisation of the displacer and power piston machines where initial required efficiencies are assumed for each machine and then subsequently adjusted to the required efficiencies during reruns of the optimisation routines in order to reach the required overall efficiency. The process shown in Figure 4.2 is therefore completely valid.
- The alternative approach is to combine the optimisation of the displacer and power piston. This will enable the direct calculation of the overall efficiency of the system.

  The process shown in Figure 4.2 does not completely describe this approach. It could however be adapted quite easily by simultaneous calculation of the relevant parameters of each of the machines for each of the steps shown in Figure 4.2. For example, where the spring force was calculated for only one of the machines, it is now calculated for both, or where the current is only determined for one of the machines, it is now determined for both. This provides for the calculation of the overall efficiency as part of the optimisation process, as well as the interesting possibility to optimise for the combined mass of the machines which is not possible with the first approach.

  For this approach, the parameter vector then includes all of the dimensions and the spring coefficients of both machines. In this case, care must be taken to determine gradient information accurately and to avoid unnecessary simulations during gradient determination.

This is because variations in some of the dimensions will only require simulation of one of the machines.

For machines where the displacer and power piston machines are combined as one, i.e. where the stator is shared, this approach is deemed to be the obvious route to optimise the machine dimensions.

Attention will now be given to the calculation of the overall efficiency.

The instantaneous input power to the power piston linear machine can be found by the product of the power piston force F_{plem} and the speed $\dot{x}_p$ of the power piston. The instantaneous input power to the displacer linear machine can be found similarly by $F_{dlem}\dot{x}_d$. The average input power to the power piston is positive for free-piston Stirling engines operating as heat to electrical energy converters, and the average input power to the displacer is normally negative, i.e. the displacer linear machine normally on average delivers power to the Stirling engine, and is normally substantially less than the average input power to the power piston.

The resultant instantaneous input power to the linear machines is equal to the addition of these two instantaneous powers, i.e.

$$p_{in} = F_{plem}\dot{x}_p + F_{dlem}\dot{x}_d. \tag{4.21}$$

Calculating the average of the resultant instantaneous power will therefore yield the average power available for conversion, i.e.

$$P_{in} = \frac{1}{T}\int_0^T p_{in}dt. \tag{4.22}$$

Now, the output power of the power piston linear machine can be found by calculating the product of the terminal voltage v_{plem} and the terminal current i_{plem}. The average of this output power will be slightly less than the input power to the power piston linear machine due to losses in the linear machine. The output power to the displacer can be similarly found by $v_{dlem}i_{dlem}$. The average of this power will again be slightly more negative than the average input power to the displacer due to losses in the displacer linear machine.

The resultant instantaneous output power from the linear machines is equal to the addition of the two instantaneous powers, i.e.

$$p_{out} = v_{plem}i_{plem} + v_{dlem}i_{dlem}. \tag{4.23}$$

Obtaining the average of the resultant instantaneous power will therefore yield the average power available from the conversion, i.e.

$$P_{out} = \frac{1}{T}\int_0^T p_{out}dt. \tag{4.24}$$

With the average output power from the power piston linear machine slightly less than the average input power, and the average output power from the displacer linear machine slightly

more negative than the average input power, it follows that the resultant output power is less than the resultant input power. All that is left is to calculate the efficiency, namely

$$\eta = P_{out}/P_{in}. \tag{4.25}$$

One issue remains, namely how the specifications are applied in the proposed optimisation framework. This is now addressed in the next section.

4.4 Applying specifications

4.4.1 Introduction

In the following sections, attention will be given to the application of the specifications as developed in Chapter 3 to the optimisation framework proposed in the previous sections. The application of the specifications have already been discussed in section 3.8.3, but this discussion concentrated on simplifying and clarifying the specifications as listed in Tables 3.19, 3.20 and 3.21. The focus was on issues such as the use of the data of one table instead of the other and the importance of the different indicators.

Some further detail is however necessary to also apply the specifications to the optimisation framework. For instance, the discussion in section 3.8.3 did arrive at data from which the maximum of the forces could be calculated, but data from which the time-based response of the forces could be derived was not provided. The optimisation framework requires such data.

The obvious source of time-based data is the original simulations of the combination of variations that led to the data listed in Tables 3.20 and 3.21. The dynamic responses of the $\Gamma_{Fxf/P}$ ratio as a function of time can be obtained from the simulations when the data of Tables 3.20 and 3.21 are being generated, i.e. instead of calculating the $\Gamma_{Fxf/P}$ ratio directly using equation 3.30, the dynamic response is firstly determined by

$$\gamma_{Fxf/P} = X_{stroke} f F_g(t)/P_t, \tag{4.26}$$

and to then calculate the $\Gamma_{Fxf/P}$ ratio from

$$\Gamma_{Fxf/P} = \max\left(\left|\gamma_{Fxf/P}\right|\right). \tag{4.27}$$

This then yields the same result for the $\Gamma_{Fxf/P}$ ratio as would equation 3.30. Do note that the lower case greek letter γ is used to indicate the dynamic response, in stead of the single ratio value designated by the capital letter Γ. Furthermore, since the frequency is also taken into consideration in calculating the $\gamma_{Fxf/P}$ response and the $\Gamma_{Fxf/P}$ ratio, the responses will be shown in subsequent sections with respect to angle and not with respect to time to merely indicate a single cycle. The moment the frequency is taken into consideration to calculate the force dynamic response necessary for the optimisation framework, the force response should be shown with respect to time and not angle. Reference to dynamic response should therefore be seen from here on as reference to angle-based or time-based, depending on the context.

The approach to obtain time-based responses is therefore to also store the dynamic responses of selected combinations of variations and to then process these responses to present candidates for use in the design optimisation process. This process will be explained in the following sections for the displacer (section 4.4.2), the power piston (section 4.4.3) and for cases where the displacer and the power piston optimisations are combined (section 4.4.4).

4.4.2 Displacer

The process to obtain dynamic response candidates will be explained in detail for the displacer and then in less detail for the power piston in the following section.

To start with, the $\gamma_{Fxf/P}$ dynamic responses that yielded the top fifty[5] $\Gamma_{Fxf/P}$ ratios for the extended range of variations (including the influence of the bounce space void volume to swept volume ratio) are shown in Figure 4.3. For these responses, the $\Gamma_{Fxf/P}$ ratio varied from the maximum of 0,8713 down to approximately 0,619. Mainly two groups of responses resulting from the different displacement patterns can be identified. Two other displacement patterns exist as well[6], but the responses resulting from these displacements did not yield $\Gamma_{Fxf/P}$ ratios that fall under those shown in Figure 4.3.

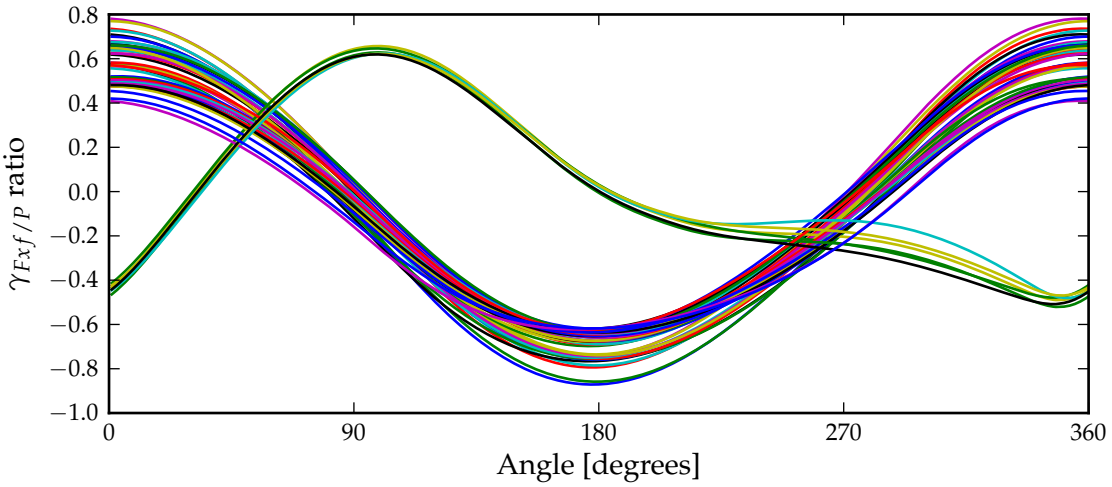

Figure 4.3: Top fifty $\gamma_{Fxf/P}$ dynamic responses with $\Gamma_{Fxf/P}$ ratios equal to or below the 100% specification level for the displacer.

One approach to establish suitable candidates to represent at least these fifty responses would be to choose one response each from the two groups of responses and to then normalise the two candidates, i.e. where

$$\max\left(\left|\gamma_{Fxf/P_{normalised}}\right|\right) = 1.0. \tag{4.28}$$

Another approach that could be followed is to obtain the average response of each of the two groups of responses, by obtaining the average of the normalised responses. The average responses should then be normalised again. By normalisation of the candidate responses, any

[5] A total of fifty was chosen to include a good number of responses, without presenting too much data. The same conclusions could be reached with more or fewer responses.

[6] There are four in total, namely two for composite displacement and two for sinusoidal displacement.

one of the responses in Figure 4.3 can be obtained approximately by merely multiplying the candidate response with the $\Gamma_{Fxf/P}$ ratio of the particular response.

Figure 4.4 shows the normalised responses of those shown in Figure 4.3. This is required for the second approach. Do note the similarity of the responses of the one group (the non-sinusoidal group). The near sinusoidal group however shows some difference, most notably a difference in the maximum positive value of the responses, with the majority of responses having a larger negative maximum.

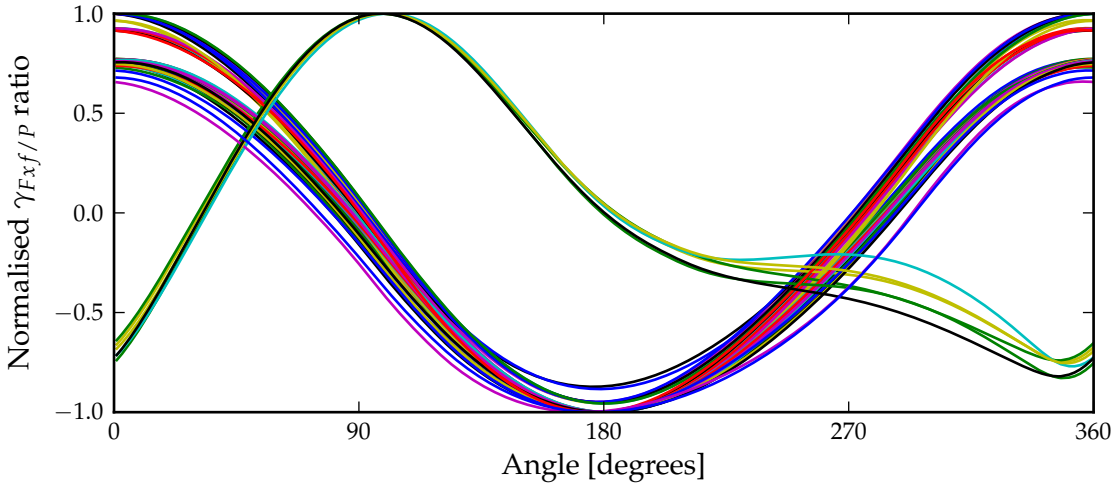

Figure 4.4: Normalised top fifty $\gamma_{Fxf/P}$ dynamic responses with $\Gamma_{Fxf/P}$ ratios equal to or below the 100% specification level for the displacer.

Figure 4.5 shows the resulting candidate responses, where two of the responses designated *1b* and *2b* (the dashed lines) were chosen by choosing the dynamic response with the highest $\Gamma_{Fxf/P}$ ratio from each of the two groups of responses and where the other two responses designated *1a* and *2a* (the solid lines) were calculated according to the averaging approach described above. Candidates *1a* and *1b* originate from composite displacement and candidates *2a* and *2b* from sinusoidal displacement.

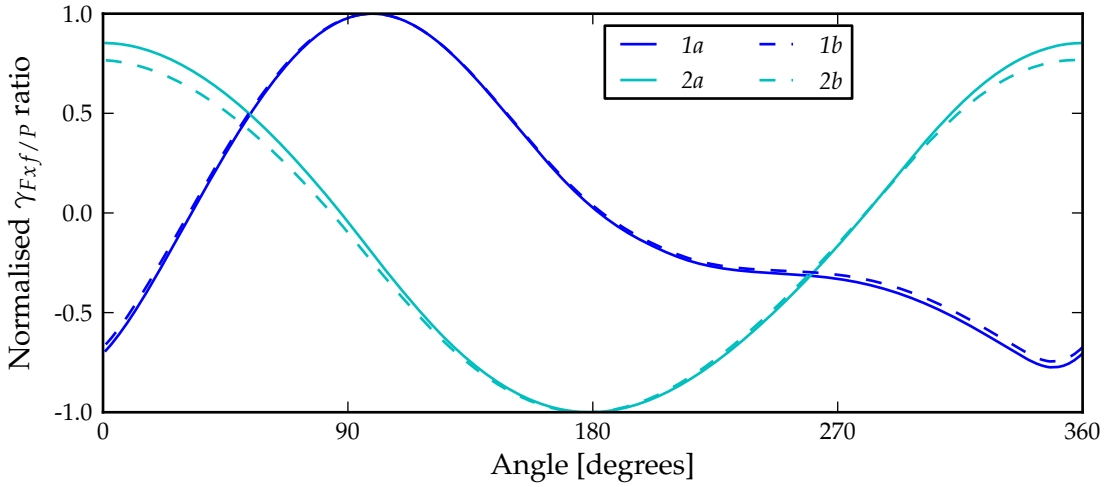

Figure 4.5: Normalised candidate $\gamma_{Fxf/P}$ dynamic responses for the displacer obtained from the top fifty dynamic responses with $\Gamma_{Fxf/P}$ ratios equal to or below the 100% specification level.

To determine the level to which these responses could be representative of all responses, the process above was repeated, but this time for the top fifty responses with $\Gamma_{Fxf/P}$ ratios equal to or below the 90% specification level listed in Table 3.20. These responses are shown in Figure 4.6. The $\Gamma_{Fxf/P}$ ratios varied from the maximum of 0,348 down to approximately 0,341. More groups can be identified than in Figure 4.3. Groups were distinguished by the displacement from which the responses originate. The normalised responses are shown in Figure 4.7.

Figure 4.8 shows the resulting candidate responses, where the responses were again determined as for Figure 4.5, with the dashed lines indicating the responses obtained by choosing the dynamic response with the highest $\Gamma_{Fxf/P}$ ratio from each group of responses and where the solid line responses were calculated according to the averaging approach described earlier.

To help with further explanation, the displacements corresponding to the various candidate responses (of the same colour) are shown in Figure 4.9. (Note that these normalised displacements also correspond with the candidates of the same colour in Figure 4.5.)

This time, eight candidate responses were identified. The responses originating from sinu-

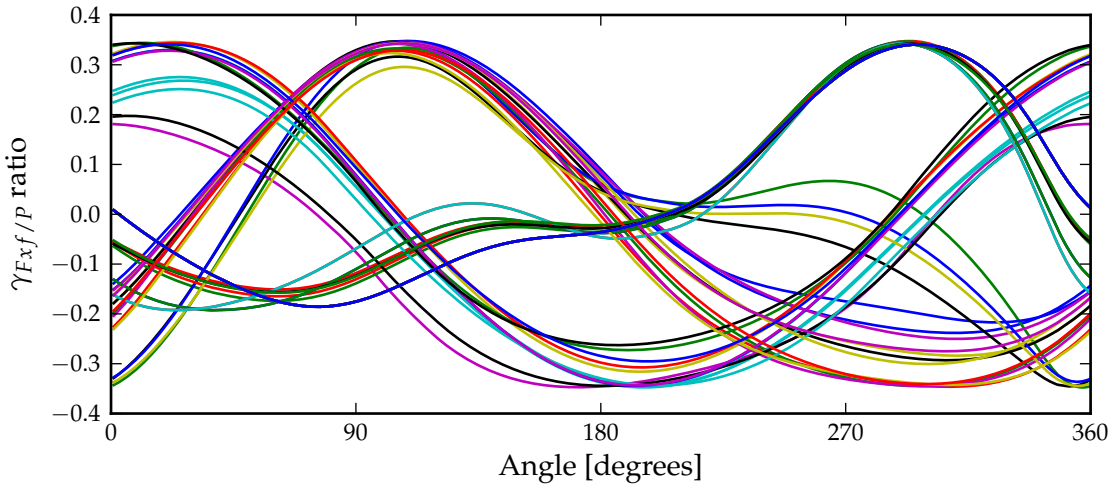

Figure 4.6: Top fifty $\gamma_{Fxf/P}$ dynamic responses with $\Gamma_{Fxf/P}$ ratios equal to or below the 90% specification level for the displacer.

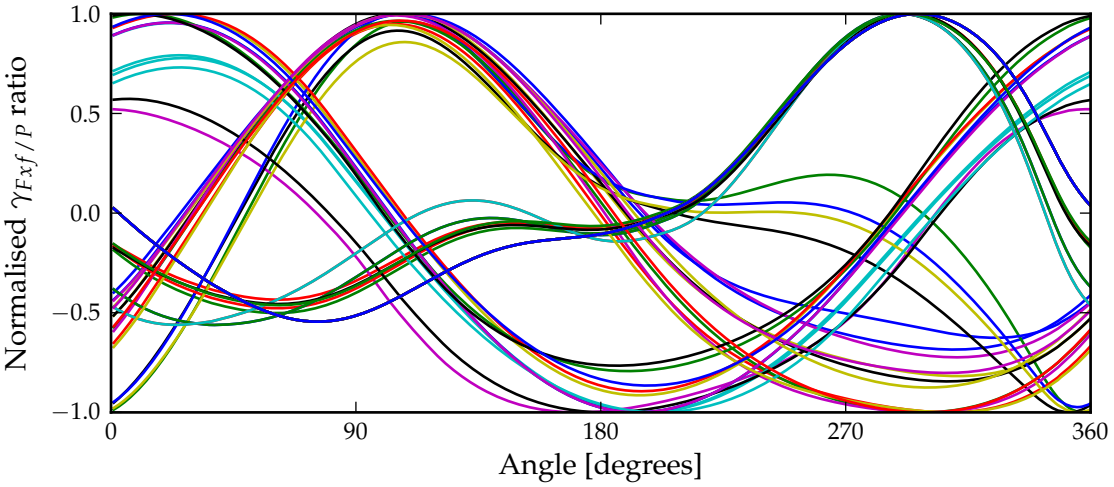

Figure 4.7: Normalised top fifty $\gamma_{Fxf/P}$ dynamic responses with $\Gamma_{Fxf/P}$ ratios equal to or below the 90% specification level for the displacer.

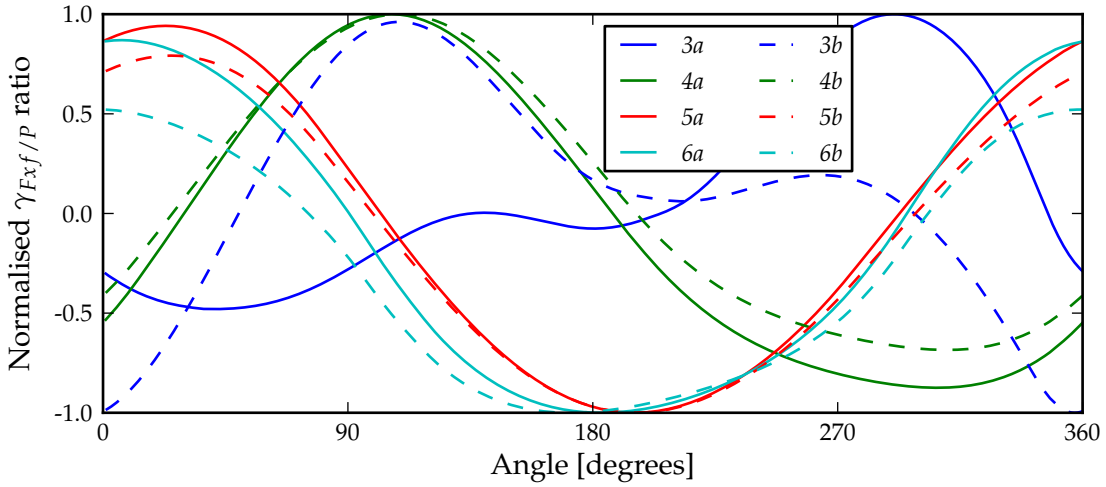

Figure 4.8: Normalised candidate $\gamma_{Fxf/P}$ dynamic responses for the displacer obtained from the top fifty dynamic responses with $\Gamma_{Fxf/P}$ ratios equal to or below the 90% specification level.

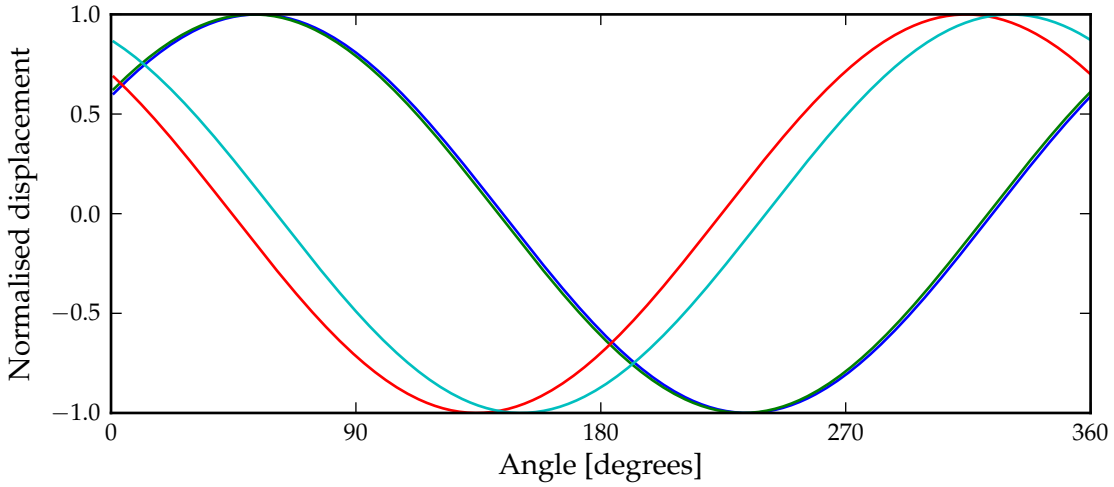

Figure 4.9: Normalised displacement associated with the candidate dynamic responses for the displacer.

soidal displacement (*5a*, *5b*, *6a* and *6b*) show some similarity to the corresponding candidate responses shown in Figure 4.5. When comparing responses *5a* and *5b* to their corresponding displacements in Figure 4.9, it is seen however that there is substantially more phase shift between the responses and the displacements than for responses *6a* and *6b*. For responses *5a* and *5b*, this means the linear machines will have to exert maximum force closer to the centre of displacement, and for responses *6a* and *6b* closer to the limits of displacement. A quick revisit of the χ_{maxF} displacement indicator in Table 3.20 confirms that a wide distribution of the location of maximum force may be expected for the displacer.

Contrary to the fairly sinusoidal response of the candidate responses originating from sinusoidal displacement, the responses originating from composite displacement (*3a*, *3b*, *4a* and *4b*) again clearly show non-sinusoidal response. While responses *4a* and *4b* are fairly similar, the responses *3a* and *3b* differ considerably. Closer examination revealed that response *3a* was for a lower displacer rod area percentage than response *3b*. The average output power for *3a* was found to be negative, i.e. the displacer linear machine will be acting on average as a motor, as would generally be the case. The average output power for *3b* on the other hand was found

to be positive, i.e. the displacer linear machine will be acting on average as a generator (this has been shown before as a consequence of higher displacer rod area percentages). Response *3a*, being an average response will have been influenced by a minority of responses equal to and/or similar to the response *3b* (remember that response *3b* is chosen from the particular group as the response with the highest maximum $\Gamma_{Fxf/P}$ ratio).

Further investigation at this point revealed that all of the candidate responses shown thus far, with the exception of response *3a*, would yield positive average output power, i.e. a large number of responses for $\Gamma_{Fxf/P}$ ratios found in the upper 10% have large displacer rod area percentages in common. If final responses were chosen from these candidates, this might skew the design optimisation of the displacer linear machine. It was therefore deemed necessary to obtain further candidate responses specifically where the displacer linear machines would be acting on average as motors. In order to do this, the previous two analyses were again performed, but with all responses yielding a positive average output power excluded.

The $\gamma_{Fxf/P}$ dynamic responses that yielded the top fifty $\Gamma_{Fxf/P}$ ratios are shown in Figure 4.10 and the resulting candidate responses are shown in Figure 4.11. (The $\Gamma_{Fxf/P}$ ratio varied from a maximum of 0,57 down to approximately 0,49. This is still way above the 90% level of 0,348). Also, the $\gamma_{Fxf/P}$ dynamic responses that yielded the top fifty $\Gamma_{Fxf/P}$ ratios equal to or below the 90% specification level listed in Table 3.20 are shown in Figure 4.12 and the resulting candidate responses are shown in Figure 4.13. (The $\Gamma_{Fxf/P}$ ratio varied from a maximum of 0,348 down to approximately 0,338.)

It is seen from Figures 4.11 and 4.13 that in both cases no responses that originate from sinusoidal displacement were among the top fifty responses. Very little difference exists between candidate responses, especially the average responses *7a* and *8a* in both figures.

To also provide dynamic responses that originate from sinusoidal displacement, the analysis was again repeated as for the results shown in Figures 4.10 and 4.11, i.e. for the $\gamma_{Fxf/P}$ dynamic responses that yielded the top fifty $\Gamma_{Fxf/P}$ ratios excluding all responses yielding a positive average output power, but with the additional exclusion of all responses originating

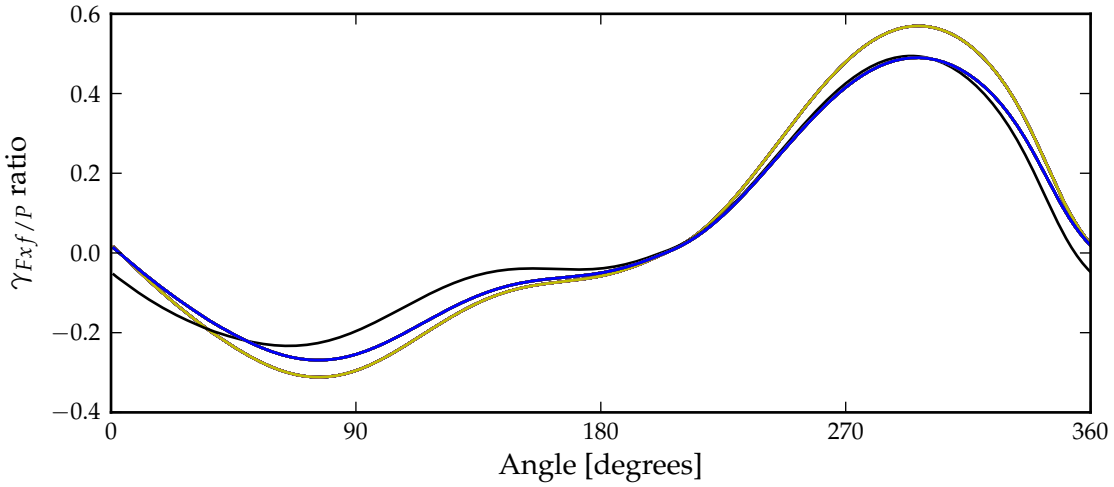

Figure 4.10: Top fifty $\gamma_{Fxf/P}$ dynamic responses with $\Gamma_{Fxf/P}$ ratios equal to or below the 100% specification level for the displacer, excluding those with average positive power.

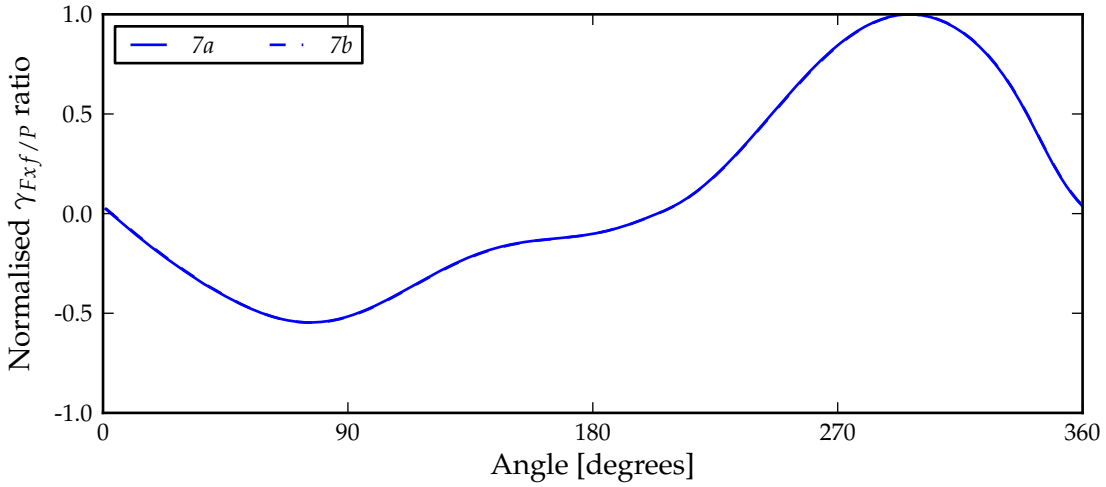

Figure 4.11: Normalised candidate $\gamma_{Fxf/P}$ dynamic responses for the displacer obtained from the top fifty dynamic responses with $\Gamma_{Fxf/P}$ ratios equal to or below the 100% specification level, excluding those with average positive power.

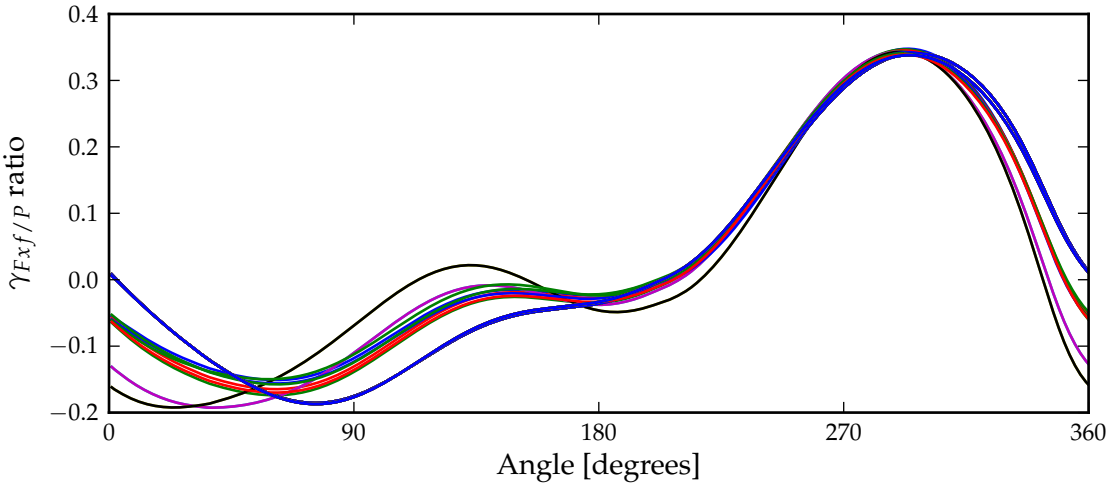

Figure 4.12: Top fifty $\gamma_{Fxf/P}$ dynamic responses with $\Gamma_{Fxf/P}$ ratios equal to or below the 90% specification level for the displacer, excluding those with average positive power.

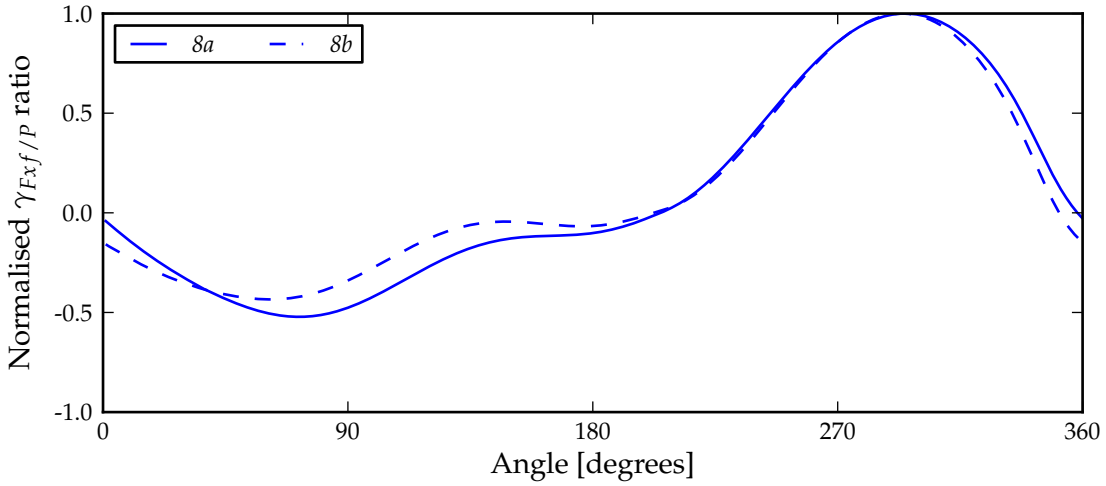

Figure 4.13: Normalised candidate $\gamma_{Fxf/P}$ dynamic responses for the displacer obtained from the top fifty dynamic responses with $\Gamma_{Fxf/P}$ ratios equal to or below the 90% specification level, excluding those with average positive power.

from composite displacement. The responses are shown in Figure 4.14 and the resulting candidate responses are shown in Figure 4.15. The $\Gamma_{Fxf/P}$ ratio varied from a maximum of 0,37 down to 0,321. The analysis was therefore not done for the 90% case, since some of the responses shown in Figure 4.14 already fall in this category.

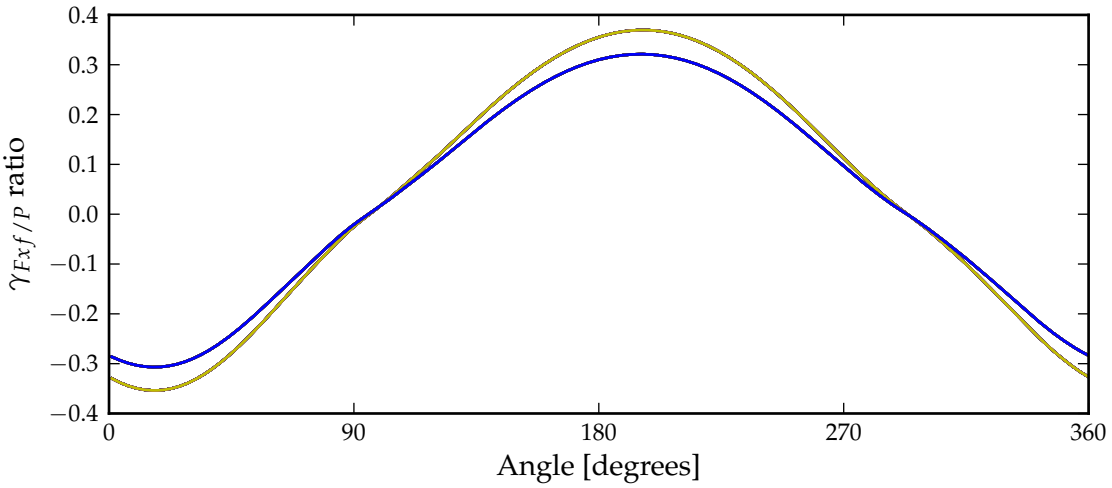

Figure 4.14: Top fifty $\gamma_{Fxf/P}$ dynamic responses with $\Gamma_{Fxf/P}$ ratios equal to or below the 100% specification level for the displacer.

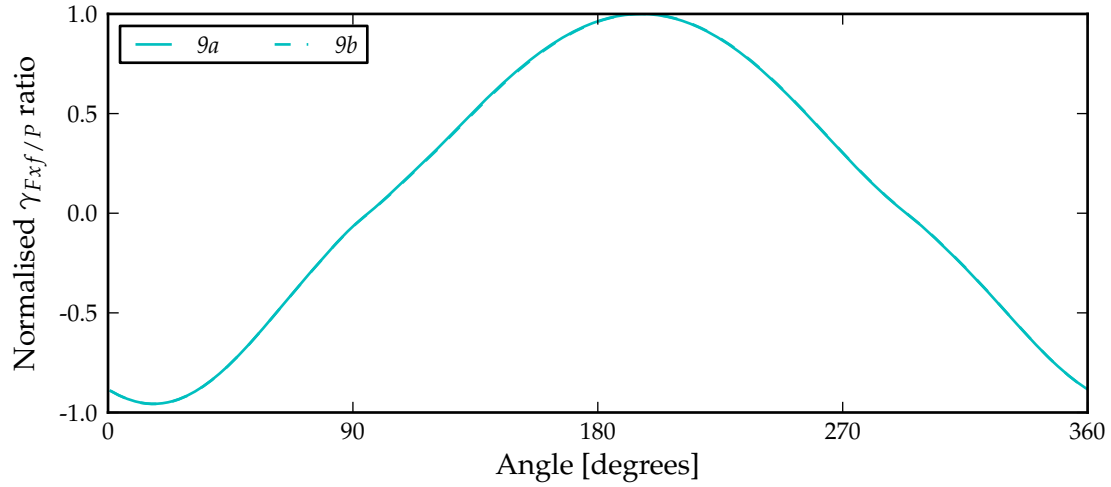

Figure 4.15: Normalised candidate $\gamma_{Fxf/P}$ dynamic responses for the displacer obtained from the top fifty dynamic responses with $\Gamma_{Fxf/P}$ ratios equal to or below the 100% specification level.

The two responses *9a* and *9b* are shown to be very similar. These responses are almost completely out of phase and are less sinusoidal than responses *2a* and *2b* in Figure 4.5.

Lastly, to verify that the candidate responses obtained from the analyses above would also be applicable to the extended range of variations, but with the influence of the bounce space void volume to swept volume ration excluded, the top fifty responses were again obtained for this reduced set of variations. The normalised dynamic responses that yielded the top fifty $\Gamma_{Fxf/P}$ ratios are shown in Figure 4.16 and the normalised dynamic responses that yielded the top fifty $\Gamma_{Fxf/P}$ ratios equal to or below the 90% specification level listed in Table 3.21 are shown in Figure 4.17. The $\Gamma_{Fxf/P}$ ratio varied from a maximum of 0,622 down to approximately

0,48 and from 0,316 down to 0,308 respectively. The normalised responses are shown here to compare with all of the candidate responses shown thus far.

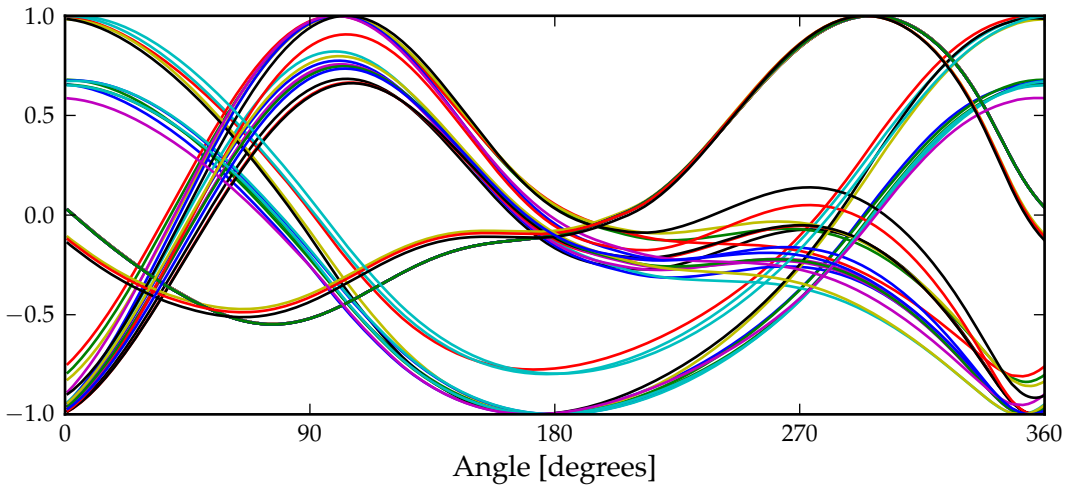

Figure 4.16: Normalised top fifty $\gamma_{Fxf/P}$ dynamic responses with $\Gamma_{Fxf/P}$ ratios equal to or below the 100% specification level for the displacer, excluding the influence of the bounce space void volume to swept volume ratio.

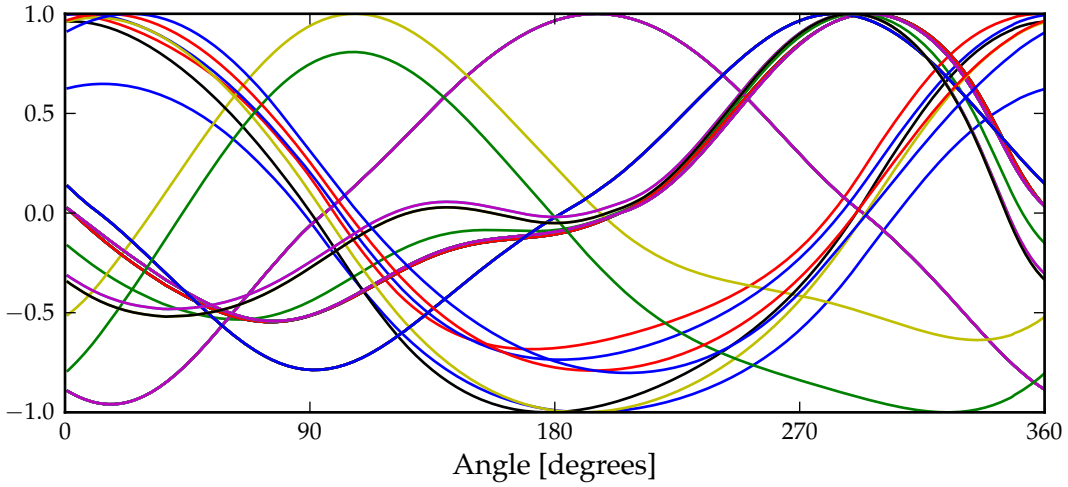

Figure 4.17: Normalised top fifty $\gamma_{Fxf/P}$ dynamic responses with $\Gamma_{Fxf/P}$ ratios equal to or below the 90% specification level for the displacer, excluding the influence of the bounce space void volume to swept volume ratio.

A quick comparison of the responses reveals that the candidate responses can represent the responses in Figures 4.16 and 4.17 as well.

Summary: Representative dynamic responses for the displacer linear machine

Up to eighteen different candidate responses have been identified. It is however not desirable to have this many responses. In the last part of this section, an effort will now be made to reduce the number of candidate responses to those suitable to represent most other responses. This requires further in depth study, and the choice of responses below should therefore be seen as a first effort.

It does seem that the different responses that originate from sinusoidal displacement in Figures 4.5 and 4.8 could be represented by a single response, since the responses themselves are fairly sinusoidal. The responses as well as a representative response could therefore be approximated by a sinusoidal response. What is necessary however is that the positive maximum of such a representative response as well as the phase shift with respect to the displacement should be adjustable. This should be fairly easy to set-up mathematically, with the maximum positive value ranging between approximately 0,5 up to nearly 1,0 and the responses lagging the displacements by between approximately 30 degrees up to approximately 65 degrees. It is expected that linear machines will generally perform worse for force responses that require maximum force closer to the limits of displacement. A phase shift closer to 30 degrees should therefore be considered.

The responses *9a* and *9b* shown in Figure 4.15 could also be approximated by a sinusoidal response, but the particular response is also seen in Figure 4.17 and it is recommended that this response is retained as is. Since fewer of these responses are seen amongst the responses with higher $\Gamma_{Fxf/P}$ ratios, it is proposed that if this response is used, then this response should be scaled by the 90% value of Table 3.20 or Table 3.21.

From the responses that originate from composite displacement, either response *7a* or *8a* could serve as the representative for linear machines operating on average as motors. The variation between these responses is fairly small. Responses *1a* or *3b* should be suitable to represent the responses where the linear machines will be operating on average as generators. Response *3b* especially represents the dynamics seen in Figures 4.7 and 4.17. The responses that originate from composite displacement also have high $\Gamma_{dF/Ff}$ ratios (between the 90% and 100% values) and will therefore be well suited for investigations where higher rate of change of force might have an influence on linear machine performance.

The remaining responses can be discarded, since both motor and generator operation are represented for both near sinusoidal and non-sinusoidal responses.

With consideration of the discussion above, the final group of responses to represent the $\gamma_{Fxf/P}$ dynamic response is shown in Figure 4.18.

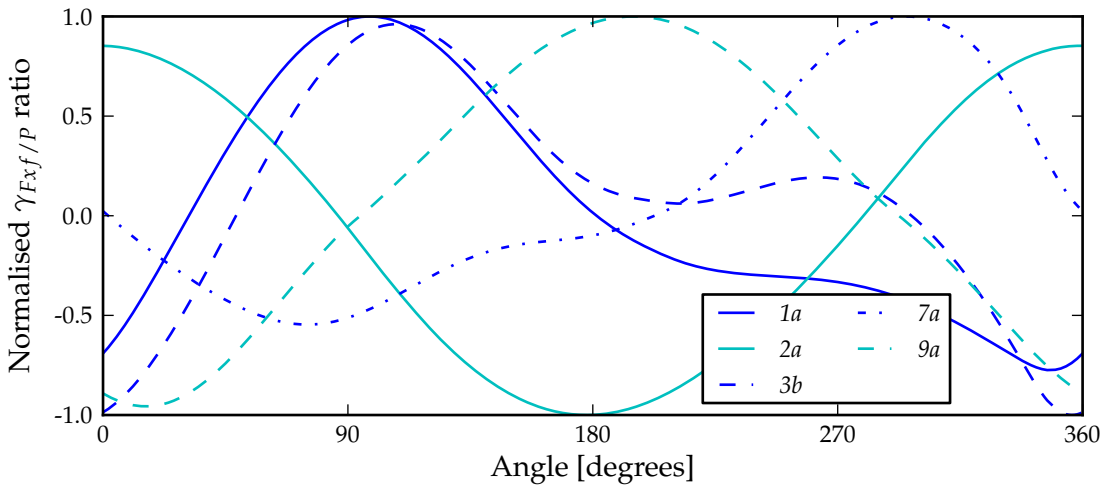

Figure 4.18: Final group of responses to represent the $\gamma_{Fxf/P}$ dynamic response.

Responses *2a* and *9a* are shown to represent near sinusoidal responses for both motor and generator operation. These responses may be approximated by purely sinusoidal responses of which the phase shift with respect to the displacement could be shifted as indicated before. Both responses *1a* and *3b* were chosen to represent non-sinusoidal responses for generator operation due to a lack of experience. In future, one may of them be chosen for this purpose.

4.4.3 Power piston

The treatment of the power piston dynamic responses will be less complicated than for the displacer, since the phenomenon of both negative or positive average output power primarily as a result of the displacer rod area percentage is not found for the power piston.

Figure 4.19 shows the $\gamma_{Fxf/P}$ dynamic responses that yielded the top fifty $\Gamma_{Fxf/P}$ ratios for the extended range of variations (including the influence of the bounce space void volume to swept volume ratio). For these responses, the $\Gamma_{Fxf/P}$ ratio varied from the maximum of 5,803 down to approximately 4,678. Two groups of responses can be identified, with one group originating from sinusoidal displacement and the other group from composite displacement. Figure 4.20 shows the normalised responses.

Figure 4.21 shows the resulting candidate responses determined as in the previous section, i.e. where two of the responses designated *1b* and *2b* were again chosen by choosing the dynamic response with the highest $\Gamma_{Fxf/P}$ ratio from each of the two groups of responses and where the other two responses designated *1a* and *2a* were again calculated according to the averaging approach. These responses are fairly similar to those shown in Figure 4.5.

To again determine the level to which these responses could be representative of all responses, the process above was repeated, but this time for the top fifty responses with $\Gamma_{Fxf/P}$ ratios equal to or below the 90% specification level listed in Table 3.20. These responses are shown in Figure 4.22. The $\Gamma_{Fxf/P}$ ratio varied from the maximum of 3,226 down to approximately 3,205. The normalised responses are shown in Figure 4.23. It is seen that most of the responses are fairly similar to those shown in Figure 4.20, except for a small minority of re-

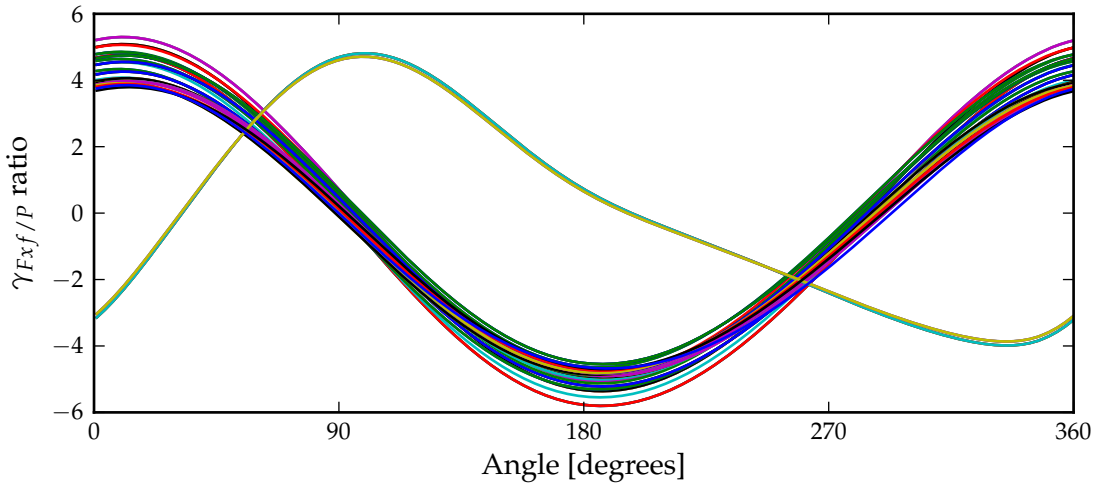

Figure 4.19: Top fifty $\gamma_{Fxf/P}$ dynamic responses with $\Gamma_{Fxf/P}$ ratios equal to or below the 100% specification level for the power piston.

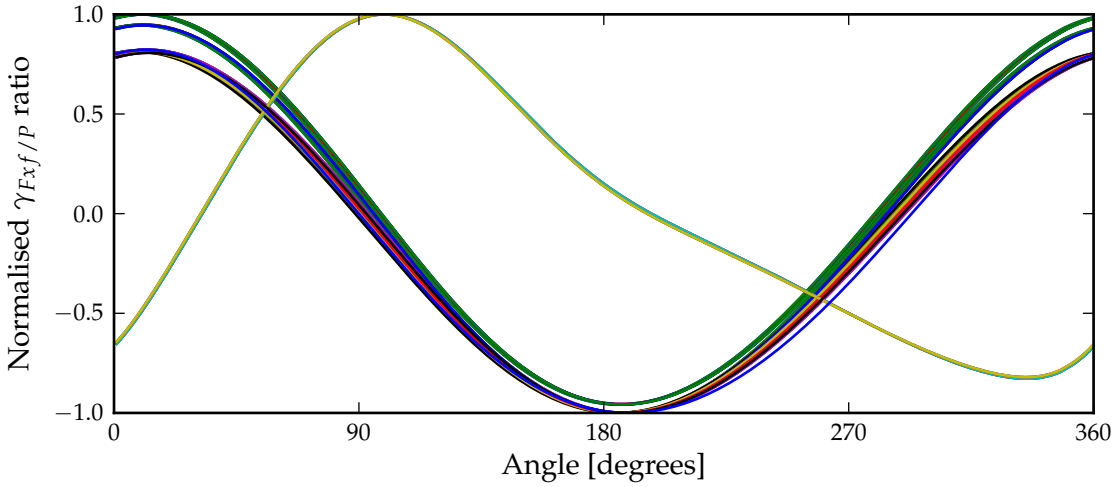

Figure 4.20: Normalised top fifty $\gamma_{Fxf/P}$ dynamic responses with $\Gamma_{Fxf/P}$ ratios equal to or below the 100% specification level for the power piston.

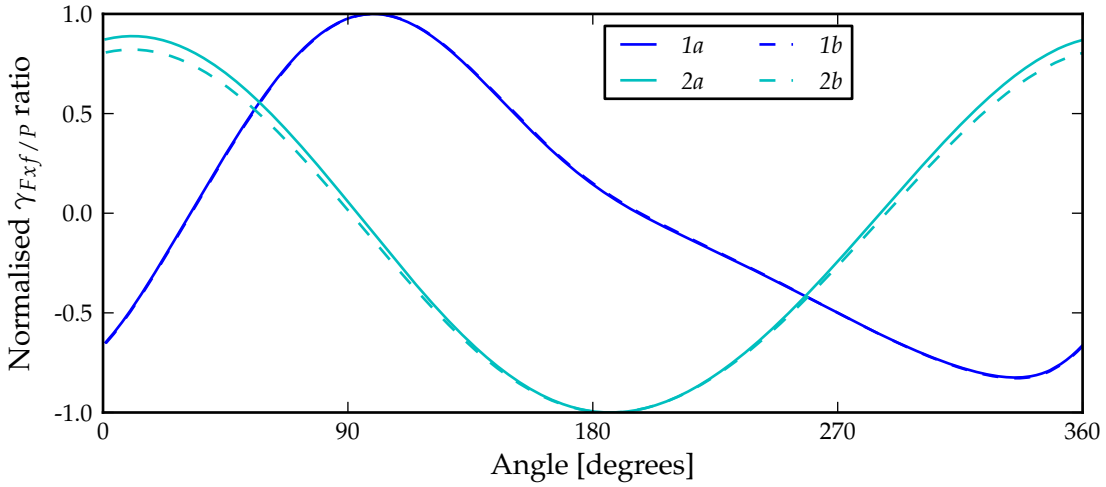

Figure 4.21: Normalised candidate $\gamma_{Fxf/P}$ dynamic responses for the power piston obtained from the top fifty dynamic responses with $\Gamma_{Fxf/P}$ ratios equal to or below the 100% specification level.

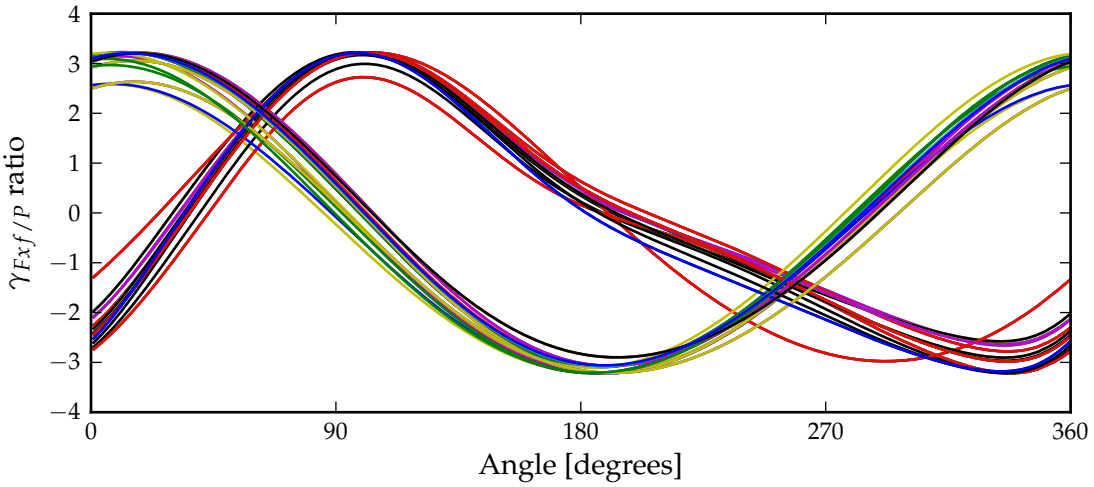

Figure 4.22: Top fifty $\gamma_{Fxf/P}$ dynamic responses with $\Gamma_{Fxf/P}$ ratios equal to or below the 90% specification level for the power piston.

sponses originating from composite displacement.

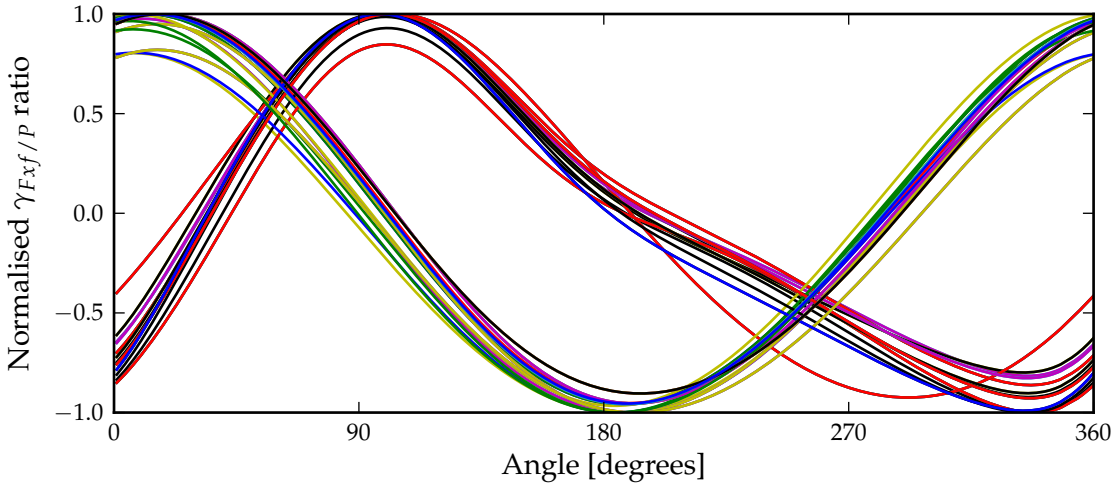

Figure 4.23: Normalised top fifty $\gamma_{Fxf/P}$ dynamic responses with $\Gamma_{Fxf/P}$ ratios equal to or below the 90% specification level for the power piston.

Figure 4.24 shows the resulting candidate responses, where a third group of responses (*4a* and *4b*) have now been added. The other two groups of responses closely resemble the responses shown in Figure 4.21, except that the responses in Figure 4.24 having slightly higher positive or alternatively negative peak values. More variation is also seen for the responses in Figure 4.23 than for those in Figure 4.20.

The displacements associated with the various candidate responses are shown in Figure 4.25 (responses and associated displacement are indicated by the same colour).

Lastly, to again verify that the candidate responses would also be applicable to the extended range of variations, but with the influence of the bounce space void volume to swept volume ration excluded, the top fifty responses were again obtained for this reduced set of variations. The normalised dynamic responses that yielded the top fifty $\Gamma_{Fxf/P}$ ratios are shown in Figure 4.26 and the normalised dynamic responses that yielded the top fifty $\Gamma_{Fxf/P}$ ratios equal to or

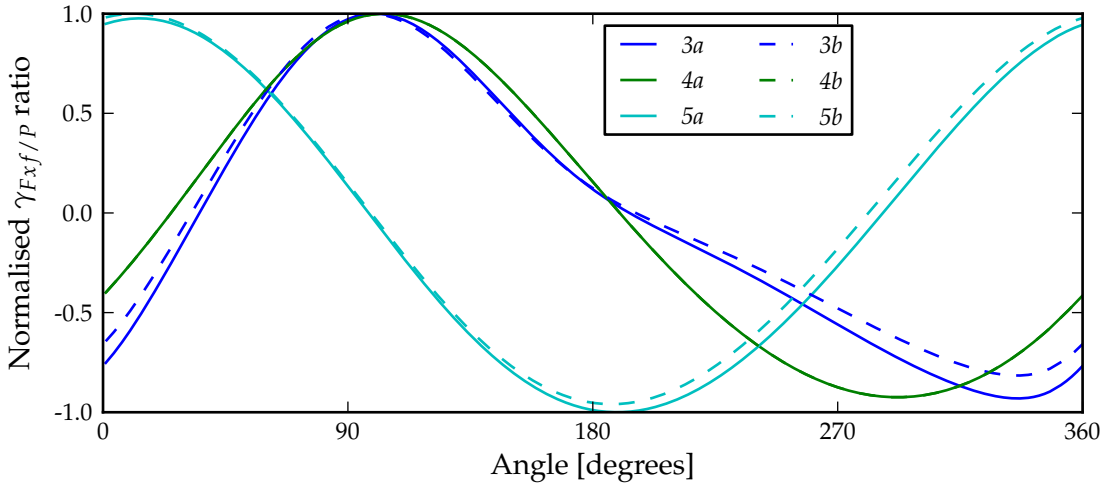

Figure 4.24: Normalised candidate $\gamma_{Fxf/P}$ dynamic responses for the power piston obtained from the top fifty dynamic responses with $\Gamma_{Fxf/P}$ ratios equal to or below the 90% specification level.

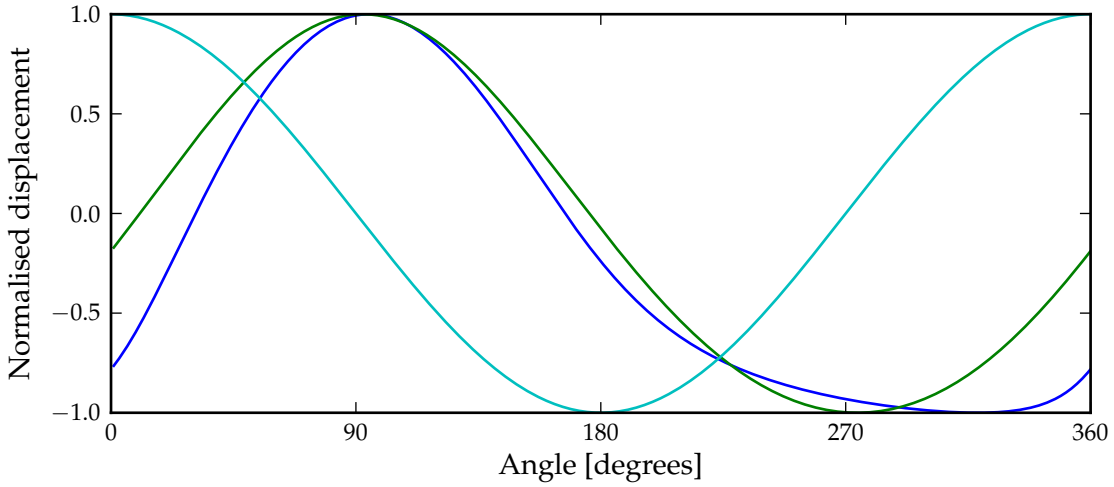

Figure 4.25: Normalised displacement associated with the candidate dynamic responses for the power piston.

below the 90% specification level listed in Table 3.21, are shown in Figure 4.27. The $\Gamma_{Fxf/P}$ ratio varied from a maximum of 3,523 down to approximately 3,085 and from 2,522 down to 2,481 respectively.

A quick comparison of the responses reveals that the candidate responses would be able to represent the responses in Figures 4.26 and 4.27 as well, with the only adjustment that could possibly be considered being the offset of the responses.

Summary: Representative dynamic responses for the power piston linear machine

Many fewer candidate responses have been identified for the power piston than for the displacer. It is also observed that the $\gamma_{Fxf/P}$ dynamic responses of the displacer are influenced more by the variations than are those of the power piston.

Figure 4.28 shows the final responses to represent the $\gamma_{Fxf/P}$ dynamic responses. From the ten responses identified as candidates, two responses are deemed to be sufficient. Response *1a*

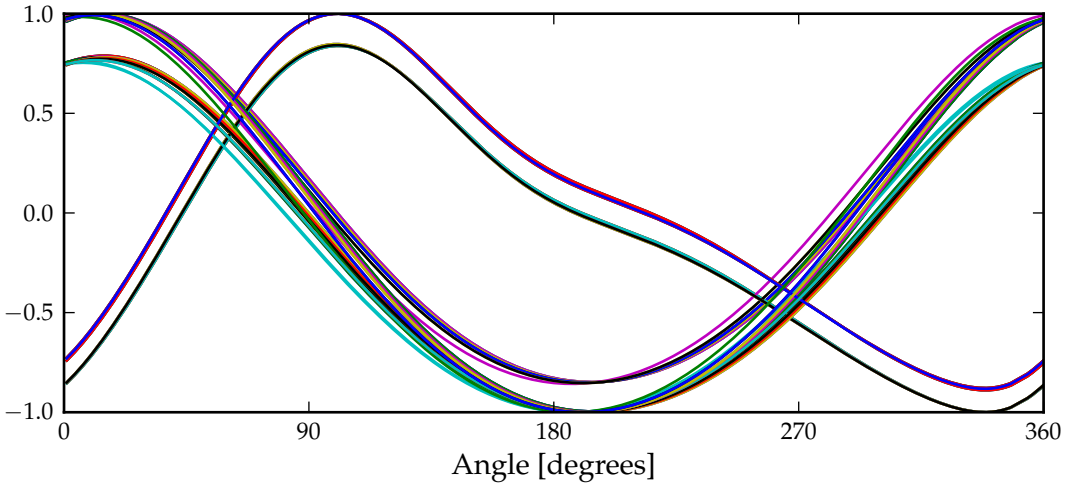

Figure 4.26: Normalised top fifty $\gamma_{Fxf/P}$ dynamic responses with $\Gamma_{Fxf/P}$ ratios equal to or below the 100% specification level for the displacer, excluding the influence of the bounce space void volume to swept volume ratio.

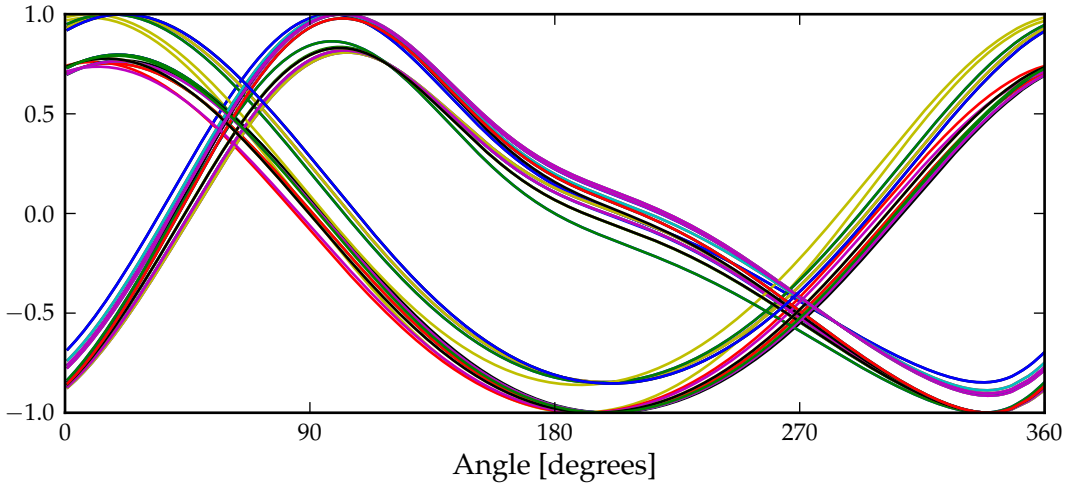

Figure 4.27: Normalised top fifty $\gamma_{Fxf/P}$ dynamic responses with $\Gamma_{Fxf/P}$ ratios equal to or below the 90% specification level for the displacer, excluding the influence of the bounce space void volume to swept volume ratio.

is sufficient to also represent responses *1b*, *3a* and *3b*. Response *2a* is sufficient to also represent responses *2b*, *5a* and *5b*. This is especially true if moderate adjustment of the responses is done in the y-axis, i.e. if the offsets of the normalised signals are altered. This can be done quite easily. If these responses are altered in this way, then the entire range of responses seen in Figures 4.20, 4.23, 4.26 and 4.27 could be represented. Response *1a* is also well suited for investigations where higher rate of change of force might have an influence on linear machine performance, with $\Gamma_{dF/Ff}$ ratios close to the 90% values as listed in Table 3.20.

Responses *4a* and *4b* may be discarded, since no new information is contained in these responses. If the dynamics of these responses are considered, then responses *4a* and *4b* are found in between the near sinusoidal response *2a* and the non-sinusoidal response *1a*. When comparing the phase shift of responses *4a* and *4b*, they are seen to be approximately the same as response *2a* with respect to the relevant displacement (refer again Figure 4.25).

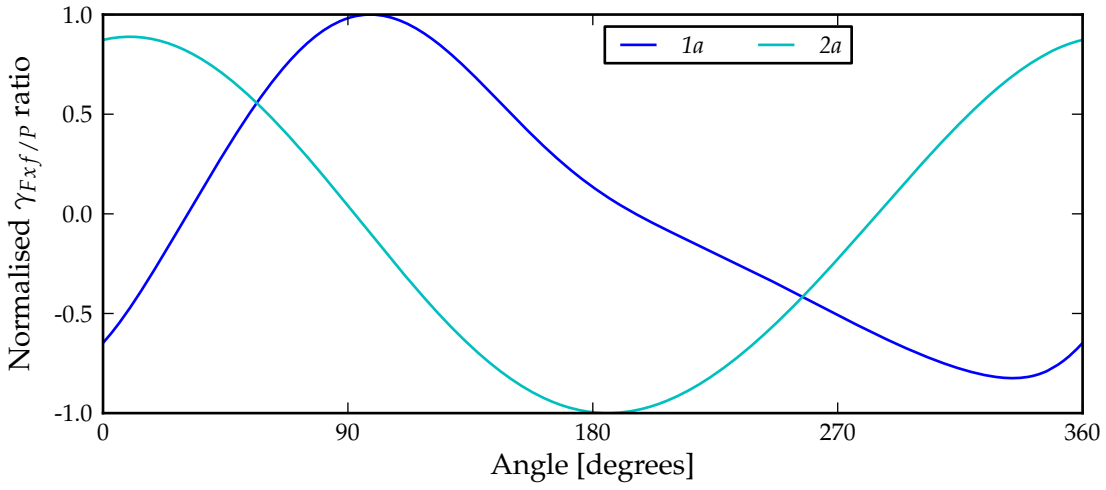

Figure 4.28: Final group of responses to represent the $\gamma_{Fxf/P}$ dynamic response.

4.4.4 Combined displacer and power piston optimisation

The combined optimisation of displacer and power piston linear machines has been discussed in the last part of section 4.3.2. Several advantages have been mentioned, e.g. the ability to calculate the overall efficiency and to optimise the overall mass of the machines. The final representative responses shown in Figures 4.18 and 4.28 were the last inputs necessary to separately optimise the displacer linear machine or power piston linear machine, but dynamic responses necessary to perform combined optimisation are still lacking. It is now necessary to consider the appropriate choice of dynamic responses to perform combined optimisation.

A quick solution would be to merely choose a few combinations from the final representative responses shown in the two previous sections, say by combining responses that originate from composite displacement or sinusoidal displacement. The question is whether this will be appropriate, i.e. will the combined responses represent what could be expected in free-piston Stirling engines in reality? Surely, a mere random combination of responses could lead to a misrepresentation of the dynamics found in free-piston Stirling engines.

Analyses were performed to determine combinations of dynamic responses where both the displacer and power piston have high $\Gamma_{Fxf/P}$ ratios. If combinations are chosen where both $\Gamma_{Fxf/P}$ ratios are high, then the linear machines that are simultaneously optimised, will be able to perform displacement control for the majority of variation combinations, while maintaining a sense of practical reality.

The analyses were done by again obtaining the $\gamma_{Fxf/P}$ dynamic responses with the highest $\Gamma_{Fxf/P}$ ratios equal to or below a specification level for one of the pistons (i.e. either the power piston or the displacer) from the extended range of variations as before, but this time subject to the $\Gamma_{Fxf/P}$ ratio of the accompanying $\gamma_{Fxf/P}$ dynamic response of the other piston being within a certain percentage of its own corresponding specification level. The goal was therefore to determine response combinations where the $\Gamma_{Fxf/P}$ ratios of these responses are both close to the 100% or 90% specification levels for the respective pistons.

No combinations exist where both the $\gamma_{Fxf/P}$ dynamic responses have $\Gamma_{Fxf/P}$ ratios close to the 100% specification level. The $\Gamma_{Fxf/P}$ ratios were therefore allowed to be as low as 60% of the 100% specification levels, i.e. as low as 0,5226 and 3,4818 for the displacer and the power piston respectively. A total of 30 combinations were found where both the $\Gamma_{Fxf/P}$ ratios were at least equal to or greater than these levels. Figure 4.30 shows the responses of the power piston with $\Gamma_{Fxf/P}$ ratios between 5,803 and 3,4818, subject to the displacer $\Gamma_{Fxf/P}$ ratio being at least 60% of its own 100% specification level, i.e. to be equal to or more than 0,5226. Figure 4.29 shows the corresponding displacer responses.

A second analysis was performed, but this time with the $\Gamma_{Fxf/P}$ ratios for both the displacer and the power piston limited to be less than or equal to the respective 90% specification levels, but not lower than 90% of these levels. A total of 48 combinations were found. Figure 4.32 shows the responses of the power piston with $\Gamma_{Fxf/P}$ ratios between 3,227 and 2,904, subject to the displacer $\Gamma_{Fxf/P}$ ratios being between 0,348 and 0,3132. Figure 4.31 shows the corresponding displacer responses.

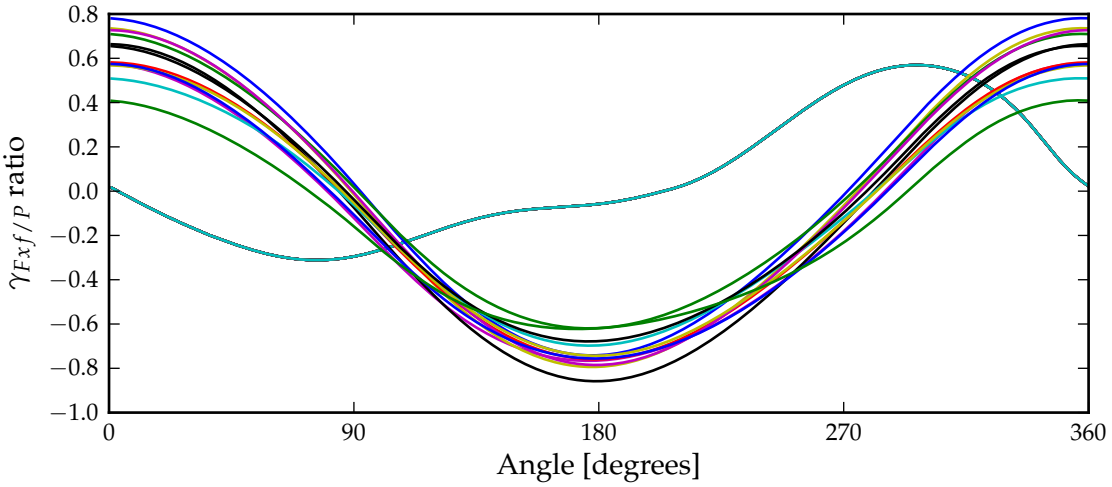

Figure 4.29: $\gamma_{Fxf/P}$ dynamic responses for the displacer, with the displacer and power piston $\Gamma_{Fxf/P}$ ratios equal to at least 0,5226 and 3,4818 respectively.

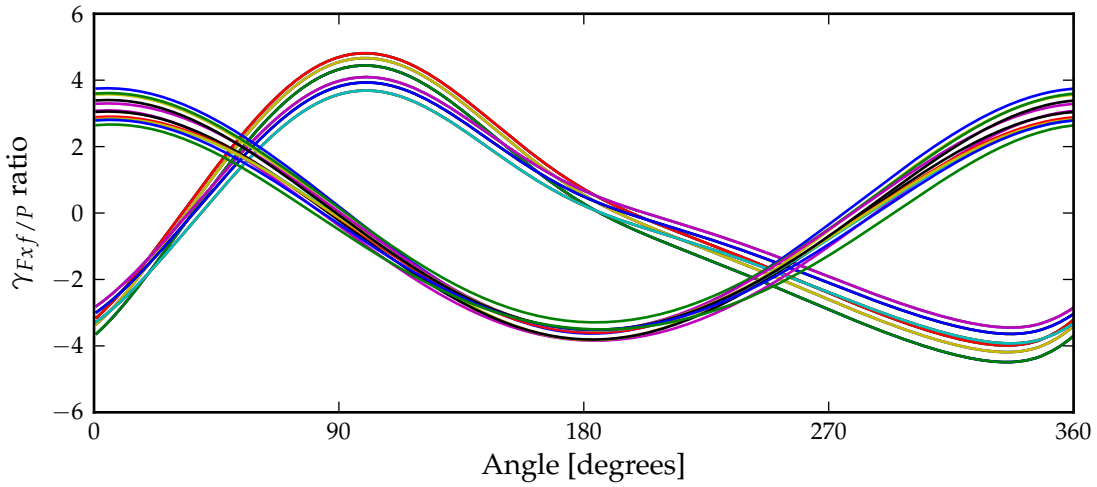

Figure 4.30: $\gamma_{Fxf/P}$ dynamic responses for the power piston, with the displacer and power piston $\Gamma_{Fxf/P}$ ratios equal to at least 0,5226 and 3,4818 respectively.

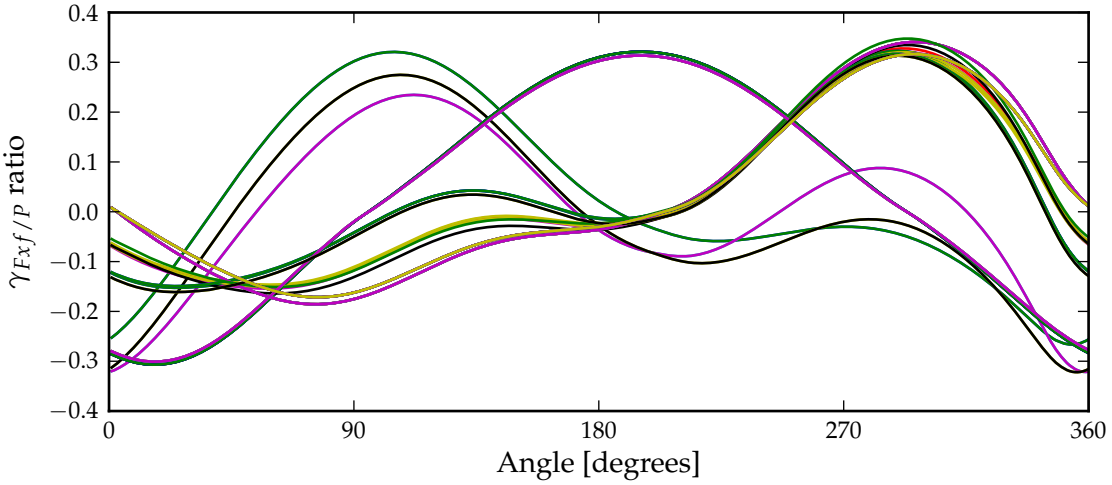

Figure 4.31: $\gamma_{Fxf/P}$ dynamic responses for the displacer, with the displacer and power piston $\Gamma_{Fxf/P}$ ratios between 0,348 and 0,3132 and between 3,227 and 2,904 respectively.

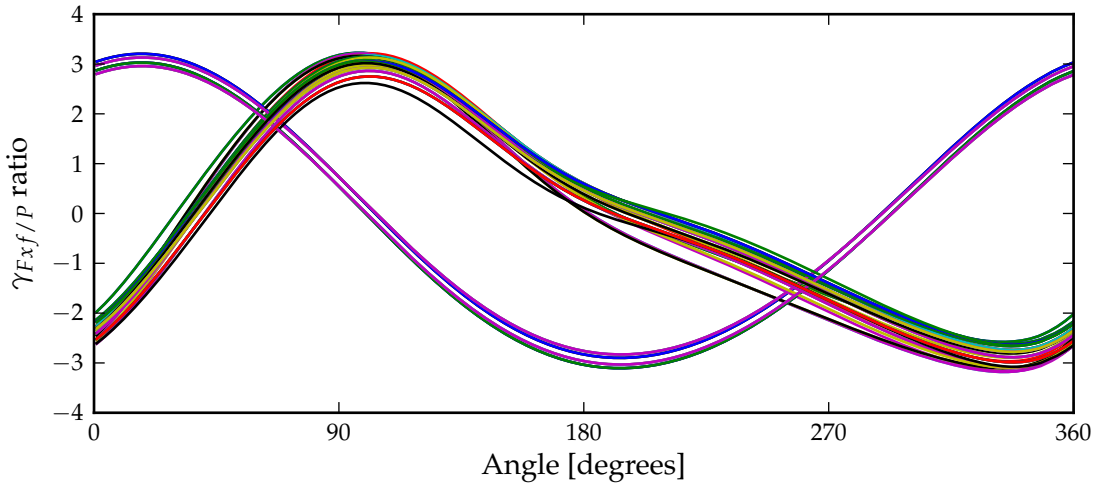

Figure 4.32: $\gamma_{Fxf/P}$ dynamic responses for the power piston, with the displacer and power piston $\Gamma_{Fxf/P}$ ratios between 0,348 and 0,3132 and between 3,227 and 2,904 respectively.

The response combinations shown in Figures 4.29 and 4.30 show a number of combinations of the type represented by response *2a* in Figure 4.18 for the displacer and of the type represented by response *2a* in Figure 4.28 for the power piston. These combinations originate from sinusoidal displacement and a large displacer rod diameter percentage as indicated before. For purposes of discussion, this combination of representative responses will be referred to as *2a-2a*, where the first *2a* refers to the displacer response and the second *2a* to the power piston response. A number of responses can be represented by response *7a* in Figure 4.18 for the displacer and response *1a* in Figure 4.28 for the power piston, i.e. representative combination *7a-1a*.

By consideration of the responses shown in Figures 4.29 and 4.30, a difficulty in applying the representative combinations *2a-2a* and *7a-1a* was identified. This difficulty arises from a lack of combinations where both displacer and power piston $\gamma_{Fxf/P}$ dynamic responses have $\Gamma_{Fxf/P}$ ratios close to the 100% specification level.

In order to rescale the normalised response combinations (i.e. *2a-2a* and *7a-1a*), one cannot merely use the respective 100% specifications levels, since such combinations do not exist in the combinations for the extended range of variations:

- For the responses that would be represented by the *2a-2a* combination, the $\Gamma_{Fxf/P}$ ratios for the displacer varied from approximately 0,859 down to 0,622, which is approximately 99% down to 71% of the 100% specification level of 0,871. The corresponding $\Gamma_{Fxf/P}$ ratios for the power piston varied between approximately 3,843 down to 3,503, which is approximately 66% down to 60% (the lowest level included in this analysis) of the 100% specification level of 5,803.

- For the responses that would be represented by the *7a-1a* combination, the $\Gamma_{Fxf/P}$ ratios for the displacer varied around approximately 0,57, which is approximately 65% of the 100% specification level of 0,871. The corresponding $\Gamma_{Fxf/P}$ ratios for the power piston varied between approximately 4,812 down to 3,93, which is approximately 83% down to 67% of the 100% specification level of 5,803.

Where the *2a-2a* combinations had higher $\Gamma_{Fxf/P}$ ratios for the displacer, the *7a-1a* had higher $\Gamma_{Fxf/P}$ ratios for the power piston. The percentages provided above could be used to better calibrate the rescaling of the responses, but extreme care should always be taken when trying to simultaneously optimise linear machines using the 100% specification levels.

In contrast, realistic combinations can be found more easily for the 90% specification level. A quick inspection yielded the following representative combinations, namely *9a-2a*, *3b-1a* and *7a-1a*. Two new combinations were identified, while the *2a-2a* combination does not exist. These combinations can be rescaled easily using the 90% specification levels, while still maintaining a good level of reality, since the $\Gamma_{Fxf/P}$ ratios are still within 10% of the 90% specification levels for both the displacer and the power piston.

The analyses with the responses shown in Figures 4.29 to 4.32, were repeated for the extended range of variations, but this time excluding the bounce space void volume to swept volume ratio variation, i.e. for the data shown in Table 3.21.

A total of 7 combinations were found where both the $\Gamma_{Fxf/P}$ ratios were at least within 10% of the 100% specification levels. Figure 4.34 shows the responses of the power piston with $\Gamma_{Fxf/P}$ ratios equal to at least 3,173, and Figure 4.33 shows the corresponding displacer responses with $\Gamma_{Fxf/P}$ ratios equal to at least 0,56.

A total of 45 combinations were found with the $\Gamma_{Fxf/P}$ ratios for both the displacer and the power piston limited to be less than or equal to the respective 90% specification levels, but not lower than 90% of these levels. Figure 4.36 shows the responses of the power piston with $\Gamma_{Fxf/P}$ ratios between 2,522 down to 2,27 and Figure 4.35 shows the corresponding displacer responses with $\Gamma_{Fxf/P}$ ratios between 0,316 down to 0,284.

Representative combinations were again identified from these analyses. From Figures 4.33 and 4.34, the combinations *2a-2a* and *7a-1a* can be identified again, although the response originating from sinusoidal displacement in Figure 4.33 is not represented very well by response *2a* from Figure 4.18.

From Figures 4.35 and 4.36, the combinations *9a-2a* and *7a-1a* can be identified again. In

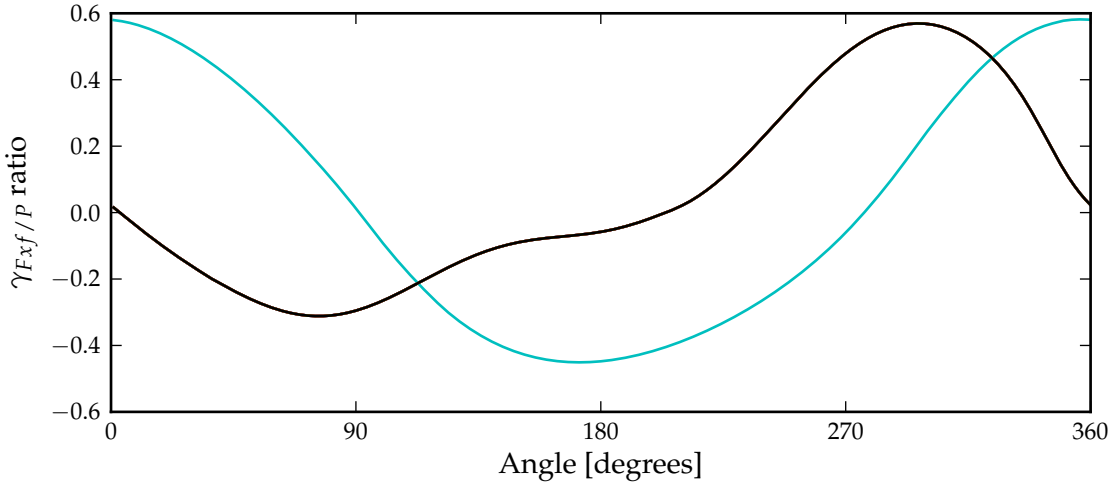

Figure 4.33: $\gamma_{Fxf/P}$ dynamic responses for the displacer, with the displacer and power piston $\Gamma_{Fxf/P}$ ratios equal to at least 0,56 and 3,173 respectively.

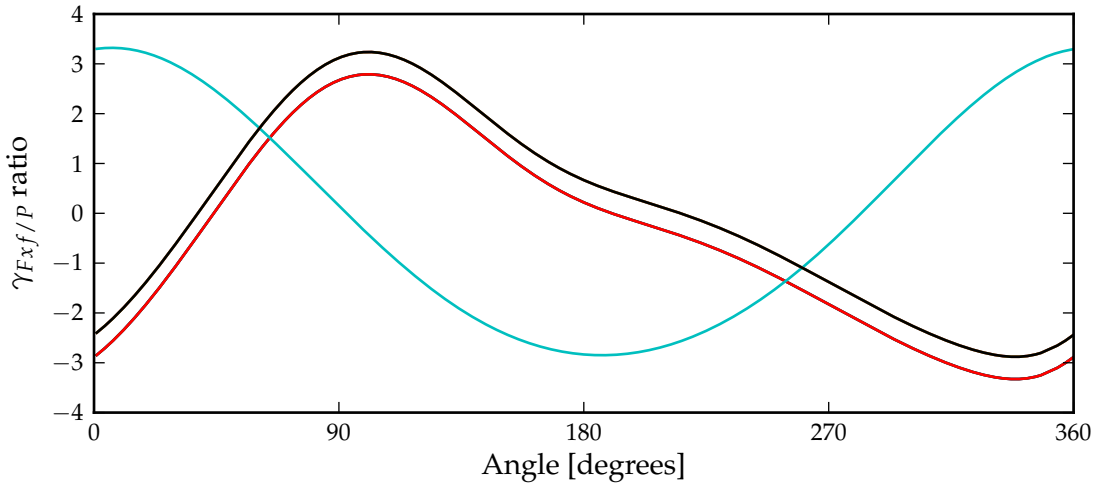

Figure 4.34: $\gamma_{Fxf/P}$ dynamic responses for the power piston, with the displacer and power piston $\Gamma_{Fxf/P}$ ratios equal to at least 0,56 and 3,173 respectively.

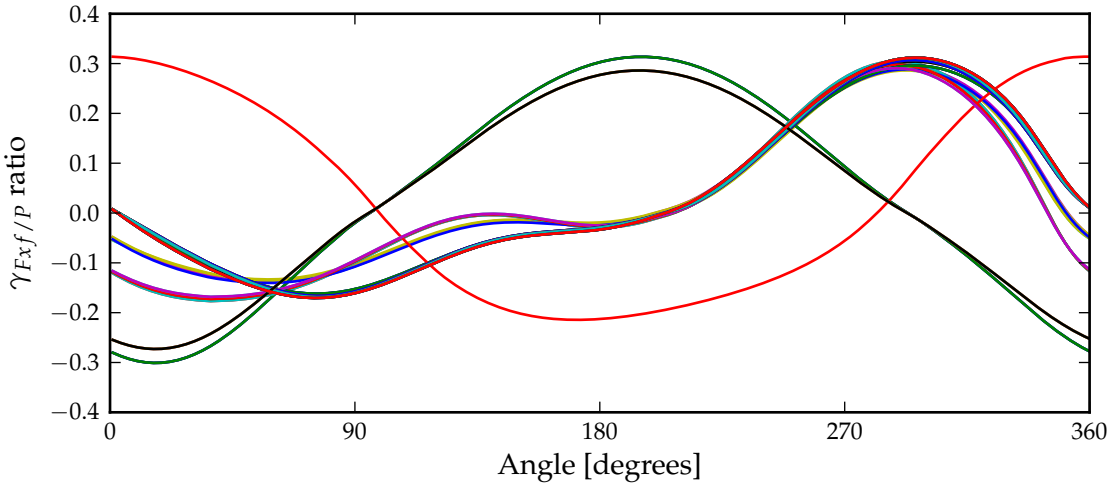

Figure 4.35: $\gamma_{Fxf/P}$ dynamic responses for the displacer, with the displacer and power piston $\Gamma_{Fxf/P}$ ratios between 0,316 and 0,284 and between 2,522 and 2,27 respectively.

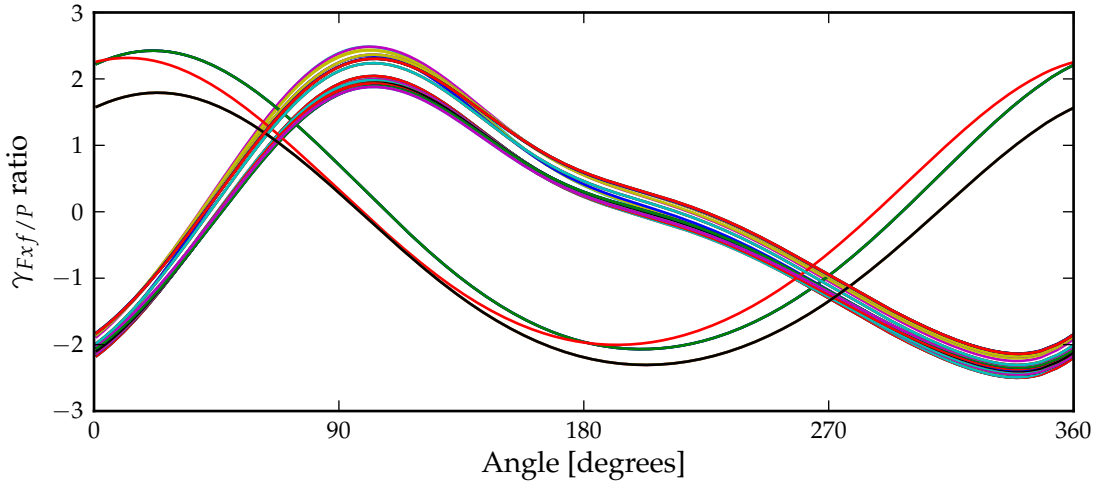

Figure 4.36: $\gamma_{Fxf/P}$ dynamic responses for the power piston, with the displacer and power piston $\Gamma_{Fxf/P}$ ratios between 0,316 and 0,284 and between 2,522 and 2,27 respectively.

this case however, the combination *9a-1a* is not found, but rather again the combination *2a-2a* (the response originating from sinusoidal displacement in Figure 4.35 is represented even less accurately by response *2a*).

The difficulty concerning representative responses for the 100% specification levels identified earlier does not exist for the extended variations excluding the influence of the bounce space void volume to swept volume ratio. Although only a few, combinations do exist where both the $\Gamma_{Fxf/P}$ ratios are close to the 100% specification level.

This concludes the investigation into combined responses.

4.5 Conclusion

In this chapter there was a discussion of a design optimisation approach to linear electrical machines for direct piston displacement control, firstly by establishing an appropriate optimisation routine and secondly by finalising the application of the specifications developed in Chapter 3. During this second part, specific attention was given to obtaining dynamic responses that could represent most of the dynamic responses having high $\Gamma_{Fxf/P}$ ratios. This enables optimisation of the linear machines using dynamic responses that would generally be found in free-piston Stirling engines.

Finally, design optimisation as discussed in this chapter does not seek to optimise linear machines for specific free-piston Stirling engines, but to optimise linear machines for application in general for free-piston Stirling engines where the variation limits given in Chapter 3 are adhered to. It should also be remembered that the representative responses are approximations of the vast majority of dynamic responses with high $\Gamma_{Fxf/P}$ ratios and therefore not the responses that will be found in a specific engine under specific conditions. This does not mean that the optimisation routine cannot be applied to the optimisation of linear machines for specific engines. In such cases however, dynamic responses should be obtained that are specifically suited for the specific free-piston engines.

To conclude, an optimisation framework now exists with which the suitability of linear machine topologies can be evaluated and compared and most importantly with which the question whether direct piston displacement control is at all possible, can be answered. In Chapter 5, a linear machine topology will be evaluated in an effort to answer this question. This will then also be a good opportunity to illustrate the application of the representative responses.

Chapter 5

Evaluation of a tubular air-core longitudinal flux linear electrical machine

5.1 Introduction

The question whether direct piston displacement control is at all possible has not been answered yet, but the contributions in Chapters 3 and 4 now make it possible to evaluate linear machine topologies as possible candidates.

A very wide variety of linear machines have been proposed and/or have been used in free-piston Stirling engines before. It is not the goal in this chapter to compare the suitability of these linear machines, but rather to establish whether a particular machine topology - an air-core longitudinal flux permanent magnet linear machine - is suitable for displacement control.

The vast majority of the linear machines that were used or that were proposed before have tubular structured topologies with iron cores [e.g. 5, 27, 42–45, 48, 49, 53–56]. Flat structured topologies are ignored, due to torsional and lateral force issues that are more prominent in these machines than in tubular structured machines. Also there are no end winding effects in longitudinal flux tubular structured machines.

Mainly two groups can be distinguished, namely longitudinal flux and transverse flux linear machines. The longitudinal flux machines suffer from a disadvantage, namely that laminations should be wedge-shaped. This is a result of the flux being in the direction of movement. This complexity of the laminations is acknowledged by Boldea and Nasar [55].

Transverse flux machines on the other hand have flat laminations, since the flux direction is in a plane perpendicular to the direction of movement. To manufacture these machines is therefore less complicated than to manufacture their longitudinal counterparts. This is however highly dependent on the particular transverse flux topology. A family of transverse flux machines have been under investigation recently as part of an ongoing effort to develop linear

machines for free-piston Stirling engines that will yield good performance, while being robust and easy to manufacture [46, 50, 51]. Good improvements have been made, but it was felt that further improvements need to be made before these topologies can be considered for piston displacement control.

Iron-core machines also suffer from reluctance forces. Reluctance forces act in a similar way to spring forces, but with the difference of normally being nonlinear as a function of displacement. The presence of reluctance forces could be an advantage or a disadvantage in piston displacement control. This can however only be determined for a specific topology during design optimisation.

One other family of linear machines remains, namely tubular air-core longitudinal flux machines. These machines do not suffer from the disadvantage of having wedge-shaped laminations. In addition, they have very low series inductance that enables effective control of the current. There are also no reluctance forces, nor any lateral attraction forces present. They may however have poor power-to-weight ratios when compared to other topologies. Nevertheless, these machines are considered to be good candidates for piston displacement control, and were therefore chosen as the family of topologies that will be evaluated.

In section 5.2, an overview of the air-core longitudinal flux topologies is presented. The results of design optimisation are then presented in section 5.3 for the traditional approach to linear machine optimisation to serve as a benchmark for subsequent design optimisation results. Design optimisation results for direct piston displacement control are then presented in section 5.4 for the displacer and in section 5.5 for the power piston. Final conclusions are presented in section 5.6.

5.2 A longitudinal flux air-core topology

5.2.1 Description

Figure 5.1 shows a *single phase*, tubular, dual airgap, air-core longitudinal flux linear machine with surface mount permanent magnets (LFPM - longitudinal flux permanent magnet). One half of the topology as seen in an axial direction, is shown to the right, with a side view to the left of the cross section, as indicated.

The coils or alternatively the yokes with the magnets could be moving members. For this investigation, a moving coil arrangement is preferred, since the mass of the coils should normally be less than the combined mass of the iron yokes and magnets. One challenge with moving coil type linear machines is how to transfer the current to the moving coils, but this can be solved fairly easily by utilising the same flexure bearings with which the mover is held in place. Some or all of the flexures are then electrically isolated for this purpose at both sides where they are connected to the mover and to the engine body. Flexures made of beryllium copper should be ideal for this purpose.

The LFPM linear machine has two iron cylinders or yokes on which the magnets are mounted. The magnets are also cylindrical and are radially magnetised. In practice, the magnet cylin-

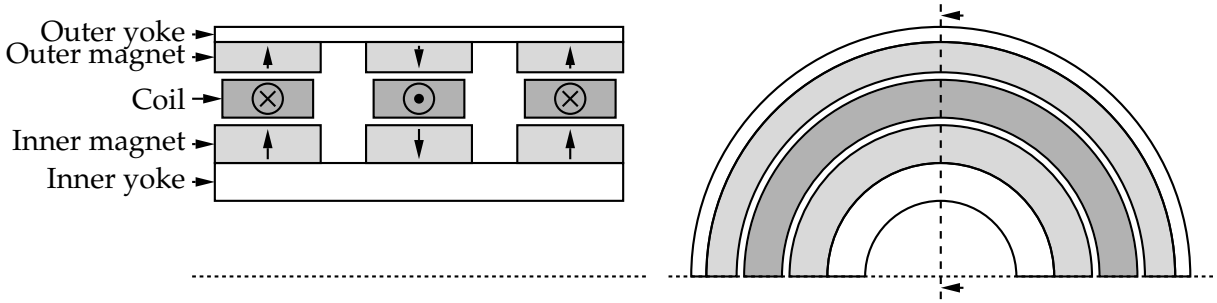

Figure 5.1: A tubular, dual airgap, air-core, longitudinal flux linear machine with surface mount permanent magnets.

ders may consist of several pieces that may be fixed separately to the iron yokes. In a tubular topology such as this one, the thickness of the inner yoke and magnets will differ from that of the outer yoke and magnets to avoid a higher concentration of flux, e.g. the inner yoke will be thicker than the outer yoke. Optimisation algorithms should therefore be allowed to separately optimise the thickness of the yokes, as well as of the magnets.

In the treatment of this machine, each magnet pair will be referred to as a *pole pair*. In Figure 5.1 for example, the machine is shown with three pole pairs. This is not completely equivalent to the use of the term *pole pair* in rotary machines. The number of pole pairs in rotary machines indicates amongst others, the amount of electrical cycles for every mechanical cycle. This is not the case for this machine. The LFPM linear machine may have two or more pole pairs, but since the stroke length will not be allowed to be more than approximately the pole pitch (the distance between adjacent pole pairs), and since this is a single phase machine, there will be one electrical cycle for each mechanical cycle. This choice is the simplest arrangement in order to obtain a fairly flat force profile per unit current over the entire stroke length. More complex machines, such as multiphase machines, may be considered in future.

5.2.2 Properties

No evidence could be found that the LFPM topology presented here has been investigated or applied to free-piston Stirling engines or to other short stroke applications before. Several slotless linear machines have however been reported in literature [e.g. 57, 58]. Most of these slotless topologies have the copper coils wound immediately inside a back iron yoke as is the case for slotted machines. An inner tubular permanent magnet arrangement then serves as the mover. With no variation in reluctance paths found, these slotless machines do not suffer from reluctance forces. In most of the topologies, the permanent magnets however move with respect to the iron yokes and will therefore cause flux variation in the yokes. This will lead to losses due to magnetic hysteresis and eddy currents in the iron yokes.

While no evidence could be found that the LFPM topology has been investigated before, direct equivalent rotary machines do exist and have been described and analysed in detail. One such equivalent machine is known as an axial flux permanent magnet (AFPM) machine. AFPM machines are also referred to as disk-type machines [59]. Wang [60] investigated design aspects and optimisation of an ironless stator variant with a double-sided rotor, i.e. the copper windings in the middle are stationary and the iron yokes with surface-mounted magnets rotate

on both sides of the windings.

Randewijk [61] investigated an air-core radial flux permanent magnet (RFPM) machine with double-sided rotor. This machine differs from the AFPM machine of Wang in that the copper windings are cylindrically arranged with the yokes and surface-mounted magnets forming an inner and outer cylinder at both sides of the copper windings. Again the copper windings are stationary and the inner and outer iron yokes with the magnets both rotate. While this radial flux machine addresses amongst others deflection issues found with the axial flux machines due to the strong magnetic attraction forces, the surface mount topology shown in Figure 5.1 can be seen as electromagnetically directly equivalent to both these AFPM and RFPM machines, since both machines consist of ironless copper windings with permanent magnets fixed to iron yokes on both sides of the windings. The LFPM topology presented here will therefore share some of the important properties of the engines investigated by Wang and Randewijk.

The following is a summary of the properties relevant to this investigation [60, 61]:

- Losses in the iron yokes and permanent magnets associated with flux variation have been ignored by both Wang and Randewijk. This is a good approximation where little flux variation is produced in the iron yokes and permanent magnets by the current in the copper windings (also known as armature reaction).
- Only conduction losses in the copper windings were considered. Mainly two copper loss components exist in these air-core machines:
  - The first and major component is the normal conduction losses due to the flow of useful current, i.e. current flowing to a load (generator operation) or from a source (motor operation).
  - The second component is conduction losses due to eddy currents induced in the parallel strands of stranded conductors. This is a consequence of magnetic flux cutting through the copper conductors in air-core machines. Unless completely balanced induced EMF is achieved for each of the conduction paths, circulating eddy currents may occur. Wang showed experimentally that with the use of proper twisted stranded conductors - or with the use of Litz wire - this loss component can be minimised to such an extend that it can be ignored.
- The power-to-weight and power-to-volume ratios of the air-core AFPM and RFPM machines reportedly compare well with traditional radial flux machines. This is in part due to the AFPM and RFPM machines investigated by Wang and Randewijk having multiple poles compared to two or four poles normally found in traditional radial flux machines. For the same rotational speed, the air-core machines therefore have a much higher rate of change of flux and therefore a higher EMF per winding than their radial flux counterparts, even though the flux density may be less due to the machines being air-core. This high frequency operation is not desirable in iron-core machines, due to excessive core losses. It is however uncertain how this applies to the linear machine topology presented here, given the particular application.

- With only conduction losses in the copper windings present and the high frequency advantage highlighted above, these machines can have very good efficiencies.
- Both the AFPM and RFPM machines have no cogging torque, nor any magnetic pull between the stator and the rotor. The former is important, since cogging forces - or reluctance forces - could be a serious disadvantage to direct piston displacement control. The latter is important, since this means that in an engine where strict dimensional tolerances apply, no lateral forces will be exerted on the mover.
- The low inductance property of these air-core machines has been highlighted. Low inductance in this application of direct piston displacement control is an advantage due to the relative ease, compared to iron core machines, of quickly forcing the current.

5.2.3 Simulation

For this investigation, the LFPM linear machine was simulated by finite element analysis (FEA). It is beyond the scope of this investigation to develop an analytical model for the machine, nor is it necessary.

Wang [60] also took the finite element analysis approach and showed by comparing simulated results with experimental data, that this type of air-core machine can be simulated quite accurately. Randewijk [61] developed an analytical model of the air-core RFPM machine that he investigated and again showed good correlation between finite element analysis results and results from his analytical model.

The LFPM linear machine presented here has the advantage of no end winding effects as is the case for both the AFPM and RFPM machines investigated by Wang and Randewijk - the windings in the LFPM linear machine are cylindrical coils and as such the entire coil moves through the magnetic field in the airgap. This holds the advantage that the LFPM linear machine can be simulated accurately by two-dimensional (2D) finite element analysis. The LFPM linear machine however suffers from another end effect not found in the AFPM and RFPM machines, i.e. the magnetic field in the airgap has a different distribution at the outer pole pairs than at the inner pole pairs. This however does not affect the ability to simulate the machine accurately by 2D finite element analysis.

The FEA package used by Wang was based on a non-commercial package implemented in *Fortran*. The *Fortran* code made use of an airgap element (AGE) originally proposed by Abdel-Razek *et al.* [62], where a single macro element replaces the finite elements that are normally used to discretise the airgap and where the field in the airgap is then solved analytically. Wang [63] expanded the capabilities of the code by also deriving the AGE for Cartesian coordinates (CAGE).

Gerber [64] modernised the *Fortran* code and further expanded the capabilities of the code by firstly to be able to have multiple airgaps and by secondly deriving an axisymmetric airgap element (ASAGE). This gave the code the ability to solve tubular linear machines of the kind presented here. Gerber named the FEA package *SEMFEM*[1].

[1]Stellenbosch Electrical Machines Finite Element Method

The accuracy of the *SEMFEM* package was evaluated by comparing simulation results with those of other commercial packages. Relevant to this investigation, Gerber tested the accuracy of the package for an iron core tubular linear machine and found that it compared well with a commercial package. Being entirely script based and license free, *SEMFEM* along with the open-source scripting language *Python*™ can quite easily be used in multiple simultaneous simulations. It was therefore decided to use *SEMFEM* for finite element analysis for the design optimisations.

It has been explained in section 4.3.2 (refer again to Figure 4.2) that for design optimisation for the piston displacement approach, the current response is determined iteratively in order to obtain a specific force response as a function of time. For the finite element analysis process, the position is determined from the relevant displacement at constant time steps. The current and the position, along with the dimensions and other relevant simulation parameters (e.g. maximum finite element mesh size), then serve as inputs. The outputs are the flux linkage and force as a function of time. The voltages, input and output power and copper losses are then determined through post-processing.

Figure 5.2 shows an equivalent circuit diagram representation of the single phase LFPM linear machine. No provision was made in the model for eddy current losses, since eddy currents are ignored.

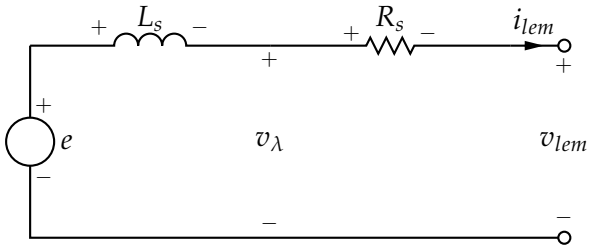

Figure 5.2: Equivalent circuit diagram representation of the LFPM linear machine.

From the flux linkage (λ), the voltage v_λ is determined by

$$v_\lambda = d\lambda/dt. \tag{5.1}$$

With the voltage v_λ known, the terminal voltage may be determined by

$$v_{lem} = v_\lambda - R_s i_{lem}, \tag{5.2}$$

where v_{lem} denotes the terminal voltage and R_s denotes the resistance of the copper coils. The input power may then by determined by

$$P_{in} = \frac{1}{T}\int_0^T v_\lambda i_{lem}\, dt, \tag{5.3}$$

or alternatively with

$$P_{in} = \frac{1}{T}\int_0^T F\dot{x}\, dt, \tag{5.4}$$

where F denotes the force response received from finite element analysis and $\dot{x}$ denotes the speed derived from the position of the mover that served as input to the finite element analysis. Ideally, the values of the input power obtained from equations (5.3) and (5.4) should differ very little. Values that differ considerably could indicate a poorly constructed finite element analysis, e.g. that the finite element mesh is too coarse. With *SEMFEM*, it was found that these two values for the input power generally differed very little (at least less than 1%).

The output power is determined with

$$P_{out} = \frac{1}{T}\int_0^T v_{lem} i_{lem}\, dt. \tag{5.5}$$

The efficiency may then be calculated by

$$\eta = P_{out}/P_{in}. \tag{5.6}$$

The calculation of the input and output power and efficiency above is of course for the case where only one linear machine is optimised for either the power piston or the displacer. In the case where the machines are optimised simultaneously, equations (4.21) to (4.25) apply.

Lastly, with no current flowing

$$e = v_\lambda, \tag{5.7}$$

where e denotes the EMF of the machine.

5.3 Design optimisation: Traditional approach for resonant FPSE's

The LFPM linear machine was optimised for traditional resonant FPSE's to serve as a benchmark for the design optimisations described later in this chapter. For this optimisation, the approach of Joubert *et al.* [51] was followed (refer again to the optimisation flow diagram shown in Figure 4.1). As optimisation algorithm, a sequential quadratic programming (SQP) method implementation from the *VisualDOC*™ optimisation suite was chosen. The SQP algorithm is a local search algorithm and normally converges quickly.

Figure 5.3 shows the cross-sectional side view of the LFPM linear machine with three poles (as in Figure 5.1). Also shown are the dimensions that formed part of the parameter vector for the optimisation routine. The dimensions indicated as r_t and h_t, i.e. the total radius and total height of the linear machine, are however not included in the parameter vector as these can be determined from the other dimensions. The airgap dimension is not shown in Figure 5.3. All airgaps were chosen to be 1 mm throughout for the results shown in this chapter.

As inputs, the position of the coils and the current through the coils were chosen to be

$$x = -(\mathrm{X}_{stroke}/2)\ \cos(\omega t), \tag{5.8}$$

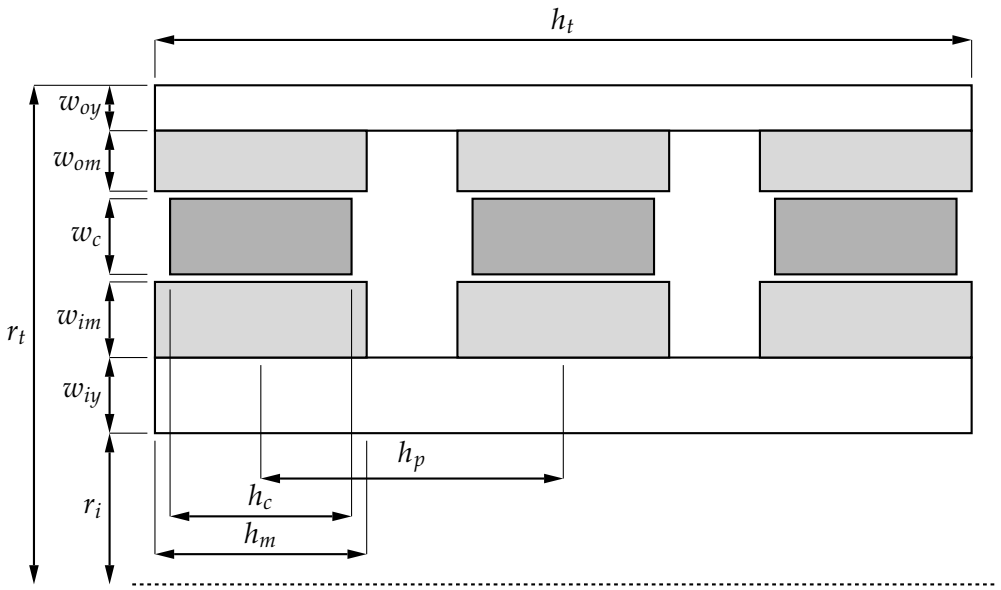

Figure 5.3: Dimensions of the LFPM linear machine.

and

$$i = \mathrm{A}\ \sin(\omega t), \tag{5.9}$$

respectively. The mover is shown to be in the centre position and the positive direction of all quantities such as displacement and force is to the right. The position was therefore chosen such that the coils start at the left most position and then move to the right most position and back.

Apart from the dimensions, the maximum current density (J_{max}) was also included as part of the parameter vector. The amplitude of the sinusoidal current waveform in equation 5.9 is therefore determined by

$$\mathrm{A} = J_{max} \times w_c \times h_c \times fillfactor. \tag{5.10}$$

In this manner, the current can be changed along with the change in dimensions in order to converge to an optimal design. Also, by calculating the current as in equation (5.10), the coils are simulated as single turn coils. The 3 pole examples shown in Figures 5.1 and 5.3 therefore consists of three single turn coils in series. Simulated results for the currents will be shown to be very large and for the voltages, to be very small. In practise, the current and the voltages will scale to more realistic levels as coils are made up by a multitude of turns - the current will scale down and the voltage will scale up by the number of turns. This does however not effect the results of the simulated force, as well as the calculated input and output powers.

Table 5.1 shows some key input parameters to the benchmark optimisations. The power level was chosen by following the designed power output of the GPU-3 Stirling engine. Several free-piston Stirling engines also exist with power ratings of this order of magnitude. The efficiency was chosen by following the specified minimum of the linear machine efficiency listed in Tables 3.19 to 3.21. The stroke length and frequency was chosen by following Joubert

et al. [51]. The remnant flux was chosen to be approximately that of N36 Neodymium Iron Boron (NdFeB) rare earth magnets. With the iron and magnet materials chosen to be fairly conservative, further improvement of designs reported later in this chapter is possible.

Table 5.1: Input specifications for the traditional optimisation of the LFPM linear machine.

Specification	Value
Input power [W]	> 3000
Efficiency	> 0,9
Stroke length [mm]	30
Frequency [Hz]	50
Copper fill factor	0,5
Iron	CR10 cold rolled steel
Magnet remnant flux [T]	1,22

Finally, the objective of the optimisations was to *minimise the total active mass, while adhering to the constraints of minimum power and minimum efficiency*. Table 5.2 shows the optimisation results for the LFPM linear machine with 2, 3, 4 and 5 poles.

Table 5.2: Optimisation results for the LFPM linear machine with 2, 3, 4, and 5 poles.

Number of poles	2	3	4	5
Masses [kg]				
Iron mass	6,49	5,77	5,82	5,89
Magnet mass	6,56	6,29	6,46	6,53
Copper mass	1,67	2,25	2,53	2,74
Total mass	14,72	14,30	14,80	15,15
Dimensions [mm]				
Total diameter $2 \times r_t$	215,52	188,21	173,69	159,76
Total height h_t	88,38	130,35	173,79	184,84
Inner radius r_i	50,18	48,31	47,53	46,83
Inner yoke thickness w_{iy}	11,11	8,62	6,82	5,76
Outer yoke thickness w_{oy}	8,39	4,84	3,90	3,38
Inner magnet thickness w_{im}	11,92	8,74	7,49	6,41
Outer magnet thickness w_{om}	12,11	9,68	8,17	7,31
Coil thickness w_c	12,08	11,92	10,89	10,20
Pole pitch h_p	53,56	49,47	47,82	46,21
Magnet height h_m	34,42	31,41	30,34	29,27
Coil height h_c	30,68	30,81	30,27	29,33

The results listed in Table 5.2 indicate that the lowest total active mass was obtained for a 3 pole LFPM linear machine. The total mass for the four different machines did however not vary considerably (within approximately 0,85 kg). The total diameter gradually decreased, while the overall length of the machines increased with an increase in the number of poles. With the goal to minimising the total mass, it can be expected that the optimisation algorithm reached the optimal copper to iron to magnet weight ratios for the specified efficiency level.

Figure 5.4 shows a cross sectional view of the optimised 3 pole LFPM linear machine with the finite element mesh as generated by *SEMFEM*, and Figure 5.5 shows the flux density and vector potential lines as simulated by *SEMFEM*. The entire air box is shown in both cases, with the lower boundary being the centreline of the linear machine.

The finite element mesh is shown to be much finer than what is generally necessary to accurately simulate this type of machine. The maximum distance between the element nodes was chosen to be small in order to simulate small machines accurately and was not scaled as machine dimensions increased. While ensuring accuracy, this could seriously slow down

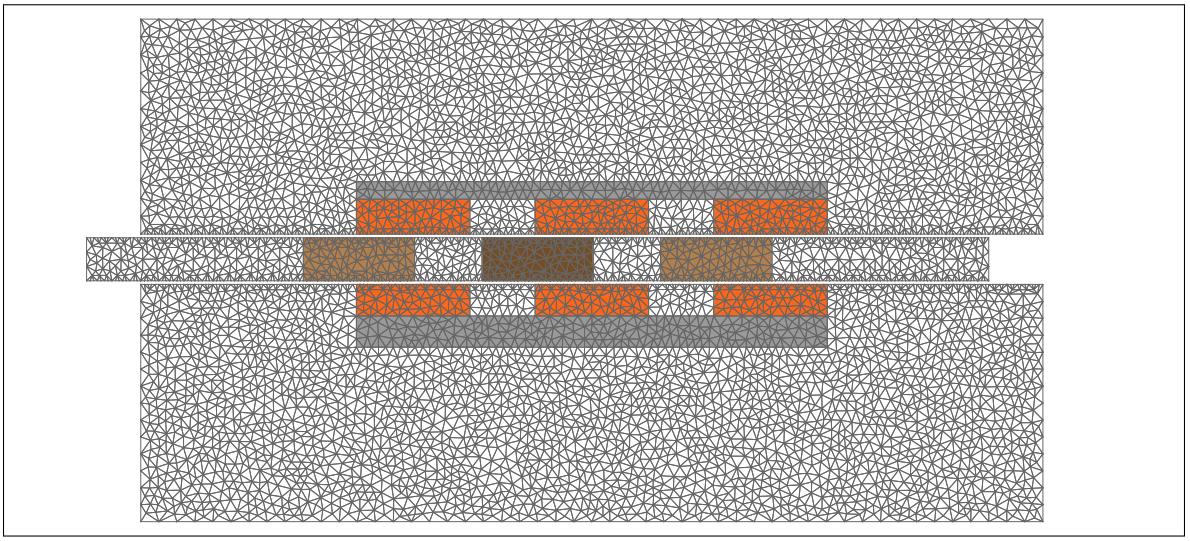

Figure 5.4: Cross sectional view of the optimised 3 pole LFPM linear machine and finite element mesh with the mover in the first position.

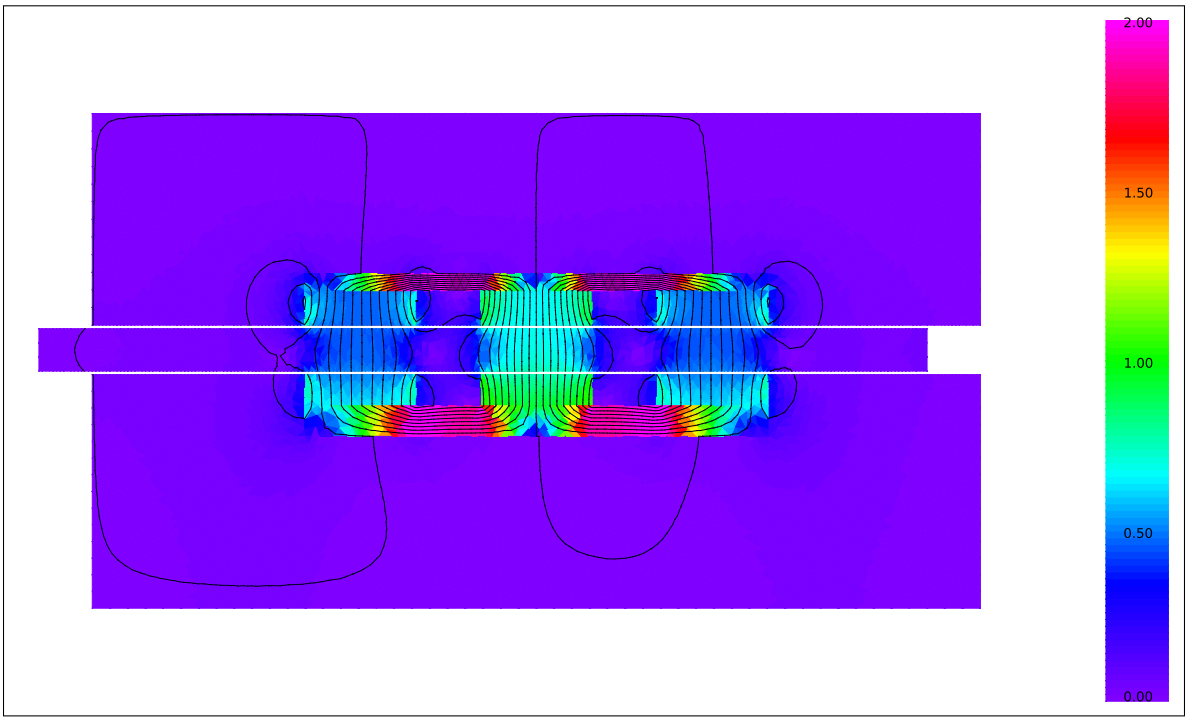

Figure 5.5: Flux density and vector potential lines of the optimised 3 pole LFPM linear machine with the mover in the first position.

the simulations of larger machines. In the case of these optimisations however, the typical simulation time was below approximately 2 minutes per machine simulation, i.e. for finite element analysis at 20 positions and post-processing.

It is shown that the highest flux density is approximately 2 Tesla in both iron yokes. This is fairly high, but with the advantage of little variation in the flux for air-core machines, resulting in very little core loss, the optimisation algorithm could increase the flux density to these levels to decrease the weight.

Figures 5.6, 5.7 and 5.8 show respectively the simulated flux linkage, the exerted force, and the voltages and current of the optimised 3 pole LFPM linear machine. The optimised linear machine was also simulated by the commercial software package *MagNet*™ to verify the accuracy of the *SEMFEM* simulation. Included in Figures 5.6 and 5.7, the flux linkage and the exerted force as simulated in *MagNet*™ are also shown. It is shown that the results in good agreement for both the flux linkage and the force.

The peak values of the voltages are shown to be of the order of a few volts, while the current is shown to have a peak value of a few kiloampere. This follows as a result of the coils being simulated as single turn coils. These values may be scaled to more appropriate levels by using

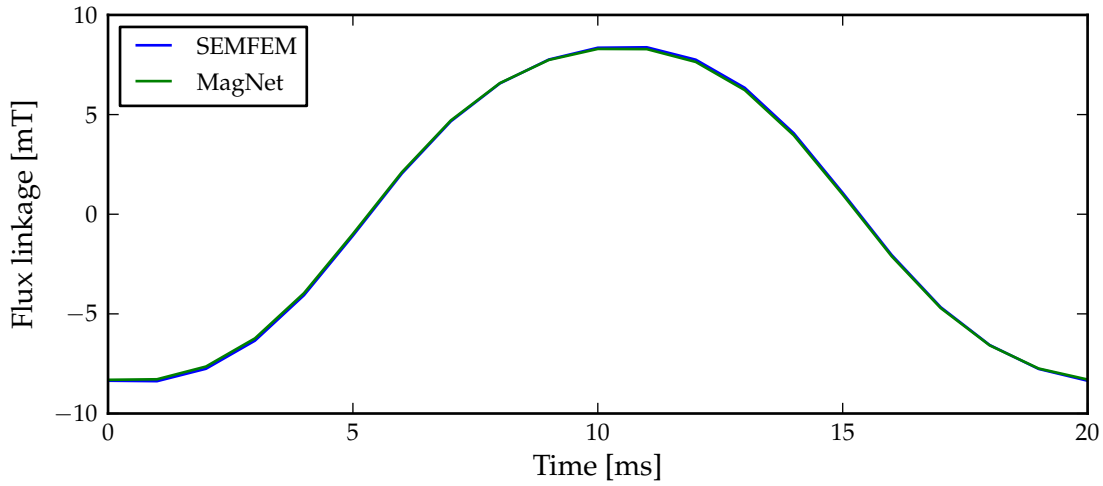

Figure 5.6: Simulated flux linkage of the optimised 3 pole LFPM linear machine.

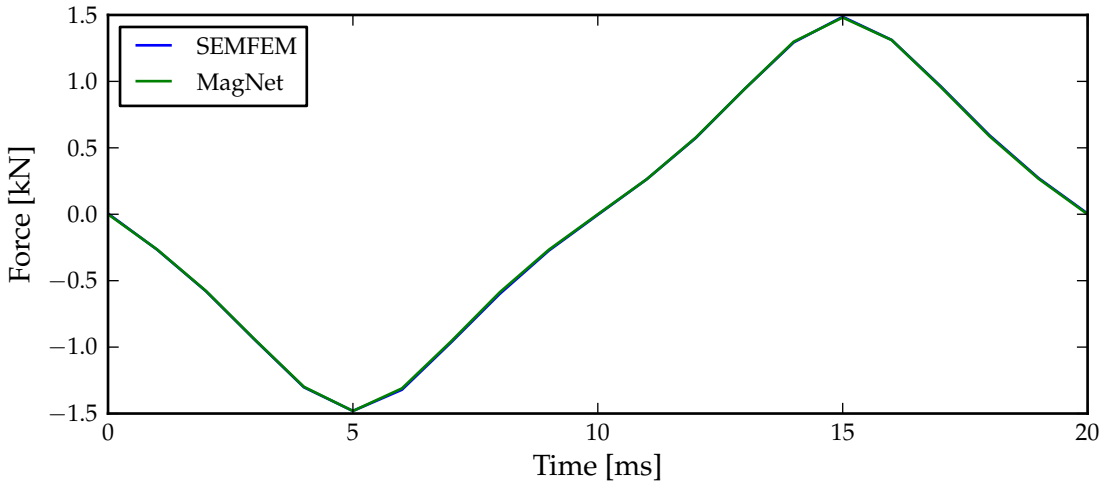

Figure 5.7: Simulated force of the optimised 3 pole LFPM linear machine.

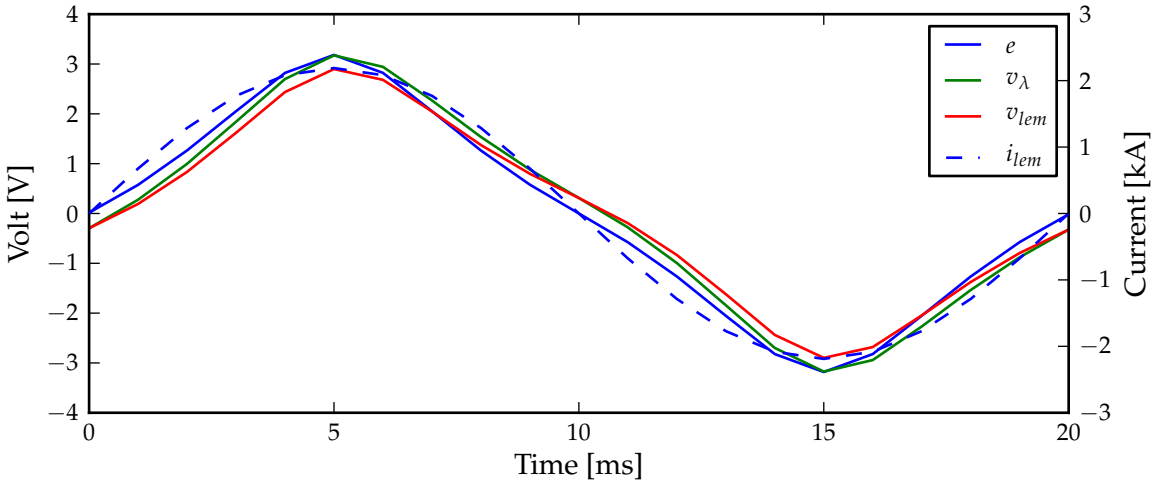

Figure 5.8: Simulated voltages and current of the optimised 3 pole LFPM linear machine.

multiple turns (e.g. 100 turns per coil would scale the voltages to increase and the current to decrease by a factor of 100).

While the current and the displacement waveforms are purely sinusoidal, the voltages are shown to be distorted. This is a direct result of the flux linkage as a function of displacement not having a constant slope over the entire stroke length. The slope of the flux linkage typically flattens towards the ends of displacement. This is a common phenomenon with short stroke linear machines [46, 50, 51].

The small difference between the voltages e, v_λ and v_{lem} is a direct consequence of the small series inductance (difference between e and v_λ) and small series resistance (difference between v_λ and v_{lem}). This property of air-core machines having small series inductance has already been highlighted.

The response of the force exerted by the linear machine is shown to be in the opposite direction than and completely out of phase with the direction of movement, i.e. the linear machine acts as a generator and will therefore act as a damper to the free-piston Stirling engine (refer again to the discussion in section 4.2.1).

5.4 Design optimisation: Displacer linear machine for direct piston displacement control

5.4.1 Overview

Results of design optimisation of a 3 pole LFPM linear machine for the various displacer representative dynamic responses proposed in chapter 4 are reported in the following sections. Detail will be provided for a range of optimisations for different specification levels and spring constants. Only a selection of possible optimisations are reported here, to avoid a too lengthy report and possible repetition of information.

Linear machines were optimised using the same input specifications as listed in Table 5.1, i.e. in order to obtain dynamic responses of the forces exerted on the linear machines by the

displacer from the normalised representative responses, the same power level, frequency and stroke length were used as for the previous section.

The one difference between the optimisations below and those presented for the traditional case in Section 5.3, is however that the power level merely serves as input parameter to calculate the force responses from the representative responses proposed in Chapter 4 and not as a constraint. Only the efficiency now serves as a constraint in the optimisation process.

Also, for the piston displacement control optimisations, it has been explained before that the current is not an input to the optimisations, but is determined during the optimisations. Refer again to the optimisation approach illustrated in Figure 4.2. The current waveforms that will be shown in results from here on, are therefore what is necessary in order for the linear machine to follow a certain displacement for the particular case. Now, with reference to the typical arrangement that was shown as an example in Figure 2.4, in a practical situation, the power electronic converters will have to control the current to follow such waveforms in order to perform displacement control.

It is especially the influence of springs on the optimisation results that should be watched carefully. In the optimisations below, spring constants were not optimised as part of the machine optimisations, but were rather chosen as constant to show their influence on the machine dimensions and performance. In many cases, no or impractical results were obtained where no springs were present. The possible consequence of this outcome, as well as others, will be further discussed in the conclusions in section 5.6.

5.4.2 Optimisations with the *7a* and *9a* dynamic responses

Design optimisations were performed with the *7a* and *9a* dynamic responses as shown in Figure 4.18 for the 90% specification level. It was determined before that the *7a* response could be used with both the 90% and 100% levels, and the *9a* response only with the 90% level. The design optimisations reported below are however only for the 90% level, but with the addition of two spring constants of 60 N/mm and 120 N/mm respectively. These two spring constants were not chosen completely arbitrarily, but to be of the order of magnitude of the force exerted on the displacer due to pressure differences (denoted later by $F_{\Delta p}$) in the 60 N/mm case and to be more dominant in the 120 N/mm case.

The dimensional and performance results of these two optimisations are shown in Table 5.3. Only the results obtained with spring constants are shown, since optimisations with no springs yielded impractical results (extremely high iron and magnet mass compared to those shown in Table 5.3).

Figures 5.9 and 5.10 show the voltages and current, and the forces respectively for the LFPM linear machine optimised with the *9a* dynamic response with a spring constant of 60 N/mm, while figures 5.11 and 5.12 show the voltages and current, and the forces respectively for the optimised LFPM linear machine with a spring constant of 120 N/mm.

In Figures 5.10 and 5.12, the force exerted on the linear machine by the displacer is denoted $F_{\Delta p}$ (refer to equation (4.9)), and the force exerted on the linear machine by the spring is de-

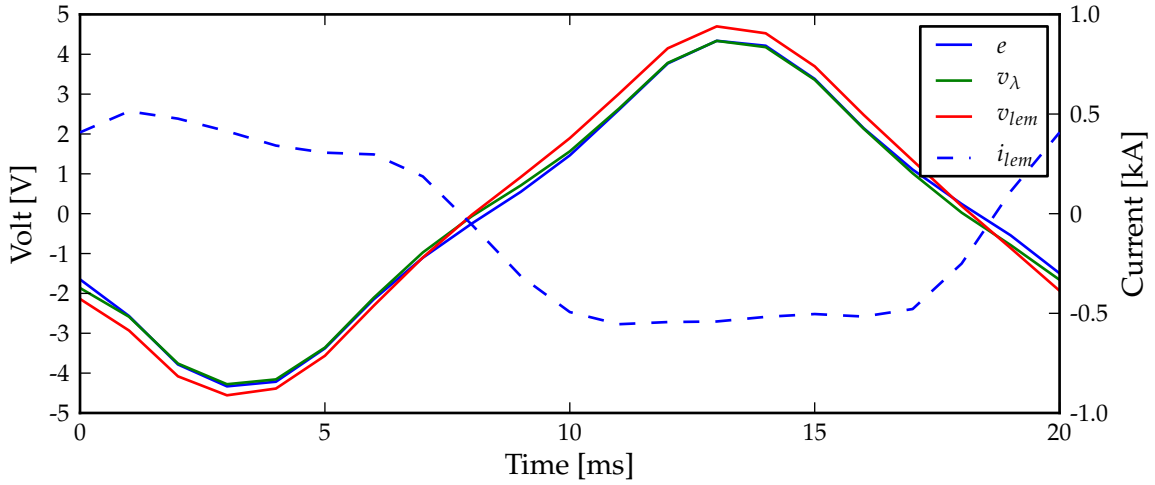

Figure 5.9: Simulated voltages and current of the optimised 3 pole LFPM linear machine for the *9a* dynamic response and with a 60 N/mm spring constant.

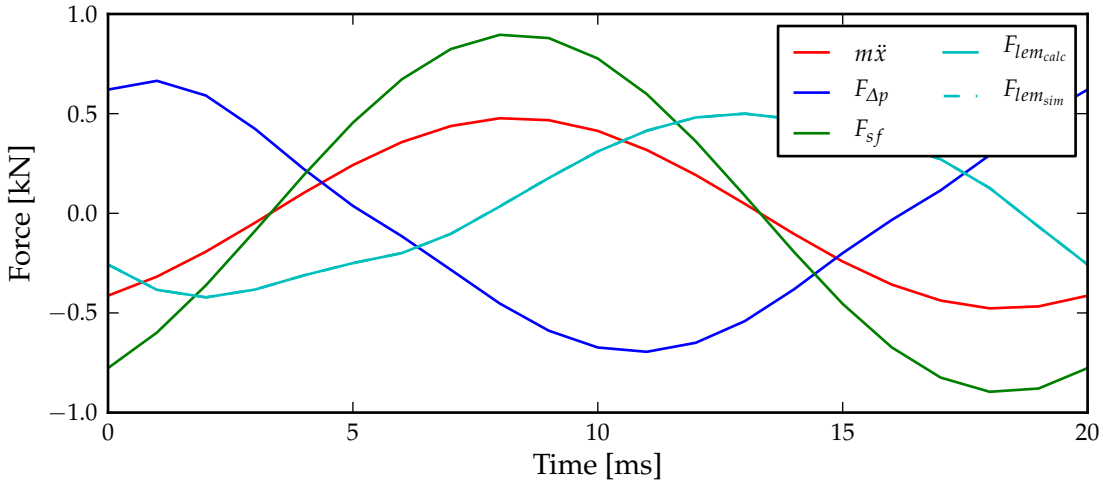

Figure 5.10: Simulated forces of the optimised 3 pole LFPM linear machine for the *9a* dynamic response and with a 60 N/mm spring constant.

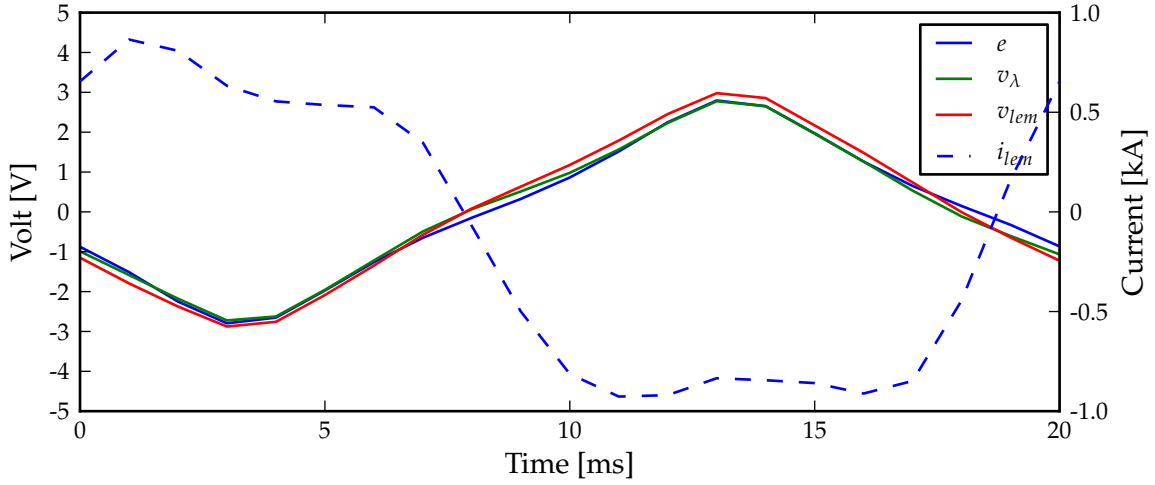

Figure 5.11: Simulated voltages and current of the optimised 3 pole LFPM linear machine for the *9a* dynamic response and with a 120 N/mm spring constant.

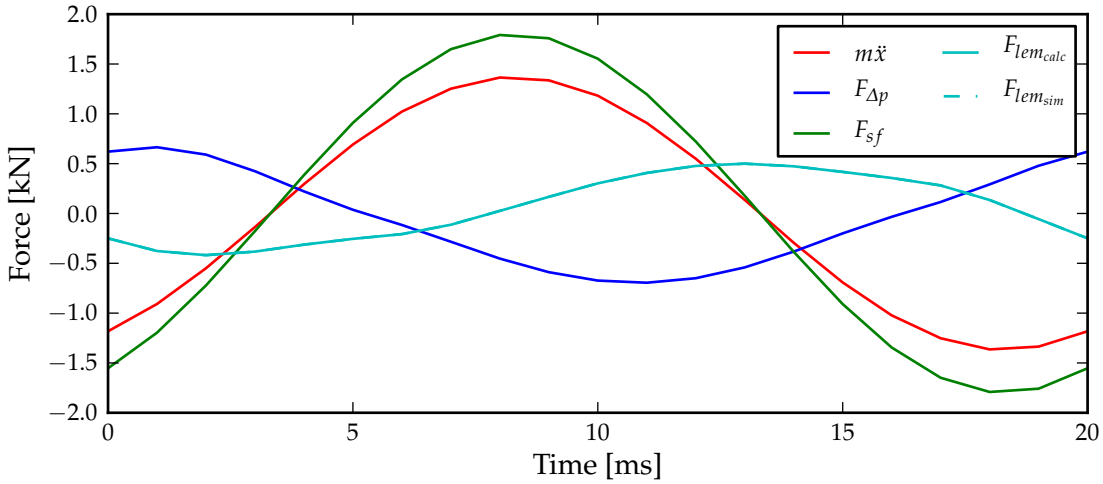

Figure 5.12: Simulated forces of the optimised 3 pole LFPM linear machine for the *9a* dynamic response and with a 120 N/mm spring constant.

noted F_{sf} (refer to equation (4.15)). The force exerted by the linear machine as calculated using equation (4.17) is denoted $F_{lem_{calc}}$ and the force exerted by the linear machine obtained through

Table 5.3: Optimisation results for a 3 pole LFPM linear machine for the displacer performed with the *7a* and *9a* dynamic responses and with the 90% specification level.

Representative dynamic response		*7a*		*9a*
Spring constant [N/mm]	60	120	60	120
Masses [kg]				
Iron mass	5,168	3,668	7,043	2,925
Magnet mass	4,006	2,534	5,348	4,632
Copper mass	0,420	1,015	0,323	0,925
Total mass	9,594	7,217	12,714	8,537
Dimensions [mm]				
Total diameter $2 \times r_t$	151,61	145,92	162,63	153,60
Total height h_t	121,57	122,68	135,18	101,14
Inner radius r_i	43,90	46,44	46,36	48,50
Inner yoke thickness w_{iy}	8,10	6,08	11,12	6,18
Outer yoke thickness w_{oy}	6,34	4,19	5,98	1,72
Inner magnet thickness w_{im}	1,03	3,77	4,03	6,17
Outer magnet thickness w_{om}	10,91	5,70	11,25	8,42
Coil thickness w_c	5,52	6,78	2,57	5,80
Pole pitch h_p	43,30	46,87	50,22	50,57
Magnet height h_m	34,96	28,94	34,54	32,26
Coil height h_c	15,90	29,29	23,43	29,20
Performance parameters				
Input power [W]	-801	-800	-1060	-1056
Output power [W]	-890	-888	-1177	-1173
Copper losses [W]	89	89	117	117
Efficiency [%]	90,0	90,0	90,0	90,0

iterative simulation is denoted $F_{lem_{sim}}$. These two forces should be identical.

The input and output power in Table 5.3 are shown to have negative signs. This is the result of choosing the direction of energy flow to be positive for generator operation. In this case the linear machines act as motors on average. The output power therefore has a higher negative value than the input power, due to copper losses in the linear machine. The copper losses will always be shown as positive, irrespective of direction of energy flow.

From the results of both responses, it is shown that the total mass decreased as the spring constant increased. The reason may be found by looking at the balance of forces in Figures 5.10 and 5.12, as well as the copper mass in relation to the iron and magnet mass. In both cases shown in the figures, the optimisation algorithm converged to a solution where the mass-acceleration term and the spring force nearly cancel each other to yield a resultant force $F_{lem_{calc}}$ where the mass could be minimised while maintaining the efficiency above the specified level. As die spring force increased with increase in spring constant, the copper mass increased accordingly to maintain approximately the same resultant force. But with this increase in copper mass, a more optimal copper mass to iron and magnet mass is reached, hence the decrease in total active mass. With a further increase in spring constant, the copper mass will have to increase accordingly, and the mass relationship could again be impacted negatively beyond some point.

While the *9a* response is near sinusoidal, the influence of it not being perfectly sinusoidal and the non-constant slope flux linkage is clearly seen on the voltages and especially the current. So even with near sinusoidal responses, the current could be particularly non-sinusoidal.

The double peak seen for both the currents is a direct consequence of the force per unit current not having a flat response for the entire stroke length.

It is shown in Table 5.3 that the input/output power for the *7a* and *9a* responses differ. This is a mere consequence of the choice of representative responses.

5.4.3 Optimisations for the *2a* dynamic response

Design optimisations were performed with the *2a* dynamic response as shown in Figure 4.18 for both the 90% and 100% specification levels. The dimensional and performance results of these two optimisations are shown in Table 5.4.

Figures 5.13 and 5.14 again show the voltages and current, and the forces respectively for the LFPM linear machine optimised for the 100% specification level.

In chapter 4, it was stated that the *2a* response originates from variation combinations sharing a common large displacer rod area-to-bore area ratio and that for this response the linear machine will act on average as a generator. That means that the force $F_{\Delta p}$ will be approximately out of phase with that for the *9a* response. A quick inspection shows that this is indeed the case (refer to Figures 5.10 and 5.14, or alternatively Figure 4.18). Contrary to the previous case with the *9a* response, this force exerted on the linear machine by the displacer and the mass-acceleration is therefore in phase to some degree, which means that up to a certain copper mass, the force needed of the linear machine will at first decrease (refer again to equation

Table 5.4: Optimisation results for a 3 pole LFPM linear machine for the displacer performed with the *2a* dynamic response.

Representative dynamic response		*2a*
Specification level	*90%*	*100%*
Masses [kg]		
Iron mass	4,570	6,875
Magnet mass	5,724	6,000
Copper mass	0,414	0,996
Total mass	10,708	13,871
Dimensions [mm]		
Total diameter $2 \times r_t$	159,00	174,62
Total height h_t	136,53	134,91
Inner radius r_i	48,51	48,17
Inner yoke thickness w_{iy}	7,80	9,81
Outer yoke thickness w_{oy}	3,38	5,94
Inner magnet thickness w_{im}	6,89	6,54
Outer magnet thickness w_{om}	10,24	10,92
Coil thickness w_c	2,68	5,93
Pole pitch h_p	51,57	51,25
Magnet height h_m	33,38	32,41
Coil height h_c	27,96	29,09
Performance parameters		
Input power [W]	777	1938
Output power [W]	699	1744
Copper losses [W]	78	194
Efficiency [%]	90,0	90,0

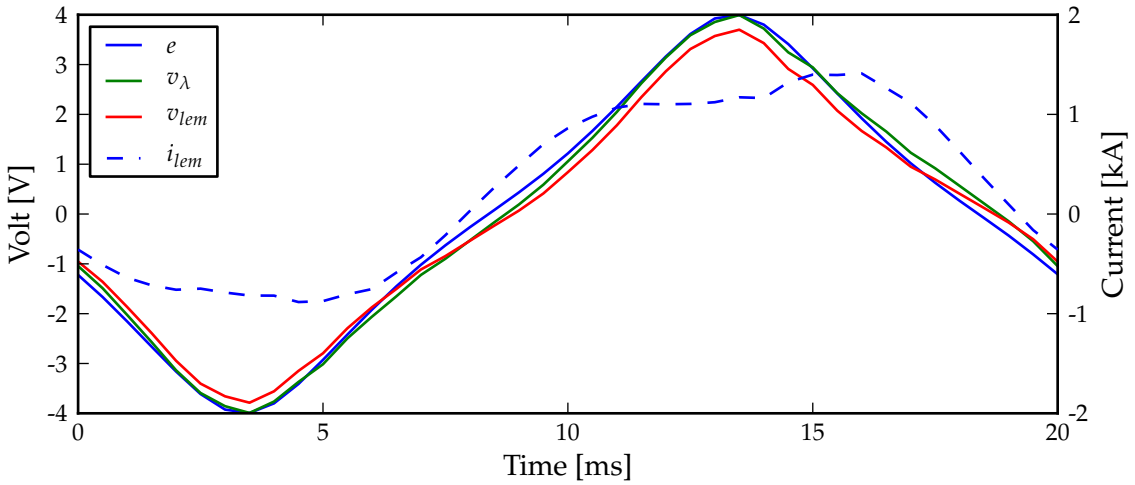

Figure 5.13: Simulated voltages and current of the 3 pole LFPM linear machine for the *2a* dynamic response.

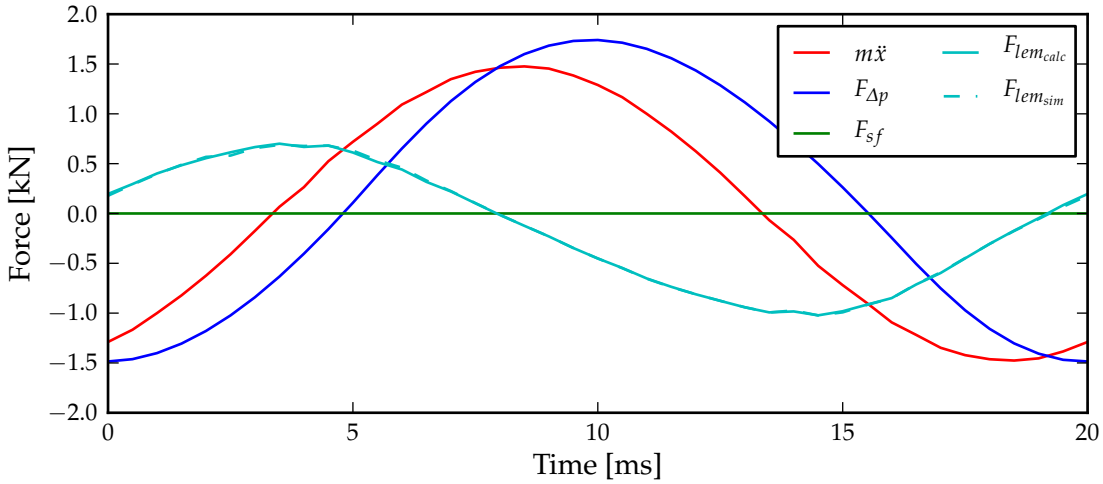

Figure 5.14: Simulated forces of the 3 pole LFPM linear machine for the *2a* dynamic response.

4.17). In the previous case the force needed from the linear machine immediately increased with an increase in copper mass and the only way to counter this increase was through the use of springs. Now in this case, no springs are needed to reach a practical result.

Another observation from the results shown here is that the LFPM linear machine could be tailored to have very low copper mass with respect to iron and magnet mass in order to reach a certain outcome. Compare for instance the copper mass with the iron and magnet mass in Table 5.4 with that of Tables 5.2 and 5.3. Again, while no spring forces were necessary here to reach practical results, the addition of spring forces will help to increase the copper mass as a percentage of iron and magnet mass and the same results should follow as in Table 5.3, where the overall mass decreased with an increase in the spring constant. This could be a decisive factor if the economical impact is considered.

5.4.4 Optimisations for the *1a* and *3b* dynamic responses

Design optimisations were also performed with the *1a* and *3b* dynamic responses as shown in Figure 4.18 for the 90% specification level and with two spring constants of 60 N/mm and 120 N/mm respectively. The dimensional and performance results of these two optimisations are shown in Table 5.5.

Figures 5.15 and 5.16 show the voltages and current, and the forces respectively for the LFPM linear machine optimised for the *3b* dynamic response with a spring constant of 60 N/mm, while figures 5.17 and 5.18 show the voltages and current, and the forces respectively for the optimised LFPM linear machine with a spring constant of 120 N/mm.

Both the *1a* and *3b* responses originate from composite displacement as in the case of the *7a* response, i.e. where the power piston does not follow a purely sinusoidal displacement, but rather that of a rhombic drive. Although the displacer itself does follow purely sinusoidal displacement, the effect of the power piston displacement does show in the pressure responses. These two responses also share a common large rod area to bore area ratio and therefore the linear machines will also act on average as generators.

Contrary to the results shown for the *2a* response, no practical results were obtained for

Table 5.5: Optimisation results for a 3 pole LFPM linear machine for the displacer performed with the *1a* and *3b* dynamic responses and with the 90% specification level.

Representative dynamic response		*1a*		*3b*
Spring constant [N/mm]	*60*	*120*	*60*	*120*
Masses [kg]				
Iron mass	5,654	3,350	8,420	4,784
Magnet mass	3,810	4,413	6,273	5,817
Copper mass	0,787	1,382	0,626	1,193
Total mass	10,251	9,145	15,318	11,793
Dimensions [mm]				
Total diameter $2 \times r_t$	157,84	159,54	173,67	169,82
Total height h_t	127,10	127,90	141,81	133,63
Inner radius r_i	44,99	48,27	46,93	49,42
Inner yoke thickness w_{iy}	8,86	6,38	11,30	7,99
Outer yoke thickness w_{oy}	5,95	2,52	7,15	3,51
Inner magnet thickness w_{im}	4,05	6,21	5,53	6,85
Outer magnet thickness w_{om}	9,17	8,24	11,90	10,27
Coil thickness w_c	5,90	8,15	4,03	6,87
Pole pitch h_p	48,79	48,70	53,79	50,70
Magnet height h_m	29,53	30,51	34,24	32,22
Coil height h_c	25,62	30,51	27,59	29,99
Performance parameters				
Input power [W]	1017	1016	954	956
Output power [W]	915	914	858	860
Copper losses [W]	102	101	96	95
Efficiency [%]	90,0	90,0	89,9	90,0

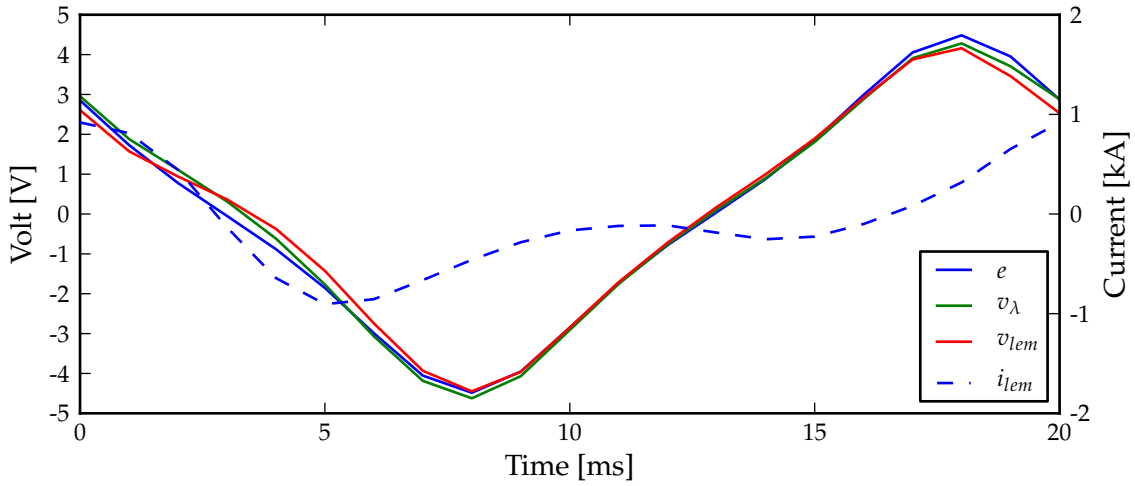

Figure 5.15: Simulated voltages and current of the 3 pole LFPM linear machine for the *3b* dynamic response and with a 60 N/mm spring constant.

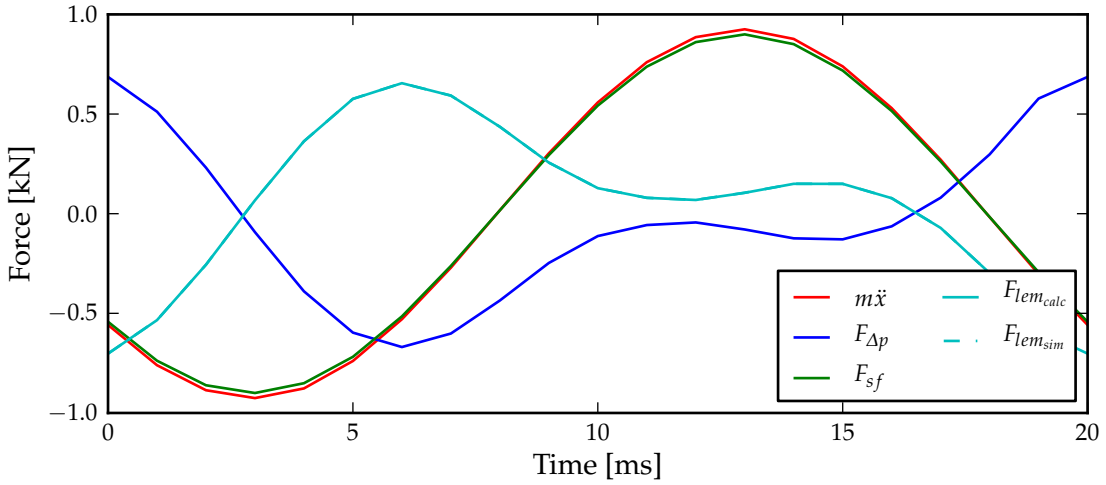

Figure 5.16: Simulated forces of the 3 pole LFPM linear machine for the *3b* dynamic response and with a 60 N/mm spring constant.

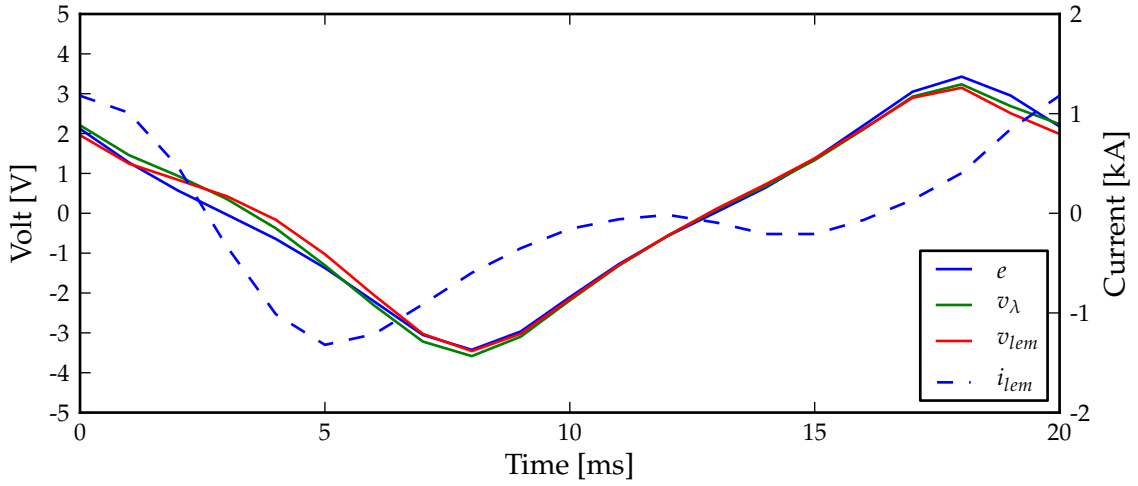

Figure 5.17: Simulated voltages and current of the 3 pole LFPM linear machine for the *3b* dynamic response and with a 120 N/mm spring constant.

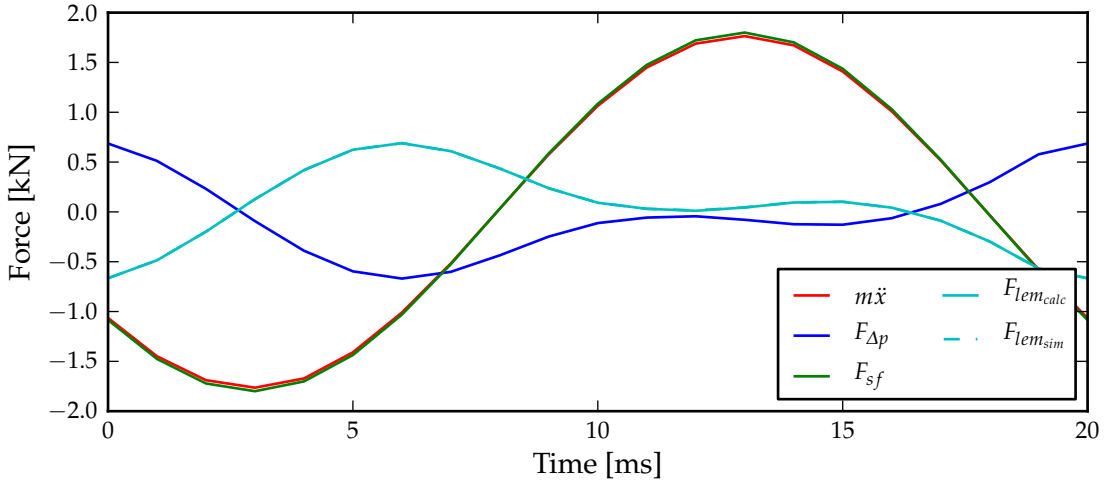

Figure 5.18: Simulated forces of the 3 pole LFPM linear machine for the *3b* dynamic response and with a 120 N/mm spring constant.

these responses without the presence of spring forces. Again, a marked improvement of the overall mass is seen as the spring constant is increased as a result of the improved ratio of copper mass to iron and magnet mass.

It is seen for the *3b* response that optimal conditions are reached when the spring force and the mass-acceleration nearly cancel each other out, i.e. when the linear machine is operated close to the natural frequency of the mass-spring combination. Although not shown here, this is also the case for the *1a* response and to a lesser extent for the *7a* response treated in section 5.4.2. With this cancellation, the required force from the linear machine is then approximately the inverse of the force exerted by the displacer on the linear machine. In Figures 5.15 and 5.17 it is shown how this impacts upon the current waveform to closely resemble that of the force.

5.5 Design optimisation: Power piston linear machine for direct piston displacement control

Design optimisations were performed with the *1a* and *2a* dynamic responses as shown in Figure 4.28 for the 90% and 100% specification levels for the power piston. The input specifications of the power level, frequency and stroke length were chosen to be same as for the displacer.

Convergence could not be reached for the the *1a* response due to the acceleration of the non-sinusoidal displacement that demanded forces from the linear machine that could not be reached by this topology, while still adhering to the minimum efficiency. Even if convergence was reached by lowering the minimum required efficiency, the design would have been impractical with excessively high iron and magnet mass. This has substantial implications for non-sinusoidal displacement under direct displacement control. Only sinusoidal displacement should be considered, at least for the LFPM linear machine topology.

Where only sinusoidal displacement was considered, i.e. for the *2a* response, practical machine dimensions have been obtained. The dimensional and performance results of these optimisations are shown in Table 5.6.

Figures 5.19 and 5.20 show the voltages and current, and the forces respectively for the LFPM linear machine optimised for the *2a* dynamic response for the 100% specification level.

Regarding the power piston, the force exerted by the piston on the linear machine denoted by $F_{\Delta p}$ is much higher than for the displacer. It has been shown in Chapter 4 that this force has a maximum close to the limit of displacement, and it can be seen in Figure 5.20 that it is therefore approximately in phase with the mass-acceleration. This force therefore largely determines the acceleration of the power piston.

The resultant force as the difference between the pressure difference force and the mass-acceleration is that required of the linear machine. It is seen in Figure 5.20 that this force is approximately 90 degrees out of phase with the other responses, placing it approximately in phase with the speed of the power piston/linear machine. The instantaneous power delivered to the linear machine/converted by the linear machine is therefore positive for most of the cycle, especially if the large offset of this force is ignored. This is supported by the volt-

Table 5.6: Optimisation results for a 3 pole LFPM linear machine for the power piston performed with the *2a* dynamic response.

Representative dynamic response		*2a*
Specification level	*90%*	*100%*
Masses [kg]		
Iron mass	6,685	10,389
Magnet mass	8,330	13,630
Copper mass	4,054	7,232
Total mass	19,069	31,251
Dimensions [mm]		
Total diameter $2 \times r_t$	206,85	244,16
Total height h_t	139,68	152,45
Inner radius r_i	51,14	53,48
Inner yoke thickness w_{iy}	10,09	12,10
Outer yoke thickness w_{oy}	3,90	5,45
Inner magnet thickness w_{im}	10,51	14,33
Outer magnet thickness w_{om}	10,44	13,01
Coil thickness w_c	17,35	23,70
Pole pitch h_p	53,32	57,81
Magnet height h_m	33,04	36,82
Coil height h_c	34,06	39,03
Performance parameters		
Input power [W]	2278	4087
Output power [W]	2050	3678
Copper losses [W]	228	409
Efficiency [%]	90,0	90,0

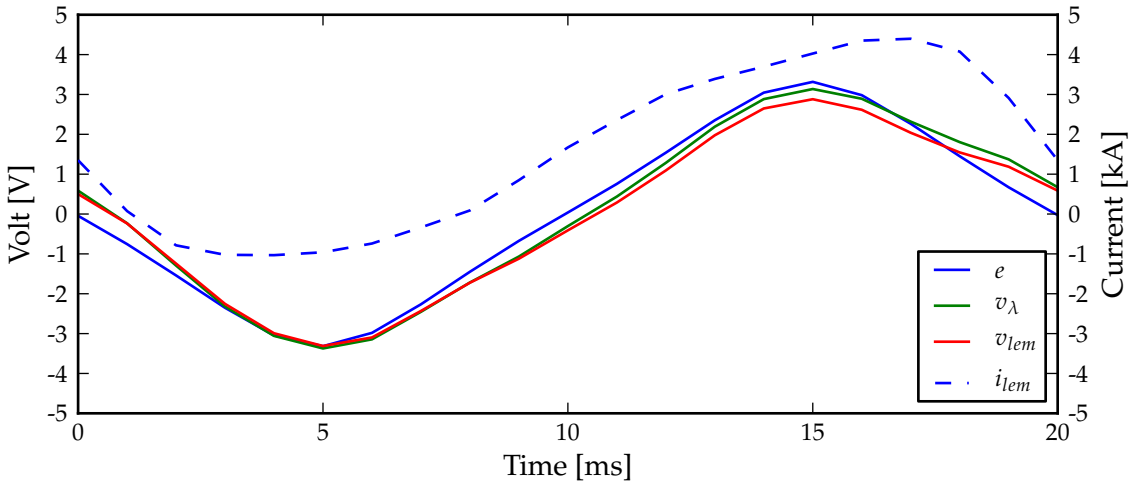

Figure 5.19: Simulated voltages and current of the 3 pole LFPM linear machine for the *2a* dynamic response.

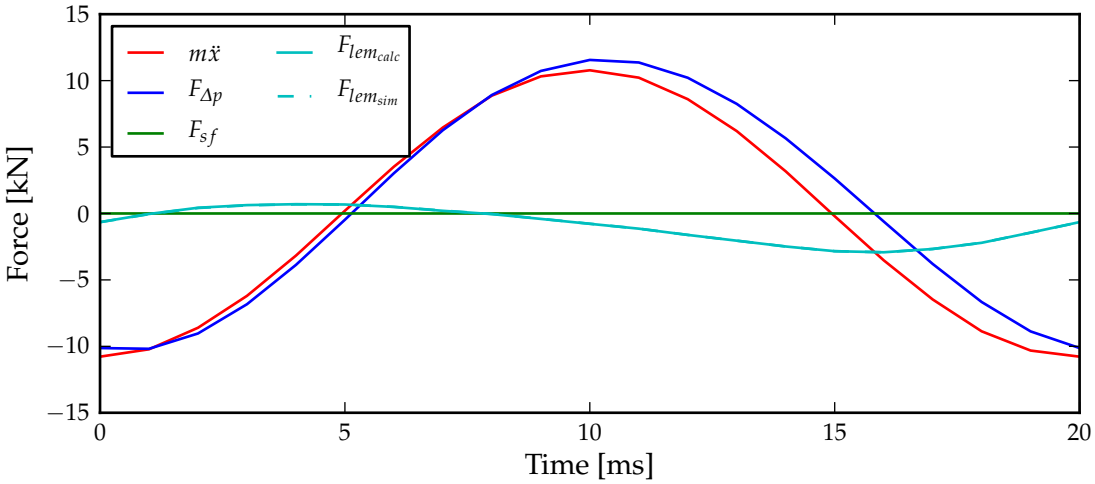

Figure 5.20: Simulated forces of the 3 pole LFPM linear machine for the *2a* dynamic response.

ages and current being largely in phase. Regarding the results shown for the *2a* response, the linear machine therefore acts as a damper to the system in very much the same way as in the traditional case, except for the current waveform being non-sinusoidal, specifically to instantaneously control the position of the power piston.

A particular difference between the displacement control approach demonstrated here and the traditional case is related to the significant offset of the current and the F_{lem} force seen in Figures 5.19 and 5.20. A variation of the difference between the average of the compression space and bounce space pressures was allowed for as part of the list of variations. This difference in the average of the pressures arises from net loss of working fluid to the bounce space due to non-linear gas flow between the compression space and bounce space, as explained in Section 3.3.2. Additional systems have been added to free-piston engines before to counter loss of working fluid to the bounce space [2, 4].

A quick inspection of the dynamic responses shown in Figures 4.26 and 4.27, shows the influence of this variation on the $\gamma_{Fxf/P}$ responses, resulting in their having different offsets. The results shown in Figures 5.19 and 5.20 confirm that the linear machine is capable of countering the force due to this pressure difference, while adhering to the minimum efficiency. It is therefore possible, in the absence of mechanisms to counter the loss of working fluid, to use the linear machine itself to counter the average pressure difference force and, as a consequence, possible piston creepage.

While it is shown that the linear machine can counter the constant force arising from this difference in average pressure, it is not clear at what cost in terms of additional active material and consequently higher economical cost. A further optimisation was performed where the offset was removed from the $F_{\Delta p}$ force. The total mass was reduced to 23,35 kg, compared to 31,25 kg listed in Table 5.6. This is a substantial decline and should definitely be considered when evaluating the manufacturability, complexity, performance and economics of choosing to counter the force resulting from an average difference between the compression and bounce space pressures versus having an additional mechanism/system to counter the loss of working fluid.

The input power (again, i.e. the input power to the linear machine or the output power from the power piston) is shown to be 4087 W and 2278 W for the 100% and 90% specification levels respectively. An inspection of the original data revealed that this rather low value of 2278 W is not the typical power level found for the variation combinations with sinusoidal power piston displacement and with $\Gamma_{Fxf/P}$ ratios at the 90% specification level - power levels upward of 3500 W are more likely. In fact, the input power levels on average for the 100% and 90% specification levels do not differ substantially.

Figure 5.21 shows the top fifty $\gamma_{Fxf/P}$ dynamic responses of the power piston with the displacer $\Gamma_{Fxf/P}$ ratios equal to or below the 100% specification level for only those combinations of variations originating from sinusoidal displacement and with negative output power from the displacer. These responses are therefore the responses obtained for the power piston when the analysis was performed that led to the responses shown in Figure 4.14 for the displacer.

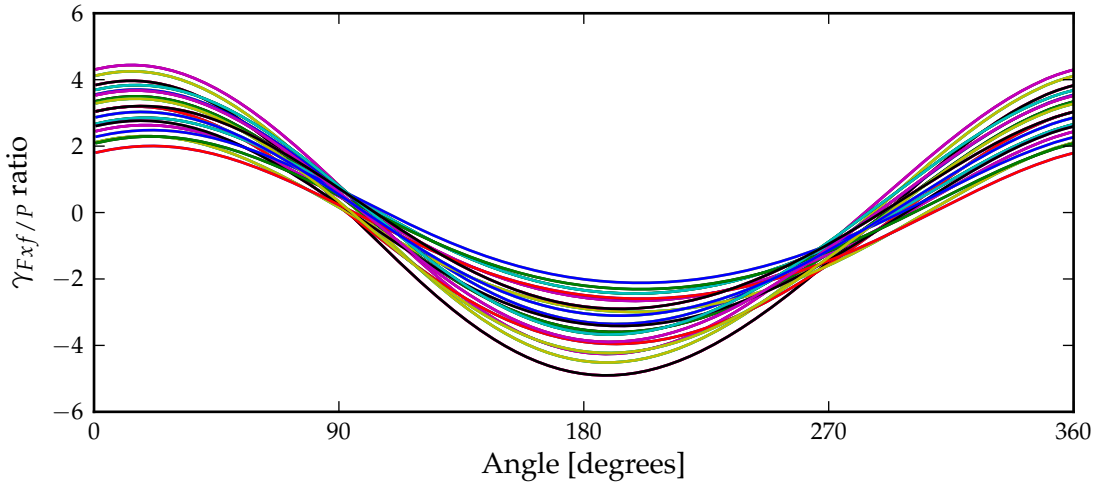

Figure 5.21: Top fifty $\gamma_{Fxf/P}$ dynamic responses of the power piston with the displacer $\Gamma_{Fxf/P}$ ratios equal to or below the 100% specification level.

The responses in Figure 5.21 clearly show a slight phase shift as the maximum value of the responses decline. It would therefore be appropriate to shift the $\gamma_{Fxf/P}$ response in phase for optimisation at the 90% specification level to obtain a more realistic input power level. Further analysis showed that a phase shift of up to approximately 8 degrees could be allowed for. During verification it was found that for a phase shift of 8 degrees the input power increased to approximately 4200 W. This increase is not important when evaluating linear machines for only the power piston. It is however important should the *2a* response be used at the 90% specification level as part of a combined optimisation.

5.6 Conclusions

In this chapter, design optimisations of an air-core LFPM linear machine were reported. The particular topology was chosen because of the many advantages that it holds. One of these advantages with respect to direct piston displacement control is the versatility of the topology to have a large range of different copper mass to iron and magnet mass ratios. A quick comparison of the copper, iron and magnet masses listed in the various tables confirms this.

This topology compares well with the transverse flux topologies investigated by Schutte and Strauss [46], Schutte *et al.* [50] and Joubert *et al.* [51] in terms of total active mass for the traditional case. It should be seriously considered for application in free-piston Stirling engines given the added advantages of no reluctance forces and lateral magnetic pull forces between the stator and the mover.

It may be concluded that direct piston displacement control is possible with this linear machine topology. This must however be qualified due to two major findings from these investigations:

- It was found that the addition of spring forces is critical to obtain practical optimisation results for the linear machines for the displacer. It was realised early and reported in Chapter 3, that spring forces could be relevant to piston displacement control of the displacer, but the real importance thereof was only understood during the design optimisations reported in this chapter.

  Only in the case the *2a* response for the displacer, the linear machine did not require the help of spring forces to converge to a practical design. But even here spring forces will help to reach a more optimal design, e.g. lowest active mass.

- It was found that sinusoidal displacement is critical in order to obtain practical optimisation results for the power piston linear machine. The impact of the acceleration of the power piston moving member is such that high efficiency cannot be reached if the displacement is non-sinusoidal.

Some of the results obtained during the investigations might improve with other linear machine topologies. The original objective of direct piston displacement control as stated in Chapter 2, is however limited for the air-core LFPM linear machine topology due to the following reasons:

- The frequency of operation is limited due to the natural frequency of the displacer moving member mass/spring constant combination. Any operation away from this natural frequency will substantially increase the losses in the displacer linear machine to maintain a certain piston displacement.

- The power piston displacement is also limited to sinusoidal displacement that also limits displacement possibilities.

While displacement control is limited with respect to the original objective, it was shown for the various design optimisations, that instantaneous displacement control of the pistons still played a critical role in obtaining sinusoidal displacement. This is important in the light of the findings of Strauss and Dobson [12] reported in Chapter 2 that showed that the highest engine efficiency is reached by purely sinusoidal displacement.

The overall efficiency as defined in section 4.3.2, has not been considered in this chapter, since combined optimisations have not been done. For the LFPM linear machine it is now clear

that two viable combinations remain, namely the *9a-2a* and *2a-2a* combinations as defined in section 4.4.4. Each of the separate efficiencies will have to be increased from the chosen 0,9, especially that of the power piston, in order to reach an overall efficiency of 0,9. Viable designs will however still be possible.

The maximum spring force for the displacer as a ratio of net output power (3000 W in this case) was up to a value of the order of 0,6 N/W, which is much higher than the design guideline provided in Table 3.18. In setting this design guideline, the interaction of the spring force and mass-acceleration as demonstrated in this chapter, was not taken into consideration. It has been shown here that the spring constant is largely determined by the moving mass and vice versa.

Additional mass from the rest of the moving member - and not only the active copper mass of the linear machines - should not pose any problem for the linear machine optimisations to converge to practical designs. In the case of the displacer, additional mass could be accommodated by increasing the spring constant to maintain a certain natural frequency. In the case of the power piston, the copper mass to iron and magnet mass ratio is still higher than was the case for the traditional approach (see Tables 5.6 and 5.2 respectively), which suggests that the copper mass could still be lowered to make provision for additional mass.

Finally, consider the optimisation results shown in Table 5.6 for the *2a* response of the power piston and the results shown in Table 5.2 for the 3 pole linear machine. It is shown that the optimisation results for direct piston displacement control yielded linear machines that are larger in size and that will consequently be more expensive when compared with the traditional case. In addition, a second linear machine is required to perform displacement control on the displacer. A direct comparison of for instance total weight, is however problematic. The design optimisations presented in this chapter were to evaluate the LFPM linear machine for direct piston displacement control in general according to the specifications determined earlier and not for a specific Stirling engine. This may result in linear machines that are larger in size than what is required for specific application.

And while the linear machines might be larger than their traditional counterparts, the addition of other mechanisms/systems needed to make traditional free-piston Stirling engines more controllable might again flip the scale in favour of direct displacement controlled free-piston engines. It has also been shown that allowing for mechanisms, e.g. to counter the loss of working fluid, could have a substantial influence on the size of the linear machine. While this would constitute a move away from pure direct piston displacement control, the combination of displacement control and other mechanisms may result in free-piston Stirling engines that are both economical, robust and controllable. Only time will tell which combinations will be best to achieve this.

Optimisations for specific engines require knowledge of the engines in order to set specific criteria/specifications. Again, this was not the aim of this investigation, although a similar process to the one presented in this dissertation could be followed to determine specifications specific to the particular engine from which linear machines could be optimised for application in the particular engine. Or where engine similarity to the GPU-3 engine could be established, a subset of the results for the extended range of variations could be used as specifications.

Chapter 6

A summary and recommendations

6.1 Introduction

An alternative approach of direct piston displacement control has been proposed in this dissertation to contribute to the field of free-piston Stirling engine control. The question was asked whether it is possible to combine some of the advantages of free-piston engines and kinematic engines. Possible advantages, but also challenges and difficulties were highlighted that led to the question being asked whether suitable linear machine technology exists or whether such technology could be established to perform direct piston displacement control. In short, is direct piston displacement at all possible?

In this chapter, a concise summary of the work presented in this dissertation and contributions will be presented, as well as some recommendations for future work.

6.2 A summary of the work presented

6.2.1 Second order simulation of the GPU-3 Stirling engine

It was realised early in this investigation that a standard had to be established according to which linear machines could be evaluated or developed. Such a standard had to take into account a number of different variation possibilities in Stirling engines, whether operational variations, engine dimensional variations or linear machine related variations.

The first challenge was to establish a simulation environment to accurately simulate Stirling engines to obtain, amongst others, accurate pressure dynamic responses for a large range of variations. Third order simulations, where all or most of the thermodynamic conservation laws are taken into consideration during cyclical simulation, are not available off the shelf. It was also considered to be outside the scope of this investigation to develop/implement a third order simulation. This has been the subject of doctoral studies in itself.

A second order simulation as developed by Urieli [13] was therefore adopted. In order to verify its accuracy, this second order simulation was subjected to thorough scrutiny by comparing simulated results with experimental data obtained for probably the best documented

Stirling engine available to the public domain, namely the GPU-3 engine. Strauss and Dobson [14] showed that the second order formulation presented here could simulate most of the cycle variables to a fair degree of accuracy (see also Appendix A).

In this dissertation, the accuracy of the second order formulation was further investigated and adjustments were made to ensure even better accuracy (see sections 3.5.2 and 3.5.3). It was concluded that, given the limitations of the second order simulation, accurate pressure dynamic responses could be obtained for further investigations.

6.2.2 Specification and design guidelines

The standard according to which linear machines could be evaluated was established by way of setting specifications to which linear machines should adhere to. These specifications were determined firstly by a case study on the influence of a variety of variations on the GPU-3 engine. The more and less dominant variations could then be identified.

The variations that were considered can be divided into three groups:

- Operational variations, e.g. variation in the hot and cold side temperatures and variation in displacement and frequency of operation.
- Dimensional variations, e.g. displacer rod area as a percentage of the bore area.
- Variations directly related to the linear machines, e.g. translator mass and spring constants.

In order to help direct insight gained from the case study, four force indicators were defined. Two of these indicators relate to the maxima of the force and the rate of change of the force itself and two of the indicators relate to the normalised position where these maxima occur. The first two indicators were then refined later to improve the usefulness thereof. Some of the variables, e.g. the frequency and stroke, were incorporated as part of the indicators and this yielded dimensionless indicators of which the $\Gamma_{Fxf/P}$ ratio is regarded as the most important.

But, while this information from the case study was useful to help direct later decisions, the influence of the combined variations had to be considered as well. This was done by performing a multitude of simulations for all combinations of the different variations. A process whereby the extent of some of the variations were limited so as not to have a completely dominant influence on the higher end of the distributions of especially the $\Gamma_{Fxf/P}$ and $\Gamma_{dF/Ff}$ ratios then followed. This not only eventually led to specifications, but also to design guidelines. Final specifications were compiled by determining the levels of the force indicators tthat would include e.g. 90% or all of the variations.

Insight was also gained concerning the cross correlation of the various specification levels of the $\Gamma_{Fxf/P}$ and $\Gamma_{dF/Ff}$ ratios for each of the pistons and between pistons. It was shown that assuming the one force indicator at a certain specification level does not automatically imply that all other indicators will be at the same level. In fact, a very poor correlation exists. In the end the choice was made to concentrate on the $\Gamma_{Fxf/P}$ ratio for design optimisation purposes

and to, by way of inspection, make sure that the $\Gamma_{dF/Ff}$ ratio is sufficiently high. This was addressed in Chapter 4 where a design optimisation approach was proposed.

6.2.3 A design optimisation approach

The setting of specifications did not address the question of how to apply these specifications. A design optimisation approach for direct piston displacement therefore followed. This approach was based on previous approaches (refer again to [46, 50, 51]), but differed in that it focussed on direct piston displacement control. It is unique due to two reasons:

- The force required of the linear machine serves as input and not the current of the machine. This is required to optimise linear machines to evaluate their capability to perform piston displacement control. The current which is derived in the simulation process, is necessary especially where the linear machines are simulated by finite element analysis.
- Specific normalised $\gamma_{Fxf/P}$ dynamic responses were proposed for both the displacer and power piston linear machines. These responses were directly obtained from the simulations that were performed previously to determine specifications, and was chosen to be representative of the dynamic responses that could be expected for combinations of variations that yielded high $\Gamma_{Fxf/P}$ ratios.

It may be added that this approach also proposes and makes provision for the simultaneous optimisation of both displacer and power piston linear machines and dual translator machines. This is also a unique idea, since no previous reference could be found to the simultaneous optimisation of linear machines. It was however not demonstrated.

6.2.4 Evaluation of a tubular, air-cored, LFPM linear machine

The application of the specifications and the design optimisation approach was demonstrated in the evaluation of a tubular, air-cored, longitudinal flux machine with surface mount magnets. This evaluation also helped to gain further insight into the challenge of direct piston displacement control.

The LFPM linear machine was first optimised for a chosen set of input parameters, e.g. the input power and frequency of operation, for 2, 3, 4, and 5 pole versions. This served as benchmark for optimisations for piston displacement control to follow. It was found that the 3 pole version had the lowest total active material and all further optimisations were then only performed for the 3 pole version.

Design optimisations of the LFPM linear machine then followed for the displacer. Optimisations were performed for all representative responses identified in Chapter 4 and mostly with the 90% specification level. With the exception of the *2a* response, no or very impractical results were obtained without spring forces present. It was shown that when spring forces were added, realistic linear machine designs were obtained. These spring forces inevitably lead to a natural frequency in the vicinity of the frequency of operation, which limits the scope of direct piston displacement control.

Design optimisations for the power piston yielded practical results only for sinusoidal displacement. It was found that with the acceleration of composite displacement, the optimisation could not converge for the minimum required efficiency. In the case of sinusoidal displacement, convergence could be reached without the addition of spring forces.

It was concluded that direct piston displacement control is indeed possible, but that it is limited with respect to the initial objective stated in Chapter 2.

6.2.5 Final conclusion

Valuable insight has been gained in the field of free-piston Stirling engines and linear electrical machines through this study of an alternative approach to free-piston Stirling engines namely direct piston displacement control. This insight is not only applicable to the displacement control approach, but could be equally valuable to those who follow the traditional approach of resonating free-piston Stirling engines.

And while a large amount of work has been covered, new questions that focus on specific issues, can be raised following this study. Some of these will be discussed shortly in the last section on future recommendations.

6.3 A summary of original contributions

The following new work has been presented in this dissertation:

- The setting of specifications and design guidelines for direct piston displacement control. This contribution included the following:
  - Force indicators were defined and subsequently refined to be, amongst others, dimensionless. This ensured improved ability to determine the maximum force in the case of the $\Gamma_{Fxf/P}$ ratio or rate of change of force in the case of the $\Gamma_{dF/Ff}$ ratio from a particular specification level for a wide variety of variation in stroke, frequency and net output power.
  - Distributions of the force indicators, amongst others, were obtained based on simulations for all combinations of a variety of operational, dimensional and other variations. This not only paved the way for the setting of specifications, but also for determining design guidelines for both free-piston Stirling engines and linear machines.
  - Finally, specifications were determined and thoroughly discussed that allowed for the evaluation of linear machines in order to determine their suitability for direct piston displacement control.
- A design optimisation approach to evaluate the suitability of linear machine topologies was established. This included the adoption of an optimisation approach followed earlier for linear machines for resonant free-piston Stirling engines to make provision for specific force dynamic responses and piston displacement. Several representative $\gamma_{Fxf/P}$

responses were then identified for the displacer, power piston and the combination of both to evaluate the suitability of linear electrical machines.

- A tubular, air-cored, longitudinal flux, permanent magnet linear machine was evaluated for application in free-piston Stirling engines. No evidence could be found that this particular topology has been considered before for application in free-piston Stirling engines. Design optimisations have been performed for both the traditional case as well as for direct piston displacement control. For the traditional case, the machine topology was found to be well suited. For the direct piston displacement control case, the machine topology was found to be suitable provided that adequate spring forces are introduced for the displacer.

Apart from the contributions listed above, the verification and improvement of the accuracy of a second order formulation for Stirling engines is also considered as a contribution to the field of Stirling engine research and design. This was an important prerequisite for the case study and the setting of specifications and design guidelines presented in Chapter 3.

6.4 Recommendations for future work

It is recommended that the following are considered for future work:

- Findings of Chapter 3 could be refined using a third order formulation. This could be combined with an effort to investigate free-piston Stirling engine design that specifically focuses on direct piston displacement control. Issues such as the advantages and disadvantages of the lowering of pumping losses in the heat exchangers could be investigated further. It is felt that a deeper understanding of the interrelated nature of the thermodynamics of free-piston Stirling engines and the ability to control the piston displacement should be further pursued.

- In the design optimisations reported in Chapter 5, start-up of the engine was not considered and the optimisation was specific to steady state operation as defined by the representative responses with which the linear machines were optimised. This issue should be concentrated on in future studies, as well as the practical operation of free-piston Stirling engines under direct piston displacement control.

- Experimental experience should also be helpful in developing an understanding of direct piston displacement control. It is therefore proposed that an effort be made to experimentally demonstrate direct piston displacement control. This could also serve to verify simulations, and simulations on the other hand, could again serve to help understand observations from an experimental study.

- Further evaluation of linear machine topologies should be undertaken. This is particularly important to gain further insight into the capabilities of other linear machine topologies with respect to the LFPM linear machine investigated here. If questions such as the

importance of spring forces for other topologies could be answered, then this could give further indication of the road ahead for direct piston displacement control and of free-piston Stirling engine design.

References

[1] C. M. Hargreaves, *The Philips Stirling engine*. Elsevier Science Publishers B.V., 1991.

[2] G. Walker, *Stirling engines*. Oxford University Press, 1980.

[3] G. T. Reader and C. Hooper, *Stirling engines*. E. and F.N. Spon, 1983.

[4] W. T. Beale, "The free-piston Stirling engine: 20 years of development," in *Proceedings of the 18th Intersociety Energy Conversion Engineering Conference*, vol. 2, Orlando, FL, August 1983, pp. 689–693.

[5] R. K. Shaltens and J. G. Schreider, "Comparison of conceptual designs for 25 kWe advanced Stirling conversion systems for dish electric applications," in *Proceedings of the 24th Intersociety Energy Conversion Engineering Conference*, vol. 5, Washington D.C., August 1989, pp. 2305–2315.

[6] Mechanical Techonology Inc., Sanders Associates Inc., Thermacore Inc., and Pioneer Engineering and Manufacturing Co., "Conceptual design of an advanced Stirling conversion system for terrestrial power generation," NASA Lewis Research Center, Cleveland, Ohio, Tech. Rep. NASA CR-180890, January 1988.

[7] A. J. Organ, *Thermodynamics and gas dynamics of the Stirling cycle machine*. Cambridge University Press, 1992.

[8] ——, *The regenerator and the Stirling engine*. Mechanical Engineering Publications Limited, 1997.

[9] D. A. Kaminski and M. K. Jensen, *Introduction to thermal and fluid engineering*. John Wiley and Sons, Inc., 2005.

[10] T. V. Adinarayan and M. V. Narasimhan, "Evaluation of displacement-time characteristics of Stirling engine drive mechanisms," in *Proceedings of the 25th Intersociety Energy Conversion Engineering Conference*, vol. 5, Reno, Nevada, August 1990, pp. 430–435.

[11] M. V. Narasimhan and T. V. Adinarayan, "Evaluation of displacement-time characteristics of Stirling engine drive mechanisms - II," in *Proceedings of the 25th Intersociety Energy Conversion Engineering Conference*, vol. 6, Reno, Nevada, August 1990, pp. 336–340.

[12] J. M. Strauss and R. T. Dobson, "Performance evaluation of a Stirling engine with different crank mechanisms," *Journal of Energy in Southern Africa*, submitted for publication.

[13] I. Urieli. (2001) Stirling Cycle Machine Analysis. Accessed: 18 May 2009. [Online]. Available: http://www.ent.ohiou.edu/ urieli/stirling/me422.html

[14] J. M. Strauss and R. T. Dobson, "Evaluation of a second order simulation for Stirling engine design and optimisation," *Journal of Energy in Southern Africa*, vol. 21, no. 2, pp. 17–29, May 2010.

[15] L. G. Thieme, "High-power baseline and motoring test results for the GPU-3 Stirling engine," NASA Lewis Research Center, Cleveland, Ohio, Tech. Rep. NASA TM-82646, June 1981.

[16] W. H. Percival, "Historical review of Stirling engine development in the United States from 1960 to 1970," NASA Lewis Research Center, Cleveland, Ohio, Tech. Rep. NASA CR-121097, July 1974.

[17] L. G. Thieme, "Low-power baseline test results for the GPU-3 Stirling engine," NASA Lewis Research Center, Cleveland, Ohio, Tech. Rep. NASA TM-79103, April 1979.

[18] D. M. Berchowitz, "Stirling cycle engine design and optimisation," Ph.D. dissertation, University of the Witswatersrand, Johannesburg, South Africa, August 1986.

[19] F. de Monte and G. Benvenuto, "Reflections on free-piston Stirling engines, part 2: Stable operation," *Journal of Propulsion and Power*, vol. 14, no. 4, pp. 509–518, July-August 1998.

[20] D. M. Berchowitz, "Operational characteristics of free-piston Stirling engines," in *Proceedings of the 23rd Intersociety Energy Conversion Engineering Conference*, vol. 1, Denver, Colorado, August 1988, pp. 107–112.

[21] M. M. Walsh, "Start-up and control method and apparatus for resonant free-piston Stirling engine," U.S. Patent 4 434 617, March, 1984.

[22] N. G. Vitale, "Externally excited resonant free-piston Stirling engine thermal amplifier system and method of operation and control thereof," U.S. Patent 4 567 726, February, 1986.

[23] T. Regan, "Free-piston Stirling convertor controller development at NASA Glenn Research Center," in *1st International Energy Conversion Engineering Conference*, Portsmouth, Virginia, August 2003.

[24] C. Genstler, I. Williford, and H. H. Bobry, "Stirling cycle generator control system and method for regulating displacement amplitude of moving members," U.S. Patent 6 050 092, April, 2000.

[25] M. Dhar, "Control scheme for power modulation of a free-piston Stirling engine," U.S. Patent 4 873 826, October, 1989.

[26] W. T. Beale and R. W. Redlich, "Linear generator or motor with integral magnetic spring," U.S. Patent 5 148 066, September, 1992.

[27] N. W. Lane and W. T. Beale, "A free-piston Stirling engine-alternator for solar electric power," in *8th International Symposium on Solar Thermal Concentrating Technologies*, Koln, Germany, October 1996.

[28] W. T. Beale, "Free-piston Stirling machine having variable spring between displacer and piston for power control and stroke limiting," U.S. Patent 5 385 021, January, 1995.

[29] ——, "Free-piston Stirling machine having a controllably switchable work transmitting linkage between displacer and piston," U.S. Patent 5 502 968, April, 1996.

[30] R. W. Redlich and D. M. Berchowitz, "Linear dynamics of free-piston Stirling engines," *Proceedings Institution of Mechanical Engineers*, vol. 199, no. A3, pp. 203–213, March 1985.

[31] J. S. Sullivan, "Nasa Lewis Stirling Engine Computer Code Evaluation," NASA Lewis Research Center, Washington DC, Tech. Rep. DOE/NASA/4105-4, 1989.

[32] A. S. Gaunekar, T. Göddenhenreich, and C. Heiden, "Finite element analysis and testing of flexure bearing element," *Cryogenics*, vol. 36, no. 5, pp. 359–364, 1996.

[33] J. Schutte, "Optimisation of a transverse flux linear PM generator using 3d Finite Element Analysis," Master's thesis, University of Stellenbosch, Stellenbosch, December 2011.

[34] I. Urieli, "A computer simulation of Stirling cycle machines," Ph.D. dissertation, University of the Witswatersrand, Johannesburg, South Africa, February 1977.

[35] H. Snyman, T. M. Harms, and J. M. Strauss, "Design analyis methods for Stirling engines," *Journal of Energy in Southern Africa*, vol. 19, no. 3, pp. 4–19, August 2008.

[36] E. D. Rogdakis, N. A. Bormpilas, and I. K. Koniakos, "A thermodynamic study for the optimization of stable operation of free-piston Stirling engines," *Energy Conversion and Management*, vol. 45, no. 4, pp. 575–593, March 2004.

[37] M. D. Kankam, J. S. Rauch, and W. Santiago, "Dynamic analysis of free-piston Stirling engine/linear alternator-load system - experimentally validated," in *Proceedings of the 27th Intersociety Energy Conversion Engineering Conference*, San Diego, California, August 1992.

[38] G. Benvenuto and F. de Monte, "Analysis of free-piston Stirling engine/linear alternator system part 1: Theory," *Journal of Propulsion and Power*, vol. 11, no. 5, pp. 1036–1046, September-October 1995.

[39] ——, "Analysis of free-piston Stirling engine/linear alternator system part 2: Results," *Journal of Propulsion and Power*, vol. 11, no. 5, pp. 1047–1055, September-October 1995.

[40] ——, "The effect of nonlinear thermo-fluid-dynamic terms of free-piston Stirling machine stability," in *Proceedings of the 31st Intersociety Energy Conversion Engineering Conference*, Washington, DC, August 1996, pp. 1224–1231.

[41] F. de Monte and G. Benvenuto, "Reflections on free-piston Stirling engines, part 1: Cyclic steady operation," *Journal of Propulsion and Power*, vol. 14, no. 4, pp. 499–508, July-August 1998.

[42] N. W. Lane and W. T. Beale, "Free-piston Stirling design features," in *Proceedings of the 8th International Stirling Engine Conference and Exhibition*, Ancona, Italy, 1997, pp. 267–276.

[43] I. Boldea and S. A. Nasar, "Permanent magnet linear alternators Part I: Fundamental equations," *IEEE Transactions on Aerospace and Electronic Systems*, vol. AES-23, no. 1, pp. 73–78, January 1987.

[44] ——, "Permanent magnet linear alternators Part II: Design guidelines," *IEEE Transactions on Aerospace and Electronic Systems*, vol. AES-23, no. 1, pp. 79–82, January 1987.

[45] ——, *Linear electric actuators and generators*. Cambridge University Press, 2005.

[46] J. Schutte and J. M. Strauss, "Optimisation of a transverse flux linear pm generator using 3d finite element analysis," in *Proceedings of the 19th International Conference on Electrical Machines*, Rome, Italy, September 2010, pp. 1–6.

[47] S. A. Nasar and C. Chen, "Study of free-piston Stirling engine driven linear alternators," NASA Lewis Research Center, Cleveland, Ohio, Tech. Rep. NASA CR-181425, 1987.

[48] S. M. Geng, G. E. Schwarze, and J. M. Niedra, "A 3-D magnetic analysis of a linear alternator for a Stirling power system," in *Proceedings of the 35th Intersociety Energy Conversion Engineering Conference*, vol. 1, Las Vegas, Nevada, July 2000, pp. 232–237.

[49] P. Francois, I. G. Burrel, H. B. Ahmed, L. Prévond, and B. Multon, "3D analytical model for a tubular linear induction generator in a Stirling cogeneration system," in *Proceedings of the International Electric Machines & Drives Conference*, vol. 1, Antalya, May 2000, pp. 392–397.

[50] J. Schutte, L. Joubert, and J. M. Strauss, "Constrainted optimisation of a transverse flux PM linear generator," in *Proceedings of the 20th International Conference on Electrical Machines*, Marseilles, France, September 2012, pp. 595–599.

[51] L. Joubert, J. Schutte, J. M. Strauss, and R. Dobson, "Design optimisation of a transverse flux, short stroke, linear generator," in *Proceedings of the 20th International Conference on Electrical Machines*, Marseilles, France, September 2012, pp. 640–646.

[52] G. Venter, "Review of optimization techniques," in *Encyclopedia of Aerospace Engineering*. John Wiley and Sons, Ltd., 2010, pp. 5229–5238.

[53] M. M. Walsh, "Resonant free-piston Stirling engine having virtual rod displacer and linear electrodynamic machine control of displacer drive/damping," U.S. Patent 4 458 489, July, 1984.

[54] J. G. Schreiber and L. G. Thieme, "Overview of NASA GRC Stirling technology development," NASA Glenn Research Center, Cleveland, Ohio, Tech. Rep. NASA TM-2004-212969, May 2004.

[55] I. Boldea and S. A. Nasar, "Linear electric actuators and generators," *IEEE Transactions on Energy Conversion*, vol. 14, no. 3, pp. 712–716, September 1999.

[56] J. Wang, D. Howe, and Z. Lin, "Comparative studies on linear motor topologies for reciprocating vapor compressors," in *Proceedings of the IEEE International Electric Machines and Drives Conference*, Antalya, Turkey, May 2007, pp. 364–369.

[57] S.-M. Jang, J.-Y. Choi, H.-W. Cho, and S.-H. Lee, "Thrust analysis and measurement of tubular linear actuator with cylindrical halbach array," *IEEE Transactions on Magnetics*, vol. 41, no. 5, pp. 2028–2031, May 2005.

[58] J. Wang, G. W. Jewell, and D. Howe, "A general framework for the analysis and design of tubular linear permanent magnet machines," *IEEE Transactions on Magnetics*, vol. 35, no. 3, pp. 1986–2000, May 1999.

[59] J. F. Gieras, R.-J. Wang, and M. J. Kamper, *Axial Flux Permanent Magnet Brushless Machines*. Kluwer Academic Publishers, 2004.

[60] R.-J. Wang, "Design aspects and optimisation of an axial field permanent magnet machine with an ironless stator," Ph.D. dissertation, University of Stellenbosh, Stellenbosch, South Africa, March 2003.

[61] P.-J. Randewijk, "Analysis of a radial flux air-cored permanent magnet machine with a double-sided rotor and non-overlapping windings," Ph.D. dissertation, University of Stellenbosh, Stellenbosch, South Africa, March 2012.

[62] A. Abdel-Razek, J. Coulomb, M. Feliachi, and J. Sabonnadiere, "Conception of an air-gap element for the dynamic analysis of the electromagnetic field in electric machines," *IEEE Transactions on Magnetics*, vol. 18, no. 2, pp. 655–659, March 1982.

[63] R.-J. Wang, H. Mohellebi, T. Flack, M. J. Kamper, J. Buys, and M. Feliachi, "Two-dimensional cartesian air-gap element (CAGE) for dynamic finite element modelling of electrical machines with a flat airgap," *IEEE Transactions on Magnetics*, vol. 38, no. 2, pp. 1357–1360, 2002.

[64] S. Gerber, "A finite element-based optimisation tool for electrical machines," Master's thesis, University of Stellenbosch, Stellenbosch, March 2011.

Appendix A

A second order formulation for Stirling engine simulations

A.1 Introduction

Throughout the years, many different approaches have been developed to analyse, simulate and assist in Stirling engine design and optimisation. What follows below is a detailed description of a second order formulation for Stirling engine simulation as developed by Urieli [13] and adopted by Strauss and Dobson [14].

In Section A.2, a brief comparison of second and third order formulations follows to give insight into the applicability of the implemented second order formulation.

A detailed description of the formulation follows in section A.3, followed by an assessment of the accuracy of the simulation in section A.4 and a short conclusion in section A.5.

A.2 Second order vs. third order formulations

Reader [3] gives a brief description of the various analysis techniques for Stirling engines developed through the years. Of these, only what became known as second order and third order formulations have the ability to provide insight into operational parameters, such as pressure and mass flow at a given time and position within the engine. While levels of complexity vary within these two broad categories, it is possible to make a distinction between the two.

Third order formulations consider the thermodynamic, gas dynamic and heat transfer aspects of the working gas as it flows within the engine. The solution to any flow problem must satisfy the underlying conservation laws, i.e. it must satisfy the equations for continuity, momentum and energy. These equations are nonlinear and require iterative solutions that will hopefully convert to a final solution. Two techniques to deal with such flow situations are known as the 'method of characteristics' and 'nodal analysis' [3].

In short, the method of characteristics is a technique for solving partial differential equations. In Stirling engine simulations, it involves a transformation of the partial differential

form of the conservation laws to axes along which the changes in thermodynamic properties are in the form of ordinary differential equations. The advantage of a method of characteristics approach according to Organ [7] lies in the ability of this approach to cope with discontinuities in gradients of all properties. It is however a method that demands programming skills and computing time.

Nodal analysis uses the same fundamental equations as the method of characteristics technique, but approaches the problem from a control volume perspective. The engine is subdivided into a number of cells and the conservation laws are applied to each cell. The individual cells are interconnected by interfaces having zero volume called nodes. The working fluid properties are considered to be constant throughout each cell, but may be discontinuous at the nodes. Property values that are assigned to the nodes are those of the neighbouring upstream cell depending on the flow direction of the working fluid. The variable volume working spaces (expansion and compression spaces) are allocated one cell each, but the heat exchangers and regenerator may be allocated several cells each. The nodal analysis technique may suffer from the problem that the physical laws can be involuntarily violated because information can be propagated faster between nodes due to finite integration time steps than can be propagated physically [3].

Second order formulations are normally simplified and/or idealised variations of the nodal analysis technique. Also called a decoupled analysis by Reader [3], second order formulations do not make provision for all thermodynamic and gas dynamic phenomena during cyclic simulation, but determine the basic energy transfers during cyclic simulation and then attenuate these values afterwards by calculating the identifiable energy losses in the system using the same cyclically calculated data. As an example, the ideal mass flow rates are calculated assuming no pressure drops during cyclic simulation, and then the pressure drops within the system are calculated using these mass flows.

The assumption that all of these loss quantities merely add up is however somewhat arbitrary. Losses in Stirling engines are interrelated, where one loss mechanism influences another. By merely adding all of the losses calculated separately, the total calculated losses could end up being higher than what is found in practice.

A.3 Detailed description

A.3.1 Overview

The second order formulation detailed below may be described as an ideal adiabatic formulation that was expanded to include several non-idealities and losses. The description below will therefore firstly deal with the ideal adiabatic formulation and will then explain the expansion thereof. While improvements have been made to the original formulation of Urieli, the reader should assume that the work described below is that of Urieli, unless indicated otherwise.

A.3.2 Ideal adiabatic formulation

General overview

Consider the generalised cell shown in figure A.1 below.

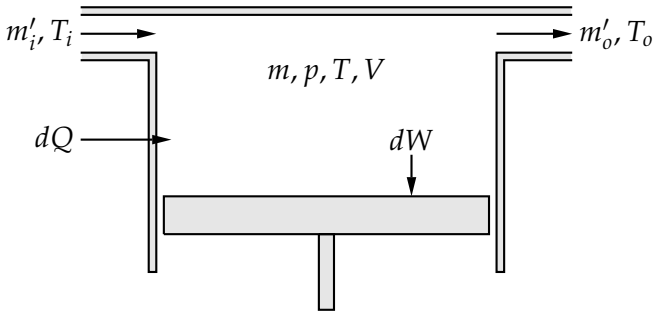

Figure A.1: Generalised cell [13].

The symbols, m, p, T and V denote the mass of gas, pressure, temperature and volume of the generalised cell respectively. The rate of heat transfer into the cell is denoted by dQ and the rate of work done on the surroundings is denoted by dW. The subscripts i and o denote inflowing and outflowing respectively.

All derivatives in this appendix, including those in figure A.1, are with respect to the cycle angle θ. The derivative operator denoted by d is used instead of $d/d\theta$ for simplified reading.

The energy equation of the working gas in the generalised cell for non-steady flow may then be formulated as

$$dQ + \left(c_p T_i m_i' - c_p T_o m_o'\right) = dW + c_v d\left(mT\right). \tag{A.1}$$

In (A.1), c_p and c_v are the specific heat capacities of the gas at constant pressure and constant volume respectively. The two terms to the left represent the rate of heat transfer into the cell and the net enthalpy convected into the cell, while the two terms to the right represent the rate of work done on the surroundings and the rate of increase of internal energy in the cell. Kinetic and potential energy terms have been neglected in (A.1).

A reasonable assumption for Stirling engines is to assume that the working gas is ideal. The equation of state for the generalised cell in standard as well as differential form is then presented as

$$pV = mRT \tag{A.2}$$

and

$$dp/p + dV/V = dm/m + dT/T. \tag{A.3}$$

Figure A.2 shows the schematic representation of the ideal adiabatic model of an alpha type Stirling engine. This formulation is equally applicable to beta and gamma type engines. The compression and expansion spaces are assumed to be adiabatic, i.e. no heat is transferred to

and from the surroundings. The heat exchangers are assumed to be ideal and the regenerator is assumed to be perfectly effective.

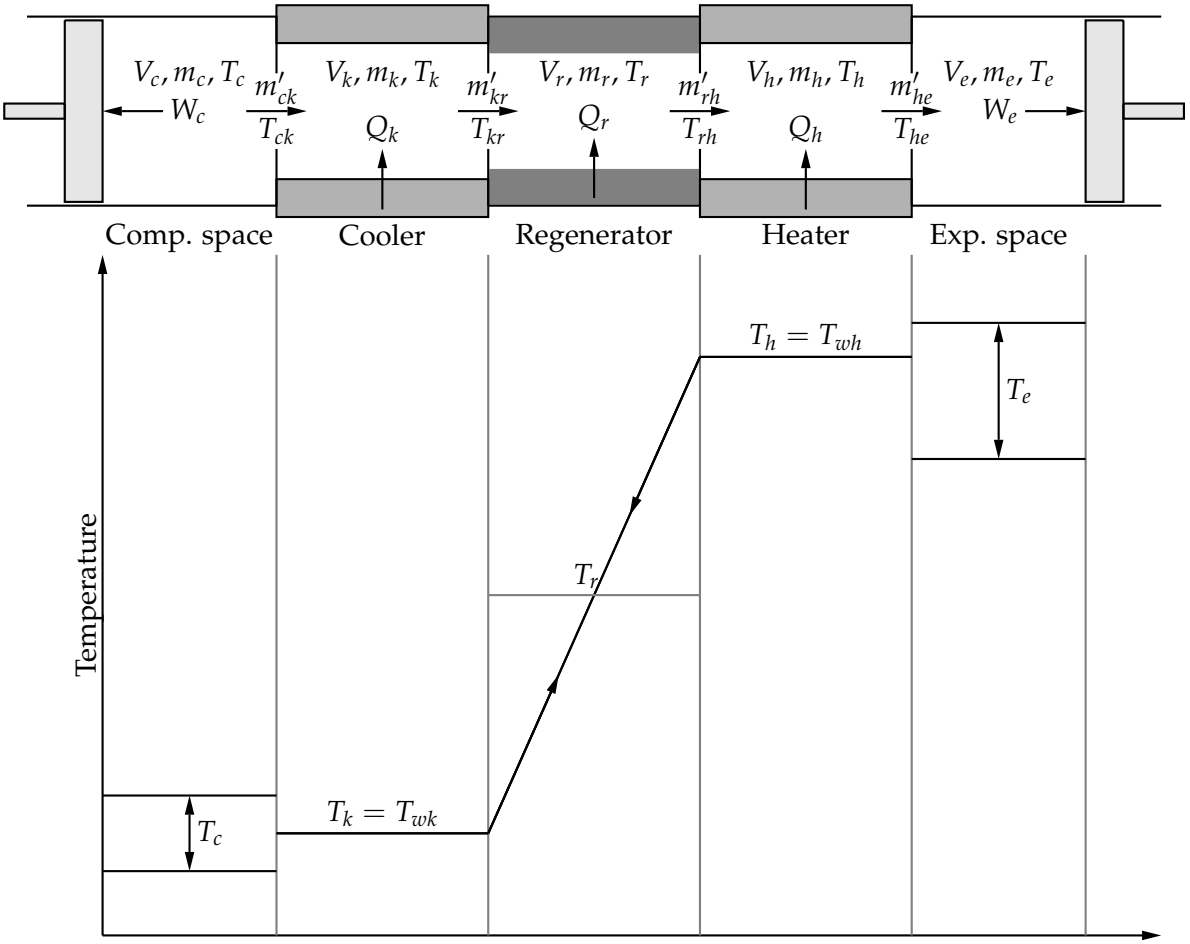

Figure A.2: Ideal adiabatic model representation and temperature profile [13].

In figure A.2, the subscripts c, k, r, h and e denote the compression space, cooler, regenerator, heater and expansion space respectively. The subscripts ck, kr, rh and he denote the four interfaces between the cells. The arrows on the interfaces represent positive direction of flow, and enthalpy is transported across the interfaces in terms of a mass flow rate m' and an upstream temperature T.

The temperatures T_{ck} and T_{he} are conditional on the direction of flow, since the enthalpies flowing across the interfaces ck and he carry the respective adjacent upstream cell temperatures. This could be defined as follows, namely

$$\begin{aligned} &\text{if } m'_{ck} > 0 \text{ then } T_{ck} = T_c \text{ else } T_{ck} = T_k \\ &\text{if } m'_{he} > 0 \text{ then } T_{he} = T_h \text{ else } T_{he} = T_e. \end{aligned} \tag{A.4}$$

The temperature diagram in figure A.2 underlines the assumptions made above, i.e. that the heater and cooler temperatures are constant due to ideal heat exchange, that the compression space and expansion space temperatures T_c and T_e vary over the cycle in accordance with the adiabatic compression and expansion occurring in the these spaces, and that regeneration is

perfectly effective (compare for instance with figure A.3).

It is further assumed that no gas leakage occurs and that there is no pressure drop in the system, i.e. the pressure p (not shown in figure A.2) represents the instantaneous pressure throughout the system.

Development of equation set

The analysis starts with the total mass of gas in the machine being constant, thus

$$m_c + m_k + m_r + m_h + m_e = M. \tag{A.5}$$

Substituting for the mass in each cell from the ideal gas equation of state given in (A.2) yields

$$p\left(V_c/T_c + V_k/T_k + V_r/T_r + V_h/T_h + V_e/T_e\right)/R = M, \tag{A.6}$$

where the mean effective temperature T_r of the regenerator is equal to the log mean temperature difference given by

$$T_r = \left(T_h - T_k\right) / \ln\left(T_h/T_k\right). \tag{A.7}$$

The pressure may now be written as

$$p = MR/\left(V_c/T_c + V_k/T_k + V_r/T_r + V_h/T_h + V_e/T_e\right). \tag{A.8}$$

Differentiation of the equation of mass given in (A.5) yields

$$dm_c + dm_k + dm_r + dm_h + dm_e = 0. \tag{A.9}$$

The temperatures and volumes of the heat exchanger and regenerator cells remain constant. The differential form of the equation of state given in (A.3) then reduces to

$$dp/p = dm/m \tag{A.10}$$

and with further manipulation yields

$$dm = mdp/p = \left(dp/R\right)\left(V/T\right). \tag{A.11}$$

Substitution of (A.11) in (A.9) yields

$$dm_c + dm_e + \left(dp/R\right)\left(V_k/T_k + V_r/T_r + V_h/T_h\right) = 0. \tag{A.12}$$

To obtain an explicit equation of dp, then dm_c and dm_e should be eliminated in (A.12). Now, consider the adiabatic compression space shown in figure A.2. Applying the energy equation

in (A.1) to this space, we obtain

$$-c_p T_{ck} m'_{ck} = dW + c_v d\left(m_c T_c\right). \tag{A.13}$$

From continuity considerations, the rate of accumulation of gas dm_c is equal to the mass inflow of gas given by $-m'_{ck}$. The rate of work done dW_c is given by pdV_c. Thus

$$c_p T_{ck} dm_c = pdV_c + c_v d\left(m_c T_c\right). \tag{A.14}$$

When substituting the ideal gas relations

$$\begin{aligned} pV_c &= m_c R T_c \\ c_p - c_v &= R \\ c_p / c_v &= \gamma, \end{aligned} \tag{A.15}$$

in (A.14),

$$dm_c = \left(pdV_c + V_c dp/\gamma\right) / \left(RT_{ck}\right) \tag{A.16}$$

is obtained after some simplification. The rate of gas flow for the expansion space may be derived similarly, i.e.

$$dm_e = \left(pdV_e + V_e dp/\gamma\right) / \left(RT_{he}\right). \tag{A.17}$$

By substitution of (A.16) and (A.17) into (A.12), and with simplification, an explicit equation for the derivative of the pressure is obtained, namely

$$dp = \frac{-\gamma p\left(dV_c/T_{ck} + dV_e/T_{he}\right)}{\left(V_c/T_{ck} + \gamma\left(V_k/T_k + V_r/T_r + V_h/T_h\right) + V_e/T_{he}\right)}. \tag{A.18}$$

From the differential form of the equation of state in (A.3), expressions for the rate of change of the compression and expansions temperatures are obtained, namely

$$dT_c = T_c\left(dp/p + dV_c/V_c - dm_c/m_c\right) \tag{A.19}$$

and

$$dT_e = T_e\left(dp/p + dV_e/V_e - dm_e/m_e\right) \tag{A.20}$$

respectively. Applying the energy equation in (A.1) to each of the heat exchangers and regenerator cells, where the work done on the surroundings is zero (i.e. $dW = 0$) and the temperatures are constant, and substituting for the differential form of the equation of state for a heat exchanger cell, as given in (A.11), the following expression is obtained, namely

$$dQ + \left(c_p T_i m'_i - c_p T_o m'_o\right) = c_v T dm = V dp c_v / R. \tag{A.21}$$

Thus, for the two heat exchangers and regenerator cells we obtain

$$\begin{aligned} dQ_k &= V_k dp c_v/R - \left(c_p T_{ck} m'_{ck} - c_p T_{kr} m'_{kr}\right) \\ dQ_r &= V_r dp c_v/R - \left(c_p T_{kr} m'_{kr} - c_p T_{rh} m'_{rh}\right) \\ dQ_h &= V_h dp c_v/R - \left(c_p T_{rh} m'_{rh} - c_p T_{he} m'_{he}\right). \end{aligned} \tag{A.22}$$

Since the heat exchangers are isothermal and the regenerator is ideal, $T_{kr} = T_k$ and $T_{rh} = T_h$.

Finally, the work done in the compression and expansion cells is given by

$$\begin{aligned} W &= W_c + W_e \\ dW &= dW_c + dW_e \\ dW_c &= p dV_c \\ dW_e &= p dV_e. \end{aligned} \tag{A.23}$$

Table A.1 lists a summary of all the relevant differential and algebraic equations required for the ideal adiabatic simulation.

Method of solution

The ideal adiabatic solution is solved numerically for a specific configuration with specific operating conditions due to the nonlinear nature of the equations, especially with regard to the conditional temperatures. In the original simulation developed by Urieli [13], the various input parameters are defined according to the following:

- V_c, V_e, dV_c and dV_e are defined by the engine configuration and geometry and the mechanical drive mechanism as analytic functions of the crank angle θ.
- The void volumes V_h, V_r and V_k are defined by the heat exchanger and renegerator geometries.
- R, c_p, c_v and γ are defined by the choice of working gas.
- T_k and T_h and thus the mean effective temperature T_r are specified by the operating conditions.
- The mass of gas M is specified by specifying the mean operating pressure and then by using the Schmidt analysis to obtain the total mass of gas.

Strauss and Dobson [14] deviated from the original simulation by expanding the capabilities of the simulation.

It is sometimes either inconvenient or impossible to define the volumetric change and rate of change as analytical functions of the crank angle θ. The simulation was therefore adopted to accept any arbitrary displacement pattern and by using spline mathematics, it is possible to calculate the first and second derivatives necessary for the simulation.

Table A.1: Summary of all the relevant equations for the ideal adiabatic simulation.

Equations for pressure

$$p = MR/\left(V_c/T_c + V_k/T_k + V_r/T_r + V_h/T_h + V_e/T_e\right)$$

$$dp = \frac{-\gamma p\left(dV_c/T_{ck} + dV_e/T_{he}\right)}{\left(V_c/T_{ck} + \gamma\left(V_k/T_k + V_r/T_r + V_h/T_h\right) + V_e/T_{he}\right)}$$

Equations for masses

$$m_c = pV_c/\left(RT_c\right)$$
$$m_k = pV_k/\left(RT_k\right)$$
$$m_r = pV_r/\left(RT_r\right)$$
$$m_h = pV_h/\left(RT_h\right)$$
$$m_e = pV_e/\left(RT_e\right)$$

Equations for mass accumulation

$$dm_c = \left(pdV_c + V_c dp/\gamma\right)/\left(RT_{ck}\right)$$
$$dm_e = \left(pdV_e + V_e dp/\gamma\right)/\left(RT_{he}\right)$$

Equations for mass flow

$$m'_{ck} = -dm_c$$
$$m'_{kr} = m'_{ck} - dm_k$$
$$m'_{he} = dm_e$$
$$m'_{rh} = m'_{he} + dm_h$$

Equations for conditional temperatures

if $m'_{ck} > 0$ then $T_{ck} = T_c$ else $T_{ck} = T_k$

if $m'_{he} > 0$ then $T_{he} = T_h$ else $T_{he} = T_e$

Equations for temperatures

$$dT_c = T_c\left(dp/pd + V_c/V_c - dm_c/m_c\right)$$
$$dT_e = T_e\left(dp/pd + V_e/V_e - dm_e/m_e\right)$$

Equations for energy

$$dQ_k = V_k dpc_v/R - \left(c_p T_{ck} m'_{ck} - c_p T_{kr} m'_{kr}\right)$$
$$dQ_r = V_r dpc_v/R - \left(c_p T_{kr} m'_{kr} - c_p T_{rh} m'_{rh}\right)$$
$$dQ_h = V_h dpc_v/R - \left(c_p T_{rh} m'_{rh} - c_p T_{he} m'_{he}\right)$$
$$W = W_c + W_e$$
$$dW = dW_c + dW_e$$
$$dW_c = pdV_c$$
$$dW_e = pdV_e$$

Given the adoption to accept any arbitrary displacement pattern, specifying the total mass of gas M according to Urieli's approach [13] now becomes problematic, since his approach is

only possible if analytical equations exist for the displacement of the power piston and displacer.

Strauss and Dobson followed another approach, namely to calculate the mass of gas during each cyclic simulation in order to maintain a certain mean or peak pressure. In their approach an initial mass of gas is assumed. The pressure as a function of crank angle is then obtained as one of the outputs of cyclic simulation. The mass of gas - as well as all of the simulation outputs directly proportional to the mass of gas - is then recalculated in order to adjust the mean or peak pressure - according to the input specifications - to the desired value. In this way the mean or peak pressure becomes part of the input specifications and the mass of gas an output parameter.

Mainly two advantages arise from this approach in determining the mass of gas. Firstly, that either the mean or the peak pressure can be specified and secondly, that the mean or peak pressure can be determined accurately. This in not the case in the approach followed by Urieli [13], where the final mean pressure is only approximately equal to the input specification.

Apart from the input parameters specified above, 22 variables and 16 derivatives should be solved over a complete cycle for the equation set in table A.1. These include:

- Seven derivatives to be integrated numerically to obtain T_c, T_e, Q_k, Q_r, Q_h, W_c and W_e.
- Nine analytical variables and derivatives W, p, V_c, V_e, m_c, m_k, m_r, m_h and m_e.
- Six conditional and mass flow variables with undefined derivatives T_{ck}, T_{he}, m'_{ck}, m'_{kr}, m'_{rh} and m'_{he}.

This problem is treated as a quasi steady-flow system, thus over each integration interval the four mass flow variables m'_{ck}, m'_{kr}, m'_{rh} and m'_{he} remain constant with no acceleration effects. Thus, we consider the problem as that of solving a set of seven simultaneous ordinary differential equations.

The simplest approach to solve a set of ordinary differential equations is to formulate it as an initial-value problem. The initial values of all the variables are known and the equations are integrated from the initial state over a complete cycle.

Let the vector $\mathbf{Y}$ represent the seven unknown variables. With the initial conditions given by $\mathbf{Y}(\theta = 0) = \mathbf{Y}_0$ and using the set of differential equations $\mathbf{dY} = \mathbf{F}(\theta, \mathbf{Y})$, as well as the other algebraic and conditional equations listed in table A.1, a solution can be obtained for the functions $\mathbf{Y}(\theta)$ to satisfy both the differential equations and the initial conditions. Urieli [13] implemented the fourth order Runge-Kutta method for solving this initial-value problem numerically.

Unfortunately, the ideal adiabatic model is not an initial value problem, but rather a boundary value problem. We do not for instance know the values of the working space gas temperatures T_c and T_e at $\theta = 0$. The only guidance that we have to their values at $\theta = 0$ is that their values at the end of the steady-state cycle should be equal to their values at the beginning of the cycle.

However, because of the cyclic nature of the simulation, the system can be approached as an initial value problem by assigning arbitrary initial conditions. Integration of the equations through several cycles will eventually lead to cyclic steady state, equivalent to the transient warm-up operation of an actual machine. Urieli [13] states the the most sensitive measure of convergence to cyclic steady state is the residual regenerator heat Q_r at the end of the cycle, which should be zero due to the assumption of perfectly effective regeneration.

A.3.3 Expanded formulation

Overview

The ideal adiabatic model in itself does not give significantly different results from those of an ideal isothermal model. However, the behaviour of the ideal adiabatic model is more realistic in that the various results are consistent with the expected limiting behaviour of real machines, e.g. in contrast with the ideal isothermal model, the heat exchangers become necessary components without which the engine will not function.

The required differential equation approach of the ideal adiabatic model and its solution reveals the considerable amount of heat transferred in the regenerator, emphasising its importance. Furthermore, it provides a natural basis for extending the analysis to include non-idealities, since all the variables of the system are available throughout the simulation process, e.g. the mass flow rates through the heat exchangers can be used to evaluate the heat transfer and flow friction effects over the entire cycle.

The expanded formulation entails the incorporation of heat transfer and flow-friction effects of the heat exchangers and regenerator into the cyclic simulation and/or consideration thereof in calculating the performance parameters afterwards.

The following non-idealities will be treated as part of the expanded formulation:

- Regenerator effectiveness and non-ideal thermal efficiency;
- Regenerator wall heat leakage;
- Imperfect heat exchange;
- Pumping losses.

Figure A.3 shows the temperature profile of the expanded formulation[1], including non-ideal heater and cooler heat exchanger temperature distribution and non-perfect regenerator effectiveness.

In figure A.3, T_{wk} and T_{wh} refer to the wall temperature of the cooler and the heater respectively. $T_{k(mean)}$ and $T_{h(mean)}$ denote the mean cooler and heater gas temperatures. Q_k, Q_h and Q_r denote the heat transfer in the cooler, heater and regenerator respectively.

[1]Compare this temperature profile with that given for the ideal adiabatic model in figure A.2.

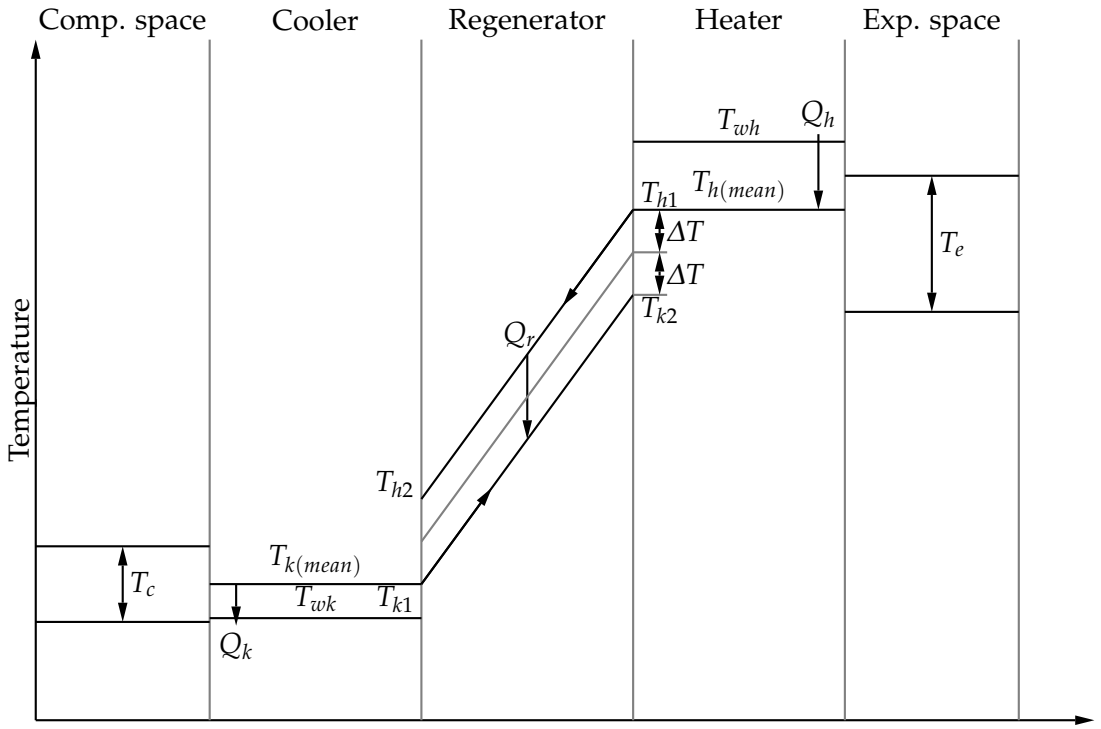

Figure A.3: Temperature profile diagram including non-ideal heater and cooler heat exchanger temperature distribution and non-perfect regenerator effectiveness [13].

Regenerator effectiveness and non-ideal thermal efficiency

A regenerator is by definition a cyclic device. During the first part of the cycle, the hot gas flows through the regenerator from the heater to the cooler and heat is transferred to the regenerator matrix. This will be referred to as a single blow. During the second part of the cycle, the cold gas flows in the reverse direction. Heat that was stored in the matrix previously is then absorbed. Thus, at steady state the net heat transferred per cycle between the working gas and the regenerator is zero.

Urieli [13] in the context of the ideal adiabatic model, proposed a definition for the regenerator effectiveness ϵ as

$$\epsilon = \frac{\begin{pmatrix}\text{amount of heat transferred from matrix to gas}^2\\ \text{during a single blow through the regenerator}\end{pmatrix}}{\begin{pmatrix}\text{equivalent amount of heat transferred in the}\\ \text{regenerator of the ideal adiabatic model}\end{pmatrix}}. \tag{A.24}$$

The regenerator effectiveness ϵ thus varies from 1 for an ideal regenerator as defined in the ideal adiabatic model to 0 for no regenerative action. The thermal efficiency of the ideal adiabatic cycle is given in terms of the energy values accumulated at the end of the cycle, i.e.

$$\eta_i = W_i / Q_{hi} = (Q_{hi} + Q_{ki}) / Q_{hi}, \tag{A.25}$$

where the subscript i denotes 'ideal' and W_i and Q_{hi} denote the work output and input heat

[2]Or alternatively from gas to matrix to be in accordance with the discussion further on in this section.

energy respectively and where Q_{ki} by choice is negative for heat flowing from the gas to the heat exchanger.

Now, for non-ideal regeneration in a system with the gas flowing from the cooler to the heater during a single blow, the gas will have a temperature somewhat lower than that of the heater on exit from the regenerator. This will result in more heat being supplied externally over the cycle by the heater to increase the temperature of the gas to that of the heater, and can be written as

$$Q_h = Q_{hi} + \hat{Q}_{ri}\,(1-\epsilon)\,, \tag{A.26}$$

where Q_h denotes the total amount of heat supplied over the cycle by the heater and $\hat{Q}_{ri}$ denotes the amount of heat transferred during a single blow of the regenerator. Similarly, when the working gas flows from the heater to the cooler, the cooler will have an extra cooling load that can be expressed as

$$Q_k = Q_{ki} - \hat{Q}_{ri}\,(1-\epsilon)\,. \tag{A.27}$$

The thermal efficiency of the non-ideal engine in given by

$$\eta = W/Q_h = (Q_h + Q_k)\,/Q_h. \tag{A.28}$$

Substituting for η_i, Q_h and Q_k from (A.25), (A.26) and (A.27), an expression is obtained for the thermal efficiency of the engine in terms of the ideal adiabatic thermal efficiency and regenerator effectiveness, namely

$$\eta = \frac{\eta_i}{1 + \left(\dfrac{\hat{Q}_{ri}}{Q_{hi}}\right)(1-\epsilon)}. \tag{A.29}$$

Do take note that in real engines the amount of heat transferred during a single blow to or from the regenerator $\hat{Q}_{ri}$ is of the order of 5 times and even more than the heat transferred to the gas in the heater Q_h. A small change in regenerator effectiveness thus has a profoundly negative effect on engine efficiency, as underlined by (A.29).

The approach to bring imperfect regenerator effectiveness into consideration will now be explained. Figure A.3 shows the difference between the temperature profile of the 'hot' gas stream, i.e. for the gas flowing from the heater to the cooler, and the 'cold' gas stream, i.e. for the gas flowing from the cooler to the heater. This difference is due to imperfect regenerator effectiveness as has been explained above.

If we assume an equal difference in temperature ΔT on the hot and cold sides and linear temperature profiles, regenerator effectiveness in terms of temperatures is then defined as

$$\epsilon \equiv \frac{T_{h1} - T_{h2}}{T_{h1} - T_{k1}}. \tag{A.30}$$

This definition of regenerator effectiveness is in accordance with the description provided in (A.24). For perfect effectiveness, the amount of heat transferred from the matrix to the gas during a single blow through the regenerator will be the same as the equivalent amount of heat transferred for the ideal adiabatic case and the value of the temperature T_{k2} will be that of T_{h1}. For no regenerative effect, no heat will be transferred to the gas and the gas will exit the regenerator at the temperature that the gas entered the regenerator, i.e. T_{k2} will be equal to T_{k1}. The temperature difference ΔT can be obtained from

$$\begin{aligned} 2\Delta T &= T_{h2} - T_{k1} \\ &= T_{h1} - T_{k2}. \end{aligned} \tag{A.31}$$

By combining (A.30) and (A.31) we obtain

$$\epsilon = \frac{1}{1 + \dfrac{2\Delta T}{T_{h1} - T_{h2}}}. \tag{A.32}$$

The change in enthalpy of the hot stream is equal to the heat transfer from the hot stream to the matrix to maintain energy balance, and subsequently from the matrix to the cold stream. Thus

$$\begin{aligned} \dot{Q} &= c_p \dot{m} \left(T_{h1} - T_{h2}\right) \\ &= 2hA_{wg}\Delta T, \end{aligned} \tag{A.33}$$

where $\dot{Q}$ is the rate of heat transfer in watt, h is the overall heat transfer coefficient (hot stream to matrix to cold stream), A_{wg} refers to the wetted area of the heat exchanger surface and $\dot{m}$ refers to the mass flow rate through the regenerator. Substituting (A.33) into (A.32), we obtain

$$\epsilon = \frac{1}{1 + \dfrac{c_p \dot{m}}{hA_{wg}}}. \tag{A.34}$$

Urieli [13] introduced the concept of Number of Transfer Units (NTU), which is a well known measure of heat exchanger effectiveness, namely

$$\text{NTU} = \frac{hA_{wg}}{c_p \dot{m}}. \tag{A.35}$$

Thus

$$\epsilon = \frac{\text{NTU}}{1 + \text{NTU}}. \tag{A.36}$$

The NTU value is a function of the type of heat exchanger, its physical size as well as the actual mass flow through the regenerator in this case. In heat exchanger analysis, local heat exchanger parameters are usually evaluated in terms of fluid property values which are independent of size. These can be obtained by defining the NTU value in terms of a Stanton number. Thus, by

defining the Stanton number as

$$N_{ST} = h/\left(\rho u c_p\right), \tag{A.37}$$

where ρ is the fluid density and u is the fluid velocity, and by expressing the mass flow rate as

$$\dot{m} = \rho u A, \tag{A.38}$$

where A is the free flow area through the matrix, the NTU value expressed in (A.35) becomes

$$\text{NTU} = N_{ST}\left(A_{wg}/A\right)/2. \tag{A.39}$$

The Stanton number has found favour because of the ease with which it can be obtained from experimental data. Tables and graphs of empirical values of Stanton number vs. Reynolds number are also available from heat exchanger texts for various heat exchanger types. Urieli [13] made provision for woven mesh and coiled annular foil type matrices.

The factor 2 in (A.39) is unusual and stems from the fact that the Stanton number is usually defined for the transfer of heat from the gas stream to the matrix. The NTU usage in this case is however for overall transfer of heat from the hot stream to the regenerator matrix and subsequently to the cold stream.

Finally, regenerator enthalpy loss is calculated using

$$\begin{aligned} Q_{rloss} &= (1-\epsilon)\,\hat{Q}_{ri} \\ &= \left(1 - \frac{\text{NTU}}{1+\text{NTU}}\right)\hat{Q}_{ri} \end{aligned} \tag{A.40}$$

Calculation of the regenerator enthalpy loss in the expanded formulation may then be summarised as follows:

- Once the cyclic ideal adiabatic simulation is completed, mass flow through the regenerator as a function of crank angle is known. This is then utilised to calculate the average Reynolds number over a full cycle.
- The Stanton number may be determined from the average Reynolds number, using formula specific to the type of regenerator matrix.
- Once the Stanton number is known, the NTU value may be determined according to (A.39).
- With the NTU value known, regenerator enthalpy loss is calculated using (A.40).

Regenerator wall heat leakage

One of the mayor heat losses associated with Stirling engines are that of heat leakage through the regenerator walls from the heater to the cooler. High performance Stirling engines operate

at very high internal pressure that in turn demands thick cylinder and regenerator walls. The rate of heat transfer along these walls is calculated by

$$\dot{Q} = \frac{kA\left(T_{wh} - T_{wk}\right)}{l}, \tag{A.41}$$

where k is the thermal conductivity of the material, and T_{wh} and T_{wk} are the wall temperatures of the heater and cooler respectively, A is the cross-sectional area for heat flow and l is the length of the regenerator. The amount of heat transferred during one cycle may be found by dividing by the frequency of operation.

Imperfect heat exchangers

From the temperature profile in figure A.3 we observe that the non-ideal heater results in the mean effective temperature of the gas in the heater ($T_{h(mean)}$) are lower than those of the heater wall (T_{wh}) and similarly, that the mean effective temperature of the gas in the cooler ($T_{k(mean)}$) is higher than that of the cooler wall (T_{wk}) due to imperfect heat exchangers.

This has a significant effect on engine performance, since it is effectively operating at a lower temperature difference than would have been the case with perfect heat exchangers. This underlines the importance of well designed heat exchangers.

As part of the expanded formulation, the differences between the heat exchanger wall temperatures and the mean gas temperatures of the heater and the cooler are determined iteratively using the convective heat transfer equations.

From the equation of convective heat transfer we obtain

$$\dot{Q} = hA_{wg}\left(T_w - T\right), \tag{A.42}$$

where $\dot{Q}$ is the rate of heat transfer, h is the heat transfer coeffisient, A_{wg} again refers to the wetted area of the heat exchanger surface, and T_w and T are the wall temperature and gas temperature respectively. To obtain the net heat transferred over a single cycle Q (i.e. joules/cycle), we divide both sides by the frequency of operation. This yields

$$Q_h = h_h A_{wgh}\left(T_{wh} - T_h\right)/f \tag{A.43}$$

for the heater and

$$Q_k = h_k A_{wgk}\left(T_{wk} - T_k\right)/f \tag{A.44}$$

for the cooler, where f refers to the cycle frequency. By rewriting (A.43) and (A.44), the respective gas temperatures T_h and T_k may be evaluated, i.e.

$$T_h = T_{wh} - fQ_h/\left(h_h A_{wgh}\right) \tag{A.45}$$

and

$$T_k = T_{wk} - fQ_k / \left(h_k A_{wgk}\right). \tag{A.46}$$

The expanded formulation algorithm requires the ideal adiabatic simulation to be invoked iteratively, each time with new values of T_h and T_k until convergence is attained. Each cyclic ideal adiabatic simulation yields values of Q_h and Q_k. By using the mass flow rates through the heater and the cooler that are also available from each cyclic simulation, the average Reynolds number and therefore the heat transfer coefficient is determined for each heat exchanger. Substitution of these values in (A.45) and (A.46) yields T_h and T_k and convergence is obtained when their successive values are essentially equal.

Pumping losses

As part of the ideal adiabatic simulation it was assumed that the instantaneous pressure is the same throughout the engine. High performance Stirling engines require high heat fluxes in the heat exchangers that in turn require large wetted areas. This requirement together with the conflicting requirement of a low void volume results in heat exchangers with many small diameter passages in parallel. Fluid friction associated with the flow through the heat exchangers (as well as the regenerator) will therefore result in a pressure drop across the heat exchangers and regenerator, which in turn has the effect of reducing the power output of the engine. This is known as pumping losses.

To determine the pumping losses, the analysis starts with the determination of the new value of work done (as opposed to the ideal adiabatic case) as the sum of the work done in the expansion space and the compression space, which in turn is determined by integration of the product of the instantaneous pressure and rate of volumetric change over the complete cycle for each volume, i.e.

$$\begin{aligned} W &= W_c + W_e \\ &= \oint p dV_c + \oint \left(p - \sum \Delta p\right) dV_e. \end{aligned} \tag{A.47}$$

The pressure drop across both heat exchangers and the regenerator is denoted by $\sum \Delta p$. Rearranging (A.47) yields

$$\begin{aligned} W &= \oint p \left(dV_c + dV_e\right) - \oint \sum \Delta p dV_e \\ &= W_i + \Delta W, \end{aligned} \tag{A.48}$$

where W_i and ΔW denote the ideal adiabatic work done per cycle and the pressure drop loss or pumping loss per cycle respectively. Thus

$$\Delta W = \int_0^{2\pi} \left(\sum_{i=1}^{3} \Delta p_i \frac{dV_e}{d\theta} \right) d\theta. \tag{A.49}$$

The pressure drop Δp is due to fluid friction as it flows through the heat exchangers and regenerator and is evaluated with respect to the compression space.

The entire second order simulation has been formulated as one-dimensional throughout. However, the fundamental concepts of fluid friction break down under one-dimensional flow. Newton's law of viscosity states that the shear stress τ between adjacent layers of fluid is proportional to the velocity gradient in these layers normal to the flow direction as shown in figure A.4.

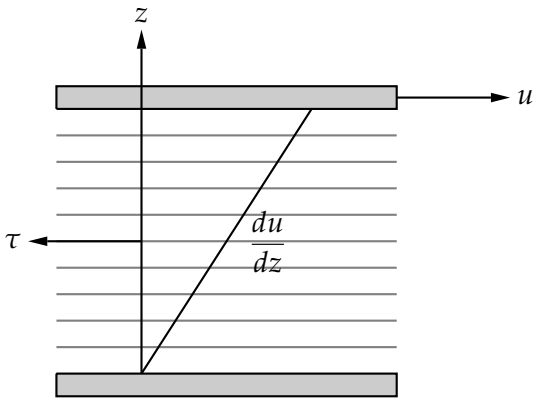

Figure A.4: Illustration of Newton's law of viscosity [13].

Newton's law of viscosity from figure A.4 can be stated as

$$\tau = -\mu \frac{du}{dz}. \tag{A.50}$$

The dynamic viscosity μ is in short a measure of the internal friction that occurs when molecules of the fluid in one layer collide with molecules in adjacent layers travelling at different speeds, and in so doing their momentum is transferred. In (A.50), the shear stress τ is thus related to the dynamic viscosity as well as to the velocity gradient. Shear stress thus cannot be sustained unless the flow is two dimensional. A way to overcome this paradox is discussed below.

The dynamic viscosity μ is independent of the pressure over the pressure range of interest, but is dependant on temperature. Urieli [13] included a diagram that shows the dependency on temperature of helium, hydrogen and nitrogen.

The frictional drag force is evaluated with

$$F = \tau A_{wg}. \tag{A.51}$$

In developing an expression to describe pumping loss, the concept of a 'hydraulic diameter' d is introduced, namely

$$d = 4V / A_{wg}, \tag{A.52}$$

that describes the ratio of the two important variables of heat exchangers, namely the void volume V and the wetted area A_{wg}. The factor 4 is included for convenience. The force equation

now becomes

$$F = 4\tau V/d \tag{A.53}$$

by substitution. A coefficient of friction C_f is now defined as the ratio of the shear stress τ to the 'dynamic head' (refer to Urieli [13]) as

$$C_f \equiv \frac{\tau}{\frac{1}{2}\rho u^2}, \tag{A.54}$$

where ρ is the fluid density and u is the fluid bulk velocity. Thus, substitution of τ in the force equation yields the frictional drag force in terms of the coefficient of friction, namely

$$F = 2C_f \rho u^2 V/d. \tag{A.55}$$

Quasi-steady flow has been assumed throughout for this formulation. The frictional drag force is then equal to and opposite the pressure drop force, i.e.

$$\Delta p A = -F, \tag{A.56}$$

where A is the cross sectional free flow area. Sustituting for F in (A.56), the pressure drop Δp is given by

$$\Delta p = -2C_f \rho u^2 V/\left(dA\right). \tag{A.57}$$

The pressure drop Δp can be positive or negative, depending on the direction of flow. The right hand side of (A.57) is however always positive, and thus the momentum conservation principle is violated in the case of reversing flow. This could be resolved by defining a Reynolds friction coefficient by multiplying the Reynolds number by the coefficient of friction, i.e.

$$C_{ref} = N_{re} C_f, \tag{A.58}$$

where the Reynolds number is

$$N_{re} = \rho u d/\mu. \tag{A.59}$$

By definition, the Reynolds number is always positive, independent of the direction of flow. Thus finally

$$\Delta p = \frac{-2C_{ref}\mu u V}{d^2 A}. \tag{A.60}$$

The momentum conservation principle is now satisfied for both forward and reverse flow, since the sign of Δp is always correctly related to the sign of the velocity u.

Calculation of the pumping losses as well as the pressure drop in the expanded formulation may be summarised as follows:

- Once the cyclic ideal adiabatic simulation is completed, the Reynolds number of each simulation step is determined for the heater, cooler and regenerator.
- From the Reynolds number at each step, the Reynolds friction coefficient is then determined at each step. This is done using formulae for pipes for the heater and cooler and formulae for mesh and foil matrices for the regenerator.
- The pressure drop at each simulation step is then calculated using (A.60) for the heater, cooler and regenerator using the Reynolds friction coefficient at each step. The instantaneous pressure drop across the individual heat exchangers or across all three passages is now known.
- The pressure drop loss or pumping loss may now be calculated using (A.49).

Algorithm for the expanded formulation

With the ideal adiabatic simulation described previously and the calculation of the major loss mechanisms also described above, the algorithm for the expanded formulation will now be discussed briefly. Figure A.5 shows a block diagram of the expanded formulation algorithm.

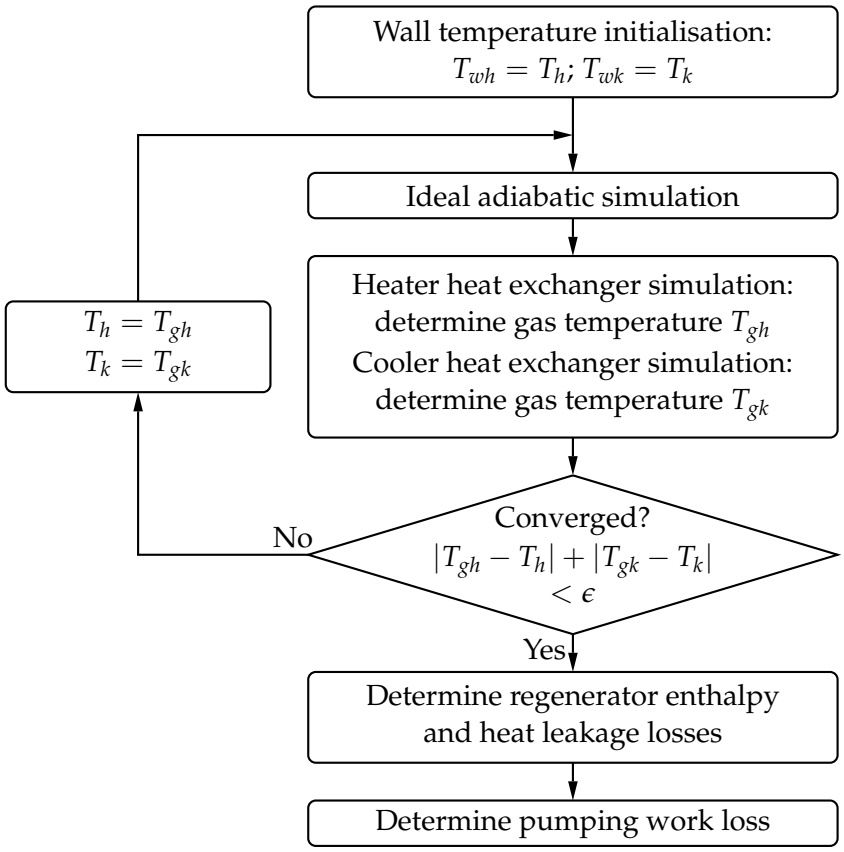

Figure A.5: The expanded formulation algorithm [13].

The algorithm starts by setting the wall temperatures of the heater and cooler to the input high and low temperatures respectively. An iterative process is then entered that entails performing an ideal adiabatic simulation (an iterative process in itself) and the subsequent deter-

mination of the mean heater and cooler gas temperatures T_{gh} and T_{gk} respectively as described in the previous section until convergence is attained.

Once the gas temperatures have converged, the regenerator enthalpy and heat leakage losses are calculated, followed by the calculation of the pumping work losses. The performance parameters, e.g. power output and efficiency may then by calculated. Other data available from the cyclic simulation may be plotted or analysed.

A.4 Simulation accuracy

Two different methods exist to calculate the performance and efficiency of the engine after the simulation is completed. These two methods are explained with the help of heat/work flow diagrams as shown in figure A.6.

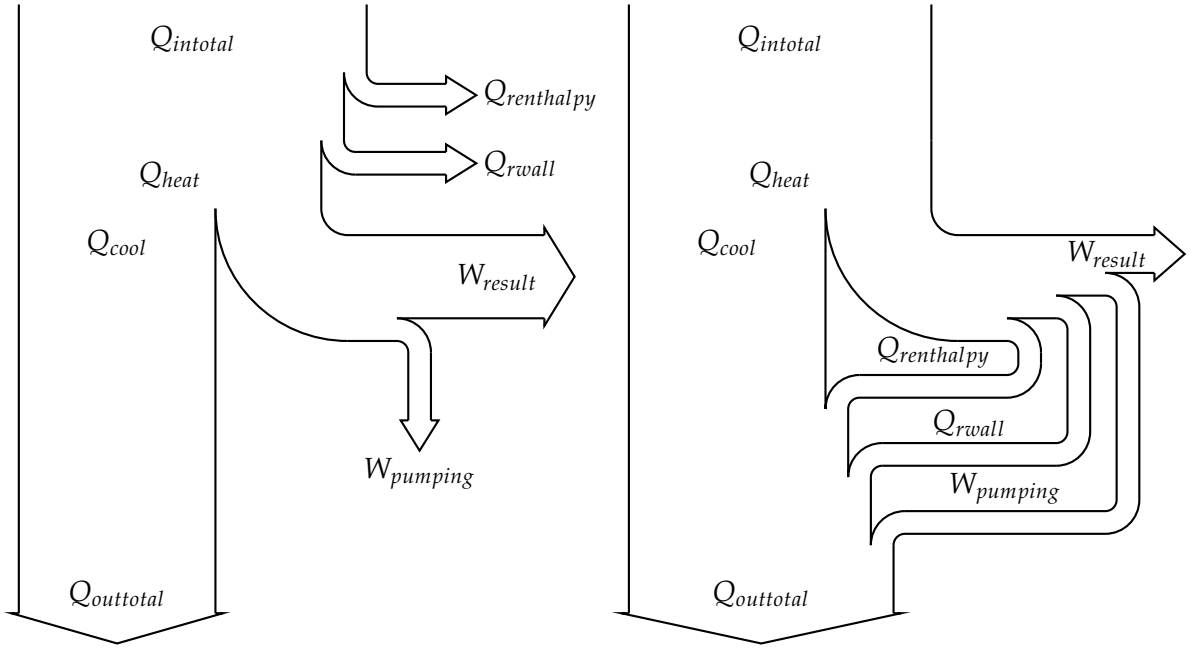

Figure A.6: Heat and work flow diagrams for performance and efficiency calculations.

$Q_{intotal}$ denotes the total input heat to the engine, $Q_{renthalpy}$ and Q_{rwall} denote the regenerator enthalpy and wall heat leakage losses respectively, Q_{heat} and Q_{cool} denote the heat input to and heat rejected from the gas cycle respectively, $Q_{outtotal}$ denotes the total heat rejected at the cooler, $W_{pumping}$ denotes pumping work loss and W_{result} denotes the resultant output work.

The first diagram shown in figure 6a represents the method used by Urieli [13] to calculate the performance and efficiency. The second method shown in figure 6b represents an alternative method introduced by Strauss and Dobson [14].

The difference between the two methods is essentially how the regenerator and pumping losses are accounted for. In the case of the Urieli method these losses are added to the simulated heat input of the cycle to obtain a new total heat input to the engine. $Q_{intotal}$ and Q_{heat} therefore differ. Although Urieli did not explain his decision to calculate engine performance in this

manner, the reason is probably that in order for the gas cycle variables obtained during cyclic simulation to remain as simulated, additional heat should be added to the engine to provide for the more realistic simulation, i.e. after also taking into account the regenerator losses. In practice the heater temperature will have to be set higher to achieve the higher heat input to the engine, effectively changing the original simulation input parameters.

The alternative method tries to avoid this by subtracting the regenerator losses from the simulated output work and adding these losses as well as the pumping losses to the heat rejected from the gas cycle to obtain a new total amount of heat that is rejected from the cooler. $Q_{outtotal}$ and Q_{cool} therefore differ. The reasoning for this alternative is that the regenerator losses calculated after the cyclic simulation will in practice degrade the engine by lowering the output power and by increasing the rejected heat at the cooler. As a result, gas cycle variables for the more realistic simulation will inevitably differ from those obtained during ideal adiabatic cyclic simulation, e.g. the maximum and minimum pressure values will decrease and increase respectively. This should be kept in mind when interpreting and when using gas cycle variables obtained during cyclic simulation.

In following Berchowitz [20], Strauss and Dobson [14] did not subtract the entire calculated pumping loss from the output work. The pumping losses that occur in the heater, regenerator and cooler are due to fluid friction where kinetic energy is converted to heat energy. Not all of this heat is rejected at the cooler. In the case of the heater, the heat due to fluid friction remains useful. This is also the case in more or less half of the regenerator. The pumping losses represented by $W_{pumping}$ in figure A.6b therefore only consist of half of the losses in the regenerator and the losses in the cooler.

It follows that the total input heat to the engine and the resultant output work is less, and that the total output heat is more for the alternative method when compared to the Urieli method.

Simulated accuracy: GPU-3

Strauss and Dobson [14] compared the simulated output of the second order formulation with experimental data of the well documented GPU-3 Stirling engine originally built by General Motors Research Laboratories in the 1960's for the US Army [16]. This is a single cylinder, beta configuration engine with a rhombic drive and was designed with a power output specification of 3 kWe [17].

Of the numerous tests that were conducted by Thieme [15, 17] on the GPU-3 engine, the results of one test each were documented in detail in the two reports prepared for the U.S. Department of Energy. Table A.2 lists the operational information of these two tests.

Table A.3 compares the simulated low power baseline performance with the test results documented by Thieme [17].

The second order formulation could predict the average expansion space and compression

[3]Simulation of expansion space pressure swing improved subsequent to publication by Strauss and Dobson [14].

Table A.2: Core operational information of the fully documented low power baseline and high power baseline tests conducted by Thieme [15, 17].

	Low power baseline [17]	High power baseline [15]
Working fluid	Helium	Hydrogen
Heater tube gas temperature	697 °C	677 °C
Mean compression space pressure	4.13 MPa	6.92 MPa
Engine speed	2503 rpm	1504 rpm

Table A.3: Comparison of simulated results with the measured low power baseline results by Thieme [17] as reported by Strauss and Dobson [14].

	Measured results	Simulated results (percentage error in brackets)	
		Urieli	Alternative
Exp. space average temperature	851 K	878 K (3.2)	
Comp. space average temperature	371 K	350 K (-5.7)	
Exp. space pressure swing	2.89 MPa	2.88 MPa (-0.3)[3]	
Comp. space pressure swing	2.94 MPa	3.01 MPa (2.4)	
Heat input to working fluid per cycle	272 J	313 J (15.1)	273 J (0.4)
Heat out of working fluid per cycle	177 J	115 J (-53.9)	165 J (-6.78)
Indicated output power and efficiency	3.70 kW @ 0.303	5.61 kW @ 0.43 (51.6)	4.39 kW @ 0.386 (18.6)
Brake output power and efficiency	2.65 kW @ 0.217	4.56 kW @ 0.35 (72.1)	3.34 kW @ 0.294 (26.0)

space temperatures fairly accurately. It should be highlighted though that it is difficult to measure the mean temperature of the gas in the variable spaces accurately.

The heat input to the engine is overestimated by the Urieli method. Sullivan [31], while comparing a nodal-analysis simulation code, obtained similar results, i.e. of the order of 20%. The alternative method overestimated the heat input by only 0.4%.

The heat rejected at the cooler per cycle was largely underestimated by the Urieli method. This was expected, since the simulation does not take into account during cyclic simulation the additional heat due to regenerator losses, appendix gap losses, etc. that should be rejected at the cooler. The alternative method again estimated the rejected heat much more accurately, since an effort is made to take into account at least the losses calculated as part of the expanded formulation (refer again to figure A.6).

The pressure swings in both the expansion and compression spaces were estimated fairly accurately.

The brake output power of the GPU-3, i.e. the output power at the shaft of the engine, was determined by Thieme [17] to be 2.65 kW. Thieme [15] also determined by experiments and calculations the mechanical losses for the conditions given in table A.3. For comparative purposes, the simulated output power is compared with the measured output power both without and with consideration of mechanical losses, denoted as 'indicated' and 'brake' respectively.

The alternative method could estimate the indicated and brake output power more accurately.

The inaccuracies for the Urieli method in predicting the output power should not come as a surprise when considering that the input heat and the heat rejected at the cooler is overestimated and underestimated by approximately 15% and 54% respectively, resulting in the overestimation of the indicated output power. Furthermore, even if all of the losses were taken into consideration, the simulated output power would still exceed the actual value. This issue was partly addressed for the alternative method, yielding better results.

Table A.4 compares the simulated high power baseline performance with the test results documented by Thieme [15].

Table A.4: Comparison of simulated results with the measured high power baseline results by Thieme [15] as reported by Strauss and Dobson [14].

	Measured results	Simulated results (percentage error in brackets)	
		Urieli	Alternative
Exp. space average temperature	847 K	887 K (4.7)	
Comp. space average temperature	345 K	335 K (-2.9)	
Exp. space pressure swing	4.23 MPa	4.74 MPa (12.1)[4]	
Comp. space pressure swing	4.43 MPa	4.77 MPa (7.7)	
Heat input to working fluid per cycle	444 J	507 J (14.2)	432 J (-2.7)
Heat out of working fluid per cycle	245 J	170 J (-30.6)	248 J (1.2)
Indicated output power and efficiency	4.91 kW @ 0.406	6.29 kW @ 0.494 (28.1)	4.47 kW @ 0.413 (-9.0)
Brake output power and efficiency	4.16 kW @ 0.344	5.54 kW @ 0.435 (33.2)	3.72 kW @ 0.344 (-10.6)

The accuracy of the expansion and compression space average temperatures are again satisfactory. The simulated expansion space and compression space pressure swings are less accurate when compared to the low power baseline test in table A.3.

The inaccuracies of the simulated heat input to the engine and heat rejected at the cooler were similar to the inaccuracies listed in table A.3, with the exception of the heat rejected calculated with the Urieli method, which improved in accuracy. The accuracy of the output power and efficiency calculated using the Urieli method show a vast improvement, but worsened using the alternative method, when compared to the results listed in table A.3.

In general, the accuracy of the results obtained using the Urieli method improved, but accuracy worsened when using the alternative method. Sullivan [31] in his investigation reported that the absolute prediction error of the power was greater for helium than for hydrogen. This is also the case using the Urieli method, where the output power was calculated more accurately for the high power baseline case with hydrogen as working gas.

Sullivan [31] also gave detail of a range of other measurements conducted at NASA Lewis Research Centre. Figure A.7 to figure A.12 show several variables against engine speed for

[4]Simulation of expansion space pressure swing improved subsequent to publication by Strauss and Dobson [14].

measurements conducted with helium as working fluid, with the average pressure close to 4.2 MPa and with the heater tube gas temperature close to 650 $^{\circ}C$. (These are the same conditions as for the measured results shown in table A.3.) These graphs are presented to compare the ability of the numerical formulation to accurately predict the different variables as a function of engine speed.

Figures A.7 and A.8 show the measured brake output power and efficiency and simulated indicated output power and efficiency as a function of engine speed respectively. Apart from the expected significant difference in magnitude, the measured output power starts to decrease with increasing engine speed, while the simulated output power still increases at a decreasing rate for both methods. The simulated efficiency however shows the same trend as for the measured case. Several reasons exist for the inaccuracy of the simulated output power:

- Thieme [15] showed that the mechanical losses, calculated using energy-balance techniques, increase linearly with engine speed, but that these losses, determined using direct motoring measurement techniques, increase at a higher order dependency. Thieme could however not conclusively state which of the two methods is more accurate.

  To compare measured and simulated indicated output power and efficiency, two additional traces are included in both figures A.7 and A.8. These tracers were determined by adding the measured mechanical losses ('$+$' marker using the results from energy-balance techniques - '$*$' marker using the results from motoring measurement techniques) to the measured brake output power. It is now seen with this more realistic comparison, the simulated trends of the indicated power are more accurate than when compared with the measured brake output power.

- The pressure profiles obtained from simulation by Urieli [34] using a third order formulation suggested that a simplified momentum equation could be used for simulation up to peak power. Urieli however showed that even at an engine speed well below that of peak power, a complete momentum equation including momentum flux and acceleration terms should be used. For helium, peak power is reached for engine speed in the region of 2500 to 3000 rpm. From more or less this point and onwards irregularities in the expansion space pressure profiles appear. Urieli found that a choking type local pressure peak appeared in his simulations using air as working fluid. This pressure peak impacted negatively on the output power. These phenomena can only be simulated with formulations more complex than the second order formulation presented here and are partly responsible for the inability of the simulated output power to follow the decreasing trend of the measured output power.

- Similar simulation inaccuracy was reported by Sullivan [31] and was attributed to inaccurate cylinder hysteresis loss modelling, amongst others. Cylinder hysteresis losses and many others are not considered here at all.

Figure A.9 shows the measured heat input to the engine and simulated heat input to the gas against engine speed, while figure A.10 shows the measured and simulated heat output of

the engine.

The heat input to the gas will be the larger part of, but will not exceed, the total heat input to the engine. The simulated heat input to the gas using the alternative method is therefore more accurate. The slope of the simulated heat input differs slightly when compared with the measured heat input slope. The heat output as determined by the alternative method closely follows the measured heat output.

Figure A.11 shows the measured and simulated expansion space pressure swing against engine speed, and figure A.12 shows the measured and simulated compression space pressure swing against engine speed. In the case of the expansion space a slight decrease in pressure swing is predicted, while the measured pressure swing remains approximately constant as engine speed increases.

For the compression space, a sharply decreasing pressure swing was presented by Sullivan [31] for increasing engine speed for measurements with average pressure at close the 4.2 MPa. However, the validity of the measured pressure swing at 3500 rpm is questioned, because no other similar decreases were observed for measurements presented by Sullivan at average pressures of 2.8 MPa and 5.6 MPa. The pressure swing obtained from measurements at these average pressures stayed fairly constant over the same range of engine speed. If it is indeed the case that the pressure swing was measured incorrectly at 3500 rpm for the data shown in figure A.12, then the simulated pressure swing is accurately predicted by the simulations.

In summary, while absolute accuracy of some of the simulated parameters was poor, the overall accuracy of the simulated trends, including the output power and efficiency, proved to be satisfactory, with the alternative method yielding more accurate results compared to the Urieli method.

A.5 Conclusive remarks

It was shown that the second order formulation presented here could simulate most of the cycle variables to a fair degree of accuracy. The two most important performance parameters, namely the output power and efficiency, could not however be calculated accurately. Where absolute accuracy was poor, the simulated trends as a function of engine speed in general follow the measured trends. The limitations of the second order formulation, e.g. the inability to account for the interrelated nature of the loss mechanisms, were highlighted.

With reference to this investigation, the ability to predict the performance trends to a fair degree of accuracy enabled the relative comparison of engine performance when fitted with different drive mechanisms as was done by Strauss and Dobson [12]. This made it possible to illustrate the significance of optimal displacement as opposed to ideal displacement and to determine whether optimal displacement is found closer to ideal displacement or closer to purely harmonic displacement.

Of particular importance to this investigation is the accuracy of the pressure profiles to determine the instantaneous forces exerted by the power piston and displacer for different scenarios, e.g. different drive mechanisms and engine speed. Snyman *et al.* [35] showed that

the profile of the pressure could be predicted accurately using this second order formulation. It is therefore expected that this formulation should be capable of following the dynamics of the pressure profile accurately. In addition, it has been shown in the previous section that pressure swing was estimated within acceptable accuracy. It is therefore expected that the absolute accuracy of the pressure profile should be acceptable.

Sullivan [31] raised another issue that he considered to have a substantial influence on the accuracy of simulations that he conducted, especially for the GPU-3. He argued that, while the pressure amplitude was predicted accurately, the power prediction error could be largely attributed to the inaccuracy in predicting the pressure phase angle, i.e. the angle between maximum gas pressure and minimum expansion space volume (or where the displacer reaches top dead position). He then went on to show that this error could be due to inaccurate modelling of the rate of heat transfer in the heater or alternatively in the rate of mass flow from the expansion and compression spaces due to gas leakage. Sullivan reported that the prediction error was approximately 12 degrees. In another table he indicated that the error was closer to between 5 to 7 degrees.

Comparable inaccuracy was also observed with the second order formulation of Urieli. The influence of this pressure phase angle inaccuracy on the ability of Urieli's formulation to predict pressure force dynamics is dealt with in section 3.5.3 in more detail.

Where more accurate simulation and more detailed information of the thermodynamic and gas dynamic behaviour are needed, a third order formulation would be more appropriate. Nevertheless, due to its simplified nature, the second order formulation presented here is considered more suitable as a first iteration design and optimisation tool and, with respect to this investigation, a suitable tool to compare the performance of different drive mechanisms and a convenient method to determine the dynamic response of the pressure profiles.

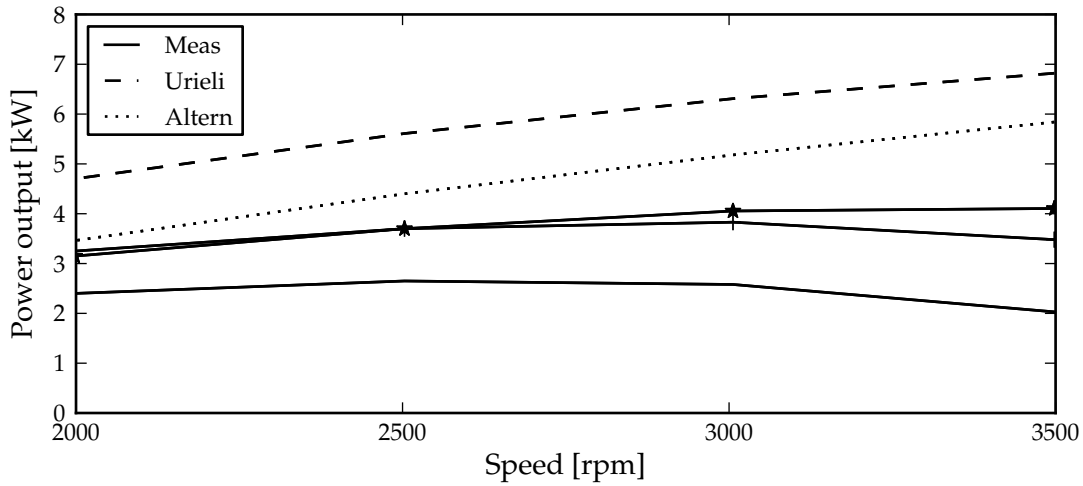

Figure A.7: Measured and simulated brake power output. Additional traces marked with '+' and '∗' to show measured indicated power.

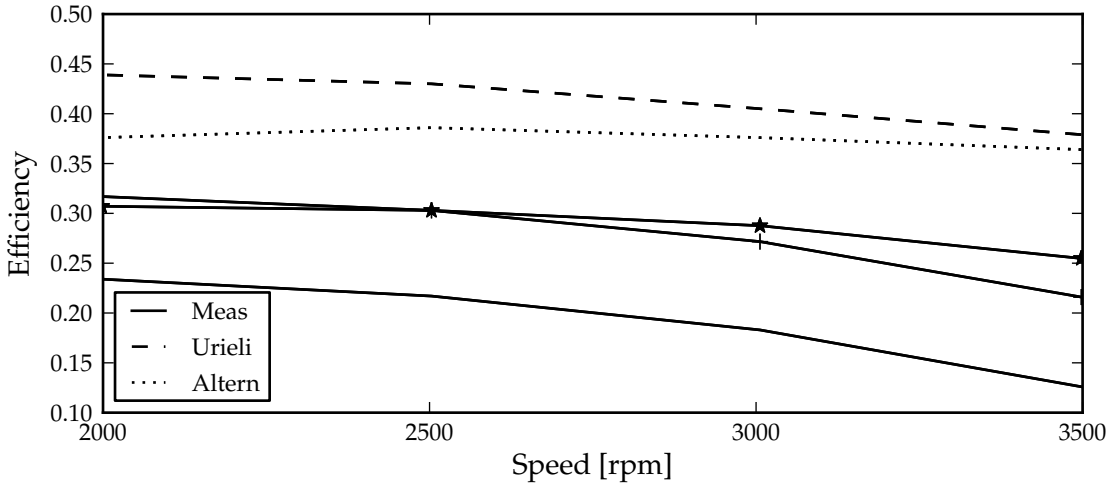

Figure A.8: Measured and simulated brake efficiency. Additional traces marked with '+' and '∗' to show measured indicated efficiency.

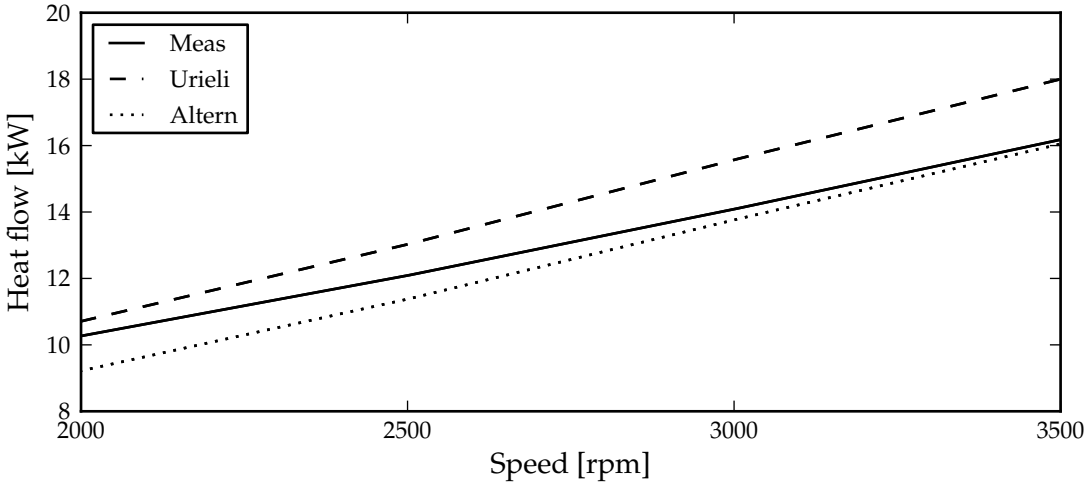

Figure A.9: Measured and simulated heat input.

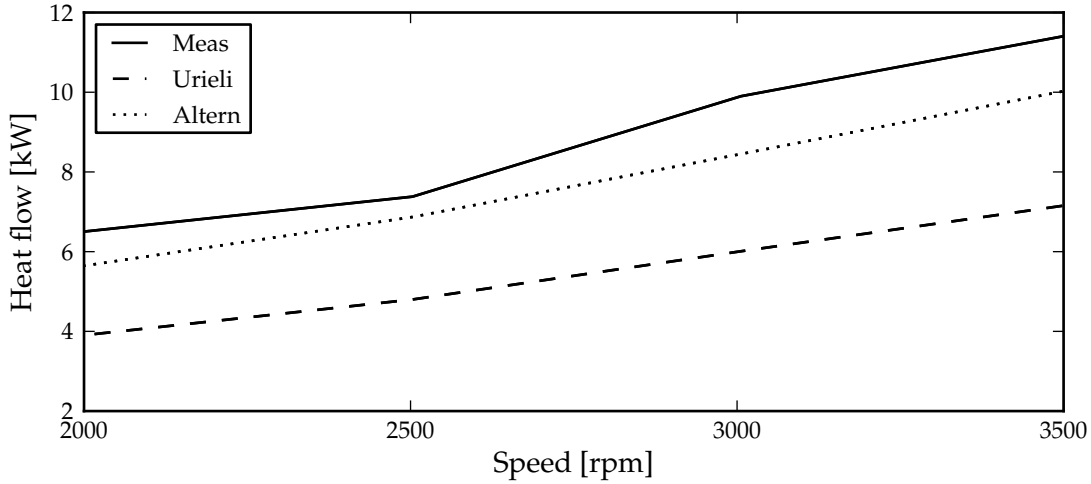

Figure A.10: Measured and simulated heat output.

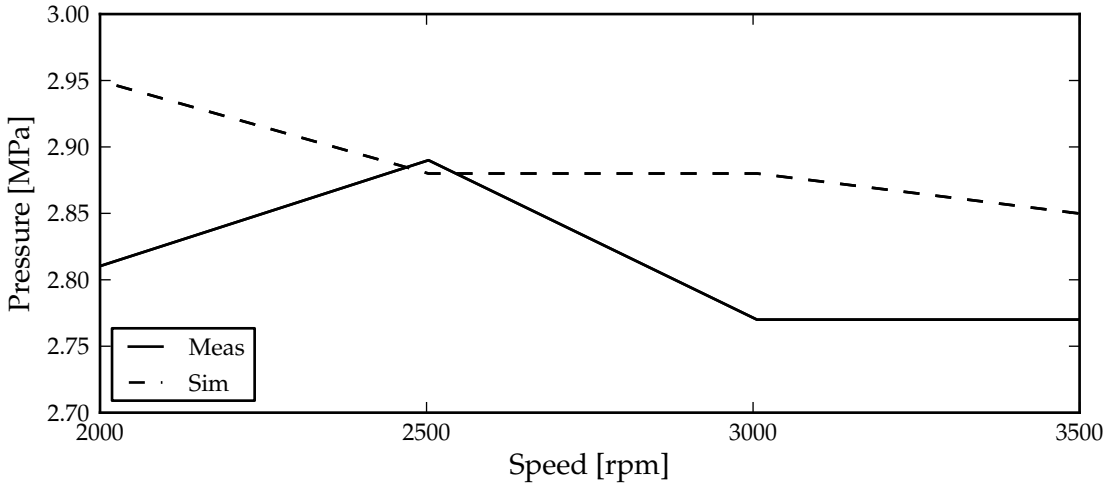

Figure A.11: Measured and simulated expansion space pressure swing.

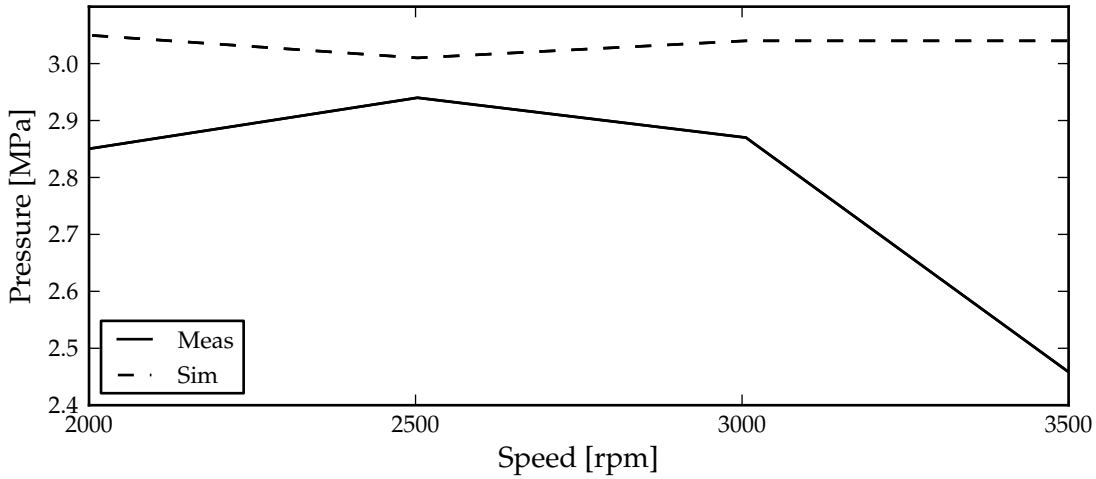

Figure A.12: Measured and simulated compression space pressure swing.

Appendix B

GPU-3 specifications

Detailed specifications and information of the GPU-3 Stirling engine are provided in table B.1 below as reference in support of GPU-3 related work presented elsewhere.

Table B.1: Specifications of the GPU-3 Stirling engine [7, 8].

General		
Configuration	Single cylinder, coaxial, uniform diameter bore with rhombic drive crank mechanism.	
Working fluid(s)	Hydrogen, Helium	
Bore	69,9 mm	
Stroke (power piston and displacer)	31,2 mm	
Volume displaced by displacer	120,88 cm^3	
Net swept volume	118,63 cm^3	
Specimen performance		
Performance points	1	2
Working fluid	Hydrogen	Helium
T_e	1019 K	977 K
T_c	311 K	288 K
p_{mean}	68 bar	41,3 bar
Angular speed	3600 rpm	2500 rpm
Indicated output power		3,96 kW
Brake output power	8,952 kW	2,649 kW
Working fluid circuit dimensions		
Heat exchangers	Heater	Cooler
mean tube length	245,3 mm	46,1 mm
length exposed to heat source/coolant	77,7 mm	35,5 mm
tube length (cylinder side)	116,4 mm	

tube length (regenerator side)	128,9 mm	
tube inside diameter	3,02 mm	1,08 mm
tube outside diameter	4,83 mm	1.59 mm
no. of tubes per cylinder	40	312
no. of tubes per regenerator	5	39
Compression-end connecting duct ...		
... length		15,9 mm
... inside diameter		5,97 mm
... no. of per cylinder		8
... cooler end cap		279 mm^3
Regenerators		
housing inside length	22,6 mm	
housing internal diameter	22,6 mm	
no. of regenerators per cylinder	8 mm	
mesh material	stainless steel	
mesh no.	7,9 wires/mm	
wire diameter	0,04 mm	
no. of layers	308	
porosity	70%	
screen-to-screen rotation	5°	
Drive mechanism		
crank radius r	13,8 mm	
connecting rod length l	46,0 mm	
crank eccentricity e	20,8 mm	
displacer rod diameter	9,52 mm	
piston rod diameter	22,2 mm	
displacer shell diameter	69,6 mm	
displacer wall thickness	1,59 mm	
linear expansion space clearance	1,63 mm	
linear compression space clearance	0,3 mm	

Appendix C

GPU-3 simulated case study results

C.1 Introduction

Complementary graphical results of an investigation into piston displacement control applied to the GPU-3 Stirling engine are provided below to support the discussions in chapter 3.

While the original GPU-3 engine is of the kinematic type fitted with a rhombic drive mechanism, the approach of this investigation was as if that engine was retrofitted and adapted as a free-piston engine with linear electrical machines (or where piston displacement control was applied to a free-piston engine with very similar geometric and operational parameters).

The purpose of this case study was to gain insight into the dynamics - especially force dynamics - of the original GPU-3 engine, as well as to investigate the influence of a wide range of variations on the dynamics of the engine - especially the force dynamics demanded of both the displacer and the power piston linear electrical machines. The influence of the following variations was investigated:

- Mean operating pressure.
- Engine speed.
- Hot side and cold side temperatures.
- Displacement connecting rod diameter.
- Stroke/bore ratio.
- Piston displacement patterns.
- Masses of the power piston and displacer moving members.
- Spring constants of flexure bearings.
- Bounce space void volume to swept volume ratio.
- Compression space and bounce space mean pressure difference.

Table C.1 below lists the default operational information for the GPU-3 simulations presented in section C.2 and should be considered as the default information for all simulation

results presented in this appendix. A complete listing of GPU-3 specifications is included in appendix B.

Table C.1: Default operational information for simulated GPU-3 case study.

	Default value or condition
Working fluid	Helium
Heater tube interior wall temperature	765,7 °C
Cooler tube interior wall temperature	20 °C
Mean pressure	4,14 MPa
Speed	2500 rpm
Mass of entire power piston moving member	0 kg
Mass of entire displacer moving member	0 kg
Displacer rod diameter	0 mm
Bounce space volume	inf
Bounce space heat flow	adiabatic

A few of the quantities were chosen not to reflect actual or practical values, but with the view to use the results as a benchmark for other simulations to follow. This explains why the masses of the power piston and displacer moving members are ignored, why the displacer rod diameter is ignored and why the bounce space void volume is set to infinite in table C.1. Lastly, the value of the heater tube interior wall temperature was chosen to yield a heater tube gas temperature of 700,0 °C as for the original engine (see table B.1 in appendix B).

C.2 Simulated results of a study under default operational conditions

Figures C.1 to C.6 show the simulated results for the displacements, volumetric changes, pressures, temperatures, forces and instantaneous powers.

Figure C.1 shows the displacement of the displacer and power piston with respect to a common zero reference as indicated in figure 3.1. The displacement of the displacer x_d in figure C.1 may be either x_{d1} or x_{d2} as indicated in figure 3.1, since no active gas volume exists between the two. Plotting the displacements with respect to a common zero reference helps to visualise the position of the piston more clearly. It can be seen that the displacement of both pistons for the original engine is fairly close to being sinusoidal.

Where plotting is done against displacement as in figure C.6, the zero references for the displacer and power piston are shifted to the centre of the respective pistons. This will be the case throughout this appendix.

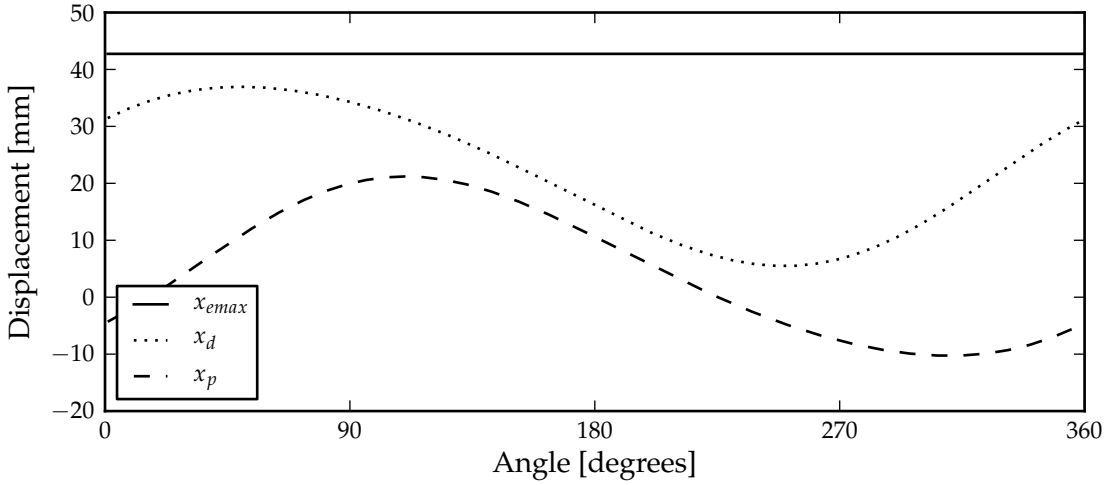

Figure C.1: Displacement of the displacer and power piston.

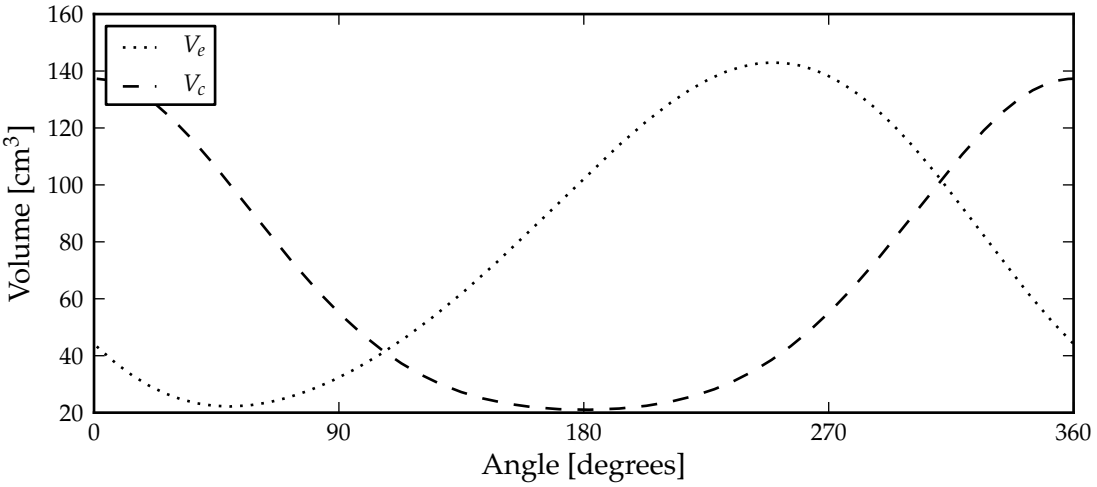

Figure C.2: Expansion space and compression space volumetric change.

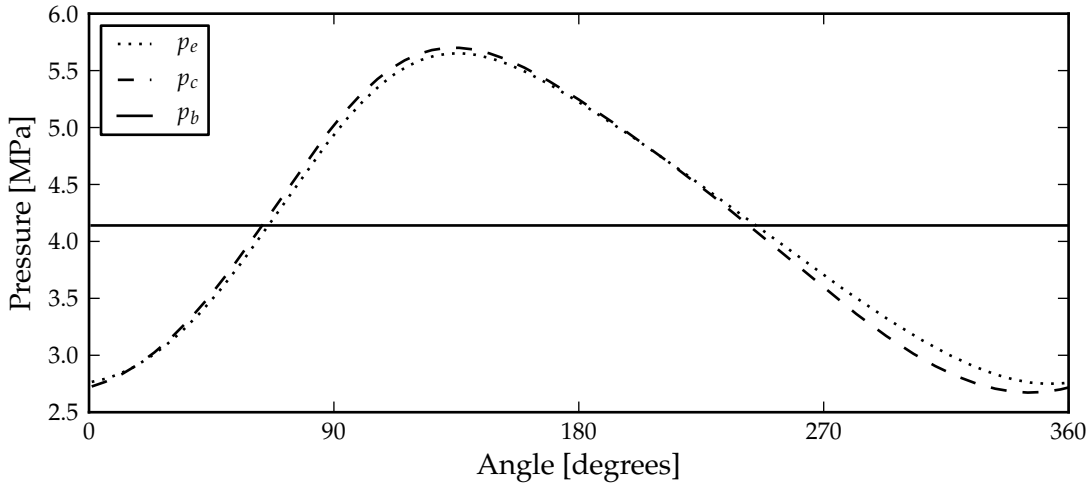

Figure C.3: Expansion space, compression space and bounce space pressure.

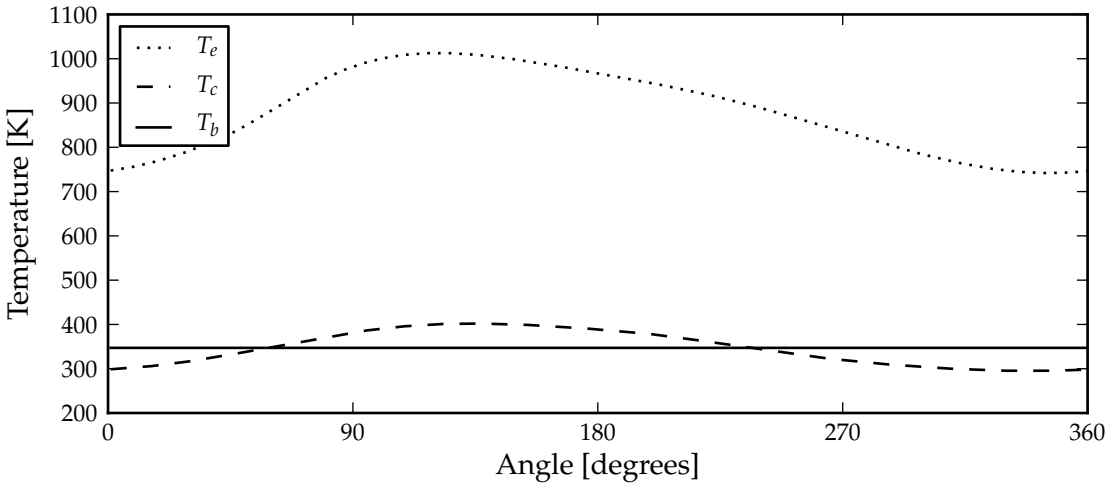

Figure C.4: Expansion space, compression space and bounce space temperature.

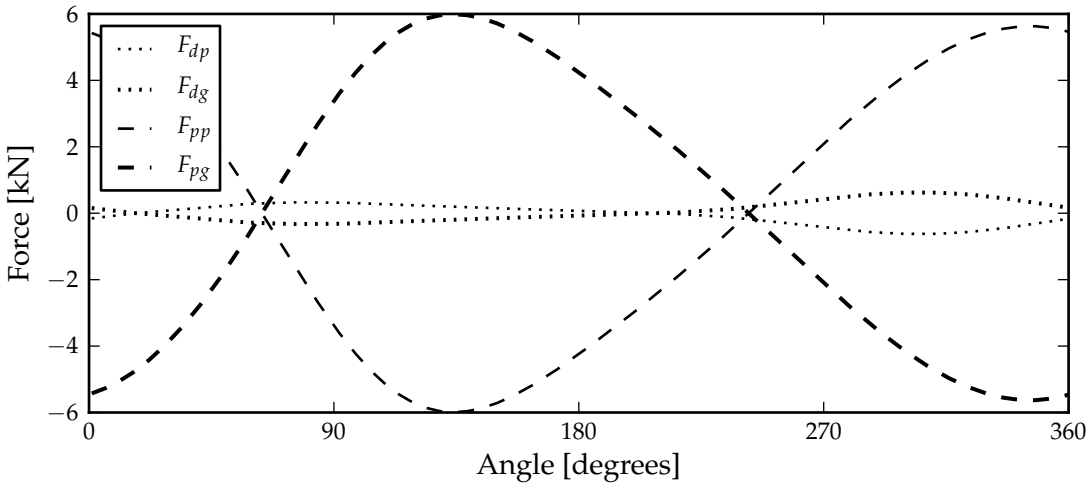

Figure C.5: Instantaneous forces exerted on the displacer and the power piston by pressure differences and by the linear machines.

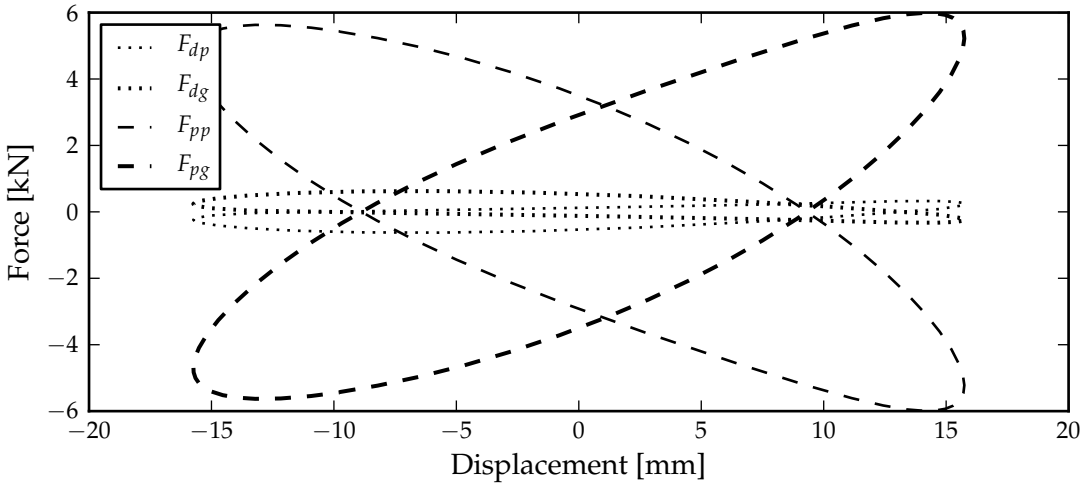

Figure C.6: Instantaneous forces exerted on the displacer and the power piston by pressure differences and by the linear machines against displacement.

C.3 Simulated results of a study of the influence of variations

Table C.2: Simulation results obtained for GPU-3 with default conditions.

	Page(s)
Pressure phase angle variation	
The influence of a variation of the simulated pressure phase angle for phase angle offset of 0°, -6°, and -12°.	
Figures C.7 to C.12	209 to 210
Mean pressure variation	
The influence of a variation of the mean operating pressure for mean pressures of 1,38 MPa, 2,76 MPa, 4,14 MPa, 5,52 MPa and 6,89 MPa.	
Figures C.13 to C.18	211 to 212
Engine speed variation	
The influence of a variation on the engine speed for engine speed of 1000, 1500, 2000, 2500 and 3000 rpm.	
Figure C.19 to C.24	213 to 214
Variation of the hot and cold side temperatures	
The influence of a variation of the hot and cold side temperatures for rod area to bore area ratios of 1%, 2%, 5% and 10% respectively.	
Figure C.25 to C.30	215 to 216
Variation of the rod diameter	
The influence of the displacement connection rod for rod area to bore area percentage ratios of 1%, 2%, 5% and 10% respectively.	
Figure C.31 to C.36	217 to 218
Variation of the stroke to bore ratio	
The influence of the stroke to bore ratio on the force dynamics of the GPU-3 was investigated for normalised stroke to bore ratios of 0,5, 1,0 and 2,0 respectively.	
Figure C.37 to C.42	219 to 220
Variation of piston displacement patterns	
The influence of piston displacement patterns on the force dynamics of the GPU-3 was investigated for rhombic and modified rhombic, rhombic/sinusoidal composite, sinusoidal and pseudo-ideal piston displacement patterns optimised for maximum power output and maximum efficiency of the GPU-3 at the default operational conditions listed in table C.1.	
Figure C.43 to C.58	221 to 226

Variation of the mass to power ratio

The influence of the mass to power ratio on the force dynamics of the GPU-3 was investigated for mass to power ratios of 0,0, 0,5, 1,0, 2,0 and 5,0 respectively.

Figure C.59 to C.64 227 to 228

Variation of spring forces

The influence of spring forces on the force dynamics of the GPU-3 was investigated for spring constants with maximum spring force of 0,0, 0,1, 2,0 and 0,5 of maximum pressure force at maximum displacement from centre position.

Figure C.65 to C.70 229 to 230

Variation of bounce space void volume

The influence of a variation of the bounce space void volume on the force dynamics of the GPU-3 was investigated for bounce space void volume to swept volume ratios of 1,0, 2,0, 5,0, 10,0 and infinity respectively.

Figure C.71 to C.76 231 to 232

Variation of bounce space/compression space average pressure difference

The influence of a variation of the bounce space/compression space average pressure difference on the force dynamics of the GPU-3 was investigated for bounce space/compression space average pressure differences of 0,0%, 1,0%, 2,0%, 5,0% and 10,0% respectively.

Figure C.77 to C.82 233 to 234

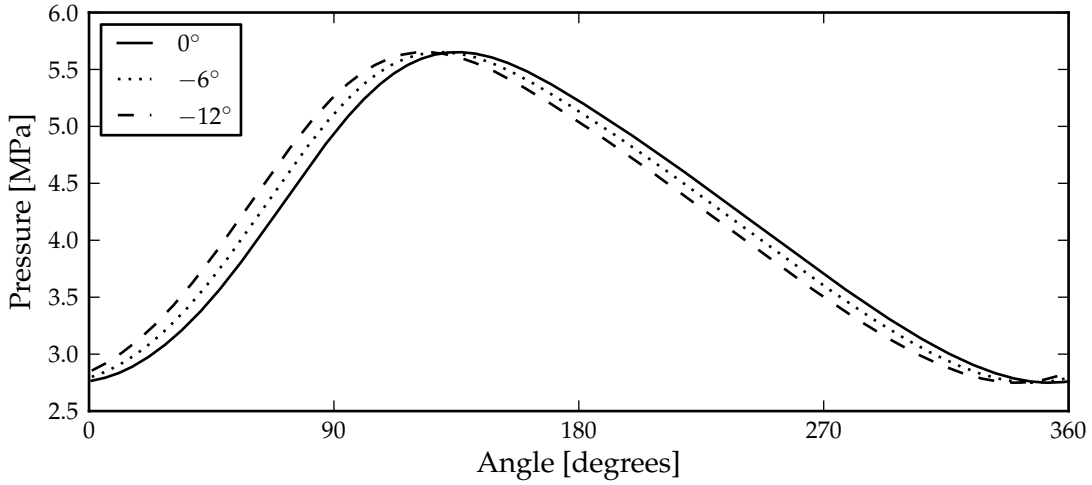

Figure C.7: Phase shifted expansion space pressure.

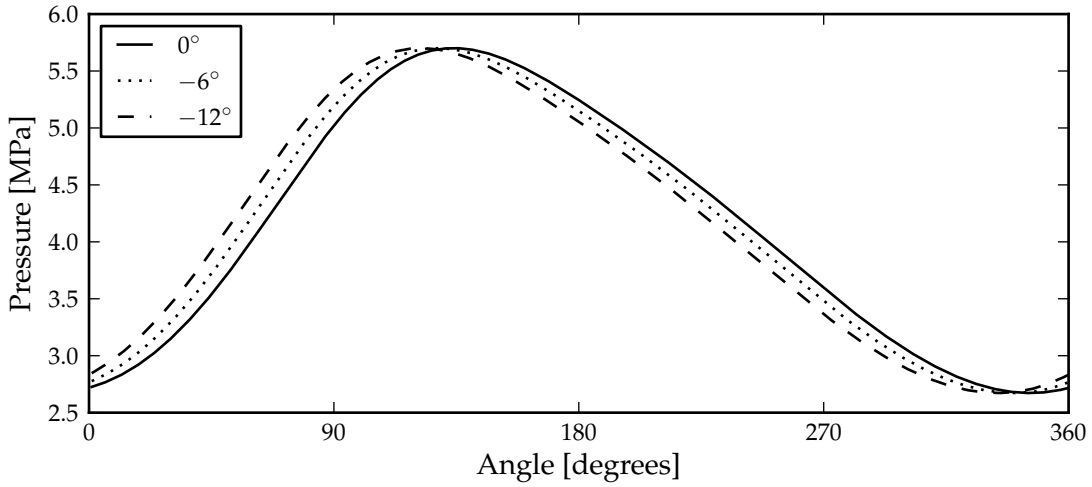

Figure C.8: Phase shifted compression space pressure.

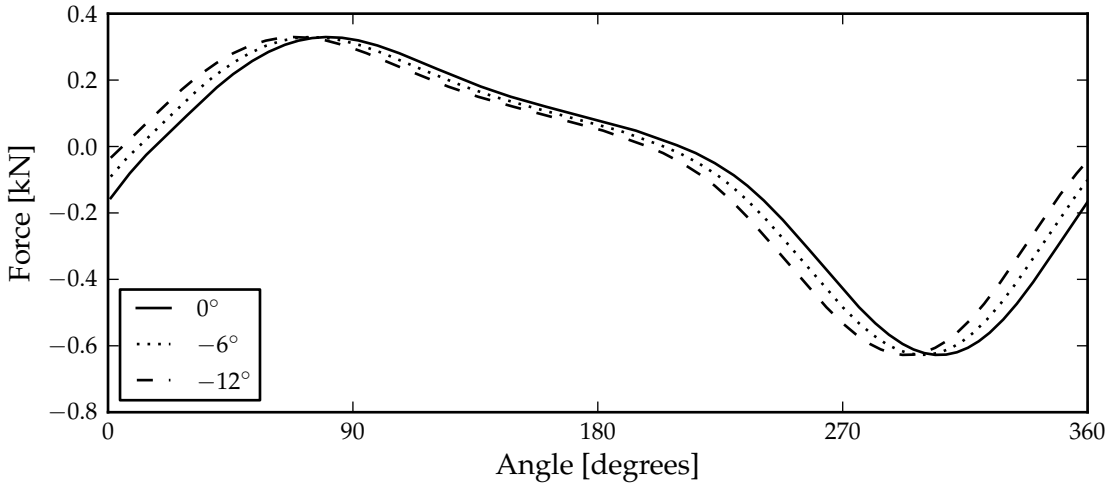

Figure C.9: Pressure difference force for the displacer as a result of pressure phase shifting.

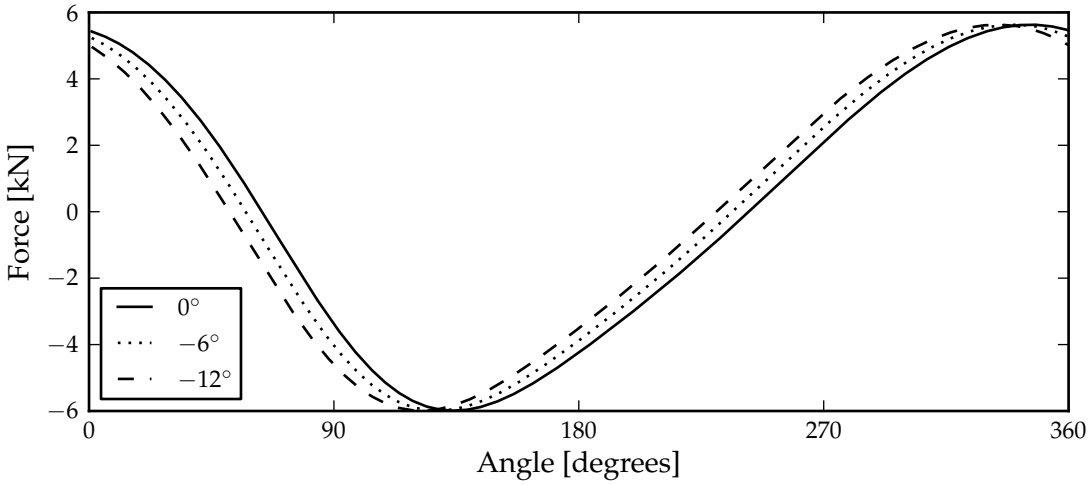

Figure C.10: Pressure difference force for the power piston as a result of pressure phase shifting.

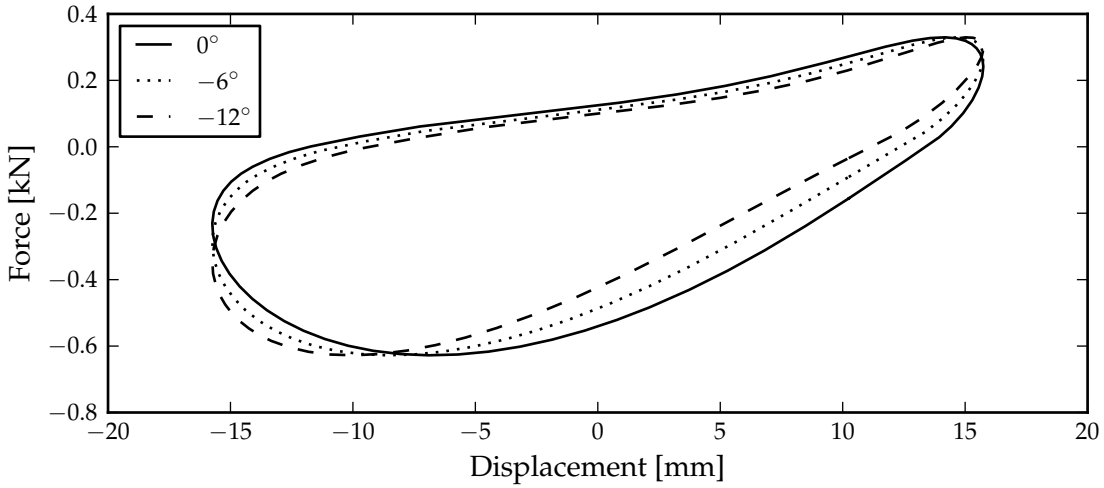

Figure C.11: Pressure difference force for the displacer against displacement as a result of pressure phase shifting.

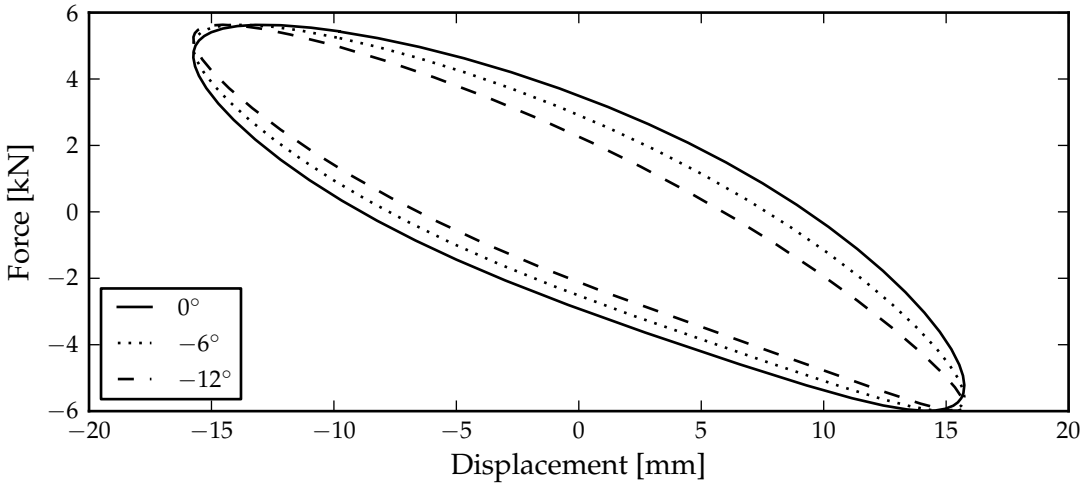

Figure C.12: Pressure difference force for the power piston against displacement as a result of pressure phase shifting.

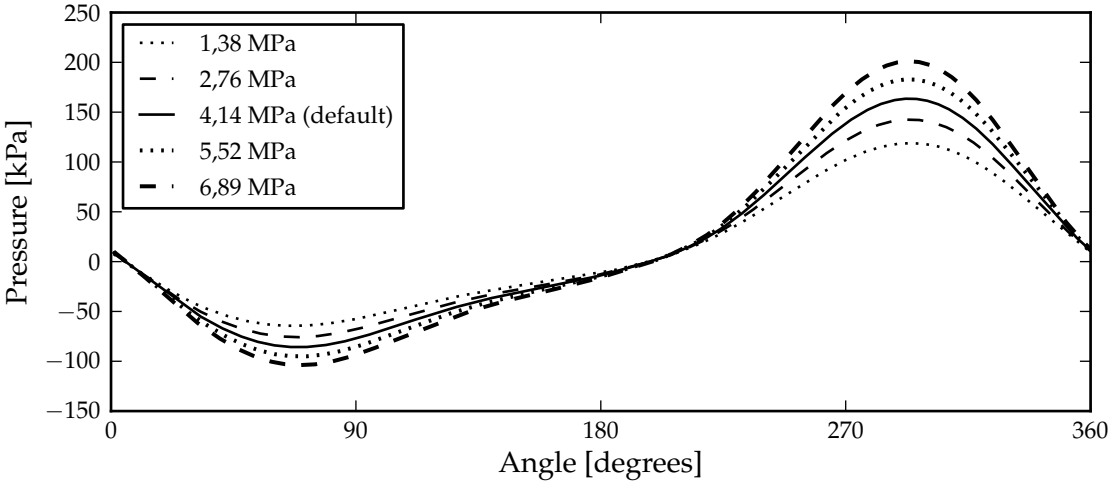

Figure C.13: Expansion to compression space pressure drop for various mean pressures.

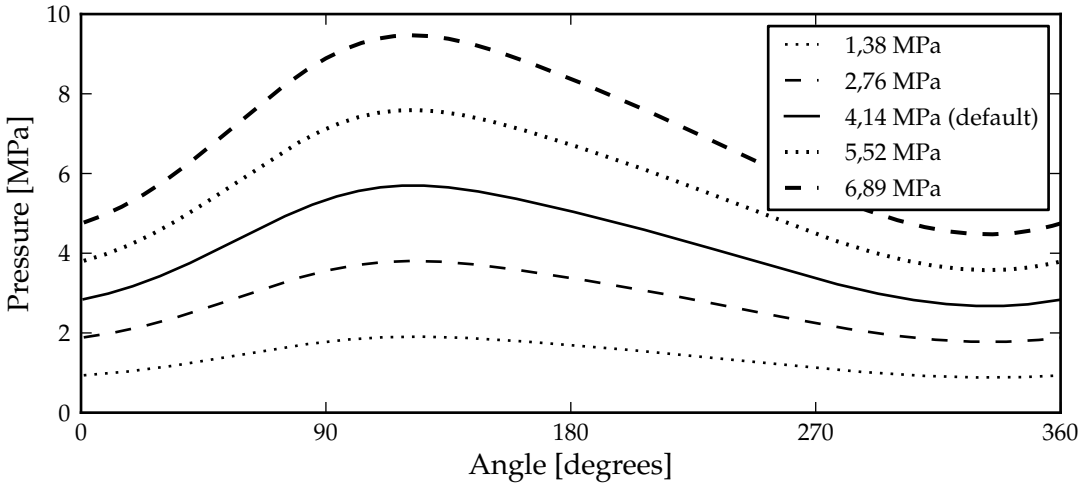

Figure C.14: Compression space pressure for various mean pressures.

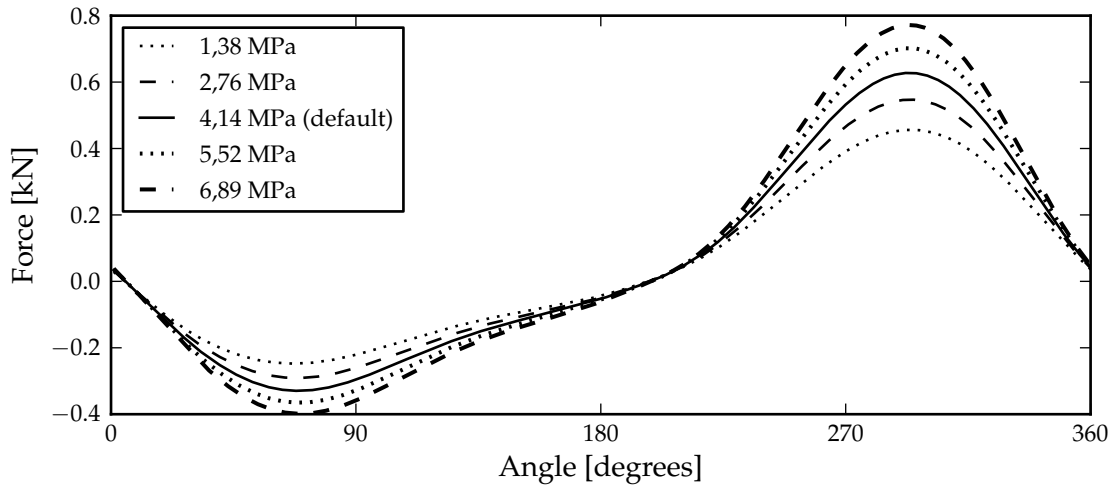

Figure C.15: Displacer linear machine force for various mean pressures.

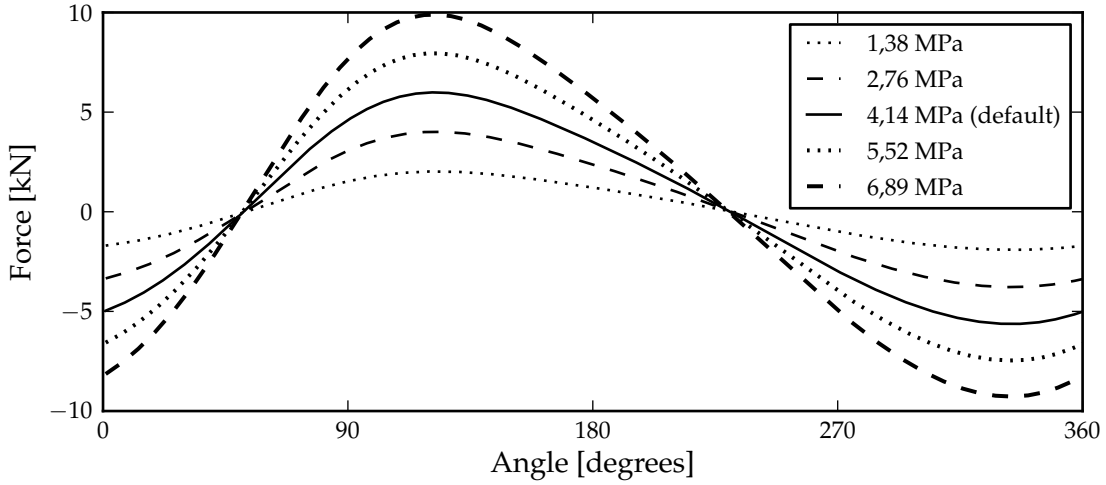

Figure C.16: Power piston linear machine force for various mean pressures.

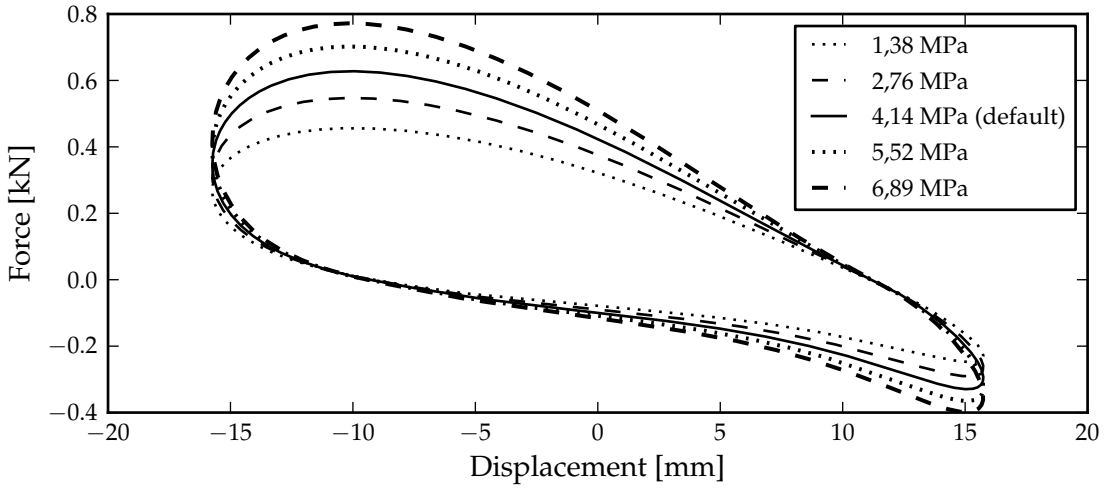

Figure C.17: Displacer linear machine force against displacement for various mean pressures.

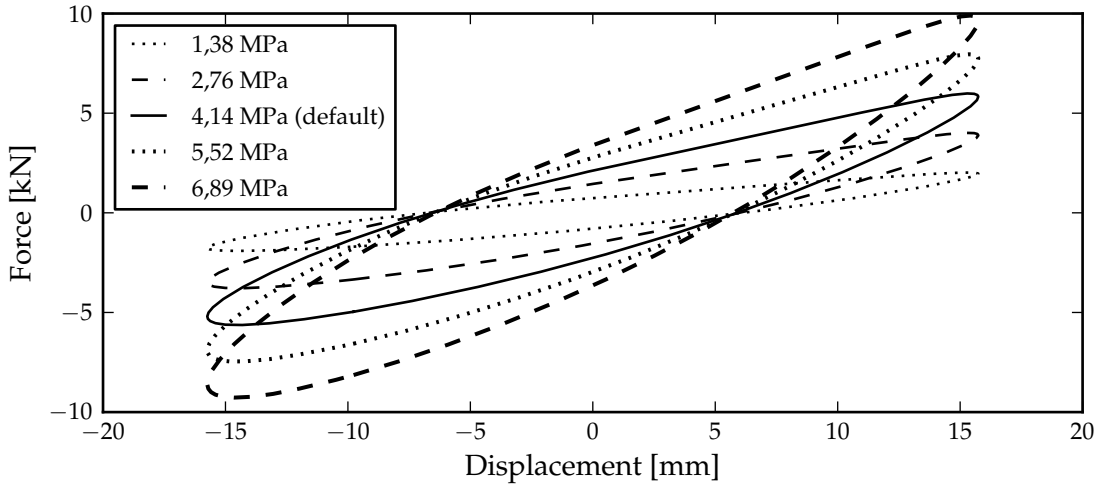

Figure C.18: Power piston linear machine force against displacement for various mean pressures.

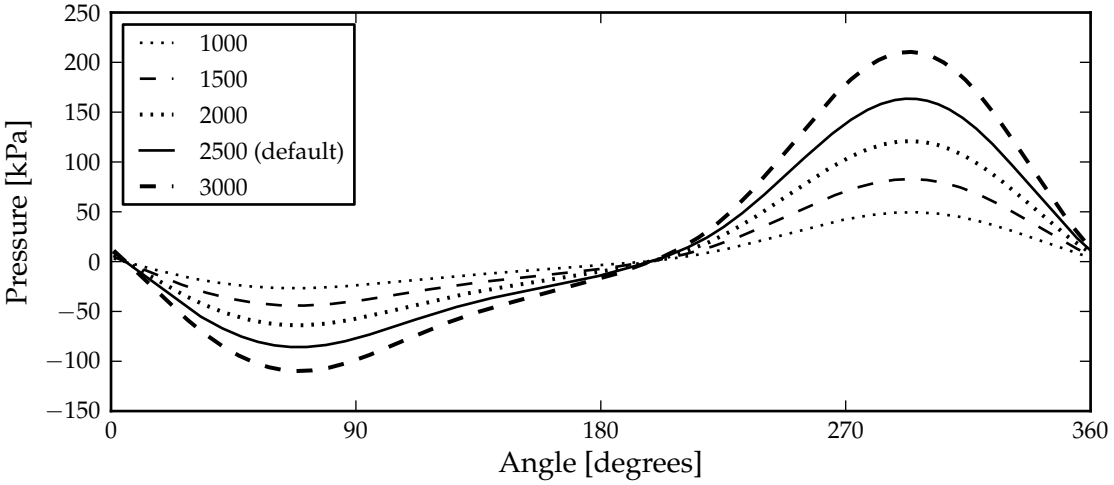

Figure C.19: Expansion to compression space pressure drop for various engine speeds.

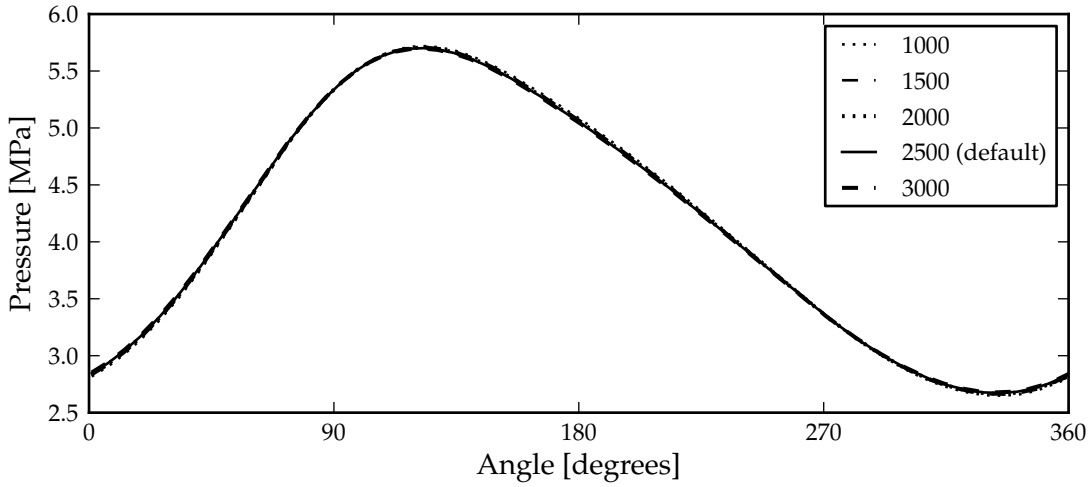

Figure C.20: Compression space pressure for various engine speeds.

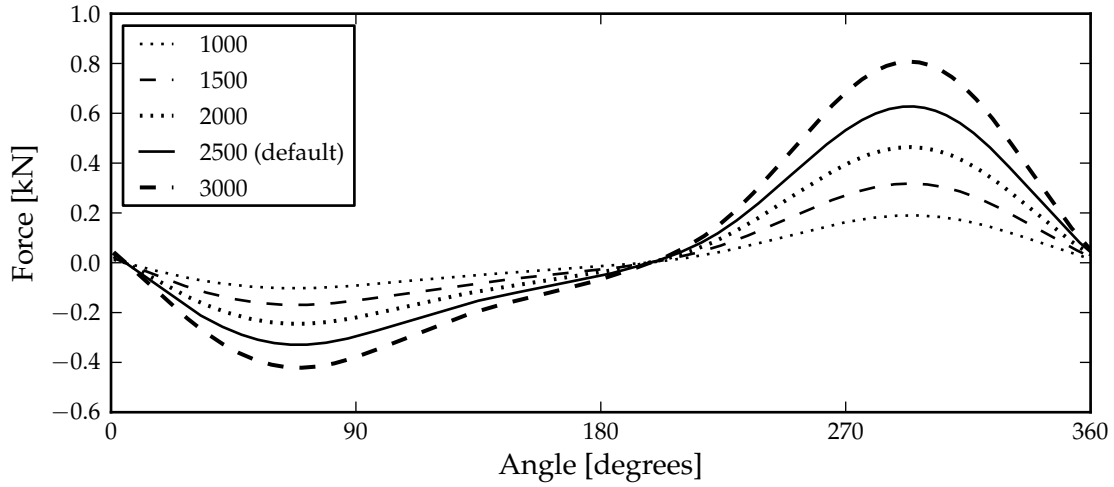

Figure C.21: Displacer linear machine force for various engine speeds.

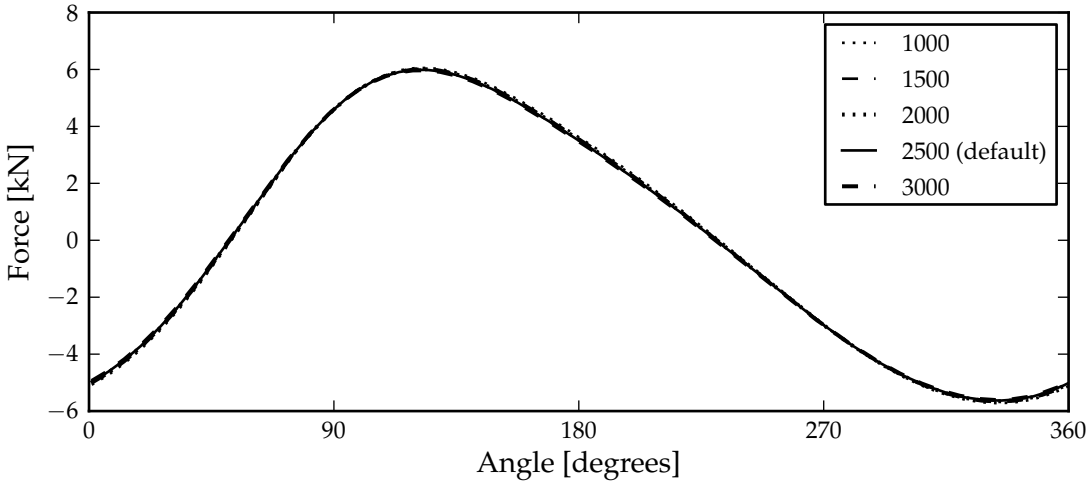

Figure C.22: Power piston linear machine force for various engine speeds.

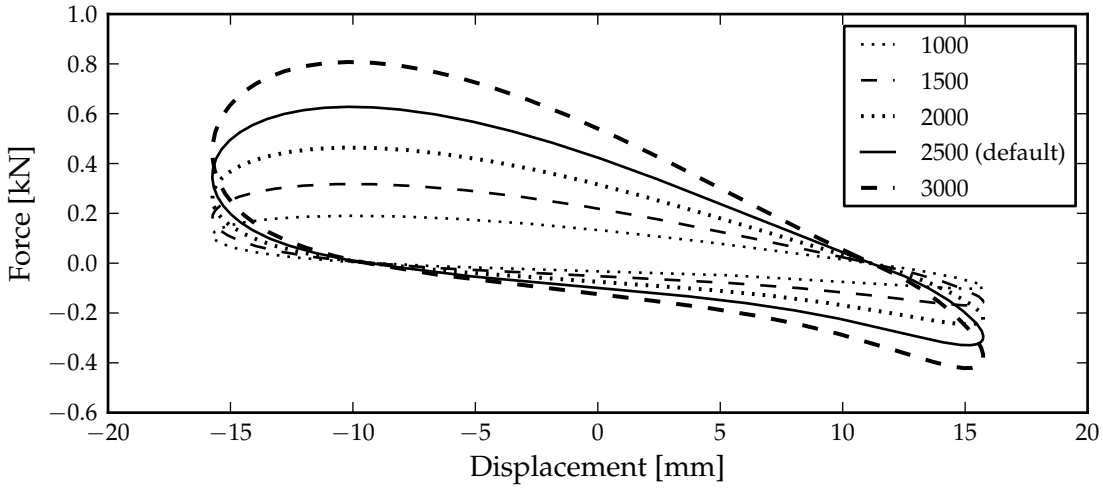

Figure C.23: Displacer linear machine force against displacement for various engine speeds.

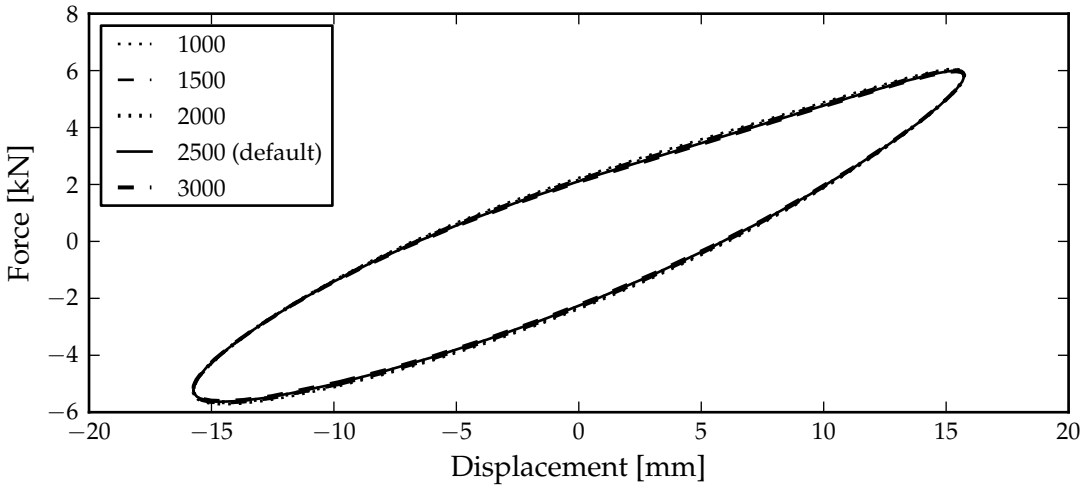

Figure C.24: Power piston linear machine force against displacement for various engine speeds.

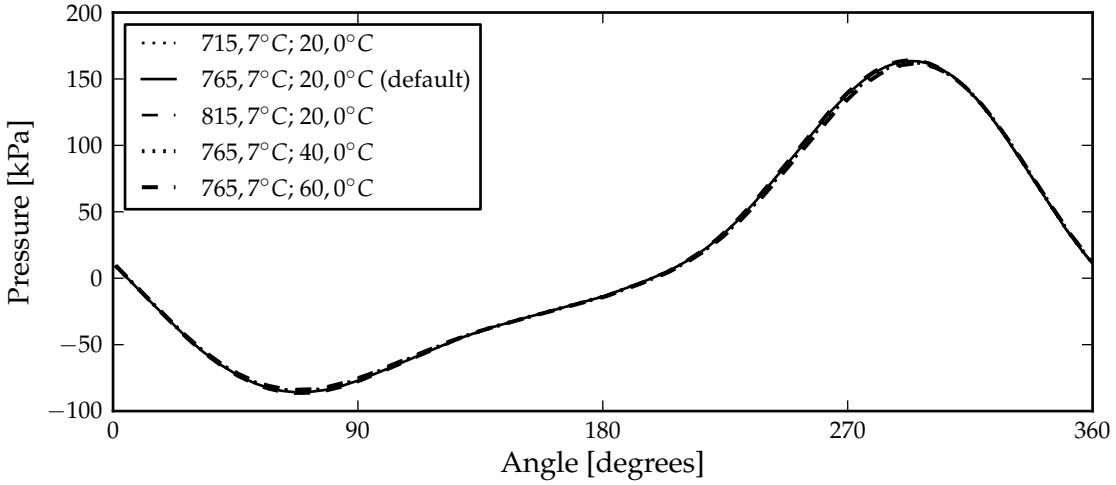

Figure C.25: Expansion to compression space pressure drop for various wall temperatures.

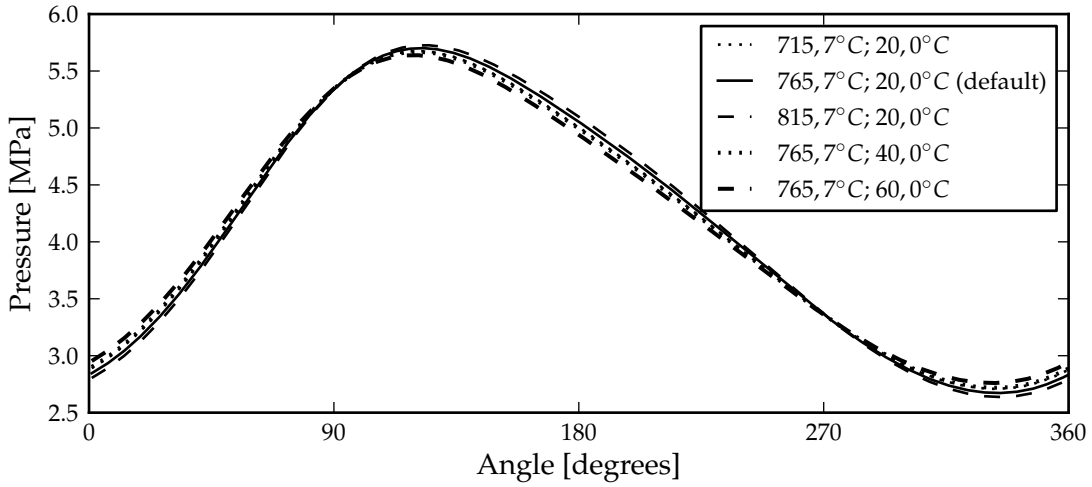

Figure C.26: Compression space pressure for various wall temperatures.

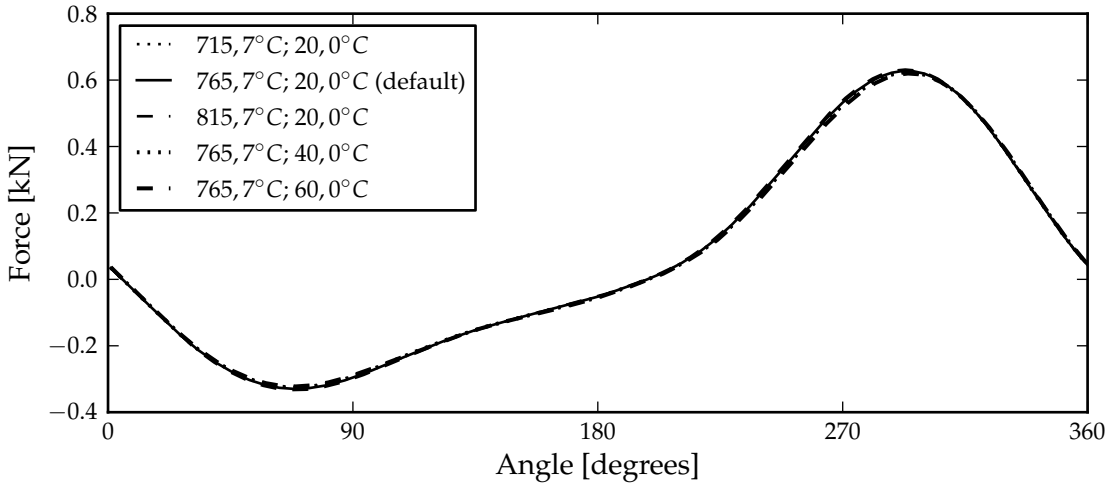

Figure C.27: Displacer linear machine force for various wall temperatures.

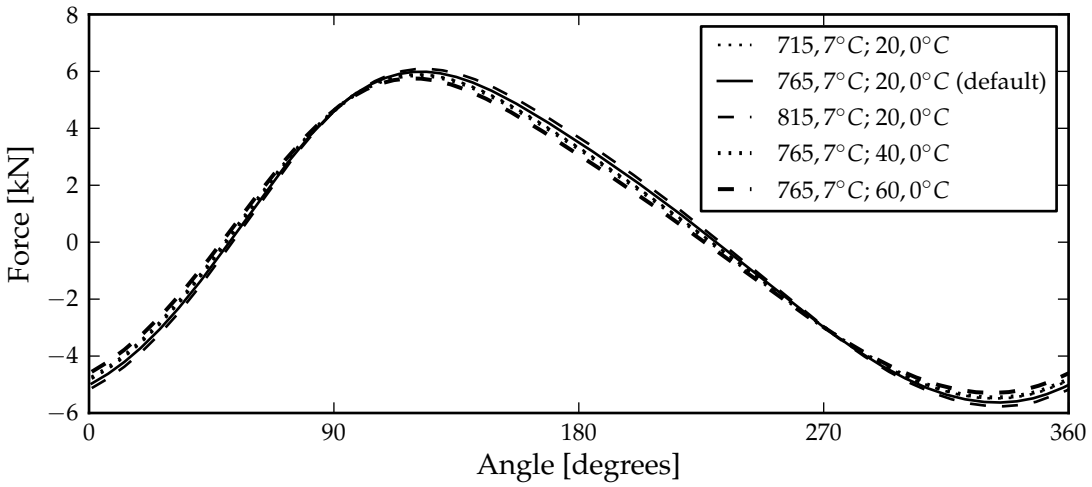

Figure C.28: Power piston linear machine force for various wall temperatures.

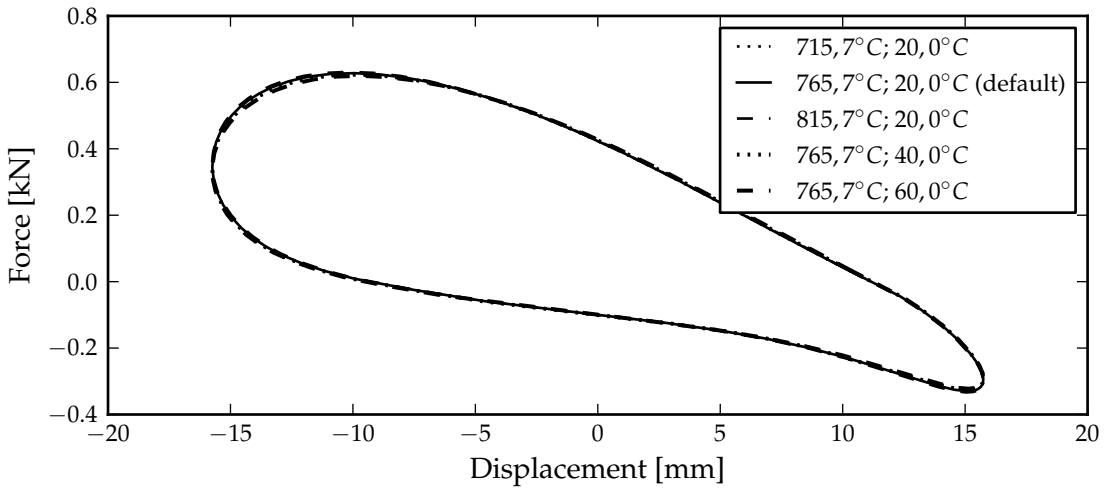

Figure C.29: Displacer linear machine force against displacement for various wall temperatures.

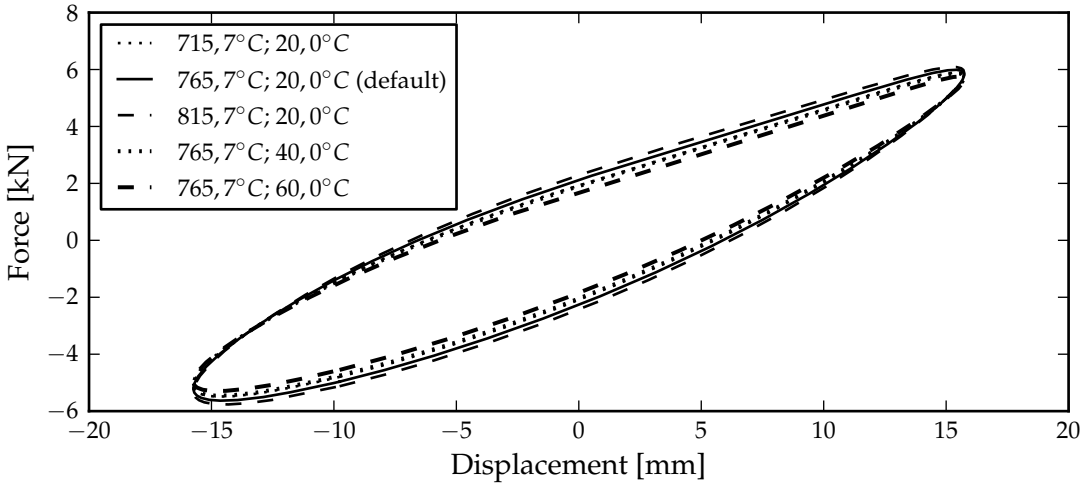

Figure C.30: Power piston linear machine force against displacement for various wall temperatures.

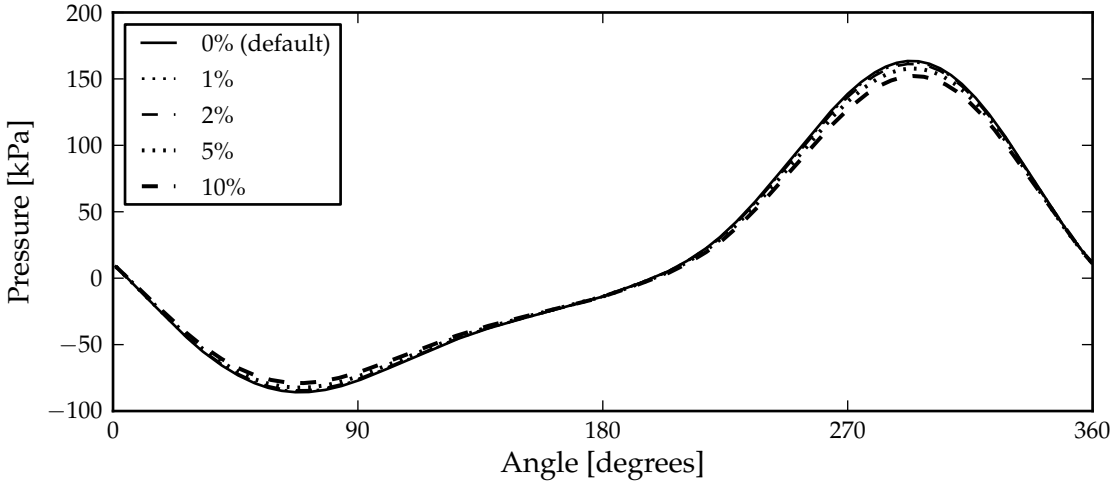

Figure C.31: Expansion to compression space pressure drop for various rod area to bore area ratios.

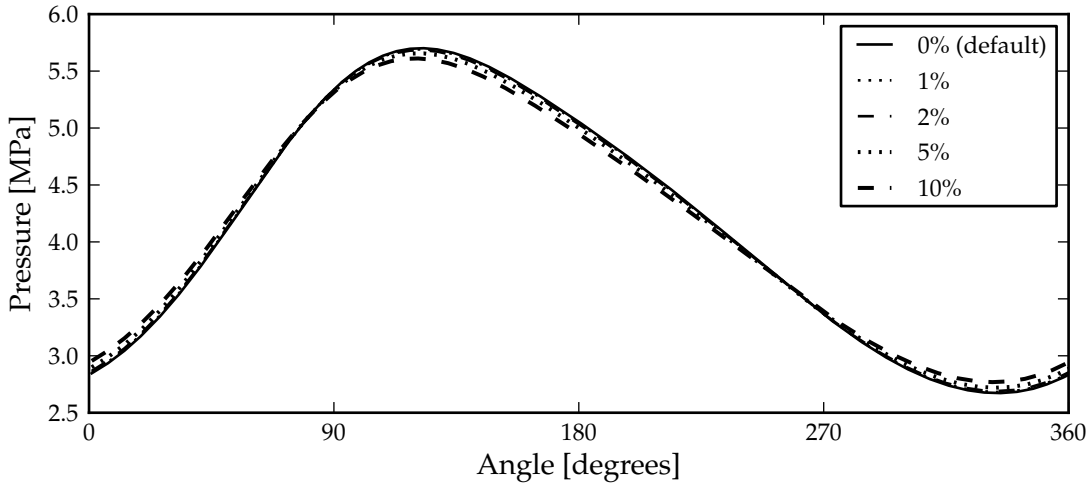

Figure C.32: Compression space pressure for various rod area to bore area ratios.

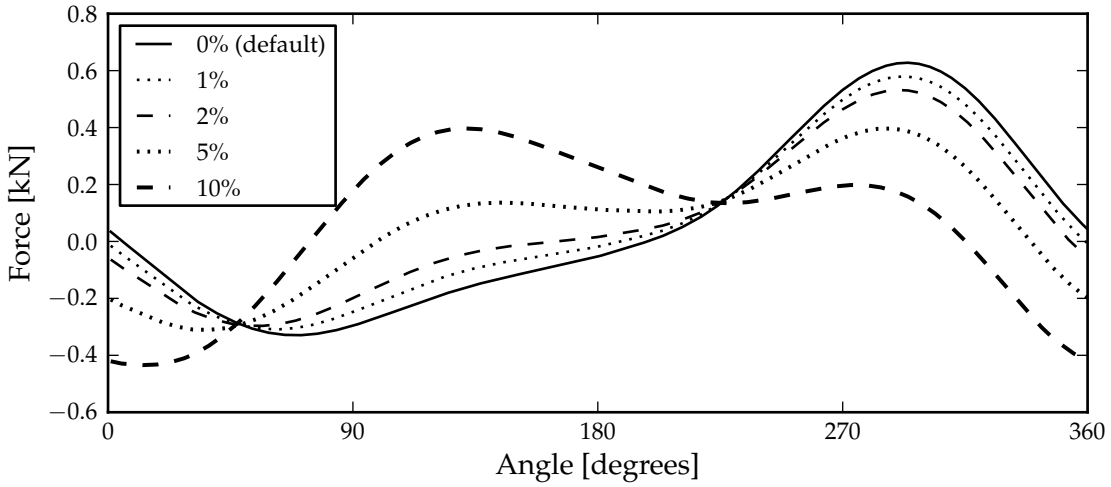

Figure C.33: Displacer linear machine force for various rod area to bore area ratios.

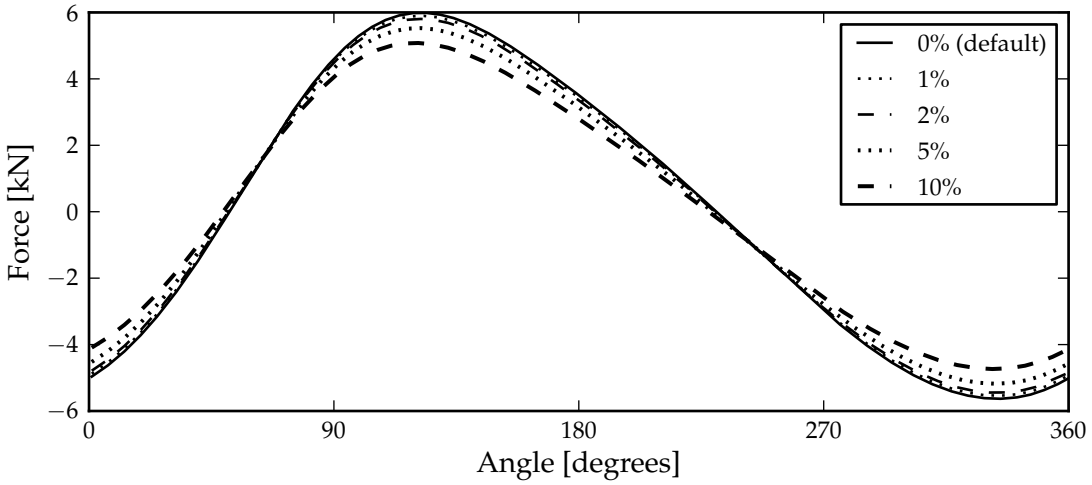

Figure C.34: Power piston linear machine force for various rod area to bore area ratios.

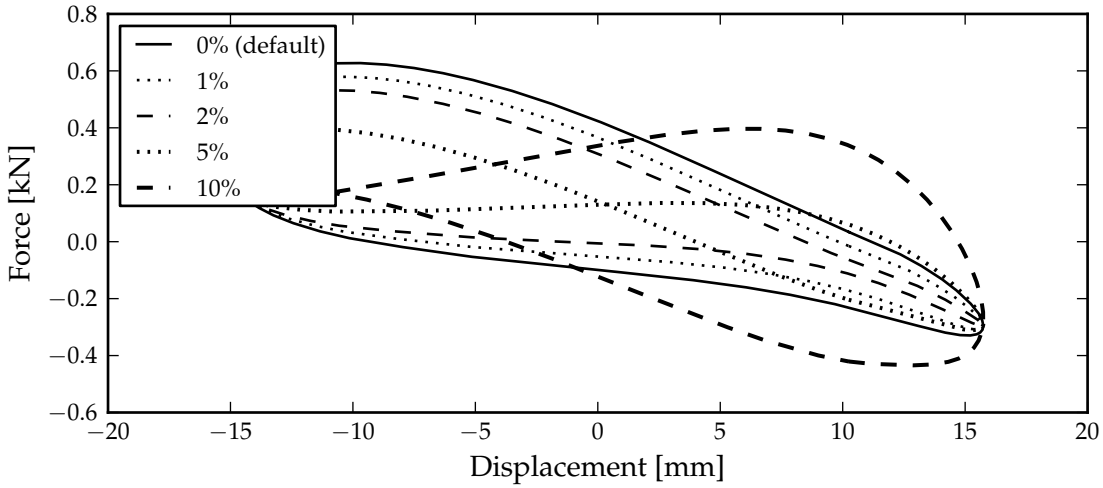

Figure C.35: Displacer linear machine force against displacement for various rod area to bore area ratios.

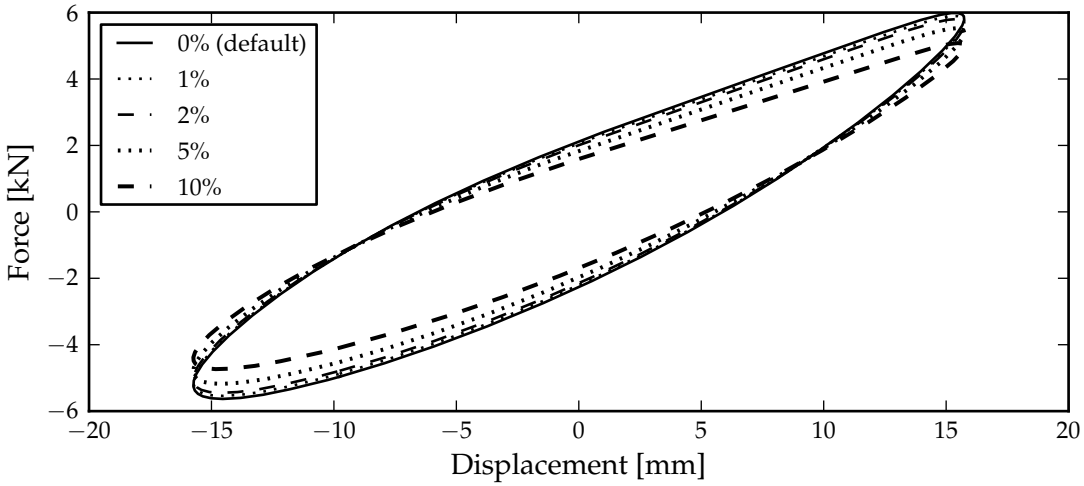

Figure C.36: Power piston linear machine force against displacement for various rod area to bore area ratios.

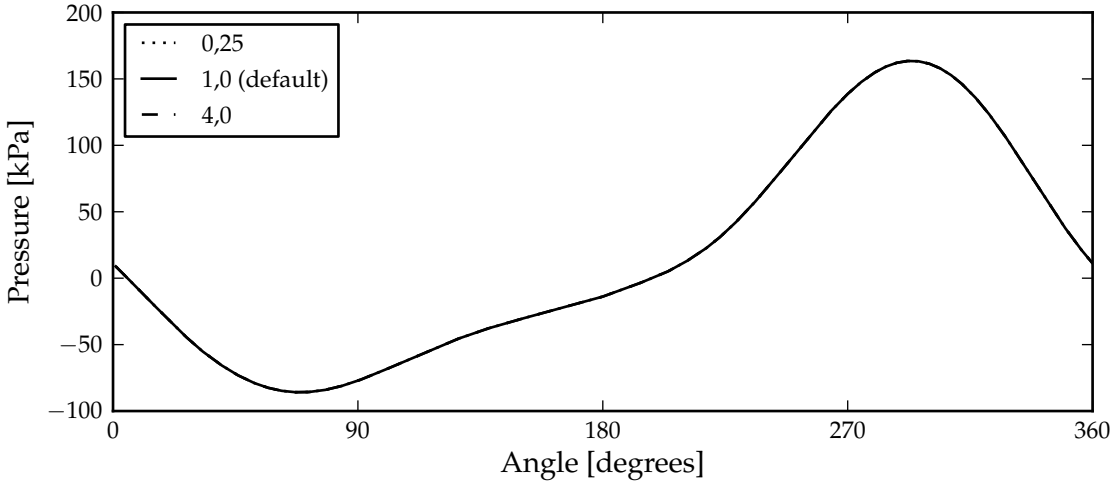

Figure C.37: Expansion to compression space pressure drop for various normalised stroke to bore ratios.

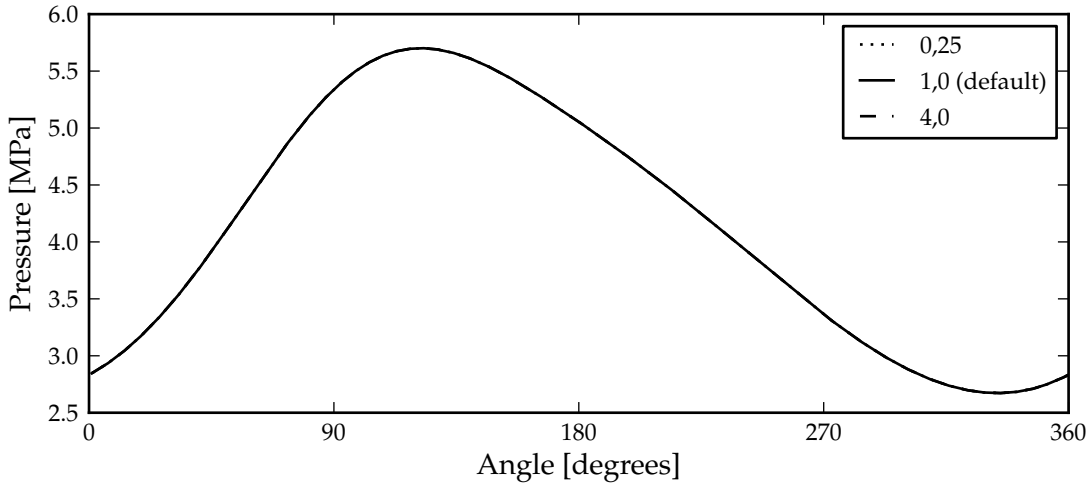

Figure C.38: Compression space pressure for various normalised stroke to bore ratios.

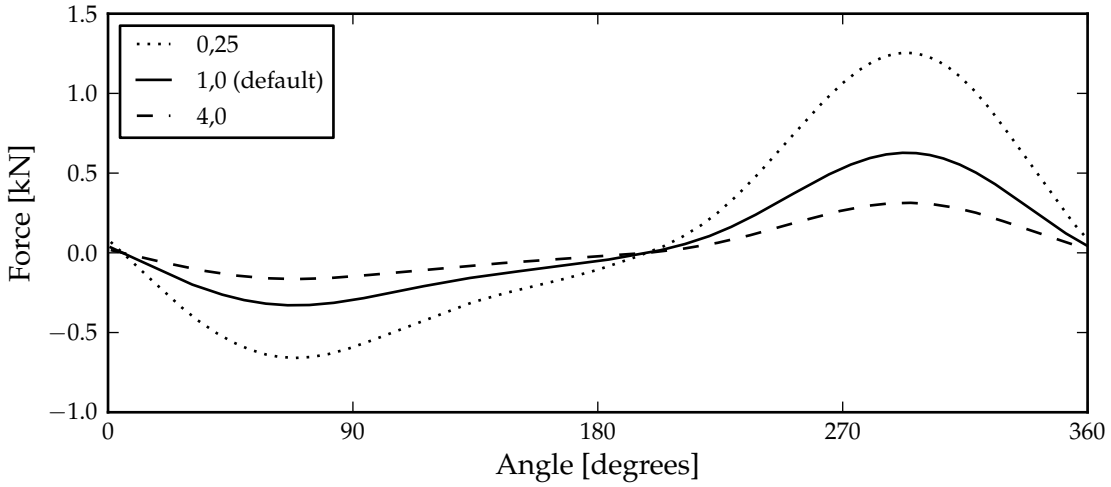

Figure C.39: Displacer linear machine force for various normalised stroke to bore ratios.

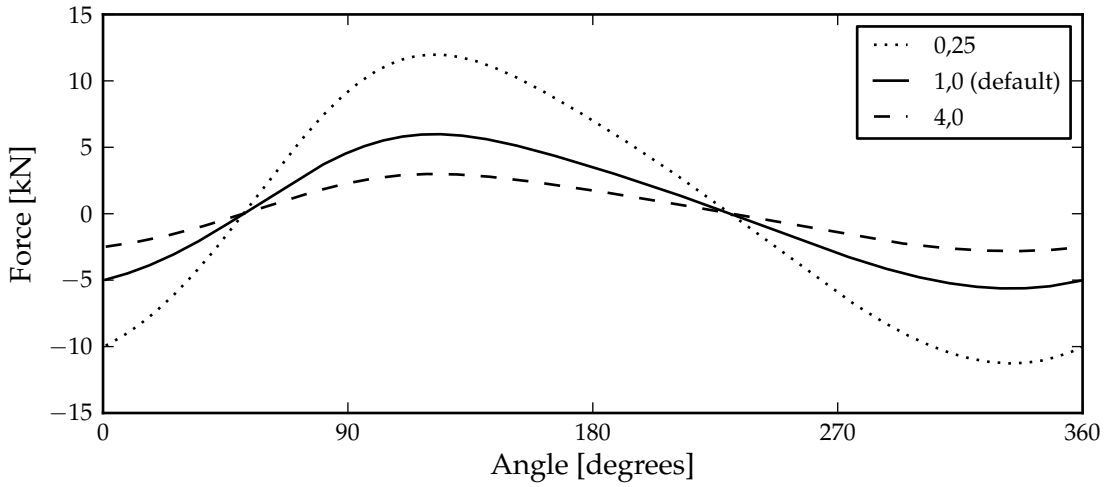

Figure C.40: Power piston linear machine force for various normalised stroke to bore ratios.

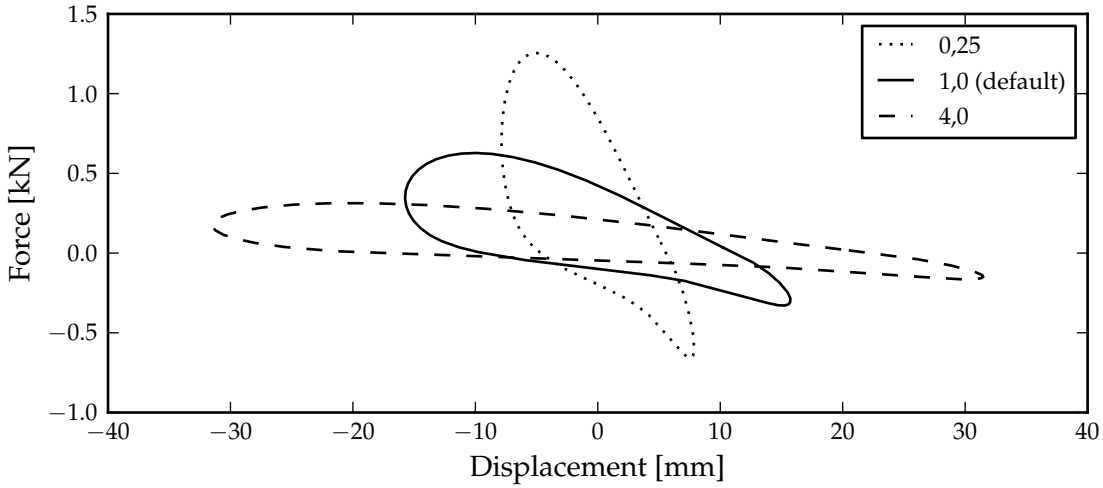

Figure C.41: Displacer linear machine force against displacement for various normalised stroke to bore ratios.

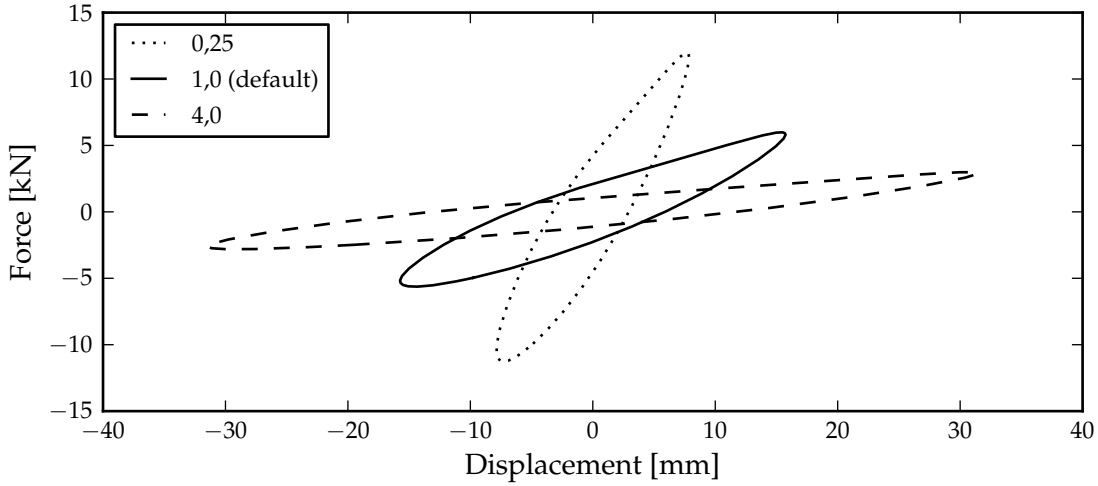

Figure C.42: Power piston linear machine force against displacement for various normalised stroke to bore ratios.

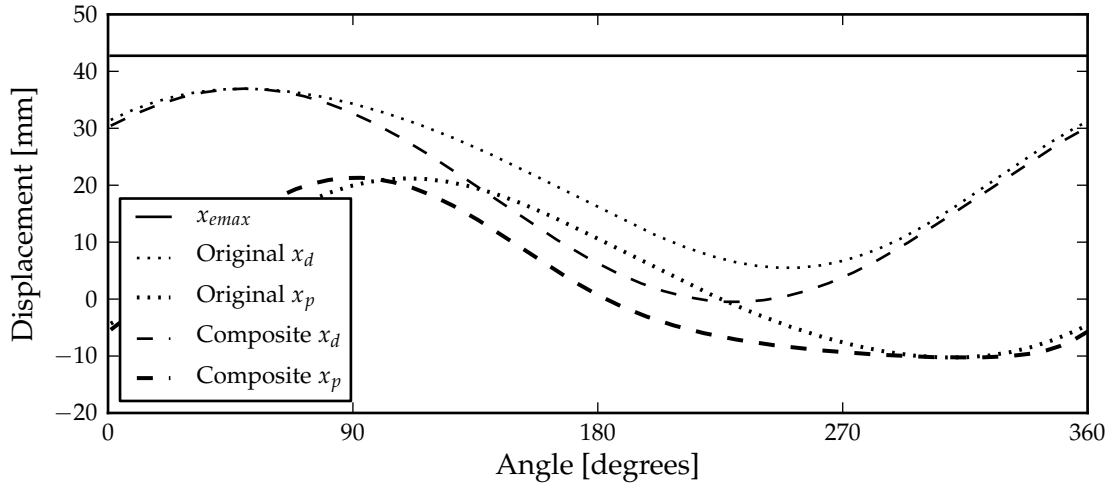

Figure C.43: Displacer displacement for different piston displacements optimised for maximum power output.

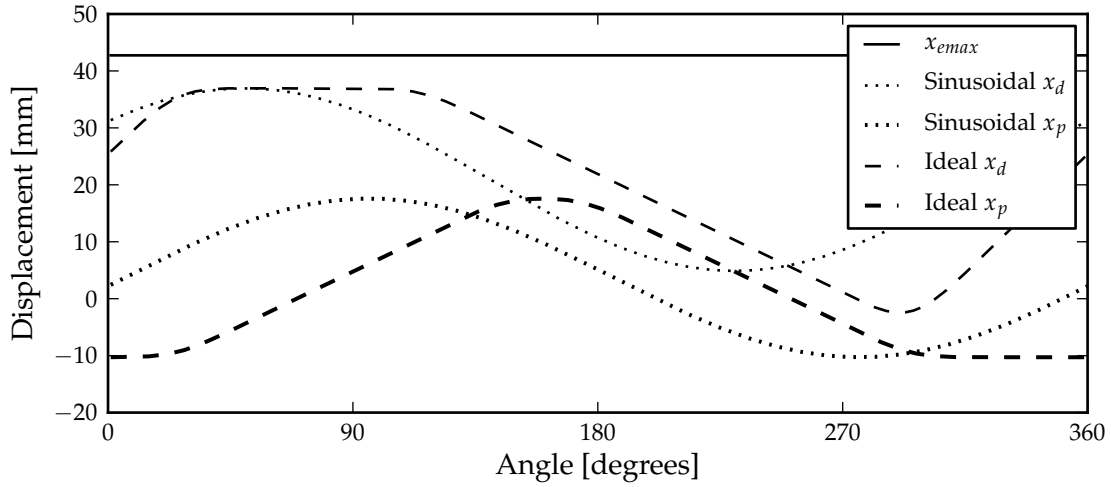

Figure C.44: Power piston displacement for different piston displacements optimised for maximum power output.

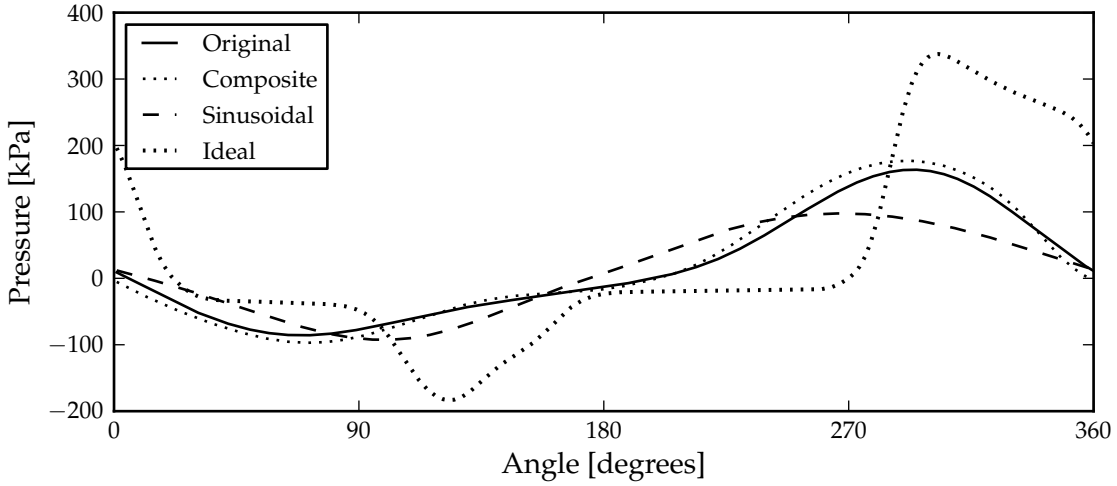

Figure C.45: Expansion to compression space pressure drop for different piston displacements optimised for maximum power output.

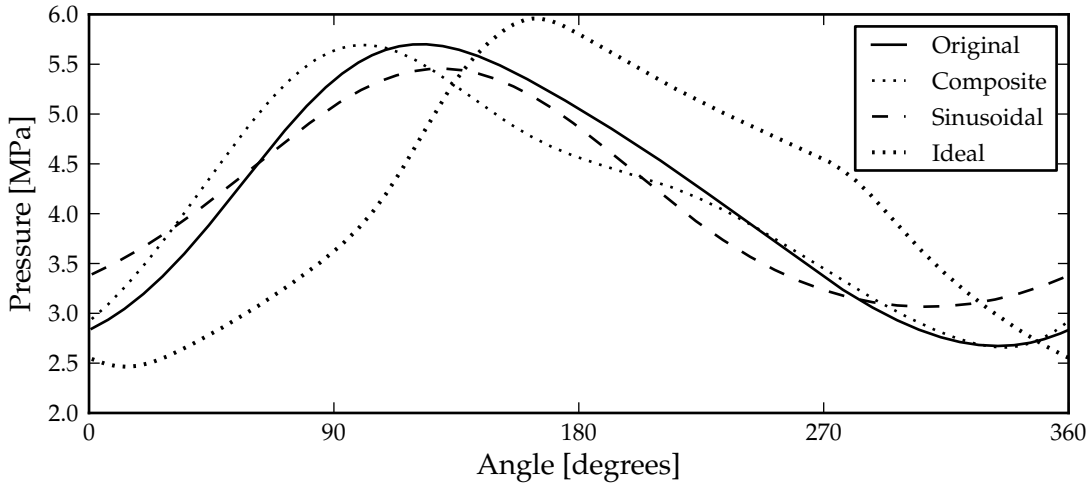

Figure C.46: Compression space pressure for different piston displacements optimised for maximum power output.

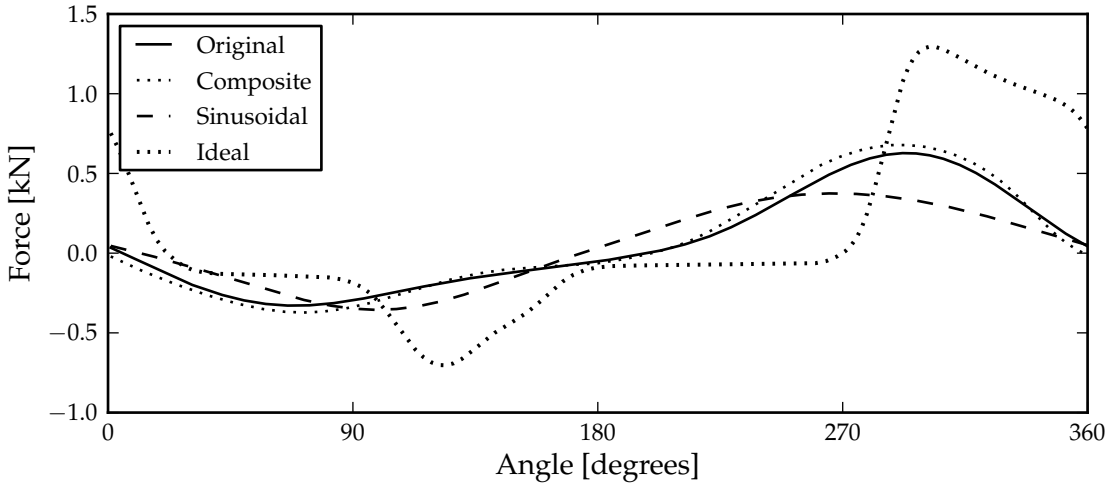

Figure C.47: Displacer linear machine force for different piston displacements optimised for maximum power output.

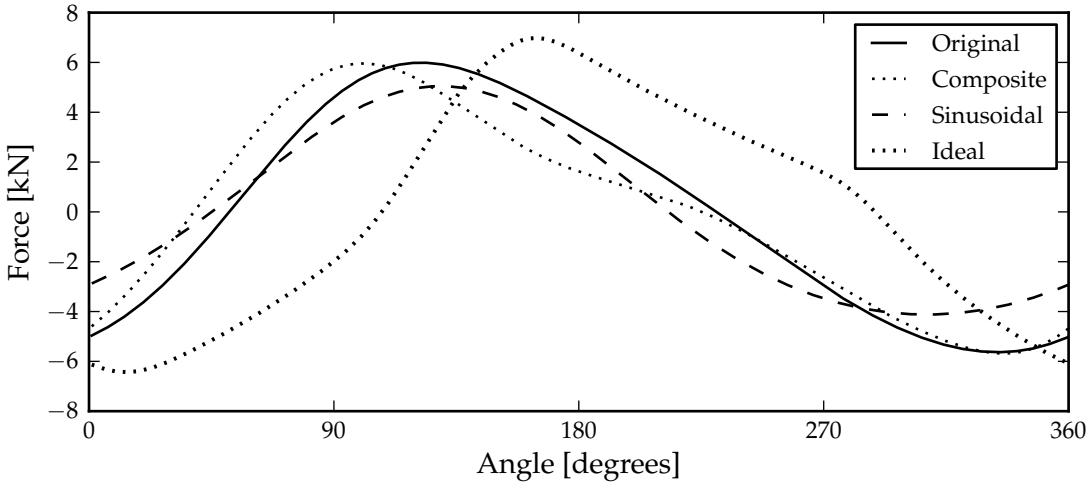

Figure C.48: Power piston linear machine force for different piston displacements optimised for maximum power output.

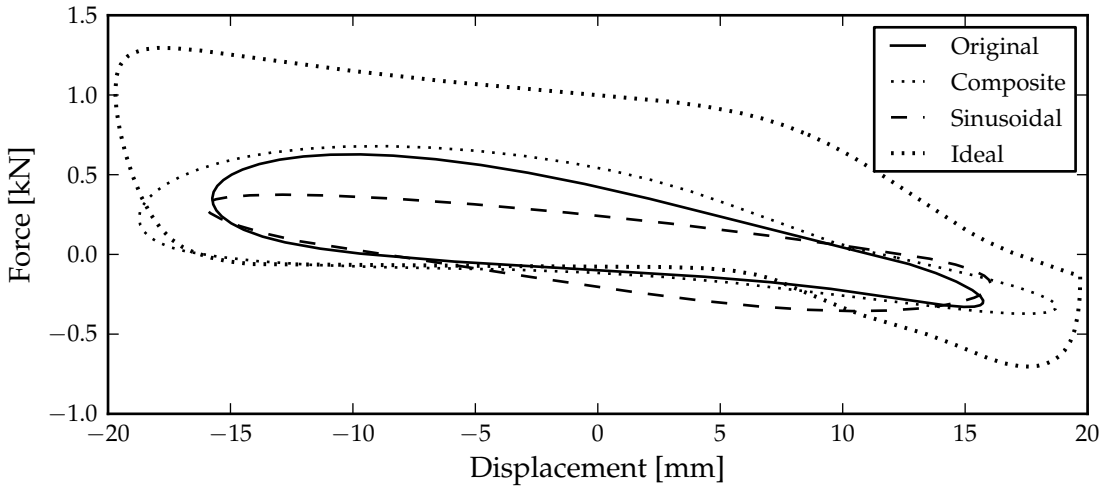

Figure C.49: Displacer linear machine force against displacement for different piston displacements optimised for maximum power output.

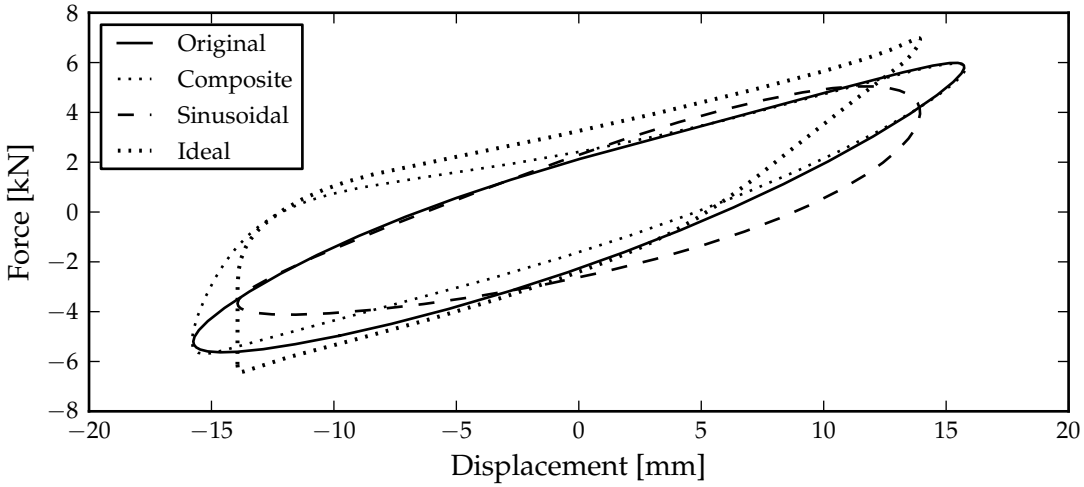

Figure C.50: Power piston linear machine force against displacement for different piston displacements optimised for maximum power output.

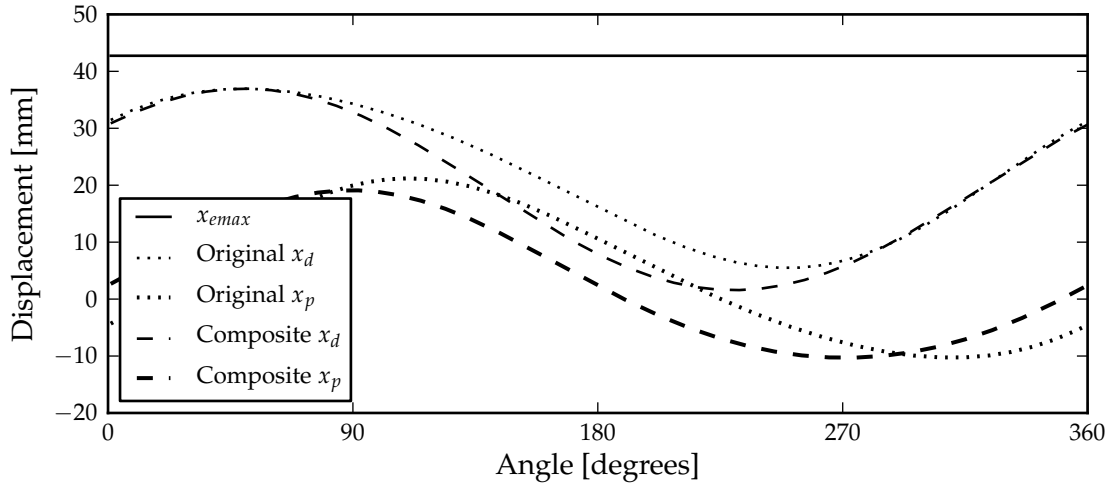

Figure C.51: Displacer displacement for different piston displacements optimised for maximum efficiency.

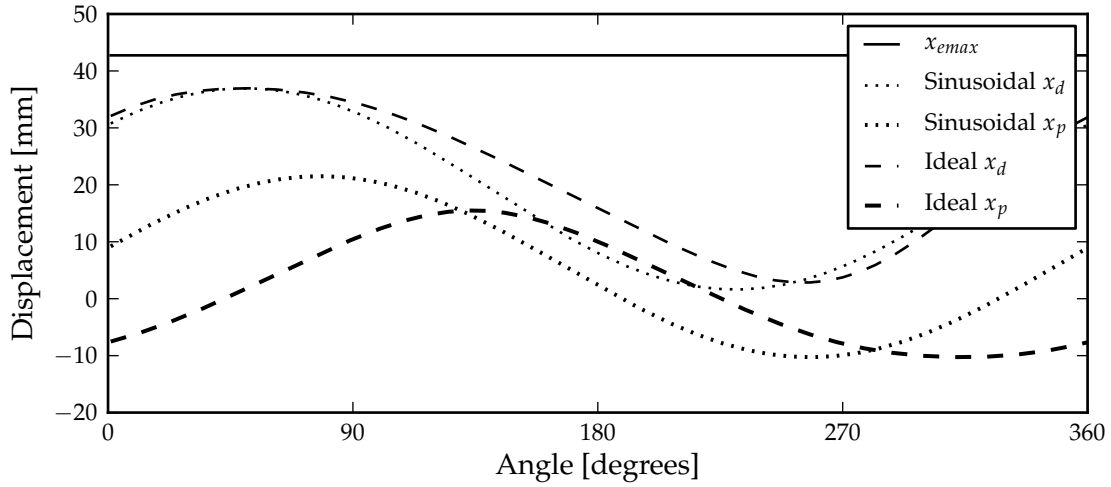

Figure C.52: Power piston displacement for different piston displacements optimised for maximum efficiency.

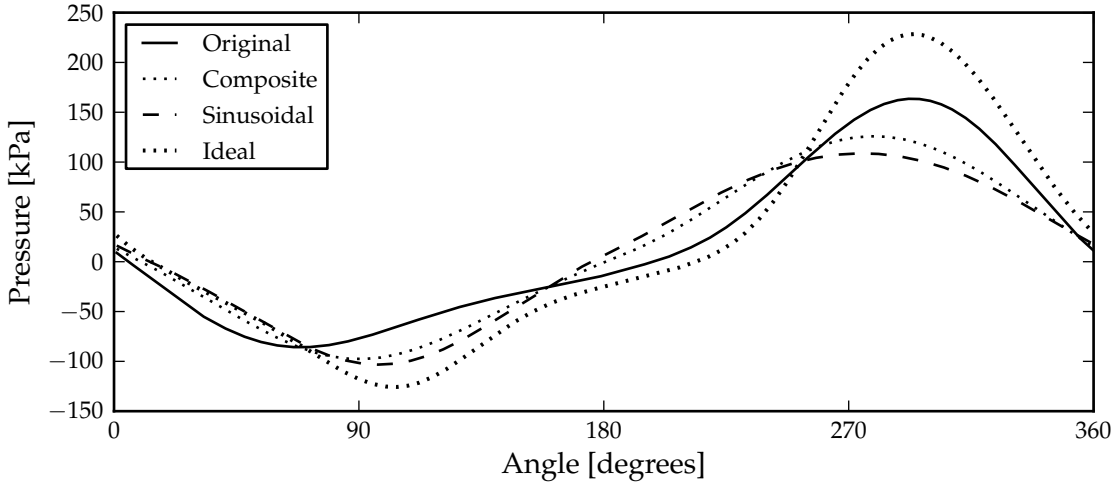

Figure C.53: Expansion to compression space pressure drop for different piston displacements optimised for maximum efficiency.

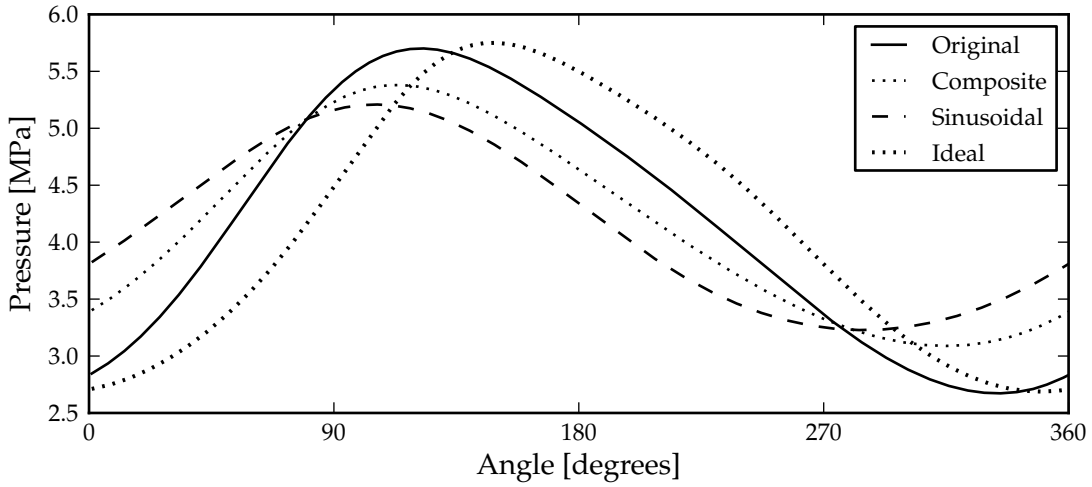

Figure C.54: Compression space pressure for different piston displacements optimised for maximum efficiency.

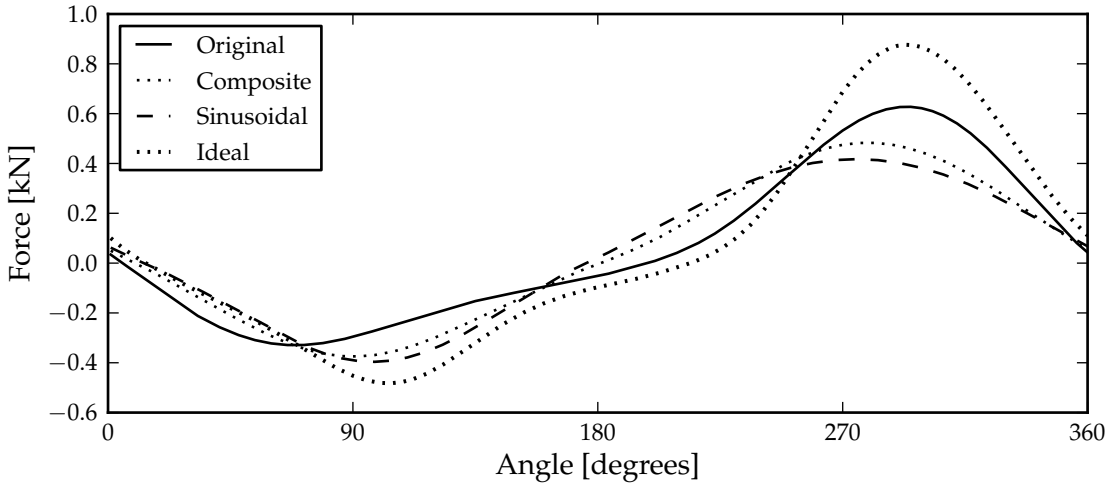

Figure C.55: Displacer linear machine force for different piston displacements optimised for maximum efficiency.

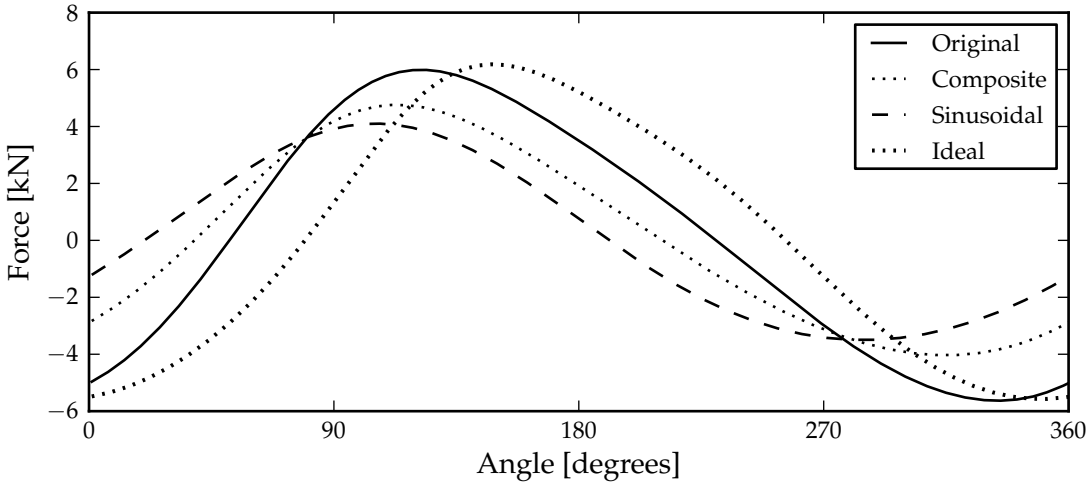

Figure C.56: Power piston linear machine force for different piston displacements optimised for maximum efficiency.

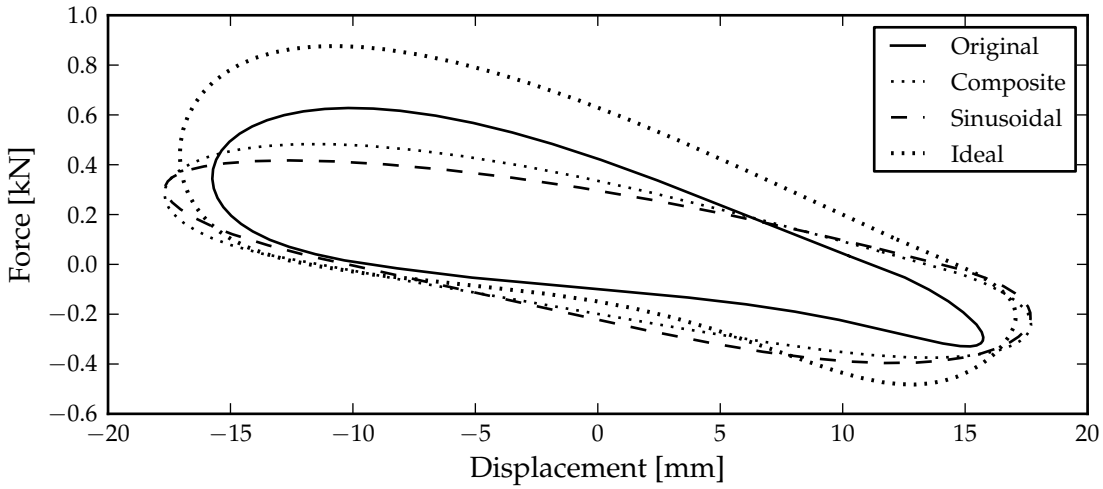

Figure C.57: Displacer linear machine force against displacement for different piston displacements optimised for maximum efficiency.

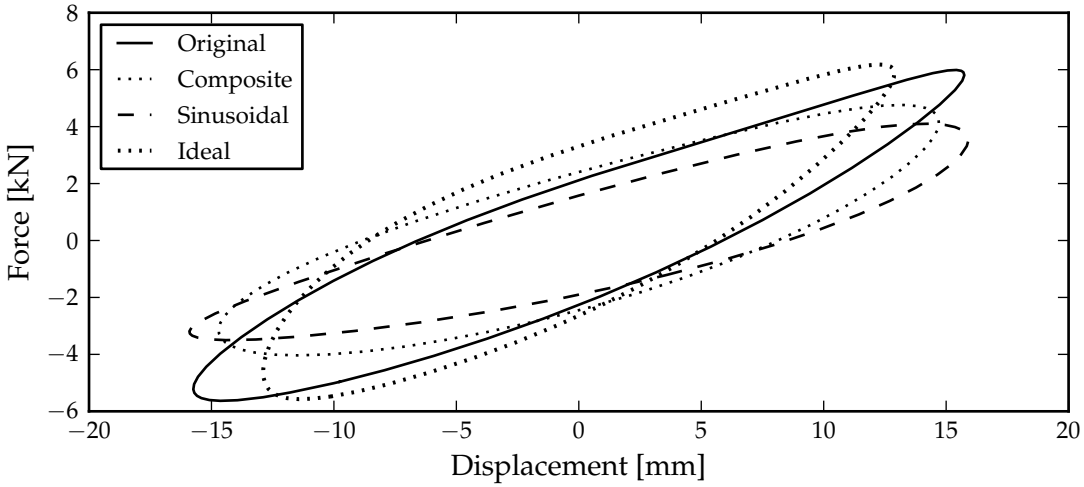

Figure C.58: Power piston linear machine force against displacement for different piston displacements optimised for maximum efficiency.

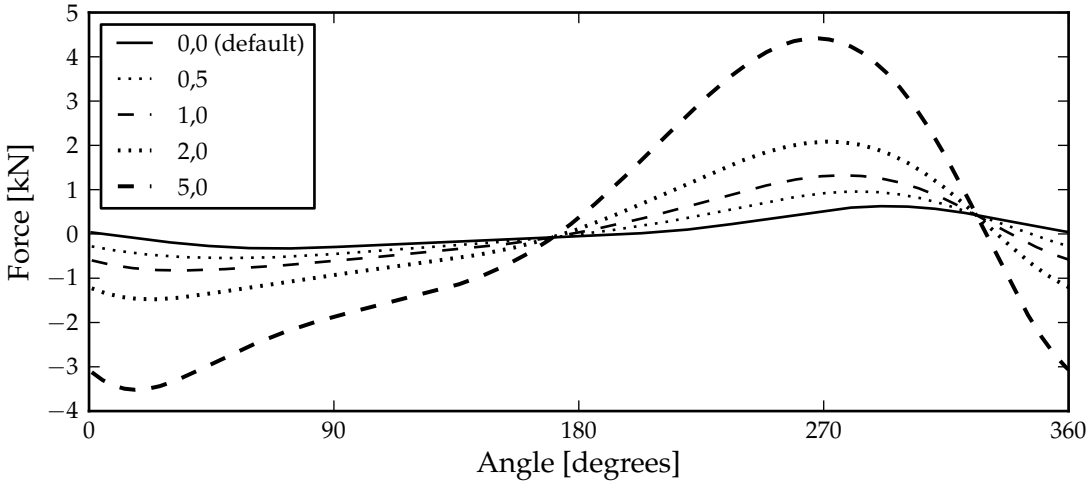

Figure C.59: Displacer linear machine force for various mass to power ratios.

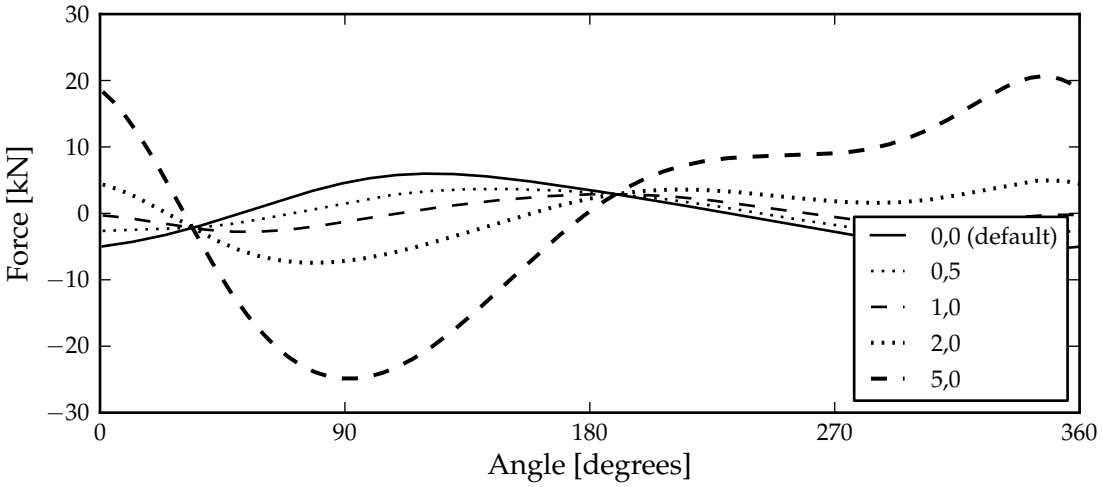

Figure C.60: Power piston linear machine force for various mass to power ratios.

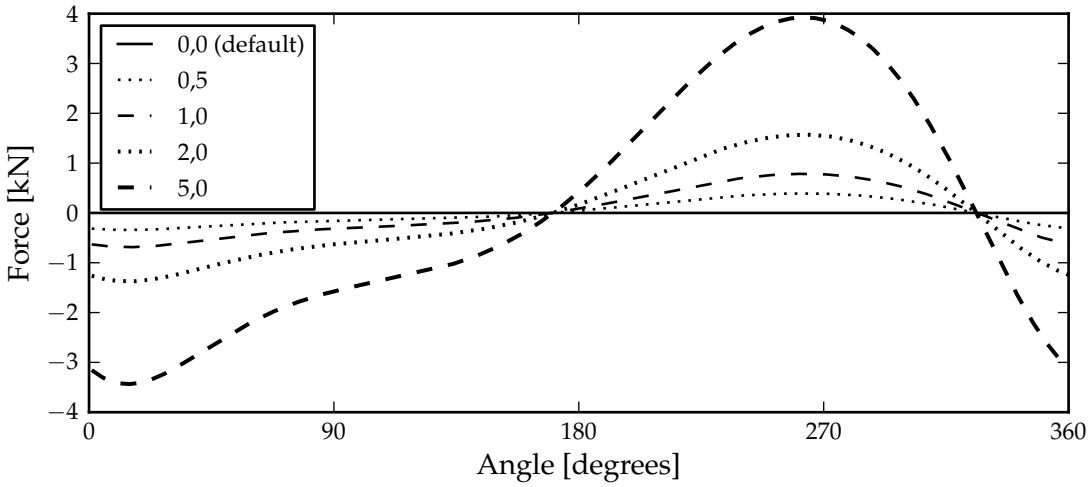

Figure C.61: Displacer mass acceleration force for various mass to power ratios.

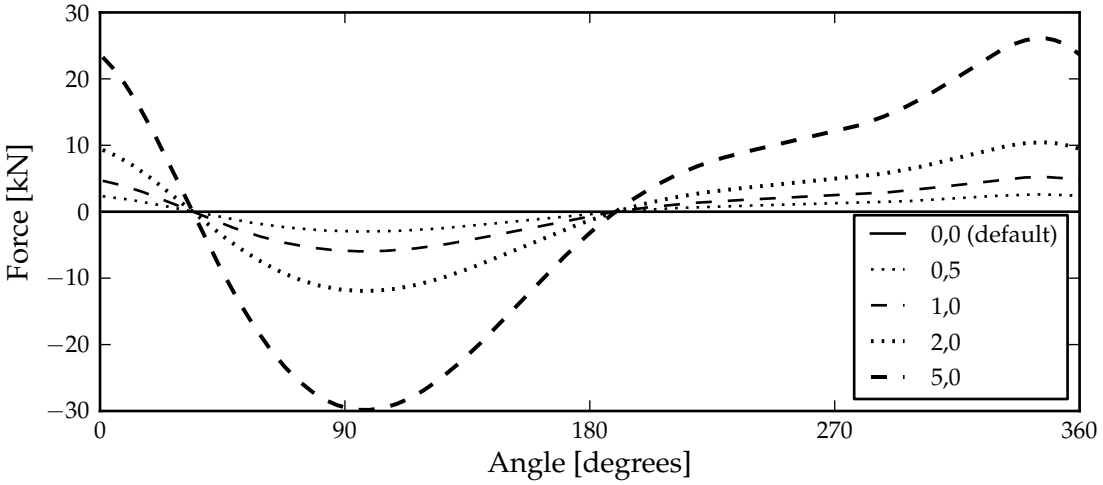

Figure C.62: Power piston mass acceleration force for various mass to power ratios.

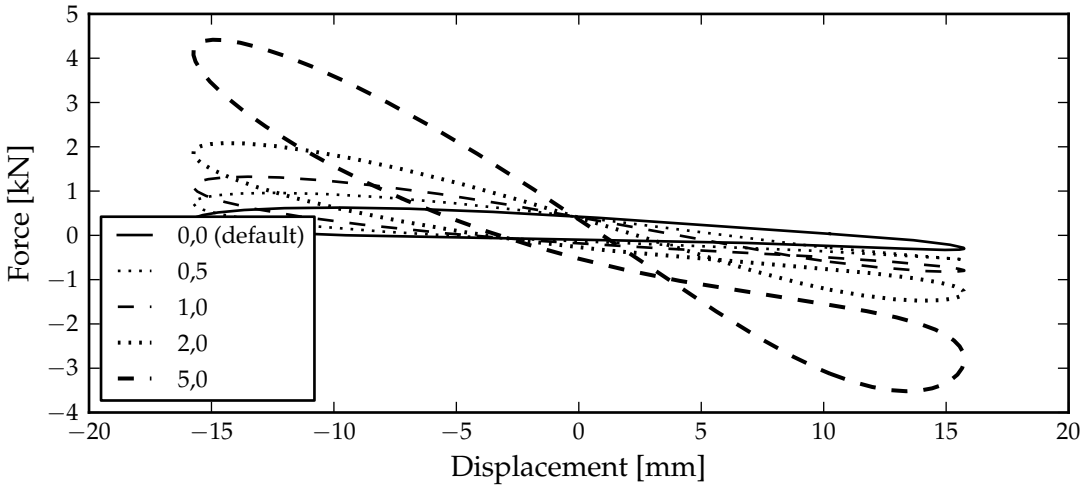

Figure C.63: Displacer linear machine force against displacement for various mass to power ratios.

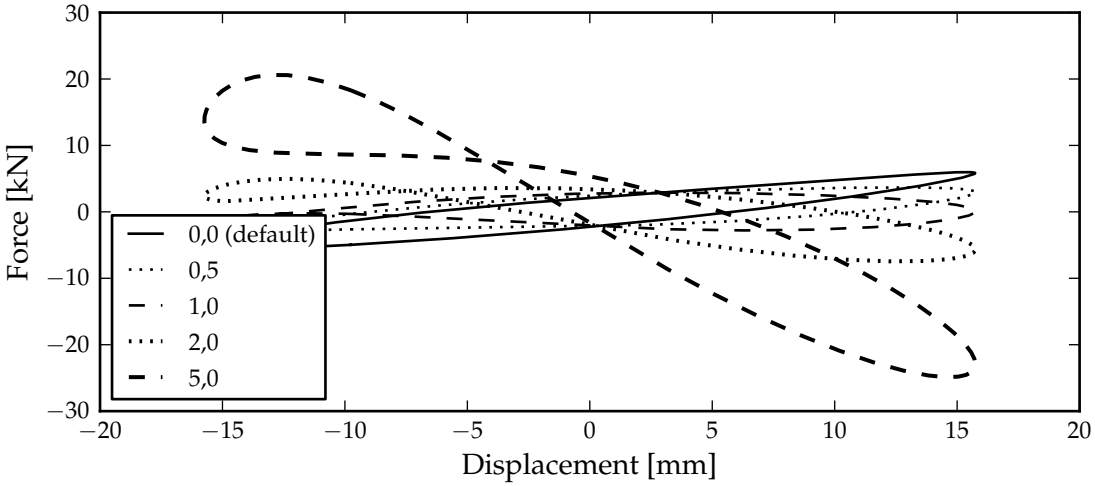

Figure C.64: Power piston linear machine force against displacement for various mass to power ratios.

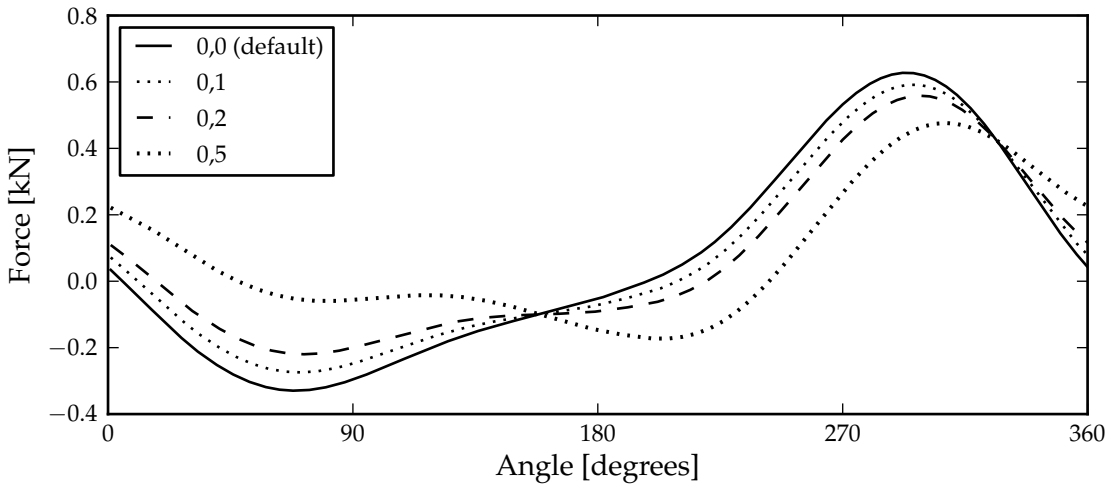

Figure C.65: Displacer linear machine force for various spring constants.

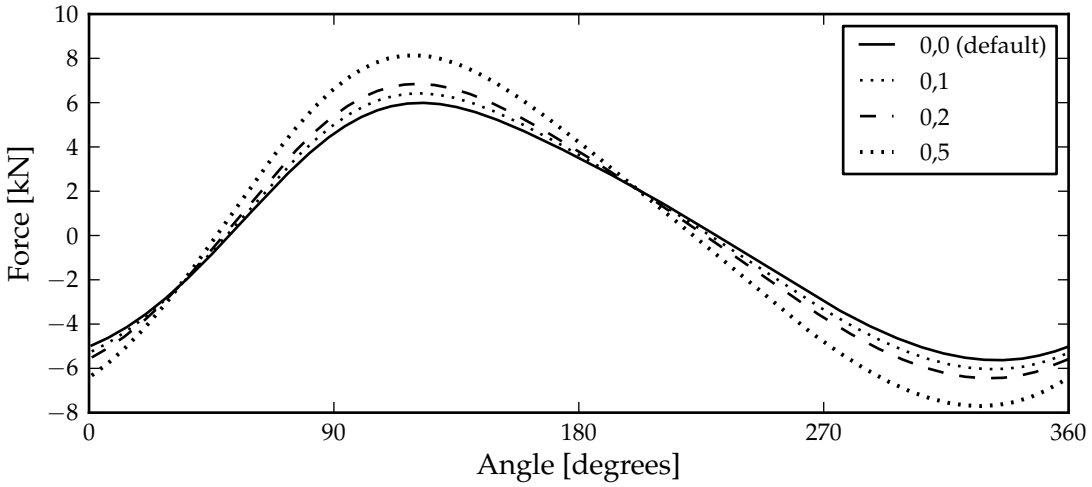

Figure C.66: Power piston linear machine force for various spring constants.

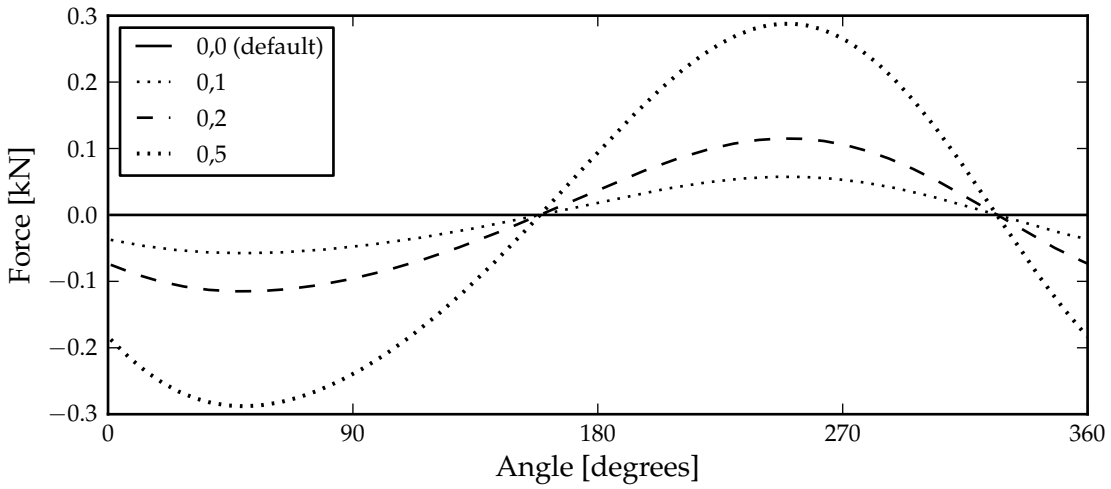

Figure C.67: Displacer spring force for various spring constants.

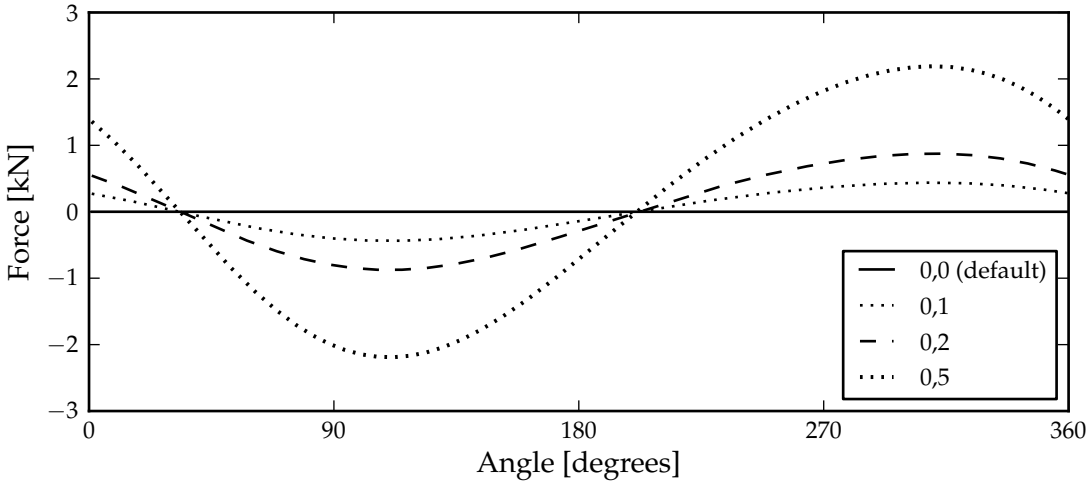

Figure C.68: Power piston spring force for various spring constants.

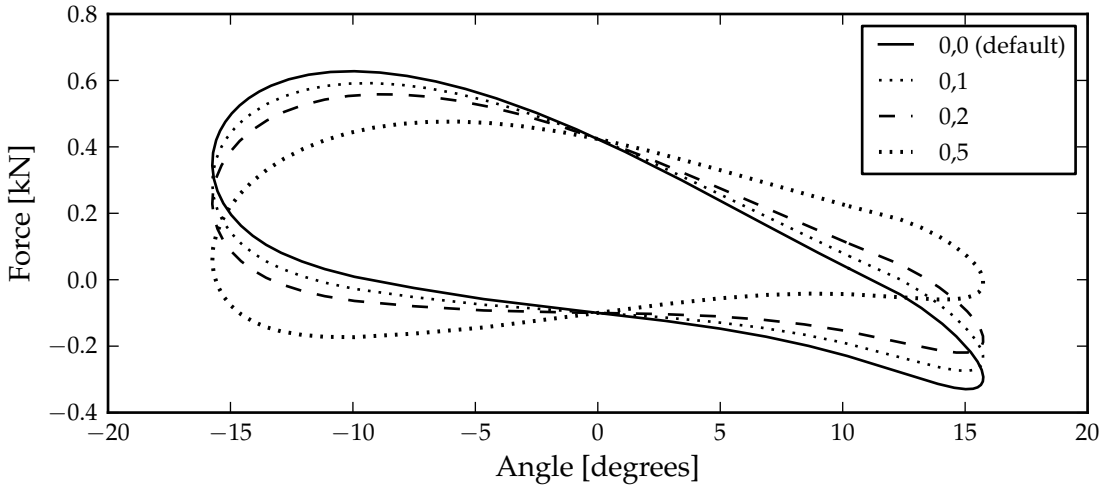

Figure C.69: Displacer linear machine force against displacement for various spring constants.

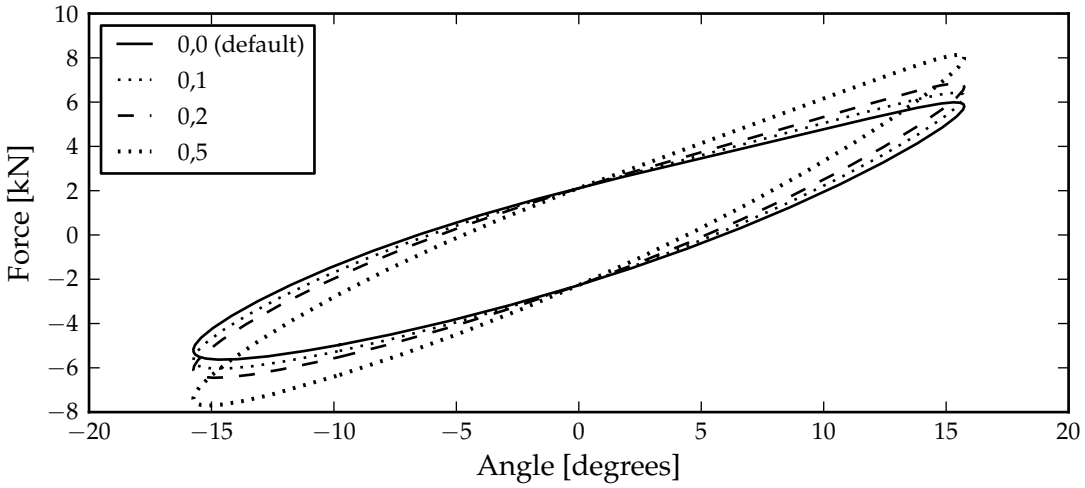

Figure C.70: Power piston linear machine force against displacement for various spring constants.

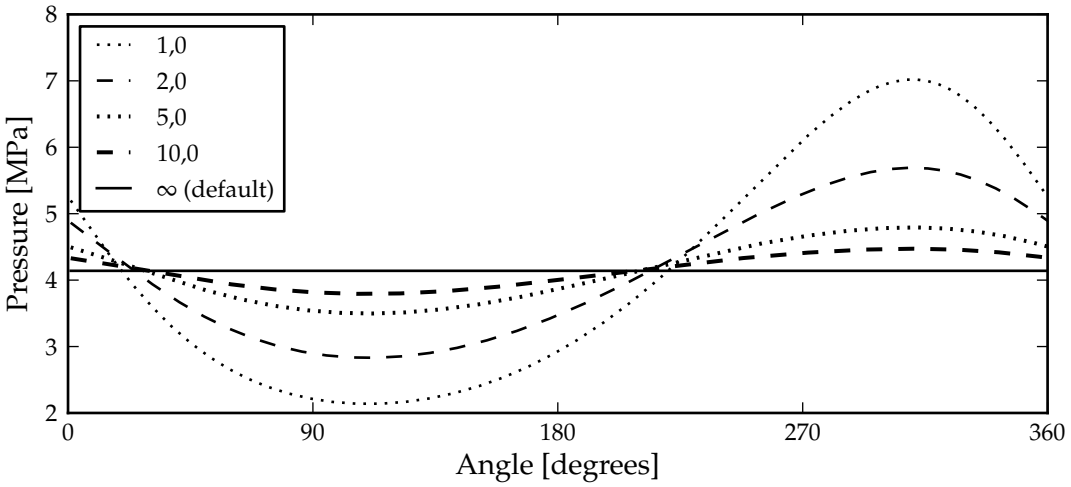

Figure C.71: Bounce space pressure for various bounce space void volume to compression space swept volume ratios.

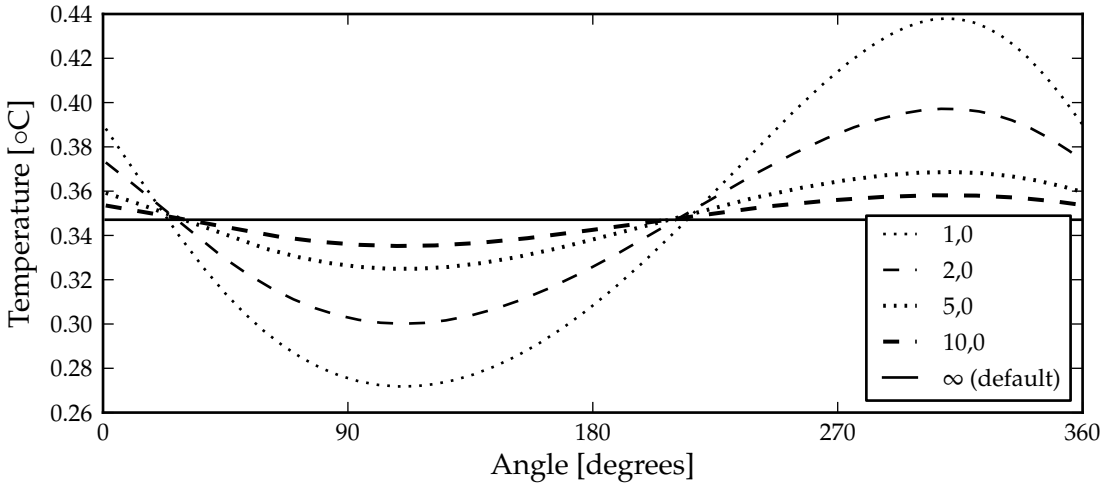

Figure C.72: Bounce space temperature for various bounce space void volume to compression space swept volume ratios.

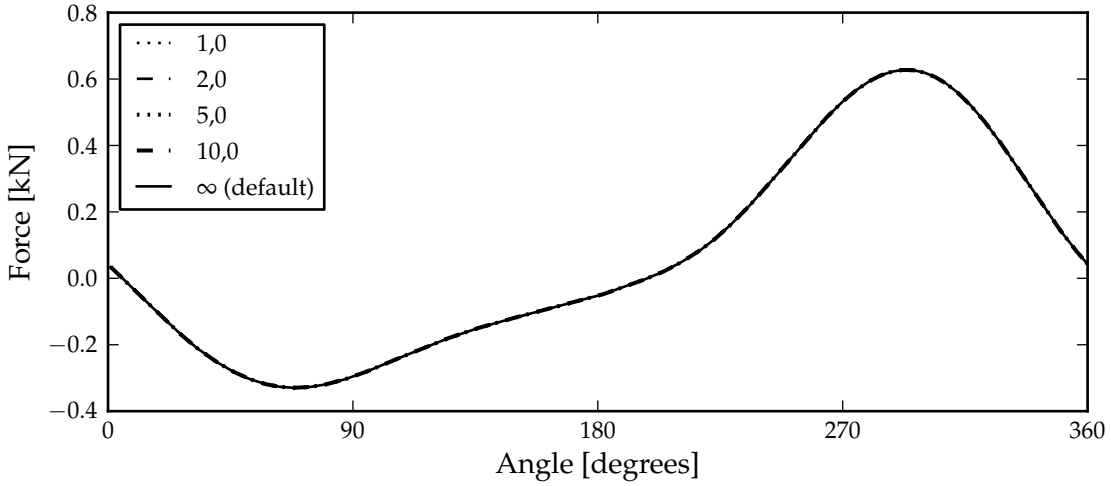

Figure C.73: Displacer linear machine force for various bounce space void volume to compression space swept volume ratios.

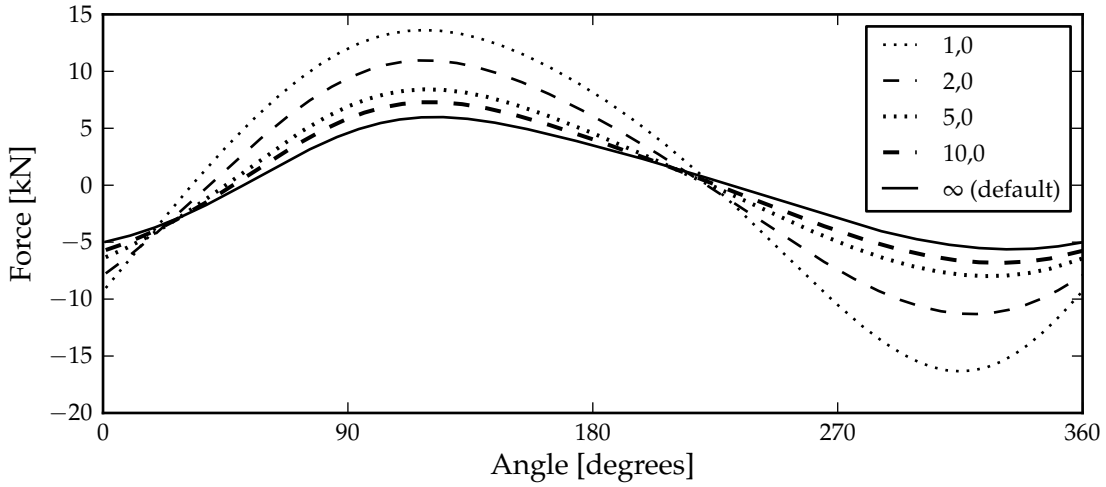

Figure C.74: Power piston linear machine force for various bounce space void volume to compression space swept volume ratios.

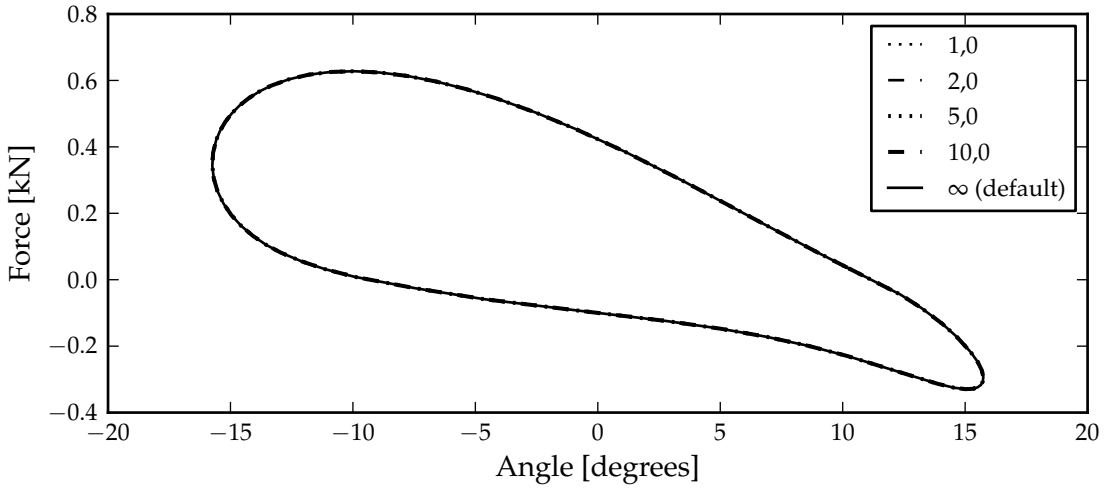

Figure C.75: Displacer linear machine force against displacement for various bounce space void volume to compression space swept volume ratios.

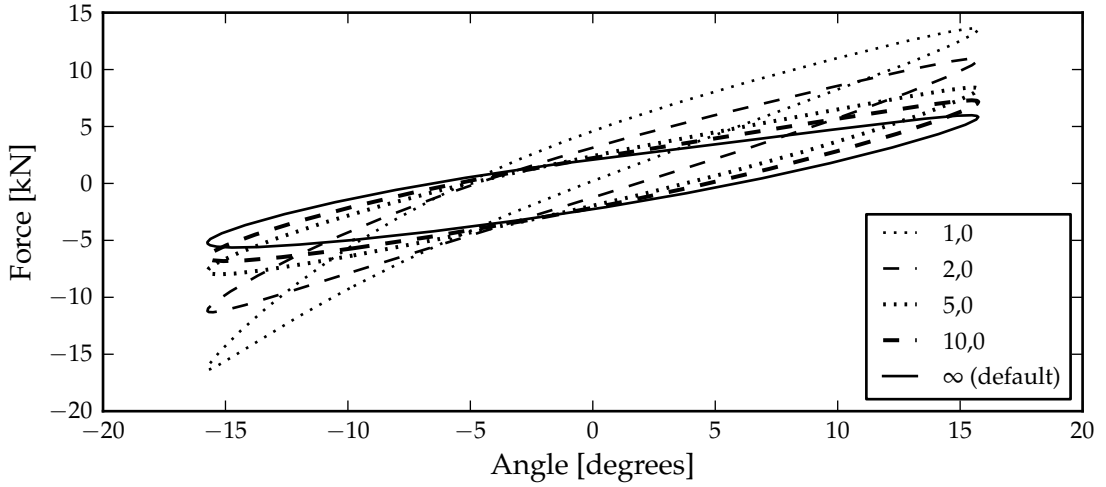

Figure C.76: Power piston linear machine force against displacement for various bounce space void volume to compression space swept volume ratios.

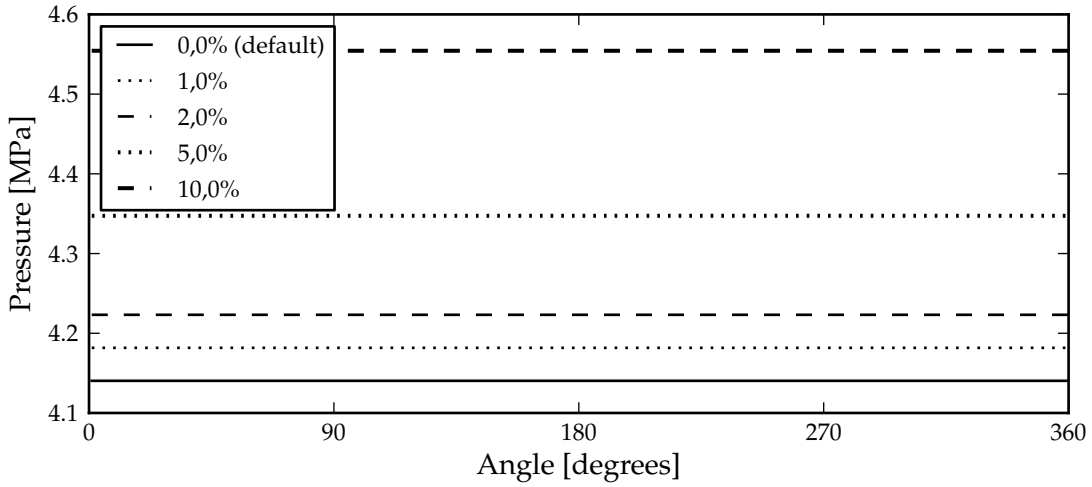

Figure C.77: Bounce space pressure for various average bounce space to compression space pressure differences.

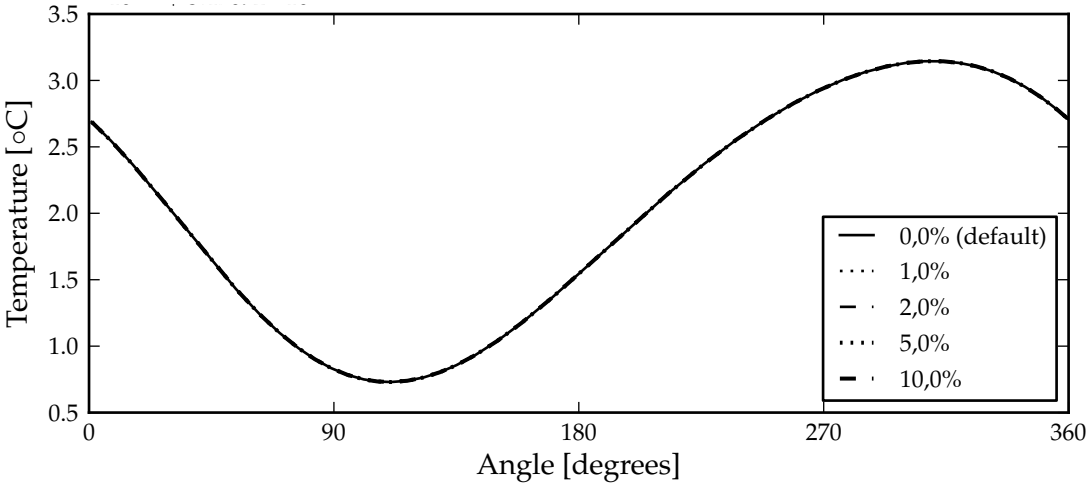

Figure C.78: Bounce space temperature for various average bounce space to compression space pressure differences.

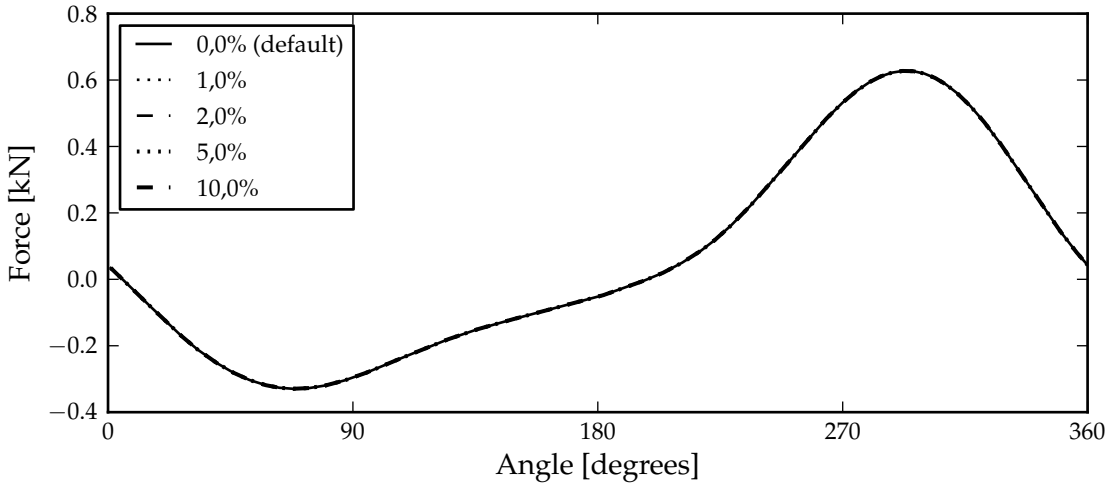

Figure C.79: Displacer linear machine force for various average bounce space to compression space pressure differences.

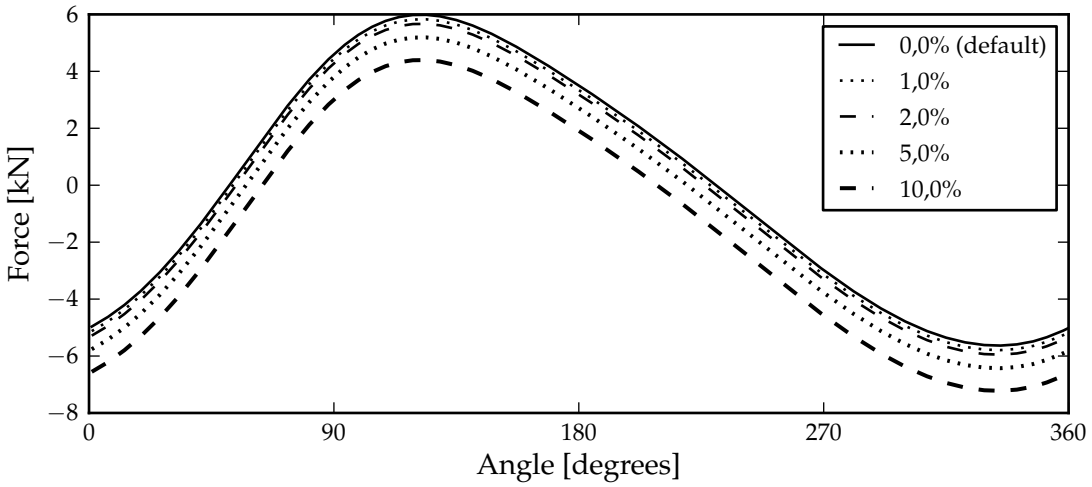

Figure C.80: Power piston linear machine force for various average bounce space to compression space pressure differences.

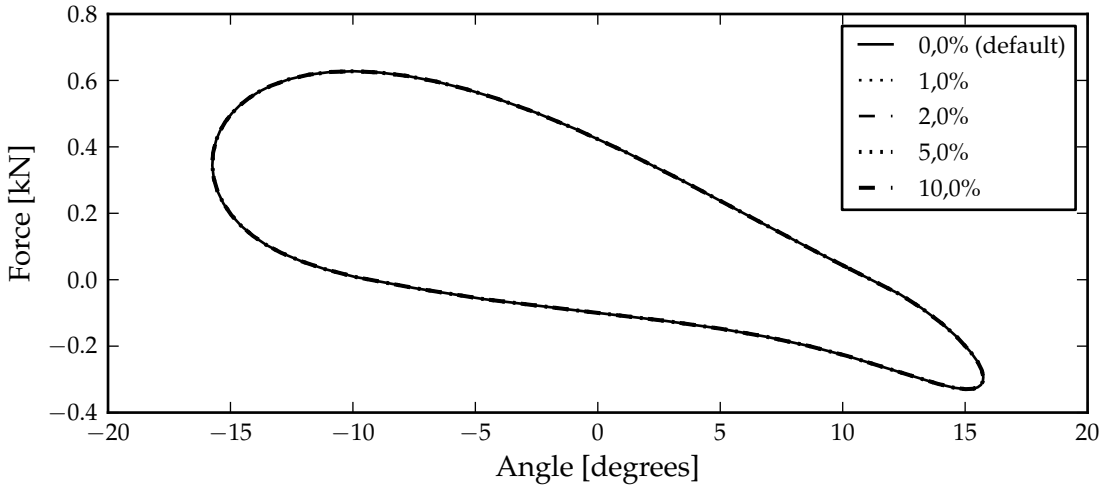

Figure C.81: Displacer linear machine force against displacement for various average bounce space to compression space pressure differences.

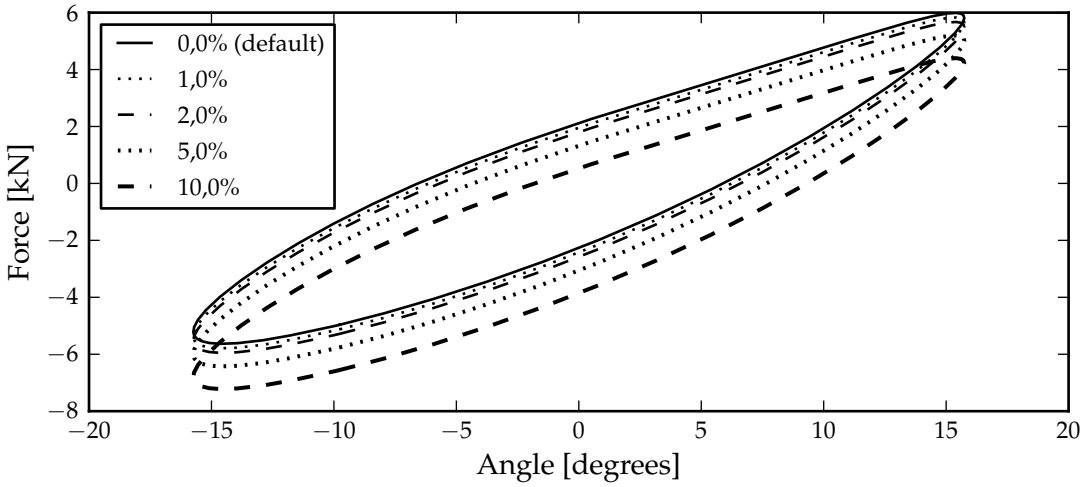

Figure C.82: Power piston linear machine force against displacement for various average bounce space to compression space pressure differences.

Appendix D

Final distributions

Table D.1: Figure listing of the final distributions of various combinations of variations.

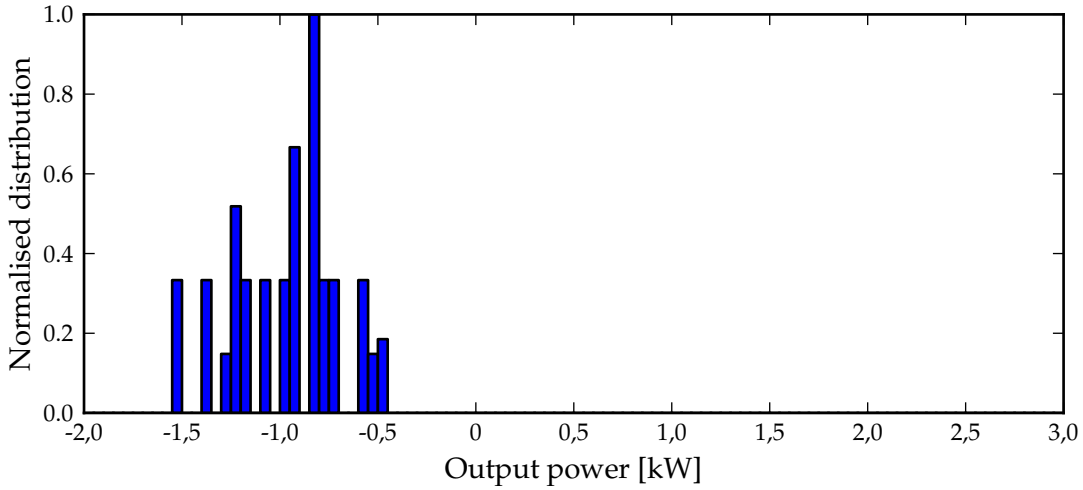

Figure D.1: Normalised distribution of the displacer electrical machine output power for only the operational variations.

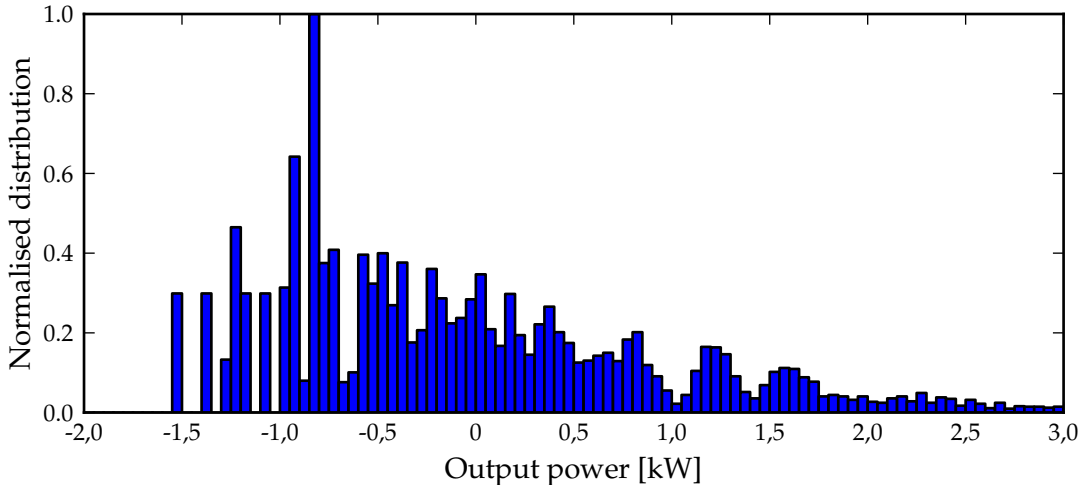

Figure D.2: Normalised distribution of the displacer electrical machine output power for the extended set of variations.

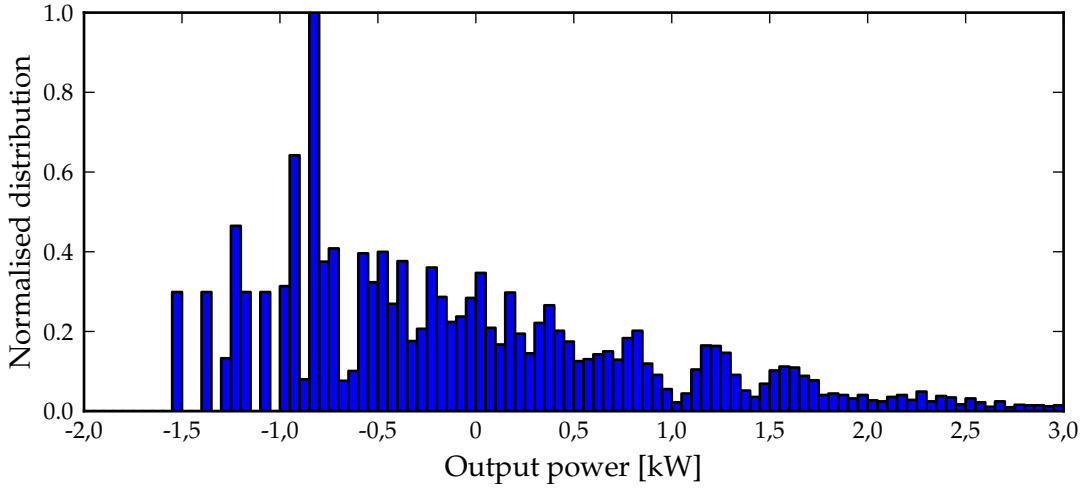

Figure D.3: Normalised distribution of the displacer electrical machine output power for all variations.

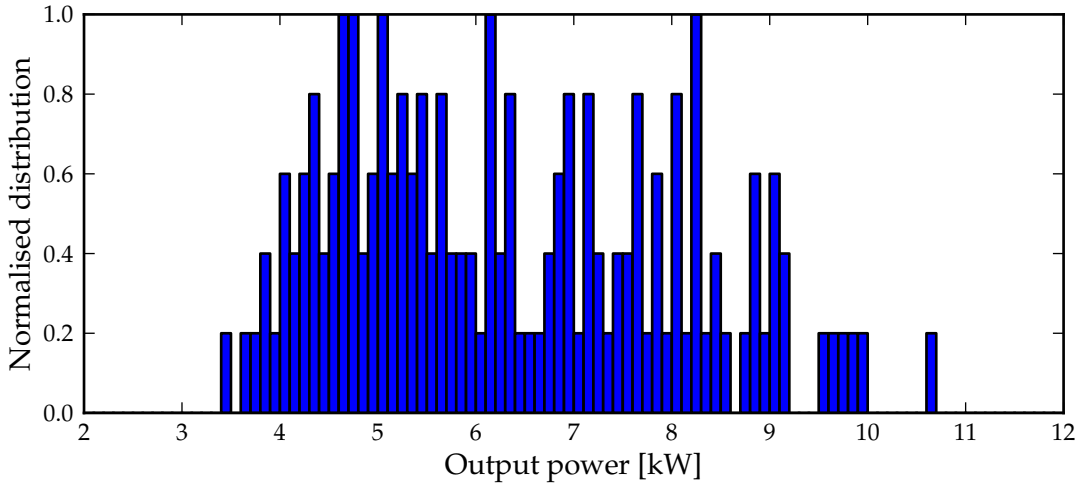

Figure D.4: Normalised distribution of the power piston electrical machine output power for only the operational variations.

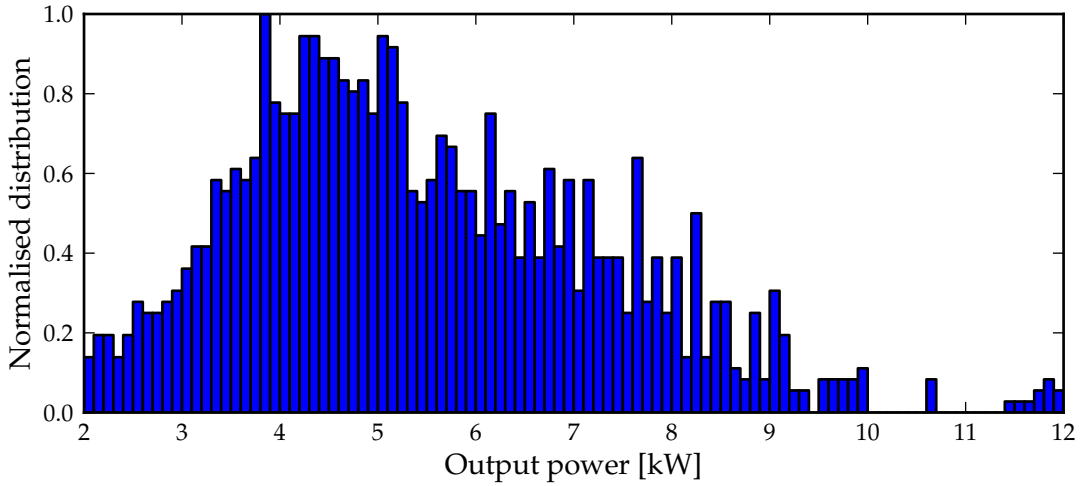

Figure D.5: Normalised distribution of the power piston electrical machine output power for the extended set of variations.

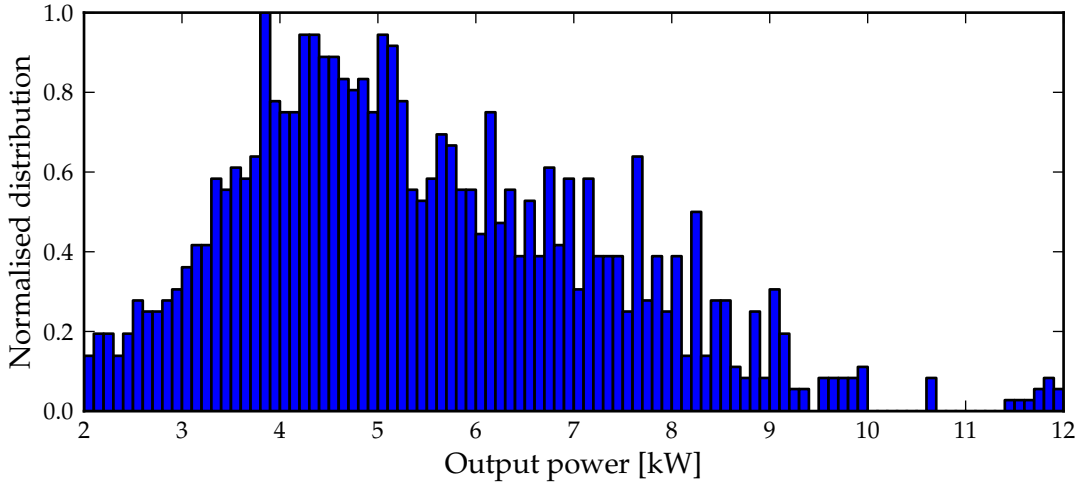

Figure D.6: Normalised distribution of the power piston electrical machine output power for all variations.

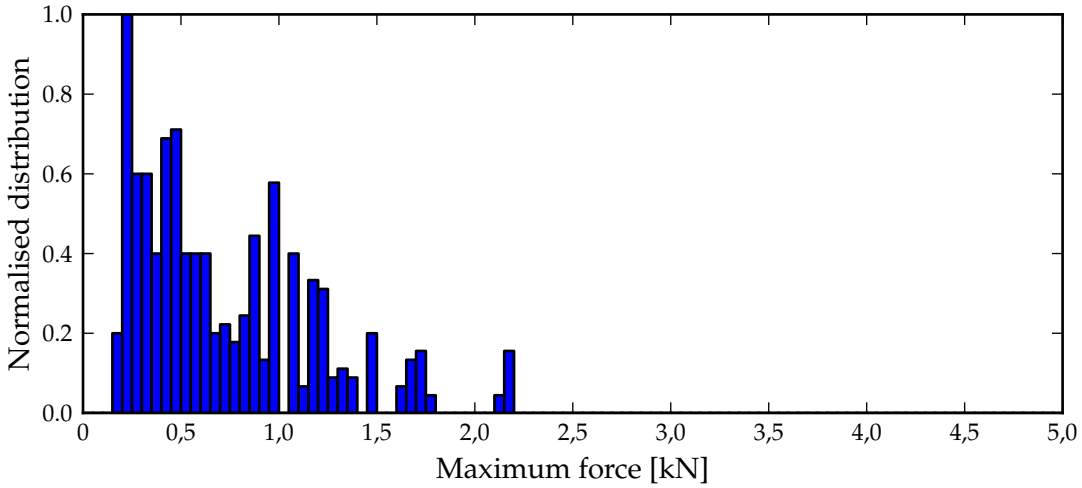

Figure D.7: Normalised distribution of the maximum force of the displacer electrical machine for only the operational variations.

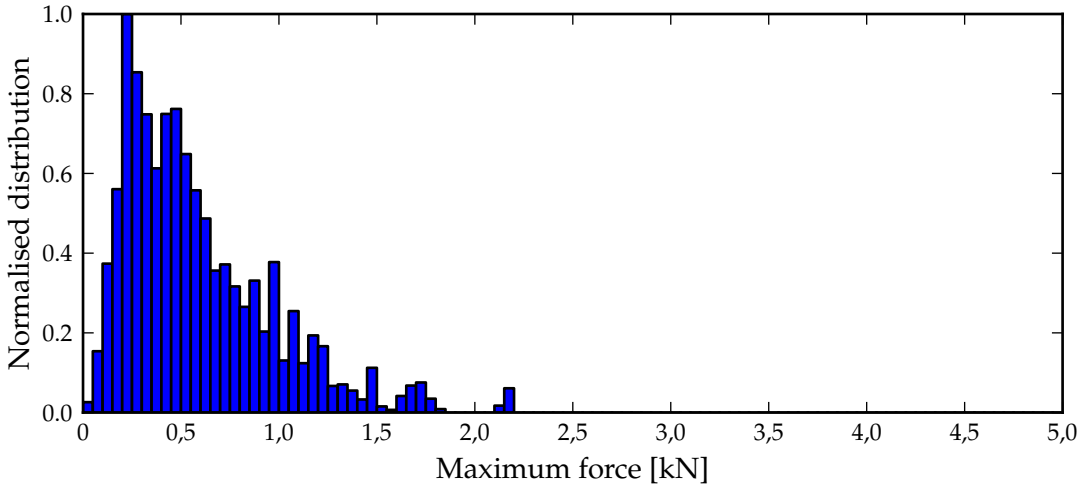

Figure D.8: Normalised distribution of the maximum force of the displacer electrical machine for the extended set of variations.

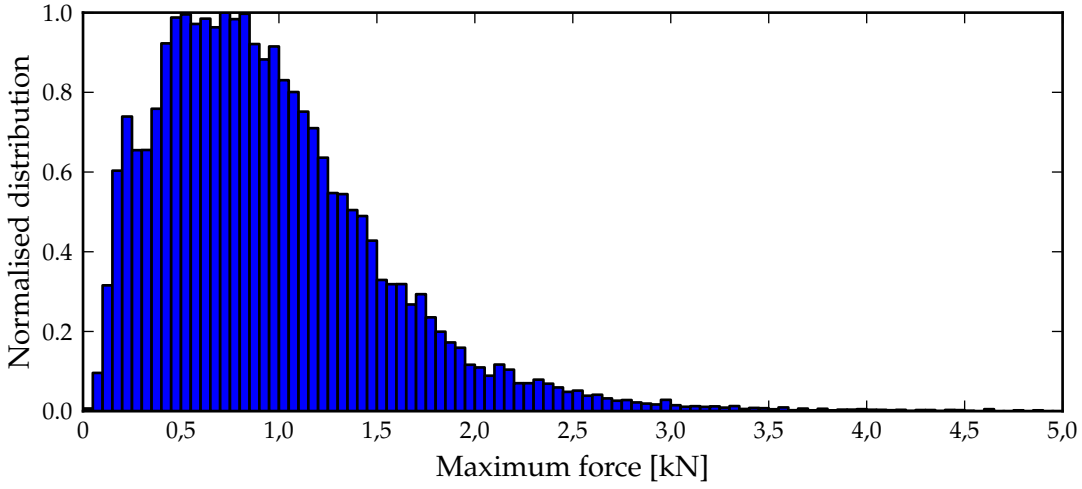

Figure D.9: Normalised distribution of the maximum force of the displacer electrical machine for all variations.

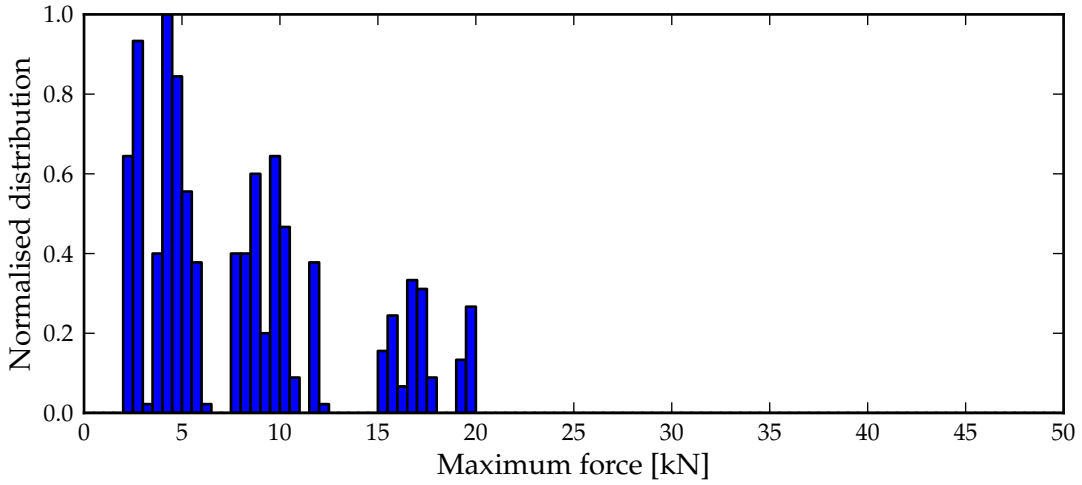

Figure D.10: Normalised distribution of the maximum force of the power piston electrical machine for only the operational variations.

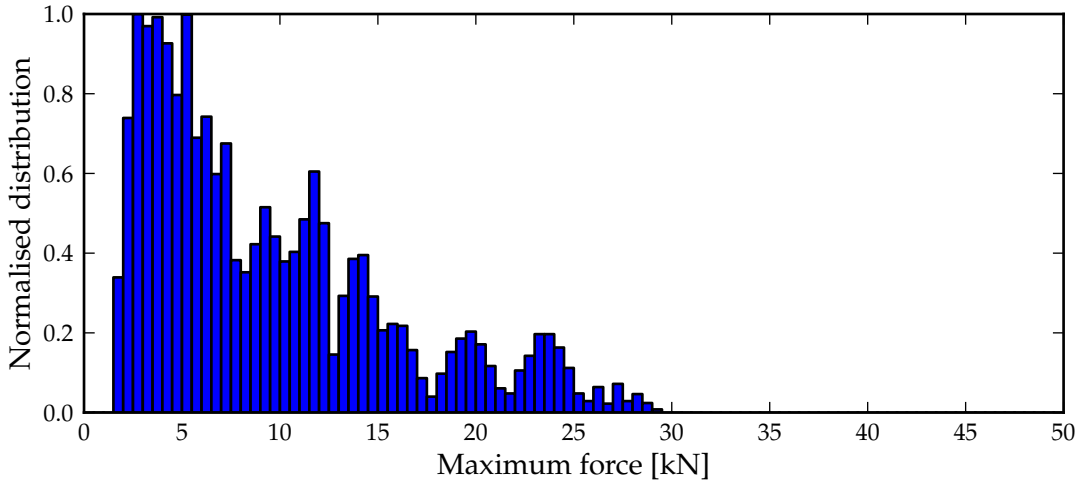

Figure D.11: Normalised distribution of the maximum force of the power piston electrical machine for the extended set of variations.

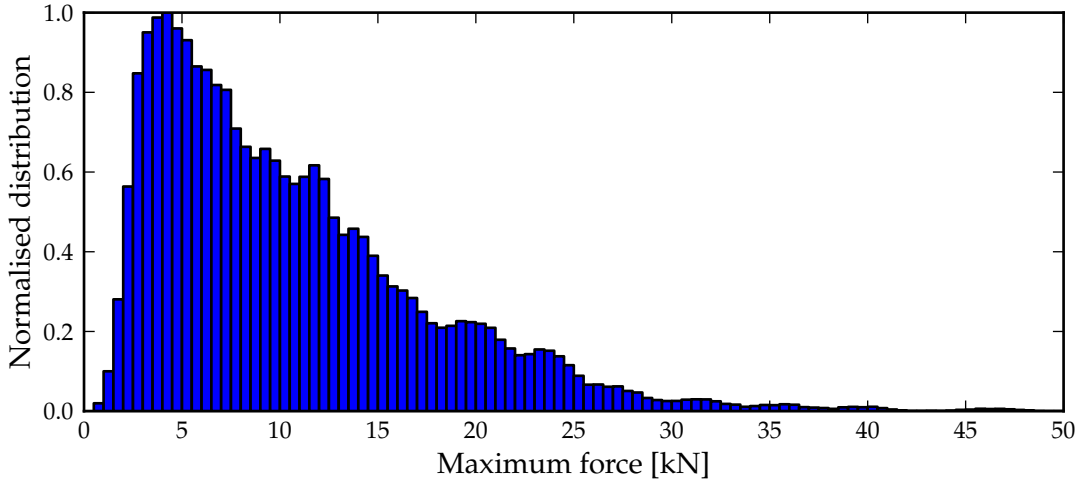

Figure D.12: Normalised distribution of the maximum force of the power piston electrical machine for all variations.

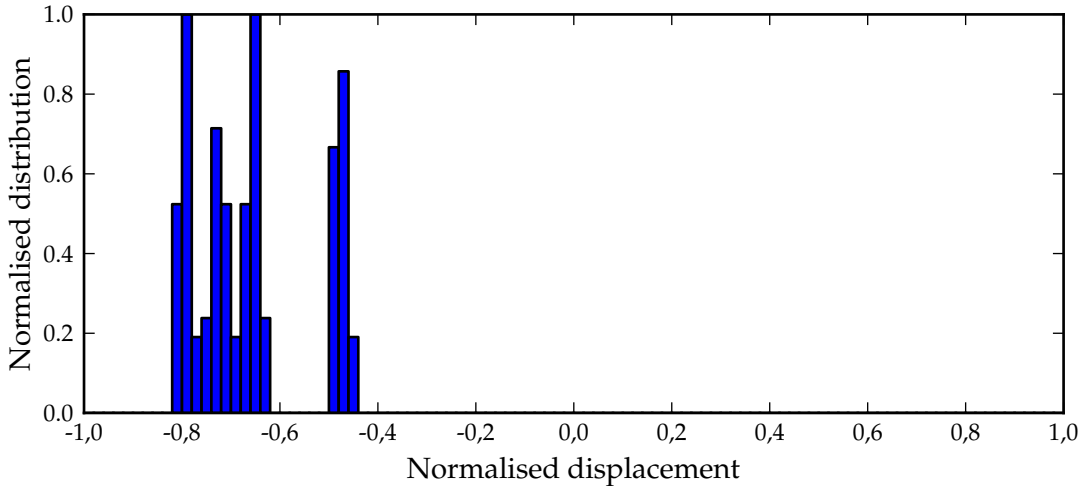

Figure D.13: Normalised distribution of the normalised location of maximum force of the displacer electrical machine for only the operational variations.

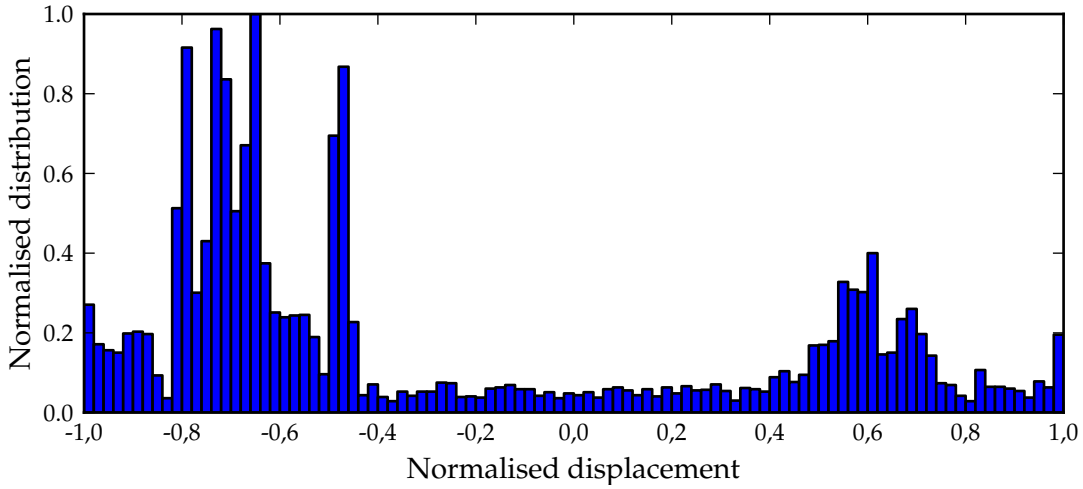

Figure D.14: Normalised distribution of the normalised location of maximum force of the displacer electrical machine for the extended set of variations.

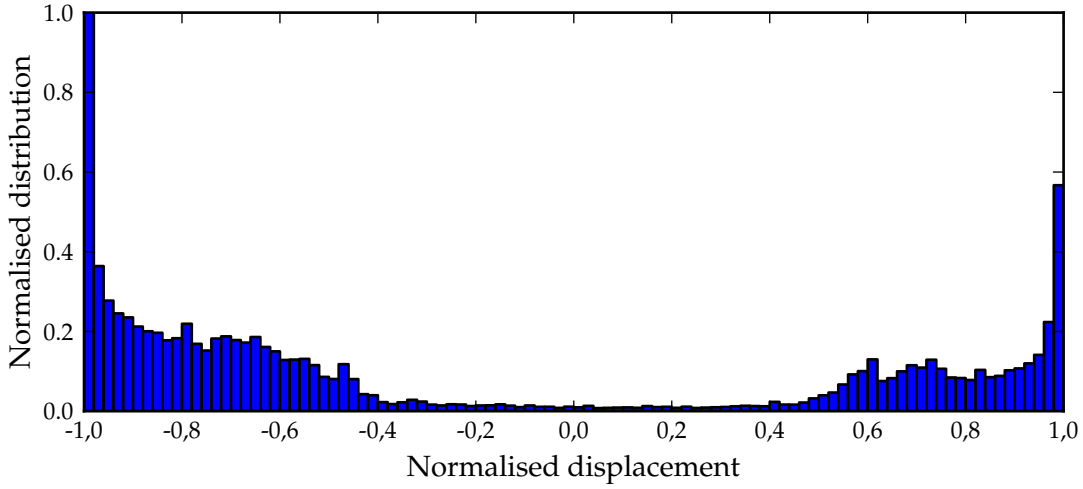

Figure D.15: Normalised distribution of the normalised location of maximum force of the displacer electrical machine for all variations.

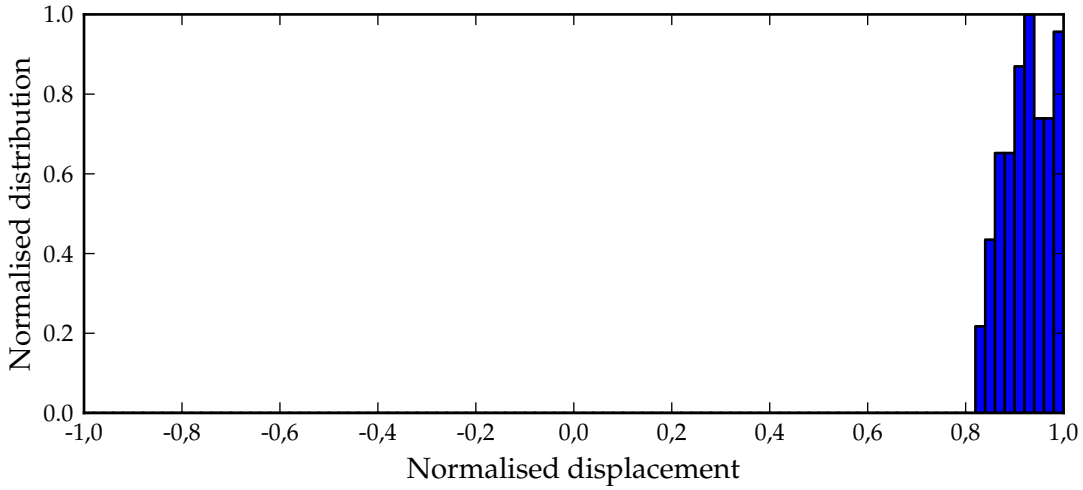

Figure D.16: Normalised distribution of the normalised location of maximum force of the power piston electrical machine for only the operational variations.

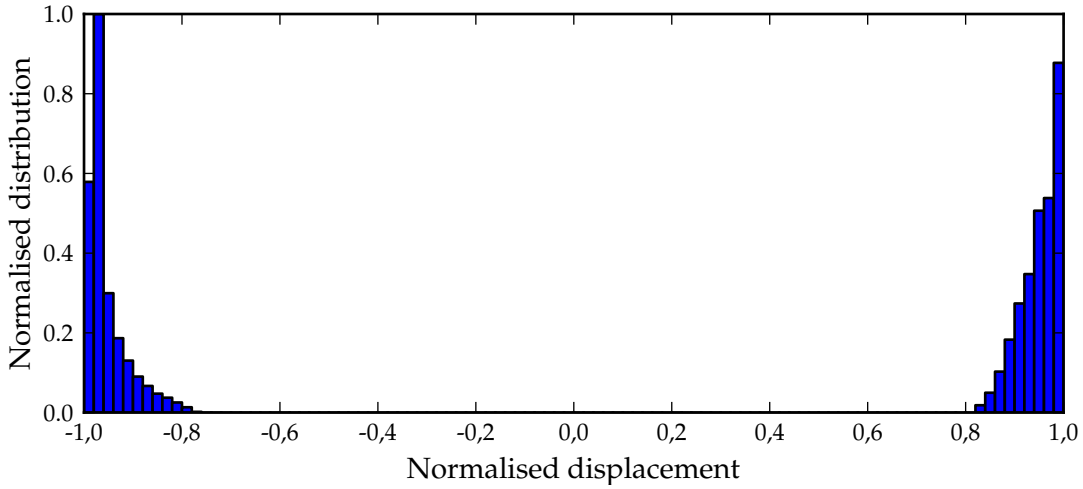

Figure D.17: Normalised distribution of the normalised location of maximum force of the power piston electrical machine for the extended set of variations.

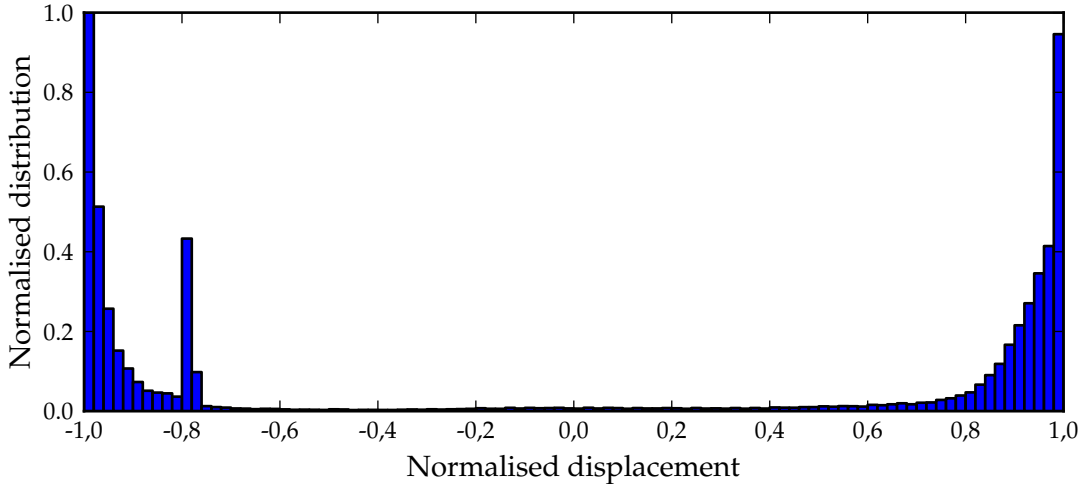

Figure D.18: Normalised distribution of the normalised location of maximum force of the power piston electrical machine for all variations.

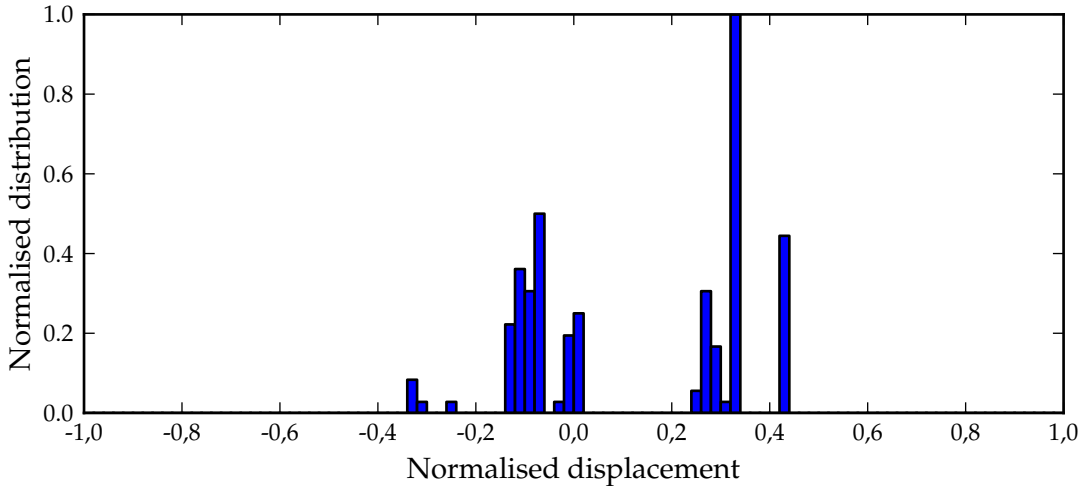

Figure D.19: Normalised distribution of the normalised location of maximum rate of change of force of the displacer electrical machine for only the operational variations.

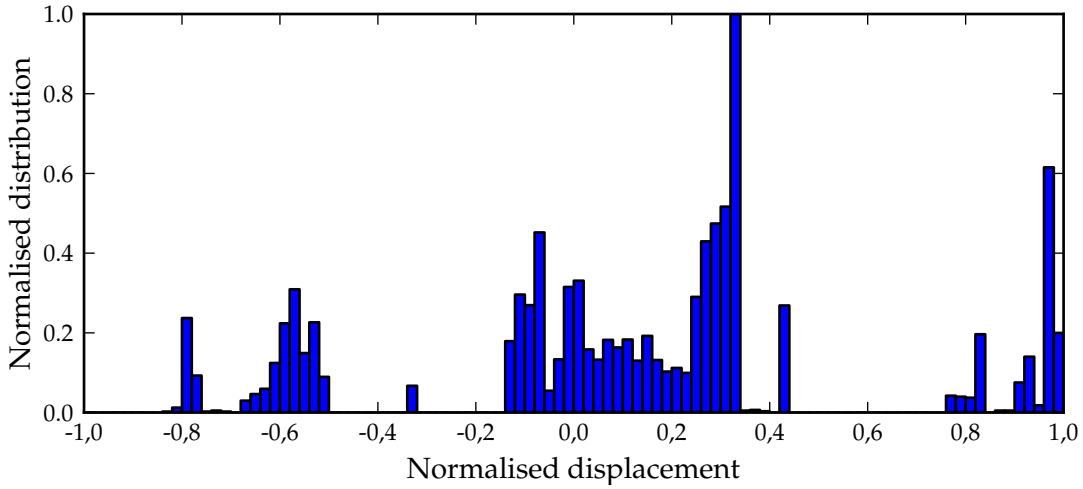

Figure D.20: Normalised distribution of the normalised location of maximum rate of change of force of the displacer electrical machine for the extended set of variations.

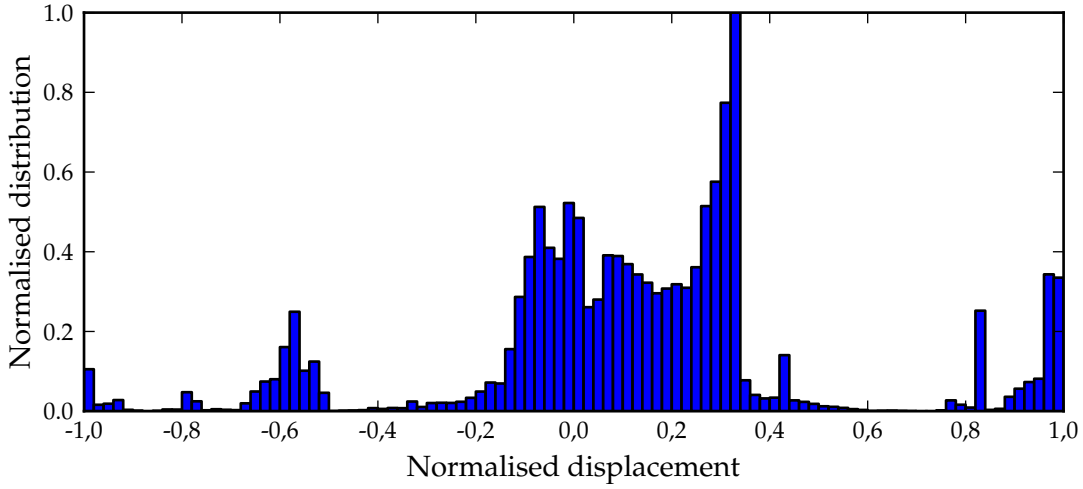

Figure D.21: Normalised distribution of the normalised location of maximum rate of change of force of the displacer electrical machine for all variations.

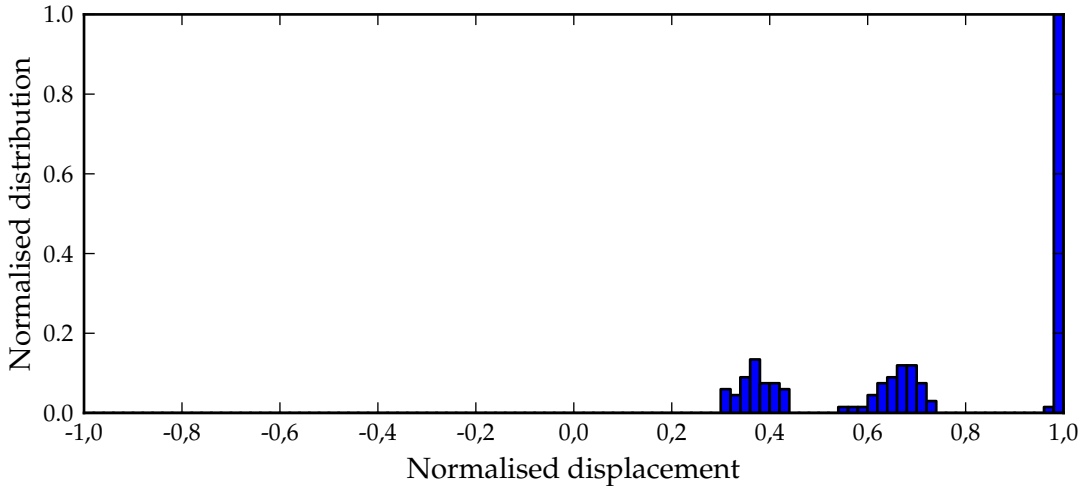

Figure D.22: Normalised distribution of the normalised location of maximum rate of change of force of the power piston electrical machine for only the operational variations.

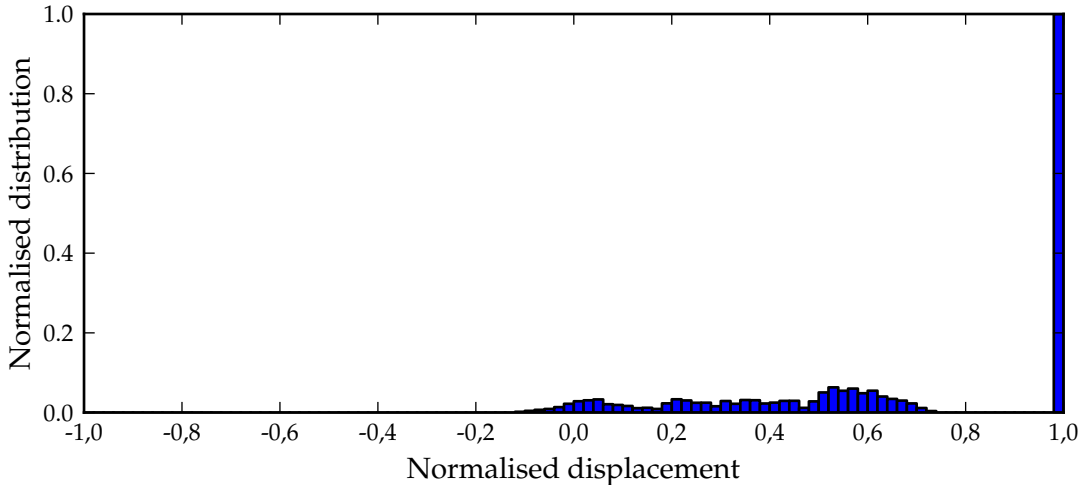

Figure D.23: Normalised distribution of the normalised location of maximum rate of change of force of the power piston electrical machine for the extended set of variations.

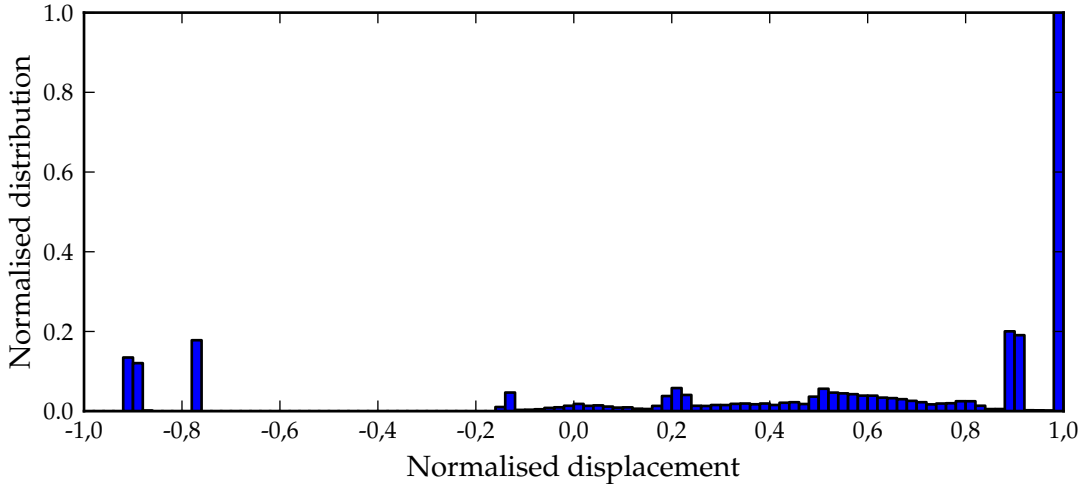

Figure D.24: Normalised distribution of the normalised location of maximum rate of change of force of the power piston electrical machine for all variations.